Tracing Gas Interaction and Mixing Processes in Natural Gases from the Sichuan and Bohai Bay Basins, China: Geochemical Insights from Noble Gas Isotopic Signatures

A Dissertation Presented

By

Jamie Robert Beagle

This dissertation is submitted to the Graduate School of Lancaster University in fulfilment of the requirements for the degree of

Doctor of Philosophy

Ph.D.

[13/01/2025]

Dedication

I would like to express my deepest gratitude to my fiancée, whose unwavering support has been a beacon of light throughout my PhD. Your belief in me has been a source of strength and inspiration. To my mum and dad, your endless love, encouragement, and sacrifices have not gone unnoticed. The time I have devoted to my studies has often meant being absent for significant moments, yet you have shown nothing but understanding and patience. It is with heartfelt thanks that I acknowledge the integral role each of you has played in reaching this milestone in my academic career.

I would also like to thank my academic supervisor, Dr. Zheng Zhou. Your advice and expertise have been invaluable in shaping my research, and I am grateful for the time you have dedicated to my academic development.

Quote

“天将降大任于斯人也，必先苦其心志，劳其筋骨，饿其体肤，空乏其身，行拂乱其所为，所以动心忍性，曾益其所不能。”

《孟子 • 告子下》

“When one is destined for great responsibility, they are first tested by hardship: their will is challenged, their body exhausted, they are subjected to difficulties, and their actions disrupted. Through these trials, their mind is stirred, patience is cultivated, and their abilities are enhanced.”

— Mencius, 4th Century BCE

Declaration

This thesis is an original piece of work that has not been submitted for consideration towards any other degree, either at this institution or elsewhere. The research presented here is my own, with collaborative contributions clearly acknowledged where relevant. Several of the concepts explored in this work were developed through discussions with my academic supervisor, Dr. Zheng Zhou.

Jamie Robert Beagle
MSc Petroleum Geoscience, BSc Earth and Ocean Science

Lancaster University, UK

Acknowledgements

I would like to express my sincere gratitude to several individuals who have provided invaluable support and assistance throughout the course of my research.

Firstly, I am deeply thankful to Dr. Greg Holland from the Department of Earth and Environmental Sciences at The University of Manchester for his guidance and expertise, as well as to his PhD student, Dr. Wanxu Zhong, for providing laboratory assistance that was essential to the successful completion of this work.

I also wish to extend my appreciation to Dr. Chunhui Cao from the Northwest Institute of Eco-Environment and Resources at the Chinese Academy of Sciences in Lanzhou, China, and Dr. Wen Zhang from the Chinese Academy of Geological Sciences in Beijing, China, for their training and mentorship in noble gas mass spectrometry methods, which have significantly contributed to the analytical aspects of this research.

Moreover, I am grateful to Professor Yunpeng Wang and Dr. Chengsheng Chen from the Guangzhou Institute of Geochemistry, Chinese Academy of Sciences in Guangzhou, China, for their insightful discussions and generous assistance during my time based in China, which greatly enriched my research experience.

Table of Contents

Table of Figures

Table of Tables

List of acronyms and abbreviations

MS – Mass Spectrometry

NGMS – Noble Gas Mass Spectrometry, a specific technique used for analysing noble gas isotopes

QMS – Quadrupole Mass Spectrometer

GC-MS – Gas Chromatography-Mass Spectrometry, used for separating and analysing complex gas mixtures

NGR – Noble Gas Ratio, often used to describe the relative concentrations of noble gases in samples

ASW – Air-Saturated Water, referring to equilibrium concentrations of noble gases dissolved in water at known conditions

BBB – Bohai Bay Basin, a significant petroleum-producing basin in northeast China, known for its complex tectonics and rich oil and gas reserves, playing a crucial role in China's energy production

HHD – Huanghua Depression, a key oil and gas-rich sub-basin within the Bohai Bay Basin, is characterised by thick sedimentary deposits and structural complexity, making it a significant focus for hydrocarbon exploration

DUM – Degassed upper mantle refers to the part of the mantle that has undergone significant degassing, especially of volatile elements like noble gases, due to tectonic processes such as plate subduction, volcanism, and mantle convection.

PLM – Primordial lower mantle, the deep, undegassed portion of the Earth's mantle, which retains a composition close to that of the early Earth. This region is thought to have preserved some of the original noble gases and isotopic ratios from the formation of the planet, making it crucial for studying Earth's early geochemical evolution

TOC – Total organic carbon content, the measure of the amount of carbon in an organic compound

VSMOW – Vienna Standard Mean Ocean Water, the standard reference for the isotopic composition of water that uses hydrogen isotope data

VPBD – Vienna Pee Dee Belemnite, the standard isotope reference for carbon that describes the relative abundance of ^{13}C and ^{12}C

Elements, Isotopes & ratios

He – Helium

Ne – Neon

Ar – Argon

Kr – Krypton

Xe – Xenon

U-Th-K – Uranium, Thorium and Potassium

$\delta^{13}C$ – Carbon-13 Isotope Ratio

δD – Deuterium Isotope Ratio (Hydrogen isotope)

R/R_a –The ratio of the measured helium isotope ratio to the atmospheric helium isotope ratio ($^3He/^4He$ of air = 1.4×10^{-6})

Selected units, constants and parameters

‰ – Per mille (parts per thousand)

GPa – Gigapascal, 10^9 Pa, the SI unit of pressure, where 1 pascal is defined as 1 N/m^2.

atm – Atmospheres, a unit of pressure that is equal to 101,325 Pa

bar – Non-SI unit of pressure, equals 10^4 pascals

cm^3 STP/cm^3 – Volume of gas (at standard temperature and pressure, STP) per unit volume (used in noble gas concentration)

ppm – Parts per million

V_g/V_w – The ratio of the volume of gas to the volume of water in a system, which helps in understanding gas-water partitioning

R – Gas constant that appears in the ideal gas law, 8.31434 J/mol-K

Chapter 1 Synthesis of research

1.1 Background and Rationale:

The principal aim of this body of research work is to compile and study the noble gas (He, Ne, Ar, Kr, Xe) inventory, bulk chemical composition (CO_2, N_2, H_2 etc.) and stable carbon and hydrogen isotopic ($\delta^{13}C_{C1-C5}$ and δD_{C1-C2}) geochemistry of multiple petroliferous basins within China, including the Sichuan Basin in southwest China and the Bohai Bay Basin in northeast China, both of which comprise conventional and unconventional petroleum systems at varying depths (<5000m). The Sichuan and Bohai Bay sedimentary basins have distinctive tectonic evolutions, which have given rise to contrasting migration, accumulation, reservoir and source rock characteristics.

Noble gases have played a pivotal role in our understanding of Earth's mantle-crust dynamics and the processes that influence the composition of the atmosphere and terrestrial reservoirs. Noble gas geochemistry represents a key component in shedding light on these complex geologic processes and the significance of meteoric waters in altering the signature of crustal fluids through mixing and partitioning due to phase changes and solubility. The application of noble gases as geochemical tracers also represents an incredibly useful tool in furthering our understanding of Earth's accretion and evolution and is equally applicable in studies that look to gain a deeper understanding of more recent fluid mixing and phase interactions in the subsurface. Helium (He) isotopic ratios, specifically the $^{3}He/^{4}He$ ratio, have long been recognised for their potential to determine the extent of mantle-crust mixing. Given that most of Earth's He originates from radioactive decay within the crust, this isotope system acts as a sensitive tracer for delineating between deep mantle-derived helium and that of atmospheric influence.

However, He is just one of a broader set of noble gases that contribute to our knowledge of geochemical processes. The isotopic and elemental ratios of radiogenic, nucleogenic and atmospheric neon ($^{20}Ne/^{21}Ne$ and $^{21}Ne/^{22}Ne$), Argon ($^{40}Ar/^{36}Ar$), krypton ($^{84}Kr/^{36}Ar$), and xenon ($^{132}Xe/^{36}Ar$) further enrich our geochemical understanding; Neon isotopes, for example, can offer insights into solar and cosmogenic contributions, helping to decipher primordial signatures and atmospheric interactions. Argon isotopes, particularly $^{40}Ar/^{36}Ar$, shed light on the Earth's radiogenic heat production and the timing of geological events through the decay of potassium. Krypton and xenon, reveal the role of adsorption and desorption processes and volatile retention

and loss throughout Earth's history, highlighting the intricacies of atmospheric evolution and planetary outgassing.

Further importance of this work stems from the scarcity of studies that focus specifically on noble gas geochemical research within the Sichuan Basin and Bohai Bay Basin, and as a result, their varied geochemical behaviour within the broader tectonic context remains largely unexplored. As the world grapples with energy challenges, understanding the geochemistry of oil and gas basins like the Sichuan Basin and Bohai Bay Basin can guide exploration efforts and shed light on the deeper geological processes influencing hydrocarbon generation and migration. This research also relates to broader themes such as sustainability, and moreover, as helium becomes an increasingly vital resource for modern technologies and medicine, understanding its geochemical behaviour and reservoir distribution becomes even more paramount.

This *synthesis* aims to connect the research carried out throughout this PhD project with the adjoining three research papers while providing a summary of the major literature, theoretical models, and methodology that have informed and underpinned this body of work.

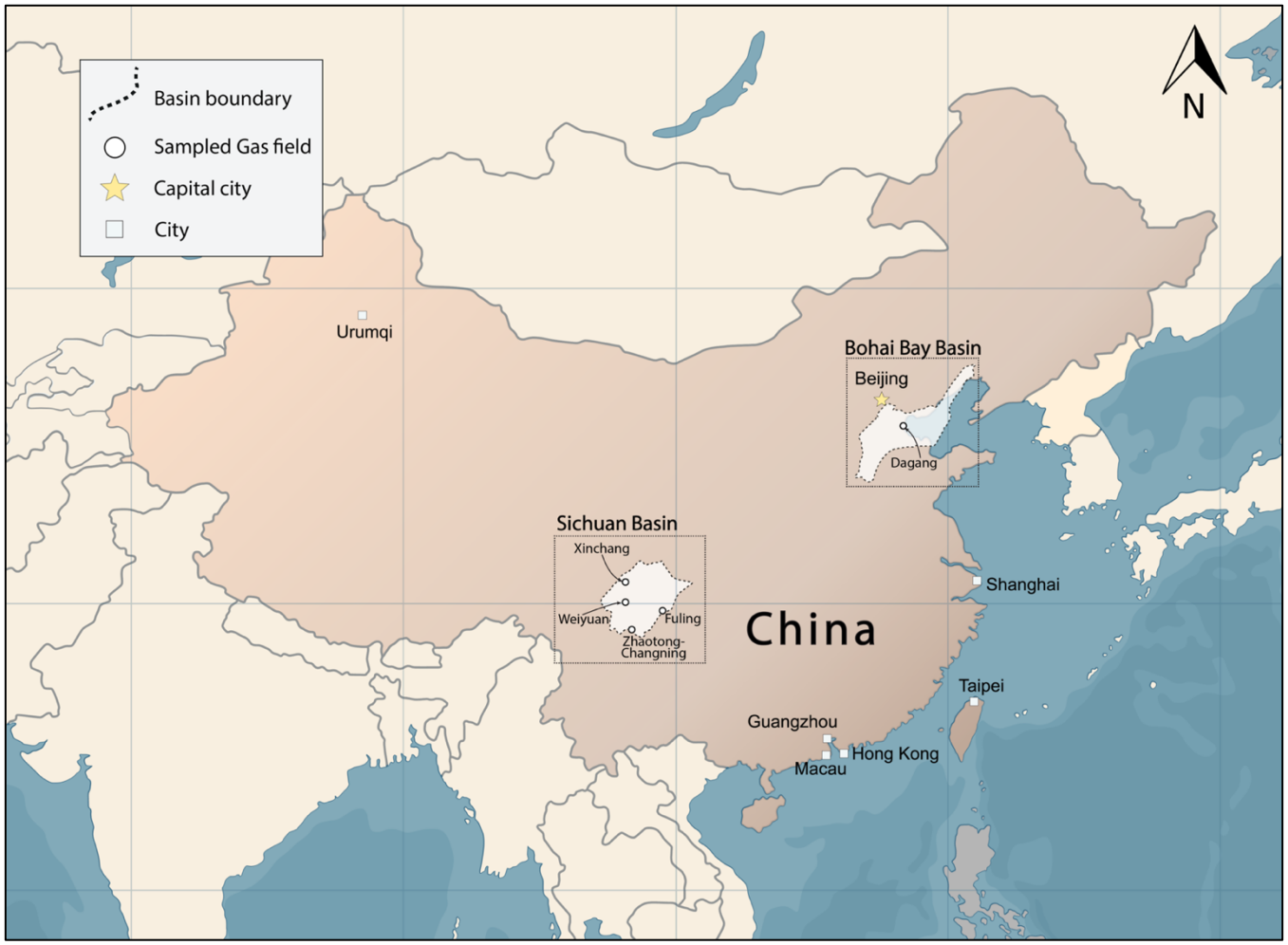

Figure 1 - Map of studied sedimentary basins (Sichuan Basin in southwest China and the Bohai Bay Basin in northeast China) and their regional context within China and continental Asia. Basin boundaries have been delineated, and the sampled gas fields that contributed to this research have also been provided within each domain and are denoted by circles.

1.2 Specific Research Context:

This thesis integrates the fields of noble gas, carbon and hydrogen isotope geochemistry, with a focus on unconventional oil and gas basins in China. This research employs a multidisciplinary approach, blending advanced geochemical methods and mathematical modelling to explore the behaviour of noble gases in the context of diverse geological and tectonostratigraphic frameworks.

Two key geographic regions are focused on; the Sichuan Basin in southwestern China and the Bohai Bay Basin in north-eastern China (as shown in Figure 1). These two basins hold considerable significance in oil and gas exploration and production, both regionally in China and on a global scale. The Sichuan Basin is one of China's oldest and most prolific hydrocarbon-producing regions, featuring extensive reserves of natural gas (CH_4). It is particularly well-known for its shale gas potential, especially in the Wufeng-Longmaxi shale (Borjigin et al., 2017, Cao et al., 2020b, Chen et al., 2021a, Dai et al., 2016, Dong et al., 2015, He et al., 2022, Jiang et al., 2021, Li et al., 2022, Li et al., 2021a, Liu et al., 2021a, Qiu and Zou, 2019, Wang et al., 2020a, Xiao et al., 2021, Zhang et al., 2021b, Zhao et al., 2016a). The basin is also noteworthy for its complex geological structures, which offer a variety of trapping mechanisms and reservoir types, which are ideal for investigating the behaviour of noble gases in these systems. The Bohai Bay Basin is similarly one of the largest oil-producing areas within China. It is characterised by its shallow marine deposits and rich source rocks, such as the Eocene Shahejie formation. The Bohai Bay Basin has garnered academic and commercial attention, in part because of its strategic proximity to nearby major industrial and population centres such as the capital city of China; Beijing. Studies within the Dagang field in the Huanghua depression yield valuable data on how oil and gas reservoirs form and how gases behave in shallow marine environments despite or owing to the influence of high heat flows through the upwelling of magma (Dong et al., 2022, Chen and Zhang, 1991, Jin et al., 2019, Liu et al., 2017, Liu et al., 2021c, Pu et al., 2018, Pu et al., 2013, Pu et al., 2011, Wang et al., 2022b, Wang et al., 2022d, Yang et al., 2022, Yang et al., 2020, Yang et al., 2021b, Yuan et al., 2021, Zhang et al., 2019a, Zhang et al., 2008, Zhao et al., 2019, Zhao et al., 2020, Zhou et al., 2021). Our understanding of these formation processes is critical for informing exploration and recovery strategies in China and analogous sedimentary basins worldwide. The use of noble gases serves as a detailed diagnostic tool uniquely suited to reveal the geochemical, geological, and tectonostratigraphic complexities of these geodynamic settings (Ballentine et al., 2002, Ballentine and Burnard, 2002, Eymold

et al., 2021, Graham, 2002, Hilton et al., 2002, Hunt et al., 2012, Kipfer et al., 2002, Marty, 1984, Prinzhofer, 2013, Sano et al., 2013, Schlosser and Winckler, 2002, Zhou et al., 2005, Zhou and Ballentine, 2006, Zhou et al., 2012). By applying noble gas geochemistry, this study aims to generate new insights into reservoir characteristics, fluid migration, and basin evolution, thus contributing to a more comprehensive understanding of these critical energy reserves in China.

Noble gases comprise a rare and inert group of elements with ideal characteristics to be used as geodynamic tracers (Ozima and Podosek, 2002). These gases inhabit the last column of the periodic table, comprising 5 elements measured throughout this study for their abundance: helium (He), neon (Ne), argon (Ar), krypton (Kr), xenon (Xe), and additionally, radon (Ra) which has a half-life of just 3.8 days, decaying too quickly to be of use for subsurface fluid tracing over extensive geological time periods (Prinzhofer, 2013). All the noble gases have fully filled outer valance shells, resulting in their inability to bond with potential atoms via a chemical reaction and rendering them unreactive. At high temperatures, Xe, which is highly electronegative, will strongly attract electrons, resulting in this element bonding via hyper-valency (where the Lewis octet rule is broken) with other elements such as F or O, which in the natural environment are already bound to more reactive elements (Burnard et al., 2013), however, at the conditions relevant to the natural processes on Earth, noble gases do not readily form compounds, and this is fundamental to their use as tracers.

The analytical utility of noble gases is derived from their unique properties, the lack of chemical reactivity, scarcity, overall inertness, and ability to diffuse relatively rapidly in low-pressure, high-temperature environments. Noble gases are often trapped in crystals, where vital information about the Earth's history is stored, such as the degassing history of the mantle and magmas and the mixing relationships which occur between different mantle components, as well as the formation of the atmosphere itself (Anderson, 2007). There are two principal sources of noble gases within the Earth: noble gases trapped during accretion (termed 'primitive', 'juvenile' or 'primordial gases') and, secondly, noble gases produced through radioactivity (which is discussed in detail in the following sections).

Research papers utilising noble gases as the basis for their analytical study into the geochemical characteristics of gases in the Sichuan and Bohai Bay Basin are wide-ranging; however, areas remain unexplored, and questions remain unanswered. The current state of research within the Sichuan Basin has looked at the fractionation of noble gas ratios to

show the presence of oil in the Wufeng-Longmaxi Shale (Liu et al., 2021a) and the He, Ne and Ar abundances of these shales to denote a mixed crustal, atmospheric and radiogenic origin (Cao et al., 2018). Weiyuan and Changning gases have also been analysed for their source and evolution history (Cao et al., 2020a), while a crustal helium component has also been exhibited in the Lower Silurian shale gases, with R/R_a = 0.01-0.05 (Feng et al., 2020) and 0.01-0.03 (Dai et al., 2014).

In principle, noble gas fractionation in groundwater can provide a sensitive and quantitative tool with which to identify both natural gas and oil migration pathways (Zaikowski and Spangler, 1990), which are poorly understood in both of the two basins investigated in this thesis. Additional context for studying the noble gas geochemistry of the Sichuan Basin was to understand the relevance of adsorption and to permit a useful adsorption model that explains the observable excesses in Kr and Xe elemental ratios ($^{132}Xe/^{36}Ar$, $^{84}Kr/^{36}Ar$) in gas samples. Adsorption of noble gases is a process whereby molecules of a gas are concentrated at the surface of a solid (the sorbent) (Ozima and Podosek, 2002); however, our understanding of this phenomenon and its relevance to noble gases is similarly incomplete. The examination of noble gas adsorption behaviour in contrasting reservoir settings, specifically Wufeng-Longmaxi shales and tight sandstone formations in the Sichuan Basin, holds significance, as this research will offer a comprehensive assessment of the adsorption characteristics of noble gases between unconventional shale and tight sandstone reservoirs within juxtaposing gas fields, thereby mitigating variables like unique tectonic histories or diagenetic influences that might otherwise confound the data. This study subsequently provided the ideal opportunity to better constrain complex fractionation processes that occur between gaseous, liquid and solid thermodynamic phases. By building upon the present literature, it is possible to derive a framework for adsorption using pre-existing adsorption isotherms and the approximation of Henry's law (section 1.3.9, page 40) to constrain adsorption volumes.

In the Bohai Bay basin, further research interest arises from an entirely distinctive basin evolution. The investigation into noble gases in the Bohai Bay Basin offers a particularly compelling avenue of research for many reasons: the basin is geologically complex and shallower than the Sichuan Basin, with a magmatic influence derived from the subduction of the 'Izanagi plate stagnant slab', which introduces another layer of complexity to the data. Magmatic activity has imbued the local noble gas inventory (i.e., $^{3}He/^{4}He$ ratios) with unique isotopic signatures that differ substantially from those in the Sichuan Basin, thereby providing a remarkable natural laboratory to study the interaction

between mantle-derived and crustal gases. The resultant variable input of mantle-derived material in gas samples and the nature of methane and hydrogen generation stemming from large-scale basin-wide tectonic processes permit us to apply noble gas and stable carbon and hydrogen isotope geochemistry to give a clearer representation of the complex subsurface gas-liquid generation and mixing processes.

Moreover, the analysis of stable carbon and hydrogen isotopes and bulk geochemistry of gases in the Sichuan Basin and Bohai Bay Basin wholly complements the suite of noble gases and strengthens our understanding further. By correlating these stable isotopes with noble gas concentrations, this research aims to offer an integrated perspective on the genesis of key gases like CH_4, CO_2, and H_2. This comprehensive approach aims to shed light on the mechanisms that control gas generation, migration pathways, and accumulation, which is fundamental for understanding basin evolution.

In summary, the Bohai Bay Basin offers a unique setting to examine noble gas behaviour under the influence of hydrothermal and shallow magmatism. This, in turn, promises to advance the study of noble gas geochemistry and make a substantive contribution to the fields of hydrocarbon exploration and resource management.

1.2.1 Geological background: The Sichuan Basin

The Sichuan Basin is a stable lithospheric, intracratonic sedimentary basin, located within the continental interior, which is to say it is singularly affected by the stresses of distant plate boundaries (Ingersoll, 1988). It currently one of China's largest gas-producing regions, covering a total area of 2.6 x 10^5 km^2 and comprises thick marine and continental strata up to 12km (Ma, 2017a). The basin is geographically bounded by the northern Micang and Daba mountains, in the south by the Daxiangling and Lou Mountains, in the west by the Longmen Mountain and in the east by the Dalou Mountains (enclosed in manuscript figures; Figure 20 and Figure 49 on pages 72 and 166, respectively). The basin is located on the western margin of the South China block, which consists of the Yangtze block in the northwest and Cathaysia block in the southeast, separated by the Jiangshan-Shaoxing-Pingxiang fault (Wang et al., 2023) and the Sichuan basin was once dominated by marine deposits overlying the relatively stable Yangtze interior craton during the Sinian to Ordovician (Liu et al., 2021b). The slab pull of the proto-Tethyan oceanic lithosphere was closely linked to global tectonic shifts that occurred during the breakup of Rodinia and the formation of Gondwana with neoproterozoic subduction and rifting (~820 Ma) recently uncovered from deep seismic reflection data (Gao et al., 2016) and Sinian to Lower Cambrian rifting episodes contributing greatly to deposition and gas generation (Li et al., 2019b).

Several distinct tectonic movements have contributed to the overall development of the Sichuan basin; these include the Caledonian (late Sinian-Silurian), Hercynian (Devonian-Permian), Indosinian (Triassic), Yanshanian (Jurassic-Late Cretaceous) and Himalayan (Paleo-Quaternary) (Zhang et al., 2013, Chen et al., 2017), the latter of these two events having the strongest influence on the overall structural morphology of the Sichuan Basin (Fan et al., 2020), as the Himalayan uplift is associated with the cessation of hydrocarbon generation (Yuan et al., 2012, Yang et al., 2016b, Xu et al., 2014).

The region tectonically evolved through the Silurian to Carboniferous to a marine-dominated foreland and a coastal passive-margin setting from the Permian to the Middle Triassic (Li et al., 2013, Liang et al., 2014, Li et al., 2015). These periods are evidenced by six major organic-rich shale formations (Dong et al., 2015), the Doushantuo Formation, Maidiping-Qiongzhusi Formation, the Wufeng-Longmaxi Formation, the Longtan Formation, the Xujiahe Formation, and the Zhiliujing Formation, which reflect the paleotectonic evolution from deep marine to lacustrine environment and the transition

from marine to terrestrial shales, when the basin underwent evolution into a foreland continental setting (Dai et al., 2018).

The widespread deposition of the Wufeng-Longmaxi shales (O_3w-S_1l) commenced following collision of the Cathaysia Plate and the Yangtze Plate (Liu et al., 1993) during two major global marine transgressions, when sea-levels rose (Zou et al., 2019, Feng et al., 2023). With a burial depth of 3500-5000m, these high quality shale reservoirs are considered 'ultra-deep' (Guo et al., 2022). The upper portion of the Longmaxi Formation consists predominantly of greyish green to yellowish green shale and sandy shale, with occasional interbedded layers of siltstone and argillaceous limestone. A noticeable increase in sandy content is observed from the base to the top of the stratigraphic sequence, indicative of an upward-coarsening depositional trend (Wang et al., 2021a). This sedimentary pattern likely reflects a progradational system driven by sediment influx (Zou et al., 2015). This facies variation suggests a dynamic depositional environment, consistent with the tectonic evolution of the basin. Total organic carbon (TOC) in the Wufeng-Longmaxi shale ranges from 2.0%-8.4%, while total porosity is between 4.6%-7.8%, 3.4%-8.4% and 3.3%-7.0% in the Fuling, Changning-Zhaotong and Weiyuan gas fields, respectively.

The Xujiahe tight sandstone formation (T_3x), located in the Xinchang gas field in the western Sichuan depression was deposited in a lakeshore setting with abundant marsh facies (Dai et al., 2012). The thickness of Xujiahe formation is 1800–2500m in the western Sichuan depression, while it becomes thinner in the central Sichuan uplift at between 600–1000m until it completely thins out to the southeast (Chen et al., 2007). It was charged by a series of interbedded coal measures and gas prone dark mudstones, the Xu-1, Xu-3 and Xu-5 members, (Wang et al., 1997), and TOC in the mudstone source rocks typically ranges from 0.5%-9.7% (Dai et al., 2009).

Further description of the characteristics of the Wufeng-Longmaxi shale and Xujiahe tight sandstone formations, including the geological setting and tectonic evolution of the Sichuan Basin can be found in later Chapters 2.3 and 4.3.

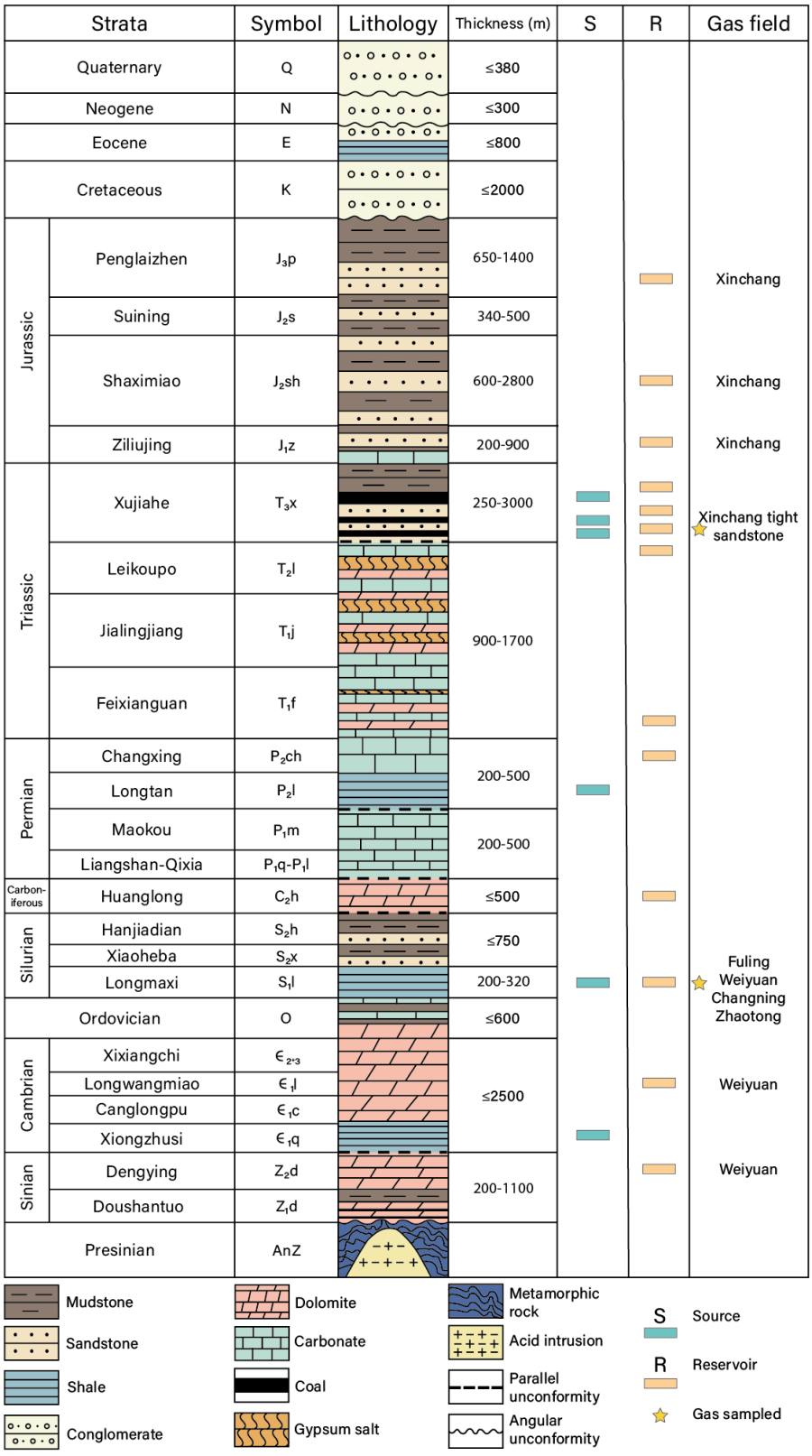

Figure 2 - Stratigraphic Column of the Sichuan Basin, which presents the main geological units spanning from the Quaternary to the Presinian period. Each stratum is characterised by its unique lithology, highlighting various rock types such as mudstone, sandstone, shale, and carbonate formations. The approximate thickness of each geological unit is given and known gas fields in the region are underscored, with both source (S) and reservoir (R) rocks shown. Key formations like the Xinchang tight sandstone are specifically marked to denote their significance in gas accumulation and production.

1.2.2 Geological background: The Bohai Bay Basin

The Bohai Bay Basin is located in the north of China, east of Hebei province, along the Bohai Sea coastline (Figure 1), covering an area of approximately 2 x 10^5 km^2 (Allen et al., 1997, Allen et al., 1998). It is one of many extensional basins that exist within East-Asia and the basin is composed of several extensional depressions that have evolved during the Mesozoic-Cenozoic (Hellinger et al., 1985). This region has been the subject of extensive research, with significant focus on the thermal history, stress distribution, onshore structural features, and Cenozoic tectonism (Wang et al., 1985, Liu, 1987, Ye et al., 1987, Zhao and Windley, 1990, Hu et al., 2001, Hou et al., 2010, Hou and Hari, 2014). The Dagang oil and gas field is situated within the central Huanghua depression, part of a fault bounded tectonic structure that comprises half grabens and complicated horst-graben structures (Chen and Zhang, 1991).

The Bohai Bay Basin has experienced four distinct tectonic phases throughout its geological history, firstly with a stage of regional stable deposition from the Neo-Mesoproterozoic to the Paleozoic, prior to basin formation, followed by a pre-rifting fold-and-thrust stage during the Mesozoic. Subsequently, a syn-rifting stage occurred in the Paleogene; and a post-rifting or regional subsidence stage from the Neogene to the present (Li et al., 2017b, Wang et al., 2019a). As a result, the Bohai Bay Basin is considered a typical extensional basin, though locally influenced by strike-slip faulting (Wang et al., 2022a). NNW-directed Andean-style subduction of the Izanagi Plate, (associated with the westward-moving Pacific plate) commenced in the Middle Jurassic strongly influencing the tectono-structural setting and the associated magma underplating induced widescale uplift during the Early Cretaceous (Sun et al., 2004). Rifting was further affected through horizontal tension caused by the upwelling of buoyant heated mantle material (Qi and Yang, 2010). The process of underplating, along with the associated heat flow led to crustal thickening and orogenic exhumation. A mechanism that also drives continental extension and the development of the continental rift basin (Ju et al., 2022). This Mesozoic rifting episode is associated with extensive volcanism along the Daxing'anling tectonic-magmatic belt (Ren et al., 2002), signified by the volcanic rock units in Figure 3.

The Bohai Bay Basin has undergone several tectonic stages, including early syn-rift, stable rifting and thermal subsidence (Chen et al., 2014), while in the Huanghua depression, thermal subsidence has driven the development of several sub-sags, slopes and buried hills, namely the Qibei sub-sag, Qibei buried hill, Qibei slope, Banqiao slope, Banqiao

sub-sag, Gangxi buried hill and Binhai slope (Figure 32). The Qibei slope of the Huanghua depression is located northwest of the Qikou subsag, this area represents a typical multi-step flexural slope (Zhao et al., 2016b). The Binhai fault nose, which is situated to the east of the central uplift on the Qibei Slope is characterised by a large nose-like feature, and is attached to the footwall of the Binhai fault, extending 25.0 km in length and 10.4 km in width, and covering an area of ~260 km^2 (Dong et al., 2022). The structural configuration of this sub-basin is controlled on its western extent by the Gangdong fault and in the East, the Huanghua depression comprises a more complex fault system influenced by the Tangjiahe fault. The Gangdong fault plays a critical role in controlling both the thickness of the stratigraphic units and the spatial distribution of hydrocarbon resources (Zhou et al., 2019) and stretches for approximately 33 km, trending SSE, penetrating through all strata above the crystalline basement.

Syn-rift deposition of the Kongdian formation (Ek) and the Shahejie formation (Es), was controlled mainly by the large strike-slip faults within a series of continued half-graben segments (Allen et al., 1998). The Dongying formation (Ed), was also formed during this syn-rift period, while post-rift stage deposition included the Guantao formation (Ng) and the Minghuazhen formation (Nm). The organic-rich intervals of the Es and Ed formations, particularly the third member of the Paleogene Shahejie formation (Es_3) and the third member of the Dongying formation (Ed_3), are recognised as the primary source rocks in the Qibei and Qikou slopes (Yu et al., 2011, Pu et al., 2013, Wang et al., 2014), with TOC values in the Es_3 formation of around 2.98% (Yang and Xu, 2004). The sandstone reservoirs within the first member of the Shahejie Formation (Es_1) are one of the primary reservoirs and are typically buried at depths greater than 2500m. These sandstones exhibit characteristics of gravity flow deposits, high-quality reservoir properties, and a significant amount of hydrocarbon accumulation (Pu et al., 2011, Pu et al., 2014, Zhao et al., 2018, Pu et al., 2020).

Further description of the geological setting and tectonic evolution of the Bohai Bay Basin can be found further on in Chapter 3.3.

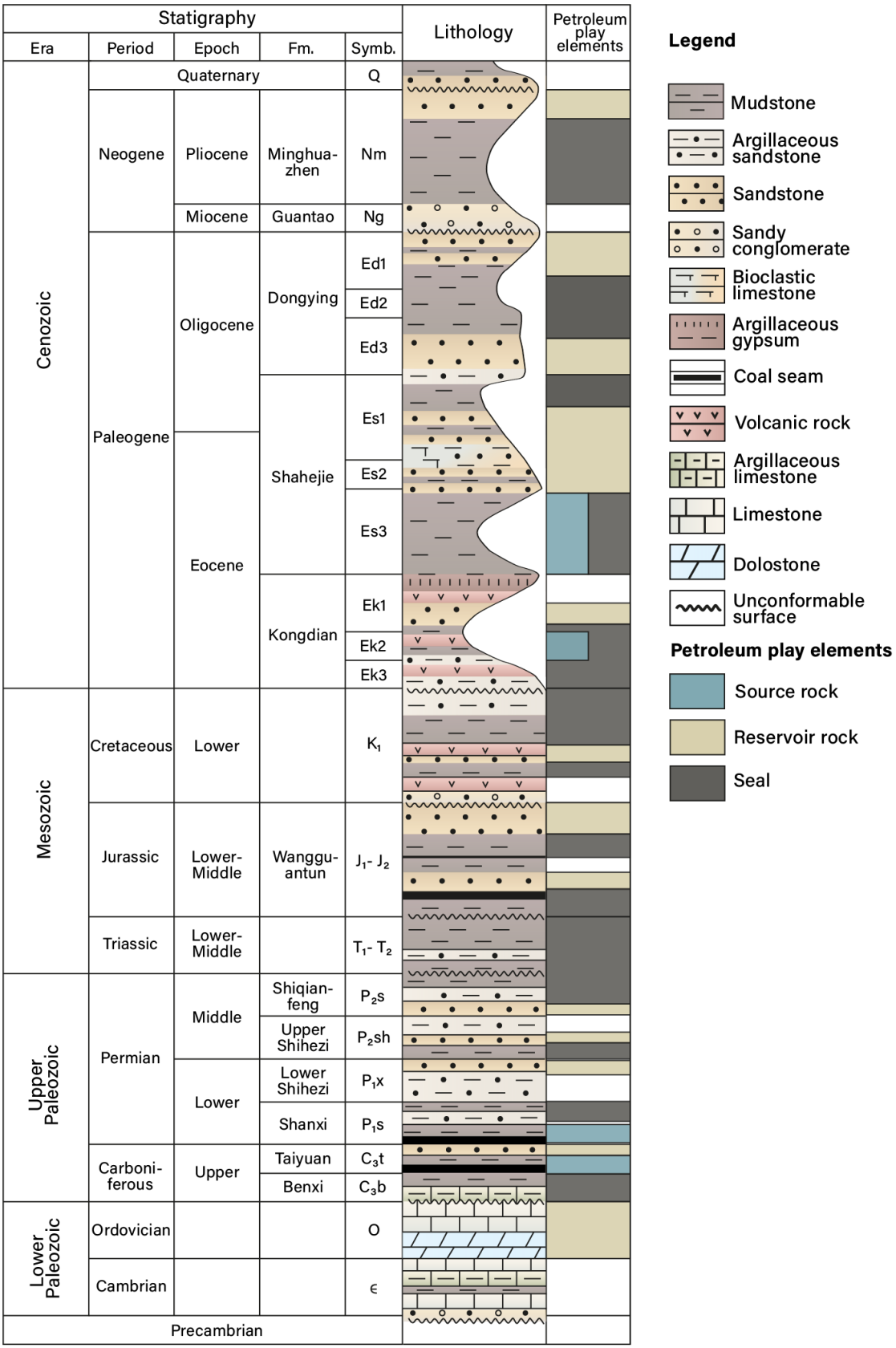

Figure 3 - Comprehensive Stratigraphic Framework of the Huanghua Depression, Bohai Bay Basin: This stratigraphic chart highlights key formations within the Bohai Bay Basin from the Precambrian through to the Quaternary. Lithologic units are shown including mudstone, sandstone, and carbonate rocks. Key petroleum play elements such as the source rocks, reservoirs, and seals are identified, providing a critical overview for hydrocarbon exploration., modified from Zhang et al. (2008) and Wang et al. (2022d).

Figure 4 – Conceptual model illustrating hydrocarbon systems and noble gas exchange: This figure provides a glimpse into the shallow crust, showcasing the dynamic interaction of noble gas isotopes between the atmosphere, crust, and mantle. These mechanisms occur within the context of conventional and unconventional gas wells. The figure further highlights the processes of radiogenic noble gas production (left inset) from elements such as Thorium (Th) and Uranium (U), aquifer recharge and infiltration from the surface, and the exchange dynamics of gases in different phases. The contrast between porous reservoirs and tight sandstone gas formations is emphasised, as well as the unique adsorption properties of specific noble gases such as Krypton (Kr) and Xenon (Xe) in relation to hydrocarbon-rich shales. This schematic figure builds upon Ballentine and O'Nions (1992), Ballentine et al. (2002) and Byrne et al. (2018b).

1.3 Geochemical components

The study of noble gas geochemistry in the context of oil and gas-bearing sedimentary basins involves multiple geochemical components, each serving as a lens through which we can examine processes like formation, migration, and trapping. We can define fluids based on their characteristic isotopic composition, as they comprise a variable proportion of noble gases originating from distinct geochemical reservoirs. Terrestrial noble gases are dominated by three distinct reservoirs (Figure 4) with well-known concentrations and isotopic ratios:

1. The atmosphere (air)
2. The crust
3. The mantle

The continuum exchange of gas initiates with the dissolution of noble gases into surface waters, such as lakes and groundwaters. The extent to which noble gases dissolve in water depends on several factors, including temperature, pressure, and Henry's constants for each noble gas, which must be ascertained (section 1.3.3, page 23). In meteoric waters like lakes and groundwaters, noble gases achieve equilibrium between the dissolved and gaseous phases, often marked by isotopic fractionation, denoted by the value of ASW, which can similarly be calculated (section 1.3.5, page 26). Depending on its genetic source type, noble gases within samples will have an accompanying isotopic signature which signifies its mixed origin relating to the geochemical endmember values associated with the atmosphere, crust and mantle. The resultant mixture is rarely a product of a singular accumulation process, and the noble gas isotopic ratio will generally represent intermixing of either two or three of these geochemical components. The presence of air-derived noble gases signifies a natural baseline, as the abundance and ratios of noble gases in the atmosphere are known for each element (Table 7) and accompanying isotope. Atmospheric components stored in subsurface reservoirs vary greatly in isotopic composition from the ratio of mantle-derived fluids, i.e., the atmospheric ratio of $^{3}He/^{4}He$ is 1.384×10^{-6}, which is lower than mantle and crustal $^{3}He/^{4}He$ ratios due to the addition of radiogenic ^{4}He from the radioactive decay of the radioelements $^{238,235}U$, ^{232}Th and ^{40}K. Conversely, ^{20}Ne, ^{36}Ar, ^{84}Kr, ^{132}Xe are not produced in significant quantities by radioactive processes in the crust and are instead a product of atmospheric input; while ^{21}Ne, ^{40}Ar, ^{136}Xe too have a crustal origin (Ballentine et al., 2002) and are produced by fissiogenic, radiogenic and nucleogenic reactions in the subsurface.

Therefore, in the absence of a magmatic contribution, are almost entirely dominated by atmosphere-derived sources. Radiogenic isotopes are more greatly concentrated in the older continental basement, specifically the top 10-15 km, where 66% of all radiogenic isotopes are thought to be generated. The remaining 34% of production occurs between depths of 10-15km and 20-25 km (28% production) and greater than 25 km depth (6% production) (Rudnick and Fountain, 1995).

Noble gas abundances are important because they highlight various transport processes, including diffusive or advective transport processes. Yet, in geological environments, the range of systems and conditions (temperatures and pressures) present a difficult challenge for experimentally investigating noble gas solubilities. Understanding the role of each noble gas and its associated provenance is critical in defining the Earth's history with greater clarity. Helium, Neon, Argon, Krypton and Xenon have all been identified in mantle mixing processes, and although their absolute abundances in the subsurface are seldom known, their isotopic signatures can bring light to the heterogeneity of the mantle, where, according to the standard model of noble gas geochemistry, is stratified into two separate zones termed the depleted degassed upper mantle (DUM) and the under-gassed primordial lower mantle (PLM) (Anderson, 2007).

1.3.1 Terrestrial noble gas inventories

1.3.1.1 Atmosphere and air-saturated water (ASW)

Noble gases in the Earth's atmosphere originate from primordial volatiles captured during planetary formation and the subsequent degassing of the Earth's interior (Ozima and Podosek, 2002, Porcelli et al., 2002). These rare gases are considered stable except helium, with atmospheric loss offset by terrestrial outgassing (Torgersen, 1989). Noble gases typically enter the subsurface via dissolution in groundwater, with concentrations altered by solubility and further influenced by environmental conditions such as groundwater salinity, reservoir temperature and pressure (Ballentine et al., 2002, Crovetto et al., 1982, Smith and Kennedy, 1983). Accurate initial ASW noble gas measurements in recharge waters are vital for tracking subsurface partitioning, though the presence of 'excess air' can lead to dissolved noble gas concentrations exceeding theoretical solubility, complicating temperature reconstructions and necessitating correction in models (Aeschbach-Hertig et al., 2000).

1.3.1.2 Continental crust

The Earth's crust is estimated to hold approximately 40% of its radioactive elements like ^{40}K, ^{230}Th, and ^{238}U, which are integral in the generation of noble gas isotopes (Rudnick and Fountain, 1995). These isotopes are produced through radiogenic, nucleogenic, and fissiogenic processes within minerals, and their release into fluids occurs via mechanisms such as recoil and diffusion or through mineral transformation (Ballentine and Burnard, 2002, Torgersen, 1980). ^{4}He and ^{40}Ar, products of U, Th, and ^{40}K decay, are created at known crustal rates, while isotopes like ^{3}He and ^{21}Ne are produced less abundantly, endowing crustal fluids with a distinctive isotope composition. The crustal $^{3}He/^{4}He$ ratio is significantly lower than the atmospheric $^{3}He/^{4}He$ (Ra) ratio, reflecting the unique isotopic signature of crustal sources (Ballentine and Burnard, 2002). Variability in noble gas production rates and isotopic compositions arises from the uneven distribution of parent elements in crustal rocks. Subsequent elemental and isotopic fractionation during release and subsurface transport further complicates crustal endmember identification. The accumulation of noble gases in fluids over time in a closed system provides a means to date fluids and understand the relative timescales of geologic processes (Zhou and Ballentine, 2006).

1.3.1.3 Mantle

The Earth's mantle is thought to contain a significant amount of primordial noble gases, with their elemental and isotopic compositions displaying heterogeneity due to varying degrees of degassing. For example, the high ratio of $^{3}He/^{4}He$ in deep mantle-derived basalts, up to 50 times the atmospheric ratio (Ra), indicates a primordial nature, while gases from the continuously melting upper mantle show ratios of 7–9 Ra and the subcontinental lithospheric mantle exhibits lower $^{3}He/^{4}He$ ratios, reflecting the addition of radiogenic ^{4}He (Day et al., 2015). Enrichments of ^{20}Ne and ^{40}Ar, are also characteristic of the mantle (Hiyagon and Kennedy, 1992). Mantle volatiles influence crustal processes and atmospheric composition via faults and magmatism (Marty and Tolstikhin, 1998, Sano et al., 2013, Sano et al., 2017, Gilfillan et al., 2011, Day et al., 2022), and tracing mantle-derived noble gases in hydrocarbon systems can elucidate the generation, migration and accumulation mechanism of oil and gas resources (Hunt et al., 2012, Barry et al., 2016, Karolytė et al., 2021, Moore et al., 2018, Darrah et al., 2015, Byrne et al., 2018b, Byrne et al., 2020, Byrne et al., 2021).

Table 1 - Fundamental physical properties and elemental abundances of noble gases relative to the composition of dry air. These gases have very high first ionisation potentials because they have full outer electron shells, making them stable and chemically inert, data from (Ozima and Podosek, 2002).

Noble gas	Atomic no.	Atomic wt.	Atomic radius	First ionisation potential (eV)	Second ionisation potential (eV)	Total atmospheric inventory (cm^3 STP)	Volume fraction
He	2	4.002602	1.8	24.59	54.42	2.076×10^{19}	5.24×10^{-6}
Ne	10	20.1797	1.6	21.56	40.96	7.202×10^{19}	1.818×10^{-5}
Ar	18	39.948	1.9	15.76	27.63	3.700×10^{22}	9.34×10^{-3}
Kr	36	83.80	2.0	14.00	24.36	4.516×10^{18}	1.14×10^{-6}
Xe	54	131.29	2.2	12.13	21.21	3.446×10^{17}	8.7×10^{-8}

1.3.2 Noble gas isotopes: Properties, abundances, and geochemical significance

1.3.2.1 Helium (He)

Table 2 - Atomic mass, isotopic abundance of He isotopes (^{3}He, ^{4}He)

Isotope	Atomic mass (amu)	Isotopic abundance (amount fraction)
^{3}He	3.016029322	0.000002
^{4}He	4.0026032545	0.999998

He is abundant in the universe, constituting about 23% of its total elemental mass, only second to H (Olive et al., 1997). Conversely, it is very rare in the Earth's atmosphere; in dry tropospheric air, He has a volume mixing ratio (VMR) of 5.24 (±0.05) x 10^{-6} (5.24 ppm). As it is atomically light (see Table 1), has a small atomic radius and is highly mobile, it tends to readily escape the atmosphere into space. The overall escape flux of He has been calculated at 10^6 atoms/cm^2s^{-1}, and due to this high thermal escape velocity, He is thought to have a short residence time in the atmosphere, calculated at 10 Ma (Day et al., 2015). He is primarily obtained from natural gas deposits containing high concentrations of radiogenic ^{4}He. Commercial He has applications in many industries, including medicine and space, which further underscores the importance of tracing and understanding the genesis and migratory mechanisms of He in natural gas fields (Zhang et al., 2019c). Owing again to its small atomic radius, He is also used for leak detection in the noble gas preparation line (section 1.5.2.4, page 63). The isotopic ratios of helium found in groundwater and natural gas samples from sedimentary basins indicate the complex subsurface mixing processes that ^{4}He has undergone (Oxburgh et al., 1986). ^{3}He

within rock-magma serves as evidence of a primordial reservoir within the mantle or cosmic dust spallation (formed at the time of the Big Bang), while cosmogenic, nucleogenic or radiogenic isotopes of He were formed later. ^{4}He is radiogenic, produced via alpha decay of uranium and thorium (page 46). ^{3}He/^{4}He ratios are often used in noble gas geochemistry studies to indicate the presence of a mantle component (Sano et al., 1990). ^{3}He/^{4}He ratios can vary remarkably; ^{3}He/^{4}He values in the upper mantle are upwards of 6-8 times greater than atmospheric values and are therefore enriched in ^{3}He. The use of ASW (air-saturated water) He is limited in unconventional reservoirs as a result of helium's very low concentration in air, as discussed above, in concurrence with its lower solubility coefficient in water versus other noble gases (Figure 5). Henry's law governs that He does not dissolve as readily in water as the other noble gases (Crovetto et al., 1982, Smith, 1985). The standard notation R/R_a is used in noble gas geochemistry in reference to the normalised ratio of ^{3}He/^{4}He ratios in a sample relative to the ratio found in the atmosphere, given by:

$$R/R_a = \frac{(^3He/^4He)_{sample}}{(^3He/^4He)_{atmosphere}} \quad (1)$$

Atmospheric ^{3}He/^{4}He is denoted by the term 'R_a', where $R_a = 1.384 \times 10^{-6}$ (there is no isotopic fractionation for helium between a water and vapour phase). Therefore, R/R_a values close to 1 are 'air-like', while crustal-influenced helium ratios are ~0.02 R_a (Ballentine and Burnard, 2002) and in the upper mantle (a mixture of radiogenic and primordial helium) = 8 R_a (Graham, 2002).

1.3.2.2 Neon (Ne)

Table 3 - Atomic mass, isotopic abundance of Ne isotopes (^{20}Ne, ^{21}Ne, ^{22}Ne)

Isotope	Atomic mass (amu)	Isotopic abundance (amount fraction)
^{20}Ne	19.9924401762	0.9048
^{21}Ne	20.99384674	0.0027
^{22}Ne	21.991385114	0.0925

Ne has a VMR of 1.818 (±0.004) x 10^{-5} (18.18 ppm). Ne isotopes provide invaluable insights into various geological processes, from mantle-crust differentiation to interactions with groundwater and the Earth's atmosphere. ^{20}Ne is of an atmospheric origin and, therefore, can highlight any interaction of water that was once at equilibrium with the atmosphere at recharge. The proportion of ^{20}Ne and other atmospheric noble gases dissolved in water at recharge is controlled by their relative solubilities (described in

section 1.3.3) and transported via groundwater (Mazor, 1972). $^{20}Ne/^{22}Ne$ ratios have been used in paleoclimate reconstruction and constraining the processes involved in magma degassing, hydrothermal circulation and gas partitioning groundwaters (Peeters et al., 2003). Nucleogenic ^{21}Ne is produced from nuclear reactions involving alpha particles and other light elements, $^{18}O(\alpha, n)^{21}Ne$ and $^{24}Mg(n, \alpha)^{21}Ne$ (Ballentine and Burnard, 2002). The pathway for nucleogenic production of all Ne isotopes was first outlined by Wetherill (1954), and this discovery allowed for the subsequent quantification of Ne production rates in the crust (Kyser and Rison, 1982, Yatsevich and Honda, 1997, Leya and Wieler, 1999). When applied in the ratio $^{21}Ne/^{4}He$ (5×10^{-8} in crustal fluids), Ne has potential use in groundwater dating, while ^{21}Ne is also often measured in extra-terrestrial materials to determine their cosmic ray exposure ages, providing insights into the history and dynamics of the solar system. The $^{21}Ne/^{22}Ne$ ratio is particularly useful for distinguishing between mantle and crustal sourced Ne (Holland and Gilfillan, 2013), and when plotted vs $^{20}Ne/^{22}Ne$, Ne becomes a useful tracer within natural gas reservoirs in determining the contribution of mantle, crustal and atmospheric endmember contributions (Figure 12). When measuring the isotopic composition of Ne, isobaric interference occurs at m/z = 20 & 22 (Figure 19) as well as from $^{40}Ar^{++}$; the NGX multi-collector noble gas mass spectrometer has a sufficient resolution to be able to separate ^{40}Ar and isotopic discrimination of Ne can be measured directly (Burnard et al., 2006).

1.3.2.3 Argon (Ar)

Table 4 - Atomic mass, isotopic abundance of Ar isotopes (^{36}Ar, ^{38}Ar, ^{40}Ar)

Isotope	Atomic mass (amu)	Isotopic abundance (amount fraction)
^{36}Ar	35.967545105	0.003336
^{38}Ar	37.96273211	0.000629
^{40}Ar	39.9623831237	0.996035

Ar is much more abundant in the atmosphere than other noble gases, with a VMR of $9.34 \pm 0.01 \times 10^{-3}$ (9340 ppm), therefore, gas samples will be strongly affected by excess air. ^{36}Ar is atmospheric derived, showing interaction with water that was once at equilibrium with the atmosphere. ^{40}Ar originates primarily from the radioactive decay of ^{40}K and is directly proportional to in-situ K concentrations. Elevated $^{4}He/^{40}Ar$ and $^{21}Ne/^{40}Ar$ indicate excess production beyond the atmospheric ratio (Hunt et al., 2012). A technique for dating very old pore waters in impermeable rocks using ^{4}He and ^{40}Ar has been refined by Osenbrück et al. (1998).

1.3.2.4 Krypton (Kr)

Table 5 - Atomic mass, isotopic abundance of Kr isotopes (^{78}Kr, ^{80}Kr, ^{82}Kr, ^{83}Kr, ^{84}Kr, ^{86}Kr)

Isotope	Atomic mass (amu)	Isotopic abundance (amount fraction)
^{78}Kr	77.92036494	0.00355
^{80}Kr	79.91637808	0.02286
^{82}Kr	81.91348273	0.11593
^{83}Kr	82.91412716	0.114
^{84}Kr	83.91149773	0.56987
^{86}Kr	85.91061063	0.17279

The VMR of Kr in dry air is 1.14 (±0.01) x 10^{-6} (1.14 ppm). ^{84}Kr isotope shows interaction with water that was at equilibrium with the atmosphere. ^{83}Kr/^{36}Ar ratios in trapped air have also been shown to be affected by gravitational separation processes such as effusion from compressed air bubbles (Craig and Wiens, 1996). Many Kr isotopes have applications in various fields of geochemistry, geochronology, and atmospheric science. Although the broader isotopic applications of krypton offer valuable insights into various scientific questions, they fall outside the purview of this study within the Sichuan and Bohai Bay basins, which aims to explore the fractionation and adsorption behaviour, as well as the geochemical significance of these selected stable krypton isotopes in the context of oil and gas basins.

1.3.2.5 Xenon (Xe)

Table 6 - Atomic mass, isotopic abundance of Xe isotopes (^{124}Xe, ^{126}Xe, ^{128}Xe, ^{129}Xe, ^{130}Xe, ^{131}Xe, ^{132}Xe, ^{134}Xe, ^{136}Xe)

Isotope	Atomic mass (amu)	Isotopic abundance (amount fraction)
^{124}Xe	123.905892	0.000952
^{126}Xe	125.9042983	0.00089
^{128}Xe	127.903531	0.019102
^{129}Xe	128.9047809	0.264006
^{130}Xe	129.9035093	0.04071
^{131}Xe	130.9050841	0.212324
^{132}Xe	131.9041551	0.269086
^{134}Xe	133.9053947	0.104357
^{136}Xe	135.9072197	0.088573

Xe is much rarer in abundance, with a VMR in dry air of 8.7 (±0.1) x 10^{-8} (0.087 ppm). A discrepancy exists in the measured abundance of Xe in the Earth's atmospheric inventory, which is around 25 times lower than the expected value compared to planetary gas patterns observed in meteorites (Podosek et al., 1981). Xe is the noble gas most sensitive to temperature, while ^{132}Xe isotope shows interaction with water at equilibrium with the atmosphere. ^{129,131,132,134,136}Xe are all also formed by the process of spontaneous fission of ^{238}U and ^{244}Pu (Ballentine and Burnard, 2002). Xe is employed in this study to better understand the kinetics and thermodynamics of adsorption onto minerals like shale and tight sandstone. This is critical for understanding the gas storage and migratory capacities of these formations.

Table 7 - Geochemical uses for noble gas isotopic and elemental ratios. Each ratio may imply significant contributions of atmospheric, crustal, or mantle-derived noble gases. These isotopic ratios are often studied in conjunction with other geochemical markers and isotopes, such as stable carbon and hydrogen isotope abundances, to offer a comprehensive geochemical characterisation of fluid reservoirs.

Ratio	Atmos. ratio	Geochemical use
^{3}He/^{4}He	1.384 x 10^{-6}	As discussed in section 1.3.2.1, this is the reference isotopic ratio for Helium, when normalised to the atmospheric ratio. This ratio principally differentiates between mantle and crustal sources and is useful in tectonic settings where evidence of magmatic activity has been established.
^{4}He/^{20}Ne	0.318	This elemental ratio reveals the extent of crustal (^{4}He) and atmospheric (^{20}Ne) contributions, and varies significantly between different gas fields.
^{4}He/^{40}Ar	0.095	Both ^{4}He/^{40}Ar are produced by radioactive decay. This ratio is a sensitive indicator of fractionation. ^{4}He is produced by decay of uranium and thorium, while ^{40}Ar is produced by decay of potassium-40 (^{40}K). This ratio is also the foundation of dating methods (U-Th)/He.
^{20}Ne/^{22}Ne	9.8	Used in distinguishing Ne genetic source as either primarily nucleogenic or atmospheric (Figure 12). ^{20}Ne is derived from air, while mantle contributions give ^{20}Ne/^{22}Ne ratios of ~12.5. This ratio is also used when correcting for atmospheric contamination.
^{21}Ne/^{22}Ne	0.0290	This ratio is similarly useful for distinguishing between mantle and crustal-radiogenic Ne endmembers. Atmosphere-resolved ^{21}Ne is given by ^{21}Ne*
^{20}Ne/^{36}Ar	0.524	Often used to investigate the solubility and partitioning behaviour of atmospheric noble gases in geological fluids and the remnants of interaction with groundwaters. It serves as an important parameter in understanding how noble gases are fractionated and V_g/V_w variability.
^{40}Ar/^{36}Ar	295.5±0.5	Utilised in determining radiogenic ^{40}Ar production and the release of radiogenic Ar from crustal sources. ^{40}Ar* indicates a radiogenic component.

Numerous studies have demonstrated a strong correlation between noble gas concentrations in open waters and the expected equilibrium state derived from air-water partitioning models. This aligns with Henry's law, where the concentration of dissolved gas in a liquid is directly proportional to its partial pressure in the atmosphere (Aeschbach-Hertig et al., 1999).

When examining these geological systems, it's typically appropriate to consider the Henry coefficient (a measure of gas solubility) as a function of temperature and salinity. Consequently, the equilibrium concentrations of noble gases encapsulate critical information about physical parameters at the point of gas exchange, that is, atmospheric pressure, water temperature, and salinity. Despite the presence of atmospheric noble gases in the water cycle potentially obscuring other geochemical signals, it also establishes a predictable baseline. This allows for the discernment of additional noble gas components when their concentrations sufficiently exceed the atmospheric background (Kipfer et al., 2002). While this feature might seem disadvantageous for conventional investigations, it offers an unexpected benefit in that most noble gas concentrations can be interpreted as a combination of two distinct geochemical components; one is a well-characterised atmospheric component, while the other is a residual component originating from a reservoir outside the atmosphere (i.e., from the crust or mantle).

1.3.3 Noble gas solubility and Henry's Law

The partitioning of noble gases between a gas and liquid phase is revealed by Henry's law (Equation (2), which is a principle that governs the solubility and, therein, the concentration of each noble gas in solution. Henry's law states that the amount of dissolved gas (x_i) is proportional to its partial pressure (p_i) in the gas phase. Assuming ideality (ideal gas behaviour), then, under equilibrium conditions, we use Henry's law in its mole fraction form to accurately determine the distribution of a noble gas isotope species "*i*" fractionated between a gas and liquid phase (Pinti and Marty, 1998).

$$p_i = K_i x_i \tag{2}$$

When accounting for the ideal behaviour of subsurface fluids, for any given quantity of gas, the product of pressure (P) and molar volume (V) is directly proportional to the number of moles of gas (n), the ideal gas constant (R = 8.314 J/Kmol), and absolute temperature (T). The ideal gas law that accounts for these fundamental conditions is stated as:

$$PV = nRT \tag{3}$$

Henry's constants are empirically derived and are commonly expressed in terms of molality (K_i^m), dimensionless (K_i^d) or in units of pressure (K_i). If the dimensionless Henry's constant for a compound is greater than 1 ($C_{air} > C_{water}$), then the compound prefers to be in a gas phase. This apportioning ratio holds until a compound reaches saturation in the air or water. To understand the solubility of a noble gas in a liquid, we may first use the ideal gas law to calculate the partial pressure of the noble gas in the gas phase, then use Henry's law to relate this partial pressure to the mole fraction of the noble gas in the liquid, which gives a measure of its solubility under these ideal conditions, for a set of varying temperatures. Non-ideality of species "*i*" must be considered by adjusting Equation (2 for the fugacity and activity coefficients, Φ and γ_i, respectively.

$$\Phi_i p_i = \gamma_i K_i x_i \tag{4}$$

1.3.4 From "ideal" to "real": Modifying solubility for non-ideal conditions

Assuming ideality, it is possible to calculate the molar gas volume for a noble gas. For non-ideality in the gas phase, however, we must account for fugacity (Φ) at a given pressure and temperature by first calculating the "real" molar volume (V_{real}) by substituting the temperature-dependent first and second-order virial coefficients B(T) and C(T) into the ideal gas law (Dymond and Smith, 1980), which yields the equation:

$$PV_m/RT = 1 + B(T)/V_{real} + C(T)/V_{real}^2 \tag{5}$$

The real molar volume (V_{real}) can be approximated by solving the following equation, applying Newton's method for approximation, which converges to the correct solution after ~10 iterations from an initial estimate where $V_{ideal} = RT/P$:

$$\left(\frac{P}{RT}\right) V_{real}^3 - V_{real}^2 - B(T)V_{real} - C(T) = 0 \tag{6}$$

We may subsequently derive an exponential function equation to calculate the fugacity coefficient (Φ) from the virial coefficients B(T) and C(T), which is related to the simultaneous change in pressure and volume from a low pressure (where the gas displays ideal behaviour) to the genuine reservoir pressure:

$$\Phi(P,T) = \exp\left[B(T)/V_{real} + (C(T) + B(T)^2)/2V_{real}^2\right] \tag{7}$$

The fugacity coefficient $\Phi(P,T)$ is a measure of how a real gas deviates from its ideal behaviour and is a function of pressure and temperature. A range of values can then be

computed for increasing depths; see Table 8 below. Where Φ = 1, the noble gas species displays ideal gas behaviour. The results of this calculation show that, with the exception of Xe, at near-surface conditions, the suite of noble gases exhibits ideal behaviour; however, at depths approaching 4500m, common in gas wells in both the Sichuan Basin and Bohai Bay Basins, the fugacity coefficients show a large deviation from ideal gas behaviour (~20%).

Table 8 – Virial and fugacity coefficients for each noble gas, which are a function of depth. Second and third-order virial coefficients, B(T) and C(T), are compiled by Dymond and Smith (1980). The fugacity coefficient (Φ) shows the deviation from ideal gas behaviour.

	Depth (m)	300	1200	2000	2800	3700	4500
	P (atm)	29	116	194	271	358	436
	T (K)	298	323	348	373	398	423
Helium	B(T)	11.74	11.58	11.43	11.35	11.24	11.07
	C(T)	75.1	72.3	94.8	90.5	93.8	109.6
	Φ	1.01	1.05	1.08	1.1	1.13	1.15
Neon	B(T)	11.42	11.86	12.21	12.52	12.86	13.1
	C(T)	221	224	224	224	105	197
	Φ	1.01	1.05	1.09	1.12	1.15	1.18
Argon	B(T)	-15.5	-11.2	-7.14	-3.84	-1.08	1.42
	C(T)	991	1230	959	918	877	833
	Φ	0.982	0.964	0.975	1	1.03	1.07
Krypton	B(T)	-52.36	-42.78	-35.21	-28.86	-23.47	-18.82
	C(T)	2612	2260	1076	1942	1842	1759
	Φ	0.94	0.846	0.839	0.861	0.894	0.93
Xenon	B(T)	-130	-110	-94.5	-81.2	-70.1	-60.7
	C(T)	6069	5306	4635	4115	3739	3469
	Φ	0.85	0.804	0.883	0.888	0.891	0.886

The activity coefficient (γ_i) helps account for deviations from ideal behaviour due to solute-solute and solute-solvent interactions and the effect of salinity on the solubility of the dissolved noble gases in liquid. This activity coefficient be defined as a function of the temperature of a species "*i*".

Table 9 - Setschenow coefficients (k_i). Constants G_1, G_2 and G_3 (Smith and Kennedy (1983), to fit Eq. 8

Noble gas Species	**G_1**	**G_2**	**G_3**
He	-10.081	15.1068	4.8127
Ne	-11.9556	18.4062	5.5464
Ar	-10.6951	16.7513	4.9551
Kr	-9.9787	15.7619	4.6181
Xe	-14.5524	22.5255	6.7513

The Setschenow equation, which is well established in determining the effects of salts on aqueous solubility, is determined for each system, given that it depends on the geological conditions and salt concentration. Rearrangement of the Setschenow equation gives the following equation, which allows for simple calculation of the activity coefficient γ_i:

$$\gamma_i = \exp\left[Ck_i(T)\right] \quad (8)$$

As this equation is a temperature-dependent exponential function, small adjustments to *C* (the salt concentration in solution) and k_i can greatly increase the activity coefficient γ_i.

$$k_i(T) = G_1 + G_2/(0.01T) + G_3 \ln(0.01T) \quad (9)$$

Where T is temperature, and G_1, G_2, and G_3 are constants specific to each noble gas, compiled by Smith and Kennedy (1983) and disclosed in Table 10.

G_1 is a constant representing the Setschenow coefficient's baseline value at a reference temperature, while the term $G_2/(0.01T)$ represents a correction to the Setschenow coefficient that varies inversely with temperature. Therefore, as the temperature increases, this term decreases, indicating that the effect of the salt on the solubility of the noble gas diminishes with increasing temperature. The term $G_3\ln(0.01T)$ represents a further correction to the Setschenow coefficient that depends logarithmically on the temperature. To derive the value of the activity coefficient, γ_i, the associated Setschenow coefficient, $k_i(T)$ can be input to determine a value for each noble gas species at varying depths intervals. In both the sampled Sichuan Basin and the Bohai Bay Basin, $k_i>0$ and $\gamma_i>1$ highlight a reduction in the overall solubility of all noble gases in the solution.

1.3.5 The gas-liquid fraction governed by noble gas solubility: Equilibrium

After investigating the solubility of the noble gases in water, we can calculate the initial distribution and partitioning of noble gases between a gas and liquid phase under equilibrium conditions (Eq. 9) for a known volume. Open waters that are a free interface to the atmosphere will contain concentrations of noble gases that have steadily, over time, equilibrated. Under these conditions, the gas/liquid fraction will behave ideally, and we then have a clear starting point to better understand the subsequent behaviour of the noble gases at varying temperatures following recharge. A second form of Henry's law, where Henry's constant is in its dimensionless form K_i^d, as both phases use the same concentration units, can be derived that expresses the concentration of a species "*i*" in the gas phase (C_i^{gas}), which is proportional to the concentration of that same gas species in the liquid phase (C_i^{water}):

$$C_i^{gas} = K_i^d \, C_i^{water} \quad (10)$$

Table 10 - Coefficients for He from Smith (1985) and Ne, Ar, Kr and Xe coefficients are taken from Crovetto et al. (1982) to fit Eq.11 and Eq.10, respectively.

Noble gas species	A_0	A_1	A_2	A_3
He	-0.00953	0.107722	0.001969	-0.043825
Ne	-7.259	6.95	-1.3826	0.0538
Ar	-9.52	8.83	-1.8959	0.0698
Kr	-6.292	5.612	-0.8881	-0.0458
Xe	-3.902	2.439	0.3863	-0.221

For high-temperature aqueous systems up to 650 K, the critical point of water at which point it becomes a supercritical fluid that exhibits properties of both liquid and gases; the partitioning effect between a gas and liquid phase due to solubility differences (Henry's constant) amongst the noble gases can be calculated using:

$$\ln(K_i) = A_0 + \frac{A_1}{(0.001T)} + \frac{A_2}{(0.001T)^2} + \frac{A_3}{(0.001T)^3} \quad (11)$$

K_i represents Henry's constant in GPa. For He, using the appropriate coefficients from Smith (1985), where the solubility of He relative to Ar was calculated, we may fit Eq.10 above by substituting $\ln(K_i)$ for $\ln(F_{He})$, where X represents the mol fraction, and F_{He} is equal to the following:

$$F_{He} = \frac{(X_{He}/X_{Ar})_{liquid}}{(X_{He}/X_{Ar})_{gas}} \quad (12)$$

To express Henry's constant in units of molality (atm Kg/mol), we use the following conversion factors:

$$1 \text{ GPa} = 9869.23267 \text{ atm}$$

$$K_i \text{ (atm)} = 55.6 \; K_i^m \text{ (atm Kg/mol)}$$

In light of this, the variability in noble gas solubilities and Henry's coefficients for noble gases in water over the temperature range specific to the Sichuan Basin and the Bohai Bay Basin may be plotted to show the molality (or dimensionless) convection as a function of temperature (Figure 5).

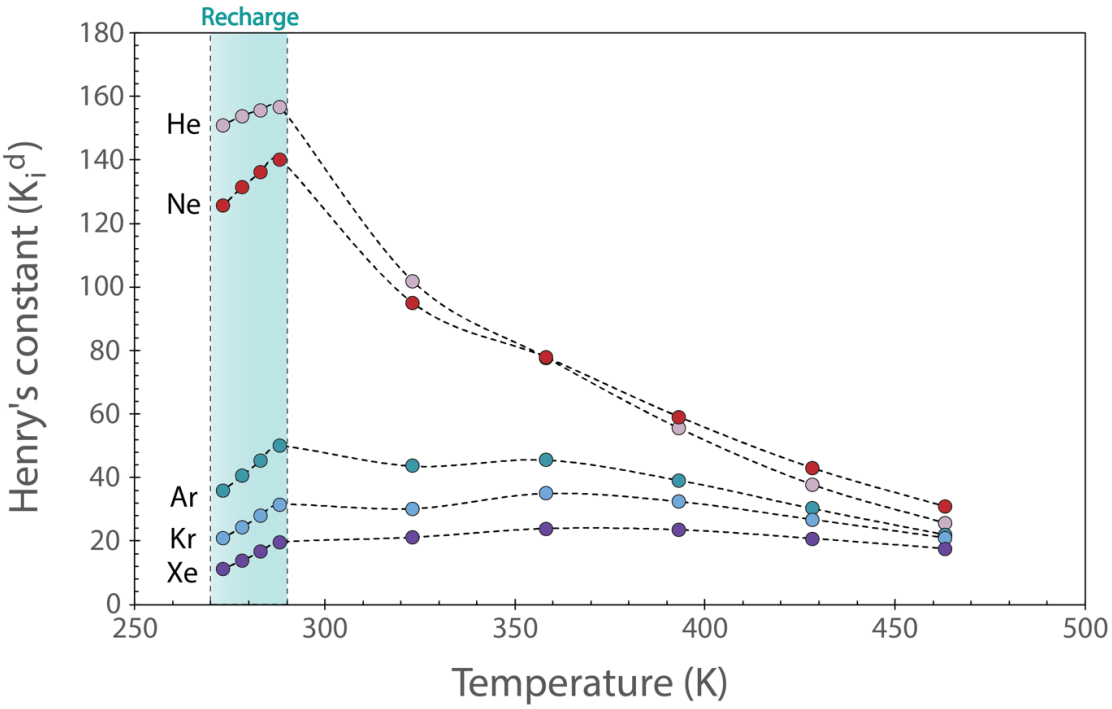

Figure 5 – Temperature-dependent dimensionless (K_i^d) Henry's coefficients for noble gases in water for the Bohai Bay Basin. At recharge conditions (the shaded region), where the temperature ranges between 275-290 K, noble gas solubility in water decreases with temperature, however, during transport and burial, where temperature increases from 290 K to 480 K, solubility of He and Ne increases. This underscores the temperature-sensitive nature of noble gas solubility in the hydrogeological context of the basin.

Lower K_i^d values show that in the context of Henry's law, Kr and Xe are more highly soluble in water, particularly at recharge conditions, where temperatures are lower. As the amount of dissolved gas is proportional to the gas species' partial pressure (p_i) in the gas phase, a lower K_i value means a greater amount of the gas will dissolve in the liquid at a given pressure. By relating Henry's constant (K_i) in units of atm, with water in the liquid phase, the mole fraction (x_i) can be related to water density (ϱ_l) and the liquid water volume (V_l). Assuming standard temperature and pressure (STP) conditions (1 atm, 273 K), 1 mole of gas occupies 22400 cm^3. The number of moles in the gas phase $[i]_g$ is proportional to the total number of moles $[i]_T$, and this relationship can be expressed as:

$$[i]_g = [i]_T \left(\frac{22400 T \rho_1 V_1}{1000 \times 273 \frac{\gamma_i}{\phi_i} K_i^m V_g} + 1 \right)^{-1} \tag{13}$$

The density of liquid l (g/cm^3) at system pressure and temperature is represented by ϱ_l. This form allows for the calculation of species "*i*" partitioning between gas and liquid phases in any water/gas equilibrium, accounting for any non-ideal behaviour. In the simplest case, the volume of gas equilibrated with groundwater can be calculated from a

single noble gas concentration in the water phase, given estimated equilibration conditions. Likewise, the volume of water equilibrated with a gas phase can be determined from the concentration of one noble gas in the gas phase. Henry's constant, given in terms of molality (atm Kg/mol) can also be expressed in terms of mole fractions, which are dimensionless quantities (Sander, 2015). As a result, the solubilities of each gas can be compared, and the determination of this dimensionless Henry's constant (K_i^d) is calculated using:

$$K_i^{\,d} = \left(\frac{1000 \times 273 \times \frac{\gamma_i}{\phi_i}}{22400 \times \mathrm{T} \times \rho_1} \right) \times \mathrm{K}_i^{\,m} \tag{14}$$

1.3.6 Conceptual models for noble gases in water: Rayleigh fractionation

Isotopic fractionation can occur when the rate at which an element moves or partitions between two reservoirs is influenced by atomic mass. Dissolved noble gas concentrations are the sum of the noble gas components that have equilibrated, partitioned or fractionated between phases. The limits on the extent of noble gas fractionation have been demonstrated through various dynamic models representing distinctive processes and end-member states within the subsurface. Rayleigh fractionation is likely the most common fractionation process and must be quantified to ascertain the equilibrium partitioning between phases with greater confidence.

Consequently, the Rayleigh fractionation law can be applied to decipher the residual elemental ratio in the liquid phase, $([i]/[Ar])_{water}$, by defining the extent of depletion, by comparing the current and initial $([i]/[Ar])_0$ states:

$$\left({}^{[i]}\!/\!_{[Ar]} \right)_{water} = \left({}^{[i]}\!/\!_{[Ar]} \right)_0 P^{(\alpha-1)} \tag{15}$$

Where P is the fraction of remaining Ar in a liquid water phase ($1 \rightarrow 0$), and α is the fractionation coefficient given by:

$$\alpha = \left(\mathrm{K}_{\mathrm{i}}^{\mathrm{liquid}} / \mathrm{K}_{\mathrm{Ar}}^{\mathrm{liquid}} \right) \tag{16}$$

This Rayleigh fractionation coefficient shows the magnitude of fractionation between a water phase that has interacted with a gas phase. Consequently, the partitioning of noble gases as a gas bubble passes through a column of liquid can be estimated, underlining the rate at which gases partition according to Henry's law as ^{20}Ne is removed from water (Figure 6):

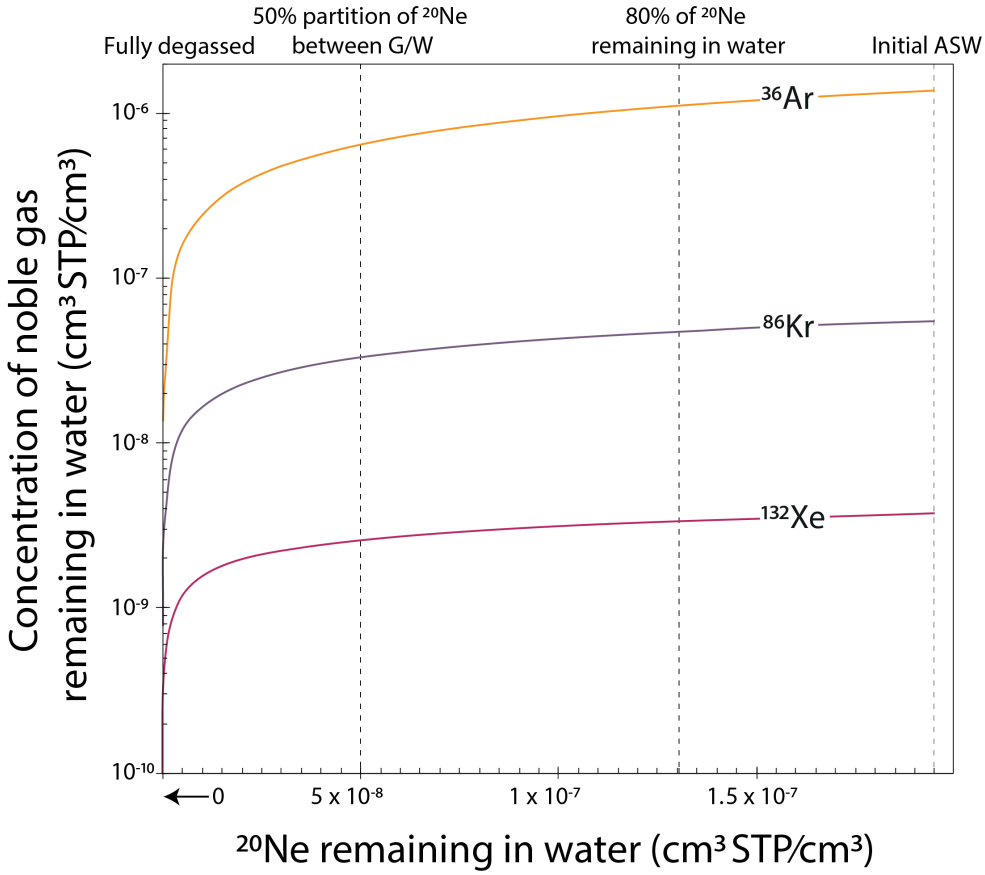

Figure 6 – Degassing behaviour of noble gas isotopes following partitioning due to solubility and the relationship between the decreasing ^{20}Ne concentration and the amount of corresponding noble gas (^{36}Ar , ^{86}Kr, and ^{132}Xe) that remains dissolved in water.

If the $V_g/V_w < 0.01$, then Rayleigh fractionation can be approximated for stepwise equilibrium degassing (Ballentine et al., 2002, Zhou et al., 2005). With the equation given by rearranging Equation (13:

$$\frac{V_g}{V_w} = \frac{22400 \times T \times \rho_{H_2O}}{\left[\left(\frac{1}{1-f}\right) - 1\right] \times 18 \times 273 \times \frac{\gamma_i}{\varphi_i} K_i} \quad (17)$$

Where f is the fraction of ^{36}Ar remaining in groundwater, and $(1/1\text{-}f)$ represents the ratio between the total number of moles of ^{36}Ar in both the gas and groundwater phase $[i]_T$ and the number of moles of ^{36}Ar in the gas phase $[i]_g$.

1.3.7 Conceptual models for noble gases in water: Phase fractionation

In simple two-phase systems, the magnitude of fractionation and enrichment of the gas phase is controlled by the equilibrium solubility law, which is similarly related to the original ratio in the system $([i]/[Ar])_T$, after Bosch and Mazor (1988):

$$\left(\frac{[i]}{[Ar]}\right)_g = \left(\frac{[i]}{[Ar]}\right)_T \frac{\left(\frac{V_g}{V_w} + \frac{1}{K_{Ar}^d}\right)}{\left(\frac{V_g}{V_w} + \frac{1}{K_i^d}\right)} \quad (18)$$

We may then derive a fractionation factor (F_{gas}) which indicates the magnitude of fractionation in the system, relative to the V_g/V_w as it approaches zero ($V_g/V_w \rightarrow 0$). This is proportional to the noble gas solubility in water (K_i^d), and incorporates the effects of non-ideality, Φ_i and γ_i on solubility (Ballentine et al., 2002), expressed by:

$$\text{When } \frac{V_g}{V_w} \rightarrow 0, \quad \frac{\left(\frac{[i]}{[Ar]}\right)_g}{\left(\frac{[i]}{[Ar]}\right)_T} \rightarrow \frac{\frac{\gamma_i}{\Phi_i} K_i^d}{\frac{\gamma_{Ar}}{\Phi_{Ar}} K_{Ar}^d} = F_{gas} \quad (19)$$

These equations reflect the subsurface conditions, including variable water solubility. In each sample, F_{gas} varies from 0 toward 1, whereby this denotes that no fractionation from the initially calculated ratio has occurred.

1.3.8 Other conceptual models that describe gas exchange and partitioning

Further conceptual models can be utilised to investigate the production, migration history, and storage mechanisms of noble gases in different geological systems. These models are similarly relevant for the calculation of volumetric gas-groundwater (V_g/V_w) estimates and are collated and described in detail by Barry et al. (2016). Each model accounts for varying amounts of 'gas-stripping', which is a process that describes the partial removal of noble gases from an initial ASW value, as well as the exchange of noble gases between gas, liquid and hydrocarbon phases. These models are particularly useful in quantifying the extent of water and hydrocarbon interaction. The average V_g/V_w for each gas field calculated using the equations described below for the entire suite of air-derived noble gases which were measured for their abundance in gas samples from the Sichuan and Bohai Bay Basins. This data is presented in Table 12, page 39.

1.3.8.1 Total gas stripping model (TGS)

This model represents a zero order endmember scenario as it assumes the complete removal of noble gases from a water phase, resulting in the highest gas-water volumetric ratios among the following models. Consequently, this model estimates the minimum volume of water (V_w) necessary to produce the measured gas concentrations in the gas phase [$C^g_{i(meas)}$] in cm^3 STP/cm^3:

$$\frac{V_g}{V_w}(\mathbf{TGS}) = \frac{[C_i^{asw}]}{Z\left[C_{i(meas)}^{g}\right]} \quad (20)$$

Where V_g/V_w is the gas-water volumetric ratio, and C_i^{asw} is the initial concentration of noble gas species 'i', which represents ASW. This model shows that in order to produce the measured ^{20}Ne values in $1cm^3$ of gas requires a very small amount of water to be totally gas-stripped, approximately 3.652×10^{-6} to $0.251cm^3$ of water. It is necessary to include a compression factor (Z) to enable the conversion from standard temperature and pressure conditions into reservoir temperature and pressure, which is given by:

$$Z = \frac{[273.15P_R]}{T_R} \quad (21)$$

Where P_R = reservoir pressure (bar) and T_R = reservoir temperature (K). Reservoir discovery pressures are specified for the Weiyuan and Fuling gas fields at equivalent drilling depths (Nie et al., 2023). In the western Sichuan basin, the Xujiahe fm. is highly overpressured, resulting in drilling difficulties and wellbore instability. The reservoir discovery pressure can be calculated for the Xujiahe fm. in the Xinchang gas field, where the pressure gradient is measured at between 20 MPa/km and 15.6 MPa/km for the Xu-4 and Xu-2 reservoirs, respectively (Zhang et al., 2020). In cases where the reservoir discovery pressure is not given, but the pressure coefficient is stated, the reservoir pressure can be calculated from the hydrostatic pressure, fluid density and reservoir depth. In the Bohai Bay Basin, pressures for depths up to 5000m are noted (Wang et al., 2021b) within the Shahejie-Dongying fm. the maximum measured pore pressure, 614.6 bar, occurs at a depth of 3768 m (Wang et al., 2019b). The average geothermal gradient in the Sichuan Basin is approximately 22.8°C/km (Dai et al., 2018) and in the Huanghua depression, Bohai Bay Basin, the geothermal gradient ranges from 24°C/km to 55°C/km, with an average value of 35°C/km (Zuo et al., 2017). Using a surface temperature of 10°C, we can determine with relative confidence, appropriate reservoir temperatures for different depths (Table 11).

Table 11 - Comparative reservoir properties of key formations and parameters used for models in the Sichuan and Bohai Bay Basins: Depth, Temperature (T_R), Pressure (P_R), and Compression Factors (Z).

Formation	Depth (m)	T_R Reservoir temperature (°C)	P_R Reservoir pressure (bar)	Z
Sichuan Basin				
Wufeng-Longmaxi fm. black shales	2300	62.44	560	449.75
""	3500	90	700	525.22
Xujiahe fm. tight sandstones	3500	90	700	""
""	5000	124	900	618.37
Bohai Bay Basin				
Kongdian and Shahejie fm. interbedded sandstones	1000	45	120	103.22
""	3800	167.5	600	372.85
Shihezi fm. sandstones	4750	176.25	700	424.31

1.3.8.2 Equilibrium partitioning and redissolution (EPR)

This first order model assumes an equilibrium exists within the reservoir between groundwater and hydrocarbon phases. Since existing formation water has been displaced in favour of upwardly migrating buoyant hydrocarbons, a quantifiable portion of noble gases will remain dissolved in water, while a volume of gas will also exsolve into the hydrocarbon phase at the gas-water contact:

$$\frac{V_g}{V_w}(\boldsymbol{EPR}) = \frac{[C_i^{asw}]}{\mathrm{Z}\left[C_{i(meas)}^{g}\right]} - \mathrm{H} \tag{22}$$

Compared to the TGS model, the EPR model requires a larger volume of water to account for the same amount of measured gas concentrations, as some of the initial ASW noble gases remain in the groundwater. We may then modify Equation 20 to include 'H', which alters the V_g/V_w according to the fraction of noble gases redissolved in water:

$$\mathrm{H} = \frac{22400 T_R \rho_w}{1000 \times 273.15\, K_i^m} \tag{23}$$

The terms T_R and ρ_w relate to the reservoir temperature and density of water, respectively, while K_i^m is Henry's constant (in atm kg mol^{-1}) for the appropriate reservoir temperature and salinity.

1.3.8.3 Progressive degassing in an open system (PD-OS)

A major distinction of this second order model is that it presupposes a partial loss of hydrocarbons from the system, and that the reservoir is open to gas-loss. Firstly, a small volume of gas (G) is assumed to reach equilibrium with a much larger static water volume (W), which contains ASW concentrations of noble gas [C_i^{asw}] during displacement of formation waters from the reservoir trap. Once the gas has reached the trap, the model assumes negligible interaction, and it is assumed that gas is then lost. This loss of gas could be a result of hydrocarbon migration and accumulation that precedes the development of the trapping structure or seal. Secondly, a 'fill and spill' scenario may also exist whereby overfilling and expulsion of hydrocarbons into adjacent traps is caused by the threshold volume or pressure being exceeded at a stratigraphic or structural trap. In such cases, the 'water bubble' is expected to evolve according to Rayleigh fractionation, and as hydrocarbons (and noble gases) are progressively lost from the reservoir, measured concentrations in both the gas and water phases $\rightarrow 0$.

Firstly, we can calculate the total number of moles remaining in the residual water (n_i^w) after degassing, and this linear relationship can be expressed by:

$$F = \left(\frac{C_{asw}^i}{C_{meas}^i}\right)^{1/d} \tag{24}$$

Where F^d signifies the fraction of the noble gas species 'i' remaining in the water phase (n_i^{asw0}) following 'd' intervals of gas-stripping. The behaviour of 'F' as a relationship

Consequently, 'F', can also be expressed relative to the partitioning between a volume of gas (G) and water packet (W), given by:

$$\mathrm{F} = \frac{\mathrm{H}}{\mathrm{H} + \frac{\mathrm{G}}{\mathrm{W}}} \tag{25}$$

The smaller the volume of gas relative to the volume of water, the smaller the amount of total gas 'stripped', and therefore the fraction of gas remaining in the water phase will be larger as $F \rightarrow 1$. When $F < 1$, which occurs when there is a greater volume of gas relative to the volume of water, each degassing step will lead to a large fraction of noble gas being stripped from water. In the majority of measured gas samples, $^{20}Ne_{meas}$ concentrations are 10^{-2}-10^{-3} smaller than $^{20}Ne_{asw}$, which suggests the system has undergone substantial degassing steps, or that a large volume of gas exists relative to the volume of water in contact with it. With little water availability, gases such as the lesser soluble Ne will strip

more readily, which is an adequate description of gas-rich systems, where gas is the dominant phase. Elevated $^{20}Ne/^{36}Ar$ ratios in the Sichuan Basin shale gas samples indicates that the gas in the system has undergone fractionation processes consistent with progressive degassing, where more of the volatile Ne is retained relative to Ar. However, since the system appears closed to gas loss, with little water availability, this gas remains trapped, leading to the enrichment of $^{20}Ne/^{36}Ar$ ratios beyond what is predicted by ASW models.

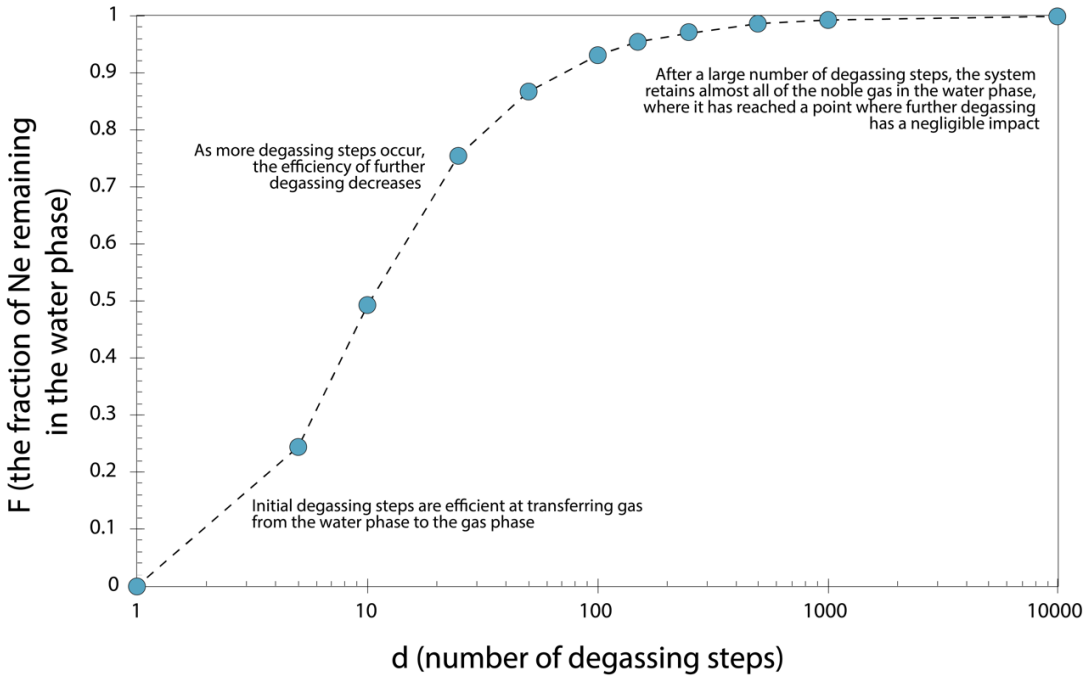

Figure 7 - Relationship between the fraction of remaining noble gas (F) in the water phase and the number of degassing steps (d) using the measured ^{20}Ne concentration of sample YS108 H4-3 (1.66×10^{-10} cm^3/ STP cm^3) in the Sichuan Basin. The graph shows an initial rapid increase in 'F' as noble gas is efficiently transferred from the water phase to the gas phase during early degassing steps. As 'd' number of steps increases, the rate of gas transfer decreases, and the system approaches an equilibrium state where further degassing has minimal effect on 'F'.

$$n_i^{asw} = \frac{WC_i^{asw}}{22400} \quad (26)$$

In a given volume of water (W) then, the number of moles (n_i^{asw}) can be estimated, whereby according to the ideal gas law (Equation 2), at standard temperature and pressure (STP), one mole of an ideal occupies 22400 cm^3.

Subsequently, we can utilise the measured gas concentrations ($C_i^{g}{}_{(meas)}$) to calculate the number of moles (n_i^{w}) in a given volume of water (W) due to 'd' degassing steps, which represents the amount of water required to impart the measured gas concentration on a particular gas volume (G).

$$n_i^w = C_{i\,(meas)}^g \left(\frac{P_R}{K_i^m} + \frac{ZG}{22400}\right) \quad (27)$$

It is then necessary to ascertain the extent of degassing or gas stripping that has transpired to produce the noble gas signature observed in our samples. Consequently, we can find the value of 'd':

$$d = \frac{ln\left(\frac{n_i^w}{n_i^{asw}}\right)}{ln(F)} \quad (28)$$

The value of 'd' for a measured noble gas concentration [$C^g_{i(meas)}$] is found by substituting the appropriate values for 'F', [n_i^{asw}] and [n_i^w], respectively, which allows for the determination of the V_g/V_w:

$$\frac{V_g}{V_w}(\boldsymbol{PD - OS}) = \frac{dG}{W} \quad (29)$$

The value of V_g/V_w (**PD-OS**) is solved for open reservoir conditions by following the equation above. Since noble gases possess varying solubilities, their elemental ratios will evolve predictably during exsolution from groundwater. Initially, gas bubbles will be enriched in the least soluble ASW-derived noble gases, as the less soluble noble gases will be preferentially exsolved. While progressive removal of the noble gases from the water body, the elemental composition of each successive gas bubble will reflect depleted concentrations relative to ASW.

In this open system model, the initial apportioning of noble gases are capable of escaping, resulting in a reservoir where highly differentiated or fractionated elemental ratios emerge. When utilising this particular PD-OS model, given the measured concentrations of Ne and Ar, and the calculated ASW values, we attain negative V_g/V_w values which strongly suggests the applicability of an open system model might be limited to this dataset, as either the initial ASW concentrations are too low or the measured concentrations are too high giving this negative, whereby this PD-OS model cannot justify the extent of degassing to fit the natural logarithm described in (28. The large difference between initial ASW concentrations and measured concentrations indicates extensive degassing or possibly even additional processes not accounted for in the PD-OS model.

Nevertheless, The V_g/V_w for this open system scenario represents the total volume of gas equilibrated with water prior to sampling. As gas stripping continues, the evolution of any

two individual noble gas species (Ne and Ar) can be determined, where an independent V_g/V_w is true for the measured elemental ratio between these two species ($^{20}Ne/^{36}Ar$). The elemental ratio of this 'first bubble' (where $V_g/V_w \rightarrow 0$) can then be ascertained using the equation:

$$\left(\frac{^{20}Ne}{^{36}Ar}\right) "First\ bubble" = \frac{K_{Ne}^{m}\left[\left(\frac{^{20}Ne}{^{36}Ar}\right)asw\right]}{K_{Ar}^{m}} \tag{30}$$

For the Sichuan Basin gas samples, we calculated $^{20}Ne/^{36}Ar$ "first bubble" values of 0.183 and 0.221 for the Wufeng-Longmaxi shale and Xujiahe tight sandstone formations, respectively, and in the Bohai Bay Basin, $^{20}Ne/^{36}Ar$ "first bubble" values of 0.226 were determined. Following Rayleigh fractionation, each successive gas stripping will lead to an elemental ratio of $^{20}Ne/^{36}Ar$ that tends toward a limit. To estimate the V_g/V_w for the elemental ratio of $^{20}Ne/^{36}Ar$ we may use the following equation:

$$\frac{V_g}{V_w}(\boldsymbol{PD - OS}\ \frac{^{20}Ne}{^{36}Ar}) = \frac{G}{W}\left(\frac{ln\left(\frac{\left(\frac{^{20}Ne}{^{36}Ar}\right)meas}{\left[\frac{K_{Ne}^{m}}{K_{Ar}^{m}}\right]\left(\frac{^{20}Ne}{^{36}Ar}\right)asw}\right)}{ln\left(\frac{F_{Ne}}{F_{Ar}}\right)}\right) \tag{31}$$

When gas samples exhibit elemental ratios below that of ASW, this may show that the system is open and that all noble gases have almost been totally degassed.

1.3.8.4 Progressive degassing in a closed system

Lastly, in a second order closed-system model, we may assume that hydrocarbon gases, having interacted with ASW, will mobilise to a trap and then remain confined within the reservoir unit. Initially, a small volume of gas (G) will achieve equilibrium with a volume of water (W), which contains an initial concentration of ASW-derived gases [C_i^{asw}]. We also assume minimal exchange between the gas-water interface, with negligible loss of gas or gas escape. This closed system produces a measurable signature of noble gases, which is determined with a mass balance equation given by:

$$\left[C_{i(meas)}^{g}\right] = \frac{\left((n_i^{asw}) - (n_i^{asw})F^d\right)22400}{ZGd} \tag{32}$$

By simplifying and expressing 'U' as the subject, we get:

$$U = \frac{\left[C^{g}_{i(meas)}\right] ZG}{22400(n_i^{asw})} \tag{33}$$

We then arrive at an expression that describes the relationship between 'U', 'd' and 'f':

$$Ud = 1 - F^{d} \tag{34}$$

Solving for 'd' using a Lambert transcendental function (where a number cannot be expressed in finite terms), ω, defined as the multivalued inverse of f(w) = we^{w}:

$$d = \frac{1}{U} - \frac{1}{ln(F)}\omega\left(F^{\frac{1}{U}} ln(F)/U\right) \tag{35}$$

Substituting 'd' into an assumed G/W volume ratio, the volumetric V_g/V_w (**PD-CS**) is:

$$\frac{Vg}{Vw}(\boldsymbol{PD - CS}) = \frac{dG}{W} \tag{36}$$

As this model assumes closed system behaviour, the first bubble elemental ratio (i/j) will be similar to that of an open system described above; however, the "final" gas bubble will have an elemental ratio that will be equal to the starting composition of ASW:

$$\left(\frac{^{20}Ne}{^{36}Ar}\right)\textit{"final"} = \left(\frac{^{20}Ne}{^{36}Ar}\right)_{asw} \tag{37}$$

To calculate the V_g/V_w for this closed system, the "first" gas bubble will contain a small V_g/V_w, until equilibrium with the ASW value is reached with a $V_g/V_w > 0.01$.

$$\frac{Vg}{Vw}\left(\boldsymbol{PD - CS}\frac{^{20}Ne}{^{36}Ar}\right) = \frac{\left[\frac{\left(\frac{^{20}Ne}{^{36}Ar}\right)_{asw}}{K^{m}_{Ar}}\right] - \left[\frac{\left(\frac{^{20}Ne}{^{36}Ar}\right)_{meas}}{K^{m}_{Ne}}\right]}{\left(\frac{^{20}Ne}{^{36}Ar}\right)_{meas} - \left(\frac{^{20}Ne}{^{36}Ar}\right)_{asw}} \tag{38}$$

Table 12 - V_g/V_w using different order models. ^{20}Ne, ^{36}Ar, ^{84}Kr and ^{132}Xe concentrations are lower than ASW values in the Bohai Bay Basin, giving potentially erroneous V_g/V_w

	$\frac{Vg}{Vw}$ (**TGS**) Total gas stripping	$\frac{Vg}{Vw}$ (**EPR**) Equilibrium	$\frac{Vg}{Vw}$ (**PD-OS**) Open system
Sichuan Basin			
Xinchang			
^{20}Ne	1.993	1.978	0.037
^{36}Ar	1.357	1.330	0.027
^{84}Kr	0.026	-	-
^{132}Xe	1.993	1.938	-
Fuling			
^{20}Ne	1.511	1.497	-
^{36}Ar	1.719	1.694	-
^{84}Kr	0.033	-	-
^{132}Xe	1.511	1.460	-
Zhaotong			
^{20}Ne	2.144	2.130	-
^{36}Ar	13.627	13.602	-
^{84}Kr	0.047	0.011	-
^{132}Xe	2.145	2.094	-
Changning			
^{20}Ne	0.706	0.693	-
^{36}Ar	11.486	11.462	-
^{84}Kr	0.036	-	-
^{132}Xe	0.707	0.656	-
Weiyuan			
^{20}Ne	0.347	0.333	-
^{36}Ar	3.734	3.709	-
^{84}Kr	0.116	0.079	-
^{132}Xe	0.347	0.296	-
Bohai Bay Basin			
Dagang			
^{20}Ne	213.557	213.539	-
^{36}Ar	166.553	116.532	-
^{84}Kr	116.938	116.915	-
^{132}Xe	213.758	213.732	-

1.3.9 Models describing mechanisms for noble gas interactions on solids: Adsorption

Adsorption of noble gases is a significant geochemical phenomenon that remains poorly understood. It has been proposed that adsorption may account for a proportion of 'missing' Xe abundances within air, which are depleted by a factor of 25 times relative to other noble gases within the Earth's atmospheric inventory (Podosek et al., 1981). It is therefore necessary to inquire as to the cause of this discrepancy and to characterise the extent of isotopic fractionation, which may result from adsorption mechanisms (Bernatowicz and Podosek, 1986). Adsorption describes the molecular interaction of gases (as a fixation mechanism) with a solid material surface (i.e., shale), and likely plays a large role in the distribution and behaviour of noble gases (Fanale and Cannon, 1971), particularly in fine-grained shales and tight sandstones. These reservoir units are especially appropriate for studying adsorption, as organic matter content is high, and in the case of shale, large amounts of kerogen and a clay mineral matrix enhance the total surface area, which promotes the availability of adsorbate atoms and molecules on the sorbent surface.

The physical molecular interactions between the sorbent surface and gas arise due to relatively weak Van der Waals forces, while the heavier noble gases are more polarisable than lighter ones, which means that they can more easily induce temporary dipoles that facilitate adsorption. The lighter noble gases (He and Ne) are considered poorer sorbates due to their lower atomic mass, and therefore, the adsorption of these gases is much less prevalent.

Consequently, in the manuscripts compiled within this thesis research, only the adsorption data for Kr and Xe is reported, and assessed using several adsorption models. Multiple isotherm models (discussed herein in the following sections) aim to describe the relationship between the amount of adsorption of a gas on the surface of a material (the concentration of the sorbate, x_i), as a function of partial pressure (fugacity), p_i in the gas phase and temperature, *T*. The dependence of concentration on partial pressure indicates that the linear relationship between these values can be given by rearranging Henry's Law in Equation 1:

$$x_i = K_i p_i \tag{39}$$

Noble gas adsorption in natural terrestrial reservoirs is unlikely to ever reach saturation, and Henry's law appears to adequately explain the relationship between an adsorbed

phase at the pressures relevant to noble gas geochemical studies. Adsorption equations reduce to Henry's law (Lee and Basmadjian, 1970), and while more complex isotherms have been used to define the adsorption equilibrium, a Langmuir isotherm suffices to represent a gas shale within a given field accurately (Tiab and Donaldson, 2016).

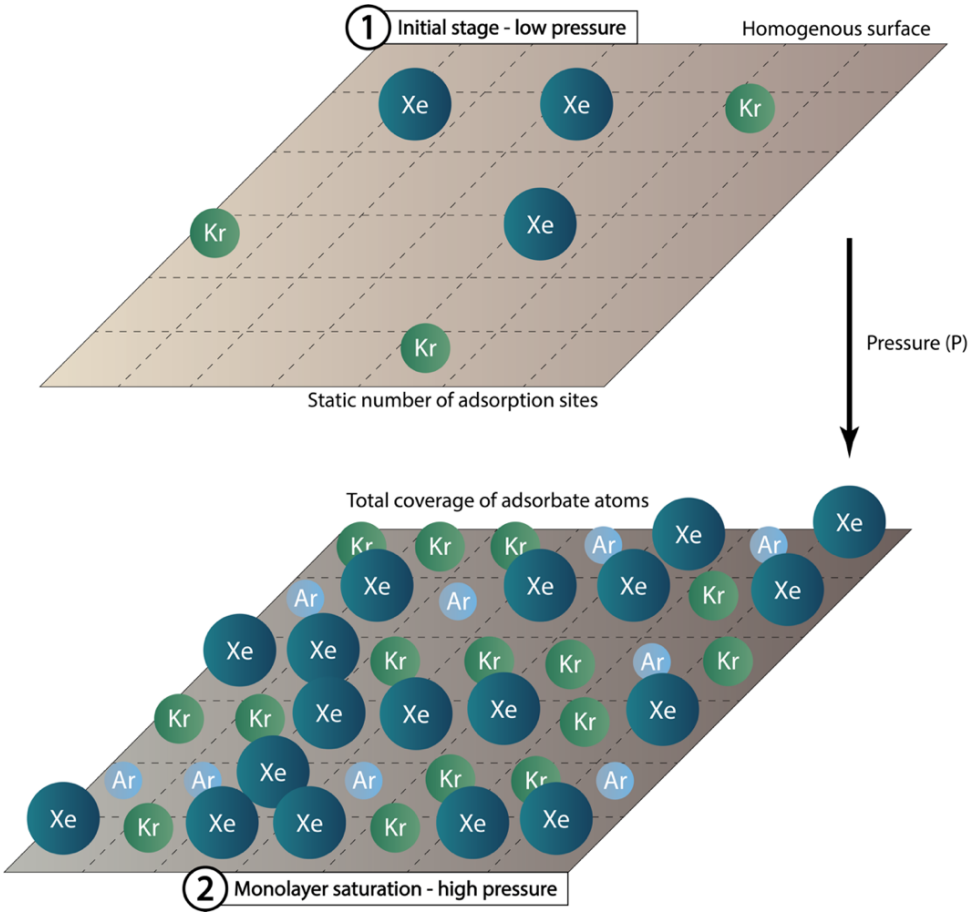

Figure 8 - Monolayer adsorption model showing the Langmuir theory of monolayer coverage in a simple two-stage process that demonstrates increasing pressure in a system, which results in saturation and total surface coverage.

1.3.9.1 The Langmuir isotherm

The Langmuir isotherm is a kinetic theory model devised by Langmuir (1918) that adequately describes the process of adsorption onto a singular-layered solid surface at an atomic level, where adsorption and desorption are reversible processes, and the adsorbate behaves as an ideal gas. The Langmuir adsorption equation denotes that the fractional occupancy of adsorption sites is characterised by the relationship between the volume of gas adsorbed, and the maximum volume of gas molecules that can be occupied by the adsorbate ($\theta = G_a/V_L$). The Langmuir model is a useful starting point for the preliminary

analysis of adsorption parameters. The adsorbed-gas storage capacity (G_a) of a shale at pressure '*P*' can be found by using a general form of the Langmuir equation:

$$G_a = V_L\left(\frac{P}{P + P_L}\right) \tag{40}$$

Where V_L represents the maximum volume of gas that can be adsorbed by the shale at infinite pressure, and P_L is the Langmuir pressure, which denotes the critical desorption pressure, which is the pressure at which half the available adsorption sites are filled (0.5 V_L). Firstly, by plotting adsorption isotherm data V vs. V/P on a cartesian plane for each gas system, we can find the values of V_L and P_L, where V_L represents the intercept, and P_L corresponds to the slope gradient, giving the equation:

$$V = -P_L\left(\frac{V}{P}\right) + V_L \tag{41}$$

We can calculate the adsorbed-gas storage capacity (G_a) at any given pressure (*P*):

$$G_a = V_L\left(\frac{bP}{P + bP}\right) \tag{42}$$

Where $b = 1/P_L$. Sorption isotherm data is available for the Weiyuan and Changning gas fields (Zhao et al., 2023a), which permits the calculation of the Langmuir isotherm constants V_L and Langmuir pressure P_L for the Weiyuan and Changning gas fields:

Table 13 - Sorption characteristics of Wufeng-Longmaxi shale from well N213 in the Changning block and well W202 in the Weiyuan block

	Changning		Weiyuan	
V cm^3g^{-1}	P (bar)	V/P	P (bar)	V/P
0.1	2	0.050	4	0.025
0.5	8	0.063	20	0.025
1	15	0.067	50	0.02
1.5	30	0.050	100	0.015
2	56	0.036	210	0.0095
2.5	120	0.021	-	-

The adsorbed-gas storage capacity, G_a, of the Wufeng-Longmaxi shale can then be estimated for the known reservoir pressure with V_L, P_L and b (Figure 9) using equation 42, which yields G_a = 0.039 cm^3g^{-1} for Fuling, Changing and Zhaotong, and G_a = 0.014 cm^3g^{-1} for Weiyuan.

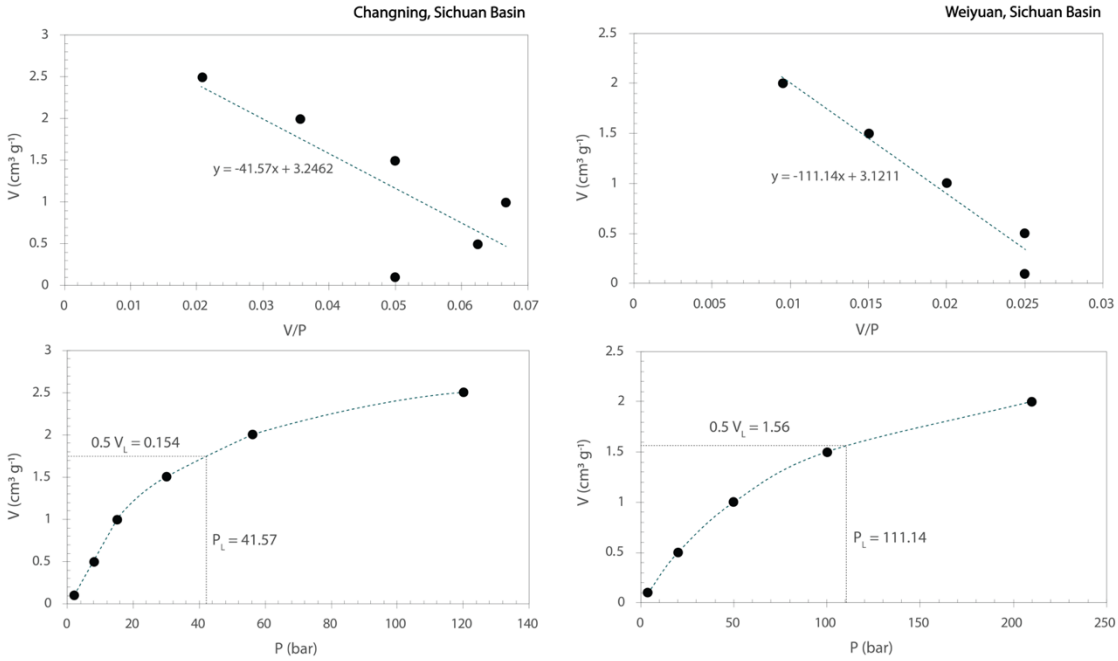

Figure 9 - Langmuir isotherm data plotted as a straight line for the Changning and Weiyuan gas fields, Sichuan Basin

The Langmuir isotherm also describes a system with increasing surface occupancy of gas molecules until saturation is reached (when the surface is entirely coated with a singular molecular layer). In this model, there are N_s adsorption sites, with equal adsorption potentials (each binding to one sorbate atom or molecule, as the Langmuir model predicts), and this is related to the gas storage capacity (42). As adsorption reaches saturation, the Langmuir isotherm begins to fail, while this model also does not consider non-ideality of the adsorbate. For a given adsorbate surface area (A), the flux of desorbing atoms ($\phi_{desorption}$), which describes the rate at which adsorbed atoms and molecules leave the surface can be determined by:

$$\phi = \theta N_s / A\tau \tag{43}$$

Where τ = Mean life against desorption, i.e., the average time an atom or molecule spends on the surface before desorbing, and θ represents the fraction of sites occupied, when maximum adsorption occurs, $\theta = 1$. The flux of adsorbing atoms ($\phi_{adsorption}$), which describes the rate at which atoms and moles in the gas phase collide with the surface and become adsorbed is given by:

$$\phi = \alpha P(1-\theta)(2\pi mkT)^{-1/2} \tag{44}$$

Where 'm' is the atomic mass, 'k' is Boltzmann's constant (1.38 x 10^{-23} J/K), 'α' is the probability that an unoccupied site will be adsorbed and a, is the area of an individual

adsorption site, which is equal to A/N_s. The terms "$2\pi mkT$" are associated with the kinetic gas theory and represent the average velocity of gas molecules. Under equilibrium conditions, the flux of adsorbing and desorbing atoms is equal and is proportional to the number of adsorption sites (N_s) and the fractional coverage (θ), represented by the equation:

$$N = N_s\theta = \frac{N_s bP}{(1 + bP)} \tag{45}$$

for:

$$b = \alpha\tau a(2\pi mkT)^{-\frac{1}{2}} \tag{46}$$

For the Sichuan and Bohai Bay Basins, with reservoir pressures of between 630 to 800 bar and 360 to 700 bar, respectively, and at exceedingly lower pressures, the Langmuir isotherm will reduce to Henry's law, giving the following:

$$K = \alpha A\tau(2\pi mkT)^{-\frac{1}{2}} \tag{47}$$

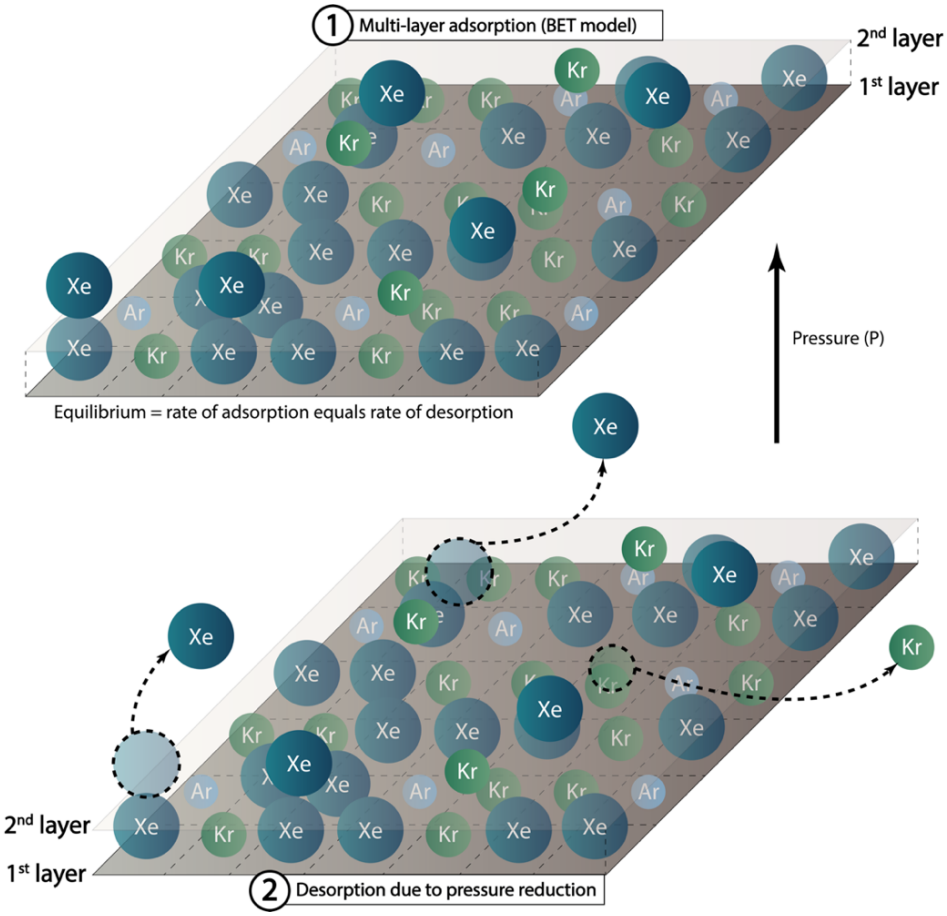

Figure 10 - Multi-layer BET adsorption model showing gas desorption of the 2nd layer of atoms when P < P_L (desorption pressure), which corresponds to 0.5V_L

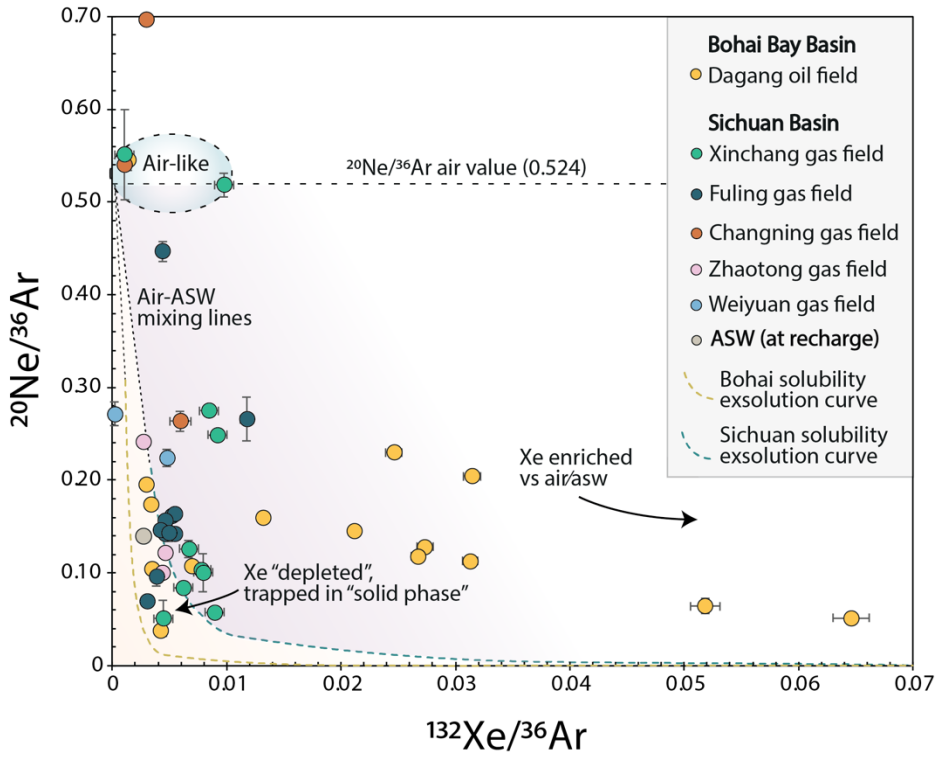

Figure 11 - Air derived ($^{20}Ne/^{36}Ar$ vs $^{132}Xe/^{36}Ar$) ratios for all gas samples, depicting the evolution of ratios according to Rayleigh and batch fractionation, and adsorption at various stages of degassing.

1.3.10 Three-volume thermodynamic phase model

By assessing free gas, gas-in-solution and adsorbed gas volumes; one can then finally consider the interactions and equilibrium states among the adsorbed gas phase (G_a), the free gas phase (G_f) and the gas in solution (G_s), depicted as a three-volume thermodynamic model. A mass balance equation can also be formulated to describe the thermodynamic equilibrium between these states, for example:

$$G_t = G_a + G_f + G_s \tag{48}$$

Where G_t is the total noble gas content in a given volume. Each state is associated with an equilibrium constant (Henry's constants, K_i, which are all described in the previous sections) representing how readily gas will dissolve in solution or be adsorbed onto a solid surface under equilibrium at reservoir conditions. Effective porosity (ϕ) has a significant impact on this three-volume model, and directly influences the available storage volume for a free gas phase (G_a), as well as increasing or decreasing the surface area for adsorption (G_a) and dictates the amount of solvent (e.g., water, hydrocarbons) that result in a higher or lower proportion of dissolved gas (G_s). A schematic model that describes the three-volume gas storage mechanisms of the noble gases in shale, denoting three phases in equilibrium within a closed system is shown in Figure 31, on page 105.

1.3.11 Resolving contributions: Crustal and air-derived He, Ne and Ar

In both the Sichuan Basin and Bohai Bay Basin, rare gas isotopic compositions were used to study the behaviour of crustal fluid systems, and therefore, resolving the geochemical contributions of crustal He, Ne and Ar in gas samples necessitates a detailed understanding of the different isotopic systems and processes that generate them. In the Sichuan Basin, helium isotopic compositions indicate a crustal origin derived from the radioactive decay of uranium (U) and thorium (Th), with no significant mantle contribution in most gas samples. This contrasts with rift basins like the Bohai Bay Basin, which have significant additions of mantle-derived helium, signified by the disparity in $^{3}He/^{4}He$ ratios across both basins. Therefore, the relative proportions of crustal, air and mantle components are vital in characterising the historical and present-day tectonic regime and the extent of magmatic activity across geologically complex sedimentary basins. For example, ^{40}Ar has recently been shown to be a key indicator in understanding mantle dynamics and mantle and crustal geochemistry, and it has been used to argue for a largely primordial, convectively isolated lower mantle, informed by lower $^{40}Ar/^{36}Ar$ ratios in the mantle source of ocean-island basalts compared with mid-ocean-ridge basalts (Tucker et al., 2022).

He, in most gas fields, is a component mixture of radiogenic and mantle-derived gas, where ^{3}He is considered 'primordial' and is associated with mantle-derived He (Ballentine and O'Nions, 1992), while ^{4}He is generated through the radioactive decay of ^{238}U and ^{232}Th, which yields alpha particle (α) emission and the production of stable ^{206}Pb, and ^{208}Pb:

$$^{238}U \rightarrow {}^{206}Pb + 8{}^{4}He \tag{49}$$

$$^{232}Th \rightarrow {}^{208}Pb + 6{}^{4}He \tag{50}$$

When the total concentration of ^{4}He in a crustal system is known, the in-situ production rate can be calculated (Equation (51) after Torgersen (1980), and then input (Equation (53) to constrain the time of formation:

$$[{}^{4}He]_{in\ situ\ production} = \frac{\rho \Lambda J_{He}(1-\varphi)}{\varphi} t \tag{51}$$

Where ρ is the density of porous rock, expressed in g/cm^3, Λ denotes the fraction of He generated within the solid phase that subsequently migrates into the pore fluid, and is a parameter that defines the efficiency of He removal into groundwater. Presuming rapid

He loss from the matrix over geologic time scales, $\Lambda \approx 1$. φ is the porosity of the material, which represents the fraction of void space within a rock, and takes on values between 0 and 1, where 0 implies there is zero pore space, and 1 indicates a completely porous rock. Time (t) corresponds to a value equal to 1, so that the equation yields a production rate of ^{4}He per year.

Using the known in-situ concentrations of U and Th (measured by spectral gamma ray and also inferred from available wireline logging data), J_{He} can then be expressed as the following in cm^3 STP ^{4}He per cm^3 fluid yr^{-1}(Craig and Lupton, 1976):

$$J_{He} = 0.2355 \times 10^{-12}[U][1 + 0.123([Th]/[U] - 4)] \quad (52)$$

Consequently, the accumulation of radiogenic ^{4}He can provide a reasonable chronometer for geological processes, allowing us to understand thermal histories, and trace fluid movements in the crust. This is particularly important in hydrocarbon exploration to determine the timing of oil and gas migration and to assess the thermal maturity of potential reservoir rocks. We can determine the groundwater residence ages for a particular system by using:

$$t = \frac{(C_{He})_{sample}}{J_{He}} \quad (53)$$

Using available data for the Zhaotong gas field; U and Th concentrations are around 26 ppm and 7.85 ppm, respectively, which yields a an in-situ production rate (J_{He}) of 18.55 x 10^{-11} cm^3 STP $^{4}He/cm^3$ H_2O year. Accordingly, the age of ^{4}He present in formation waters is calculated at 182 million years. This suggests that the system has behaved as a closed system for a considerable part of geological time, which implies minimal escape of helium and, by extension, possibly other gases, allowing for the accumulation of ^{4}He concentrations.

While ^{4}He is incredibly useful for understanding the timing of these geological processes, we can also study ^{21}Ne since it is less mobile than He. Yet, both isotopes share a common origin through decay and nucleogenic spallation. The production of ^{21}Ne occurs through nuclear reactions involving the interaction of α particles and neutrons that result from (α,n) reactions with $^{235,238}U$ and ^{232}Th, with a non-significant contribution of neutrons derived from ^{238}U spontaneous fission. This nuclear reaction is described by the following decay equation:

$$^{18}O(\alpha, n)^{21}Ne \quad (54)$$

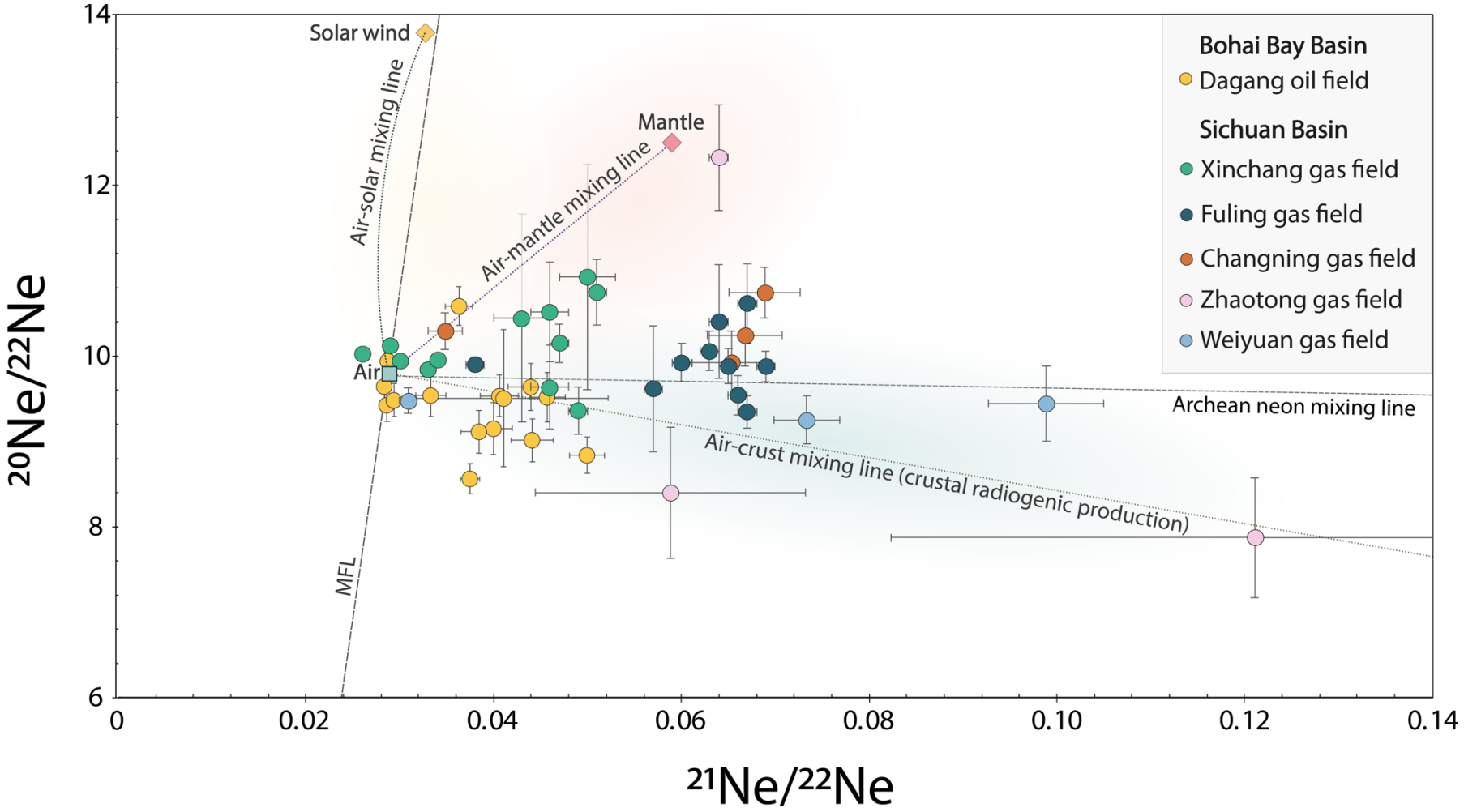

Figure 12 – Plot of $^{20}Ne/^{22}Ne$ vs $^{21}Ne/^{22}Ne$ isotope ratios for all gas samples across the Sichuan Basin and Bohai Bay Basins. The plotted mixing lines represent potential processes or sources influencing Ne compositions, including mantle outgassing and crustal radiogenic production. This plot highlights the mixing between three distinct sources of Ne in shale and tight sandstone hydrocarbon reservoirs. Tight sandstone and conventional sandstones are considerably more "air-like" than the highly radiogenic in-situ shale gases.

Crustal radiogenic ^{40}Ar production predominantly arises from the decay of ^{40}K, found ubiquitously in crustal minerals:

$$^{40}K \rightarrow {}^{40}Ar + {}^{40}Ca \quad (55)$$

In this decay process, ^{40}K decays to the daughter isotope ^{40}Ar through electron capture, while ^{40}K can also decay to ^{40}Ca through beta (β) decay. The quantity of ^{40}Ar in gas samples is proportional to the amount of ^{40}K, representing the time the system has been closed to gas loss. Deep groundwaters in sedimentary basins can be sufficiently old (> 10 ma) to have accumulated both radiogenic ^{4}He and ^{40}Ar (Zaikowski et al., 1987), while the atmosphere also contains a significant amount of ^{21}Ne and crustal radiogenic ^{40}Ar (Ballentine et al., 2002). As outlined in Section 1.3, terrigenic noble gases are dominated by three well-defined geochemical reservoirs (Figure 4). Therefore, those noble gases not sourced from the mantle arise from a mixed atmospheric and crustal-radiogenic input. In a two-component mixing model, we can compare measured isotopic ratios with the known atmospheric ratio to identify the crustal excess (^{21}Ne* and ^{40}Ar*), which represents the input of noble gases produced by nuclear reactions of U and Th in the crust, which have subsequently mixed with atmospheric Ne and Ar:

$$^{21}Ne^{*} = {}^{22}Ne_{meas} \times [(^{21}Ne/^{22}Ne_{meas}) - (^{21}Ne/^{22}Ne_{air})] \quad (56)$$

$$^{40}Ar^{*} = {}^{36}Ar_{meas} \times [(^{40}Ar/^{36}Ar_{meas}) - (^{40}Ar/^{36}Ar_{air})] \quad (57)$$

The process for deconvoluting ^{4}He contributions from the crust involves firstly determining the quantity of 'primitive' ^{3}He preserved following planetary accretion and to correct the measured He compositions for air-derived contributions following Craig (1978):

$$(^{3}He/^{4}He)_{c} = \frac{(^{3}He/^{4}He)_{meas} \times (^{4}He/^{20}Ne)_{meas}/(^{4}He/^{20}Ne)_{air} - (^{3}He/^{4}He)_{air}}{(^{4}He/^{20}Ne)_{meas}/(^{4}He/^{20}Ne)_{air} - 1} \quad (58)$$

Where $(^{3}He/^{4}He)_{c}$ refers to the corrected ^{3}He/^{4}He ratio. We may use ^{4}He/^{20}Ne in the correction calculation, as Ne is not fractionated in the same way as He during degassing. For the Sichuan Basin, gas samples have ^{3}He/^{4}He ratios that are very 'crustal-like', and in the Bohai Bay Basin, ^{3}He/^{4}He ratios are as high as 2.17, denoting a large mantle He component relative to crustal He.

Having accounted for helium derived from the atmosphere, the ^{3}He/^{4}He ratio represents a binary mixture formed of two distinct components: the crust and mantle. Corrected

$^3He/^4He$ ratios in the Sichuan Basin are negligibly different from measured $^3He/^4He$ ratios (10^{-14}), whereas in the Bohai Bay Basin, the difference between corrected $^3He/^4He$ and measured ratios is around 10^{-11}, which suggests that the $^3He/^4He$ ratio is more altered in the Bohai Bay Basin following this correction, indicating a larger influence of atmospheric He. In both basins, however, this atmospheric He contribution is minimal, demonstrating that in both cases, He is predominantly derived from a deep reservoir, with little mixing and interaction with an air He component. The quantification of the pure crustal ^4He contribution can be calculated by substituting $(^3He/^4He)_c$ from Equation (58 into the following:

$$[^4He]_{crust} = \frac{[^4He]_{tot} \times [(^3He/^4He)_{mantle} - (^3He/^4He)_c]}{[(^3He/^4He)_{mantle} - (^3He/^4He)_{crust}]} \quad (59)$$

This equation determines the contribution of ^4He by accounting for the differences in the $^3He/^4He$ ratio observed in mantle and crustal reservoirs, where the $^3He/^4He$ ratio is known $(^3He/^4He)_{crust} = 0.01\ R_a$, while $(^3He/^4He)_{mantle} = 8\ R_a$ (Ballentine and Burnard, 2002).

1.3.12 Resolving contributions: Mantle derived He

In a similar two-component mixing model that comprises both crustal and mantle-derived $^3He/^4He$, it is possible to determine the contribution of mantle-sourced He (both ^3He and ^4He sourced from the mantle). This is particularly useful in regions with a known mantle influence and/or an active fault system, such as the Bohai Bay Basin. We can quantify this crust-mantle interaction by substituting the known mantle and crustal He ratios, $(^3He/^4He)_{crust}$ and $(^3He/^4He)_{mantle}$, as well as the measured $^3He/^4He$ ratio of samples $(^3He/^4He)_{sample}$ into the equation:

$$He_{mantle}(\%) = \frac{[(^3He/^4He)_{sample} - (^3He/^4He)_{crust})]}{[(^3He/^4He)_{mantle} - (^3He/^4He)_{crust}]}\ x\ 100\% \quad (60)$$

This deconvolution helps to provide evidence for a mantle-derived input, as well as the extent of tectonic activity and deep pathways within each sedimentary basin.
Resolving these contributions, the extent of mantle derived He in the Sichuan Basin and Bohai Bay Basins can be determined (Table 14).

Table 14 - Mantle derived He and composition of He in gas samples across China's major basins (Sichuan and Bohai Bay Basins)

	$^3He/^4He$ (R/R_a)	$(^3He/^4He)_c - (^3He/^4He)_{meas}$	He_{mantle} (%)
Mantle	~8.0	-	-
Crust	~0.01	-	-
Sichuan Basin			
Xinchang gas field	0.0039 – 0.025	10^{-14}	0.1 - 0.2
Fuling gas field	0.0062 – 0.013	10^{-14}	n/a
Changning gas field	0.0088 – 0.0096	10^{-14}	n/a
Zhaotong gas field	0.0037 – 0.0063	10^{-14}	n/a
Weiyuan gas field	0.017 – 0.038	10^{-13}	0.1 - 0.35
Bohai Bay Basin			
Dagang oil field	0.023 – 2.17	10^{-11}	2.66 – 26.97

The $^3He/^4He$ ratios (R/R_a) across the Sichuan Basin gas fields range from $0.0037R_a$ to $0.038R_a$, which is considerably lower than the mantle endmember ($8R_a$). This indicates a predominance of crustal helium ($0.01R_a$), with negligible contributions from the mantle (0.1%-0.2% and 0.1%-0.35% for the Xinchang and Weiyuan gas fields, respectively). Weiyuan gas field He ratios are an order of magnitude larger than other Sichuan Basin gas fields, and this difference indicates variations in the source and mixing history of He in the Weiyuan field.

The $^3He/^4He$ ratios in the Dagang oil field show a much broader range from $0.023R_a$ to $2.17R_a$, with values approaching the lower end of mantle contributions. This range suggests a significant presence of mantle-derived helium in this field compared to the Sichuan Basin gas fields. The mantle-derived helium percentage (He_{mantle}) in the Dagang oil field ranges from 2.66% to 26.97% which suggests there is a greater influence of mantle-derived helium, due to tectonic or magmatic processes in the Bohai Bay Basin. These results highlight that geological and tectonic differences between these basins have played a significant role in controlling He isotope compositions and the mixing of mantle and crustal gases.

1.4 The Role of Noble Gas Geochemistry in China's Natural Gas Exploration

This thesis and the numerous works cited throughout demonstrate that noble gas geochemistry has the potential to aid our understanding of the complex multistage evolution of different petroliferous sedimentary basins within China, and worldwide. Many recent and ongoing studies aim to describe the geochemical characteristics of natural gases and the role that noble gases play in assessing the influence of different fluid sources on gas migration, accumulation and reservoir connectivity (Scott et al., 2021, Pearce et al., 2024, Karolytė et al., 2021, Ju et al., 2020, Eymold et al., 2021, Moore et al., 2018, Byrne et al., 2020, Cao et al., 2020a, Wang et al., 2022c, Zhang et al., 2024).

The findings of these studies could have important scientific and policy implications for future resource exploration, as China and many other nations have identified sustainable gas extraction of natural gas reserves as a primary ambition (Li, 2023).

China has abundant natural gas reserves and is ranked second globally for recoverable natural gas resources (Dai et al., 2021), it offers a fundamental setting to apply noble gas analytical techniques, offering deeper insights into shale gas dynamics. This work aims to contribute valuable scientific insights that can inform future policymaking in the UK, China, and other regions where unconventional gas exploration is widespread.

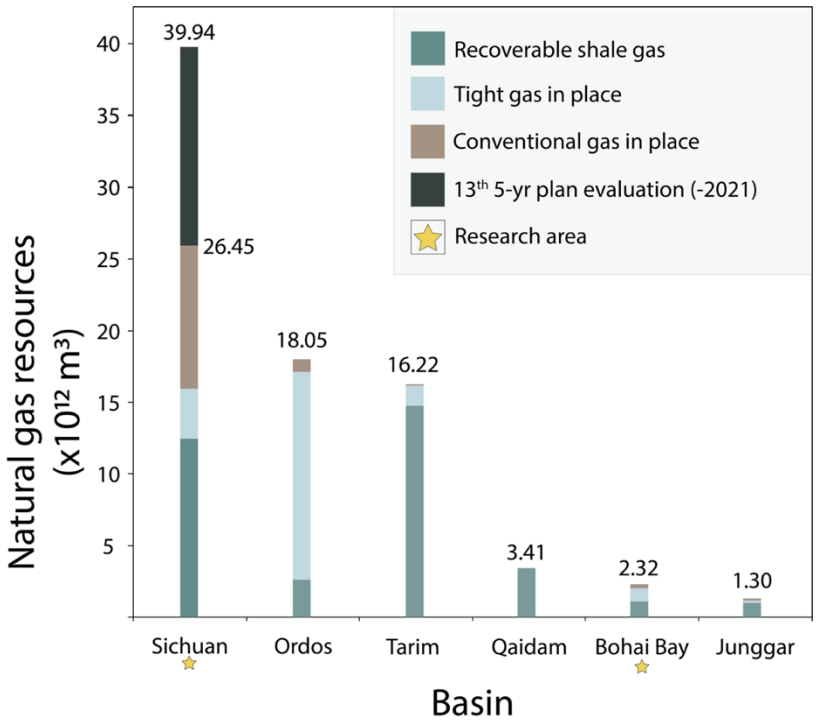

Figure 13 – Histogram showing discovered resources within the major petroliferous basins of China as of 2022, modified from Ma (2017a) and with updated natural gas resources for the Sichuan Basin, from China's 13th Five-year plan evaluation (Zhang, 2022). Gas reserves are categorised into recoverable shale gas, tight gas in place, and conventional gas in place. The Sichuan and Bohai Bay Basins are highlighted as research areas, denoted by the star symbol.

1.4.1 Exploration history and development of China's natural gas

China's natural gas industry has grown exponentially, with production growing from 274 x 10^8 m^3 in 2000 to 1925 x 10^8 m^3 in 2020 (Li, 2022). Total gas production in 2018 saw the Sichuan Basin lead with the highest volume of natural gas resources (Figure 13) at 26.45 x 10^{12} m^3, comprising a broad mixture of all three gas types: recoverable shale gas, tight gas, and conventional gas. According to both Jia et al. (2021) and Dai et al. (2019), the evolution of China's natural gas industry can be separated into three distinct phases, each characterised by its rate of gas production:

1. Initiation (1949–1977): Commencing in the Sichuan Basin, the industry gradually increased annual gas production from 10^7 m^3 to 10^{10} m^3 by 1977. During this period, the cumulative proven gas reserves in the country did not exceed 2×10^{11} m^3.

2. Slow Growth (1977–2001): Over these 24 years, annual gas production steadily rose to 3×10^{10} m^3, and cumulative proven gas reserves reached 3.4×10^{12} m^3.

3. Rapid Growth (2001–2020): This recent period witnessed an 83.4×10^8 m^3 increase in annual gas production, reaching 1.93×10^{11} m^3 in 2020. Cumulative proven gas reserves were 1.96×10^{13} m^3 by 2020. The pace of domestic natural gas development accelerated following the 18th National Congress of the CPC. During the 13th Five-Year Plan, annual gas production successively accounted for 1.37×10^{11} m^3, 1.48×10^{11} m^3, 1.60×10^{11} m^3, 1.75×10^{11} m^3, and 1.93×10^{11} m^3, reflecting an annual increase of 9.4%. The Sichuan Basin in China has seen significant progress in shale gas exploration and development, particularly in the black shales of the Upper Ordovician and Lower Silurian formations. The petrological and geochemical characteristics of these black shales have been studied extensively; (Dai et al., 2014, Dai et al., 2018, Dai et al., 2016, Feng et al., 2019, Yan et al., 2015). The black shale primarily contains clay, carbonate, and quartz, with an average total organic carbon (TOC) content of 2.21% (Li et al., 2022). Whilst the first large mono-block gas field, the Weiyuan gas field was discovered in 1964, it wasn't until 2005 that theoretical research into the exploration and development of shale gas in China commenced. Natural gas production began in earnest in 1937 with the inaugural Ba-1 Well in Banian County (now the Banian District, Chongqing), and following this the Sichuan Petroleum Administration was set up in 1958. By 2015, 140 gas fields with proven reserves had been established, accounting for a quarter of all natural gas production in China (Ma, 2017b). Exploration into the southernmost verge of the Sichuan Basin has only recently occurred, within the National Shale Gas Exploration Demonstration Zone of China and the Zhaotong area, which comprises 27 production

wells with a total output of 5.0 x 10^8 m^3 in 2016. In the east, development of the Fuling shale gas field began in 2011 and is still mostly driven by government strategic policy. Commercial development of the JY-1 well in the Fuling gas field took place at the end of 2012. By 2019, Fuling shale gas production output reached around 1.8 x10^7 m^3d^{-1} of natural gas (Zheng et al., 2020). The Xujiahe tight sandstone reservoirs in the western Sichuan depression has similarly high proven potential with 1250.44 x 10^8 m^3 of proven reserves and 44 wells that have been drilled in the Xinchang tectonic zone alone (Liu et al., 2020a). In contrast to shale gas developments in North America, surface and geological conditions are vastly dissimilar and this has made development more challenging (Sun and Bao, 2018). Studies that centre upon the geochemical analysis of these shale gases in China are still emerging (Dai et al., 2014, Dai et al., 2018, Dai et al., 2016, Feng et al., 2019, Yan et al., 2015), those that delve into the geochemistry of noble gases within these basins are less abundant still; (Zhang et al., 2019b, Zhang et al., 2019c, Cao et al., 2016, Cao et al., 2018, Cao et al., 2020a, Li et al., 2020, Liu et al., 2021a).

Table 15 - Prospective future gas production in China between 2020-2040 (Li, 2022).

	Gas production per year (10^8 m^3/yr)			
	2020	**2025**	**2030**	**2040**
Conventional gas (incl. tight sandstone gas)	1645	1900-2000	2200-2300	2200-2300
Shale gas	201	300-400	600-800	600-800
Coalbed methane (CBM)	79	100-120	100-200	100-200
Total	1925	2300-2520	2900-3300	2900-3300

The Wufeng-Longmaxi formation has been identified as a high-quality deep shale gas reservoir (He et al., 2022), whereby the sedimentary environment of this formation transitions from an anoxic water environment to an oxygen-rich oxidising environment. The deep shale gas reservoir exhibits overpressure and rich gas characteristics, with high formation pressure, high porosity, and high gas content (Chen et al., 2021b).

Shale gas exploration in the Cenozoic extensional Bohai Bay Basin has focused on the Paleogene Kongdian Formation and the Palogene Shahejie Formation in the Dongying Sag. Areas of particular interest that have favourable conditions for forming large-scale shale gas reservoirs are located in the Bozhong and Banqiao sags (Xue and Wang, 2020). An acceleration in published data that better outlined the importance of the Bohai Bay Basin and its regional geology, commenced in the 1990's, yet there is a lack of published material that utilises noble gases in this region.

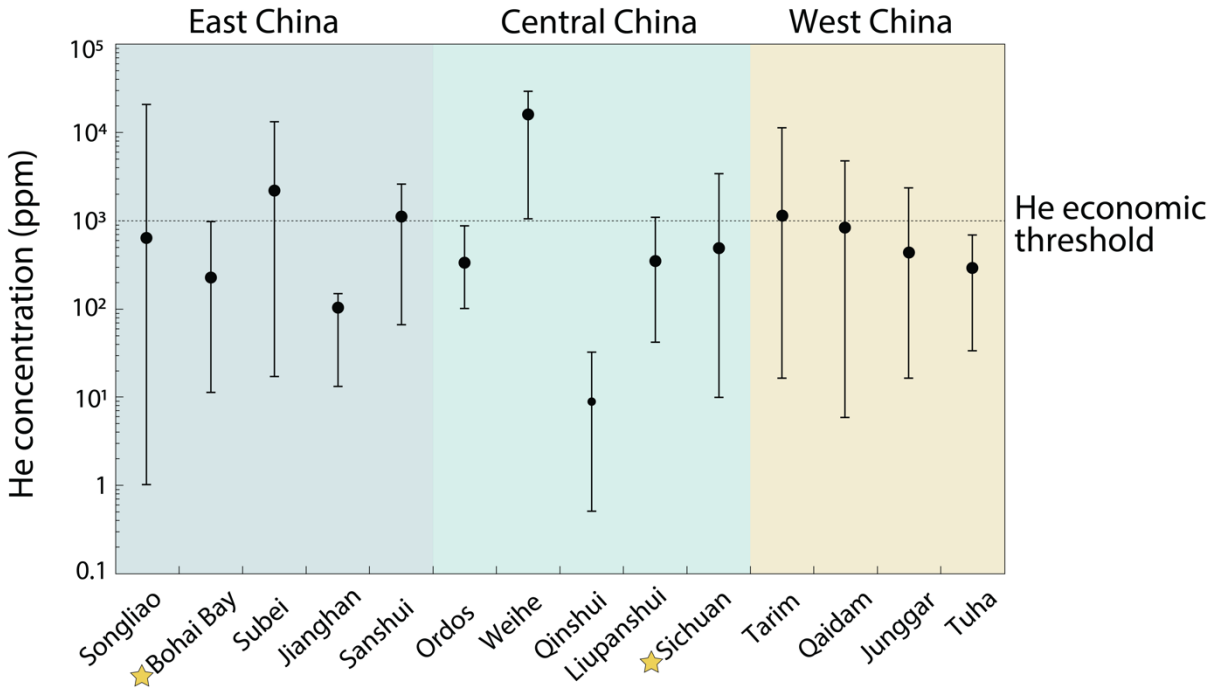

Figure 14 - Variations in helium (He) concentration across different basins in East, Central, and West China. The data points with error bars represent the range of He concentrations measured in parts per million (ppm) for each basin, with the dotted line indicating the economic threshold for viable extraction. This chart illustrates the significant regional differences in He concentrations (Cao et al., 2018, Chen et al., 2019, Chen et al., 2022, Dai et al., 2017, Dai et al., 2008, Jin et al., 2009, Li et al., 2020, Liu et al., 2016, Ni et al., 2014, Yunyan et al., 2009, Wang et al., 2020b, Zhang et al., 2019c, Zhang et al., 2019b).

1.4.2 He resources, research, exploration and usage

Helium has a wide range of applications across aerospace, national defence, high-tech, and civil industries. It is used as rocket fuel, in nuclear magnetic resonance (NMR), semiconductor manufacturing, optical fibre production, deep-sea diving operations, and in the development of fourth-generation nuclear reactors (Tang et al., 2023, Anderson, 2018, Zhang et al., 2022b, Zhou, 2022, Zhou et al., 2022). Since the 1970's, significant research has been carried out on the geochemical characteristics of He in China, (Xu, 1976, Xu and Wang, 1979, Dai et al., 1994, Liu and Xu, 1993) and He-rich gas fields were primarily discovered as a bi-product of petroleum exploration (Figure 14), with total He reserves in China are measured at approximately 4.782 x 10^9 m^3 (Liu et al., 2024). Oil and gas exploration technologies are well-established, but techniques for emerging strategic resources like helium are still in the early stages of development and require further advancement. Understanding the origin and source of helium, as well as identifying the key factors that control helium enrichment, are essential to improving its exploration and extraction (Li et al., 2024, Tao et al., 2024).

1.5 Research methods and approaches:

The research was designed to utilise experimental, quantitative data. Data were collected during two sampling campaigns within the Fuling, Weiyuan, Changning, Zhaotong and Xinchang gas fields in the Sichuan Basin and one sampling campaign within the Dagang gas field within the Huanghua depression in the Bohai Bay Basin.

For the suite of noble gases, experimental analyses were carried out using the Isotopx NGX Noble gas multi-collector mass spectrometer at Lancaster University, which is a relatively newly designed analytical system that permits the extraction, purification, separation and measurement of noble gas isotopes, including their determining their relative abundances and isotopic ratios. Major gas abundances, including the bulk chemistry and significant gas species that make up the remaining gas fraction (CO_2, N_2, H_2) were measured using the MAT271 mass spectrometer at the Key Laboratory of Petroleum Resources Research, Institute of Geology and Geophysics, Chinese Academy of Sciences in Lanzhou, China. Hydrocarbon (CH_4, C_2H_6, C_3H_6, C_4H_{10}) abundances were measured using the Agilent 6890N gas chromatograph (GC) equipped with a fluid-ionisation detector (FID).

Stable carbon ($\delta^{13}C_{C1\text{-}5}$, $\delta^{13}C_{CO2}$) and hydrogen isotopes ($\delta^{13}D$) were analysed at the Key Laboratory of the Research Institute of Exploration and Development of PetroChina using a MAT253 gas isotopic mass spectrometer.

The specific methodological procedures are outlined below and are made in reference to each respective manuscript's methodology, which contain further insight and detail.

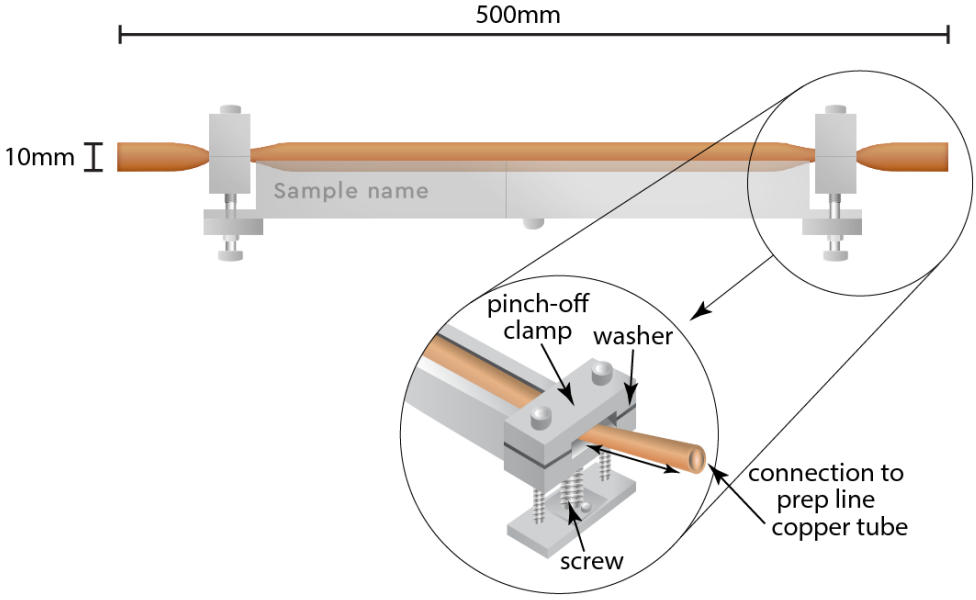

Figure 15 - Illustration of the welded shut copper tubing and steel pinch-off clamps that house the gas samples, which are later affixed to the NGX sample preparation line for detailed isotopic analysis.

1.5.1 Gas sample collection

A total of 36 gas samples were procured using internally polished copper tubes of 10 mm diameter and 50 cm length, which are of standard refrigeration grade. These tubes were connected to a stainless-steel pressure regulator situated on the wellhead via a high-pressure hose. It is crucial to handle each sample with care during the processes of sampling, transportation, and storage, given the high volatility of noble gases and the need to prevent any gas exchange, as emphasised by Beyerle et al. (2000).

To eliminate any residual air contamination, gas was allowed to flow unobstructed through the collection system for a minimum duration of 10 minutes. Subsequently, the downstream end of the copper tubes was cold-welded shut using a steel pinch-off clamp. The upstream end of the tubes was then sealed while still maintaining an over-pressure condition to prevent degassing and this was achieved using steel pinch-off clamps. The internal pressures were regulated to approximately 1 bar above atmospheric pressure. Following these procedures, the sample could be stored without significant interference. Even helium, which is the most mobile among noble gases, has a maximum leak rate to a vacuum of less than 10^{-9} cm^3 STP yr^{-1}. The methodologies employed for collecting gas samples were in accordance with the procedures outlined by Zhou et al. (2005).

1.5.2 Noble gas analytical methods

The procedural extraction and analyses of the noble gases were carried out on the NGX Static multi-collector Noble Gas Mass Spectrometer (Isotopx) at the subsurface fluid isotope geochemistry laboratory at the Lancaster Environment Centre, Lancaster University.

The noble gas mass spectrometer consists of three major components: the 'Nier' type ion source, a mass filter and a series of collectors, including nine Faraday cups in fixed positions (H1-H4, Ax and L1-L4), and one ion counting multiplier (L6), the arrangement of which is denoted in Figure 5. The ion source is configured in a way that the long-term stability and reproducibility of the noble gas analysis are guaranteed.

A blank and an air standard were measured at equal intervals throughout the analysis. The precision of the noble gas analysis is governed by the sample size, including this blank correction. A novel 'ATONA' Faraday amplification system was also employed, which includes a capacitive transimpedance amplifier to boost the precision of smaller ion beams (<1mV), giving an overall dynamic range of below 10^{-16} to above 10^{-9} A (Mixon et al., 2022), and provide better baseline stability (Cox et al., 2020).

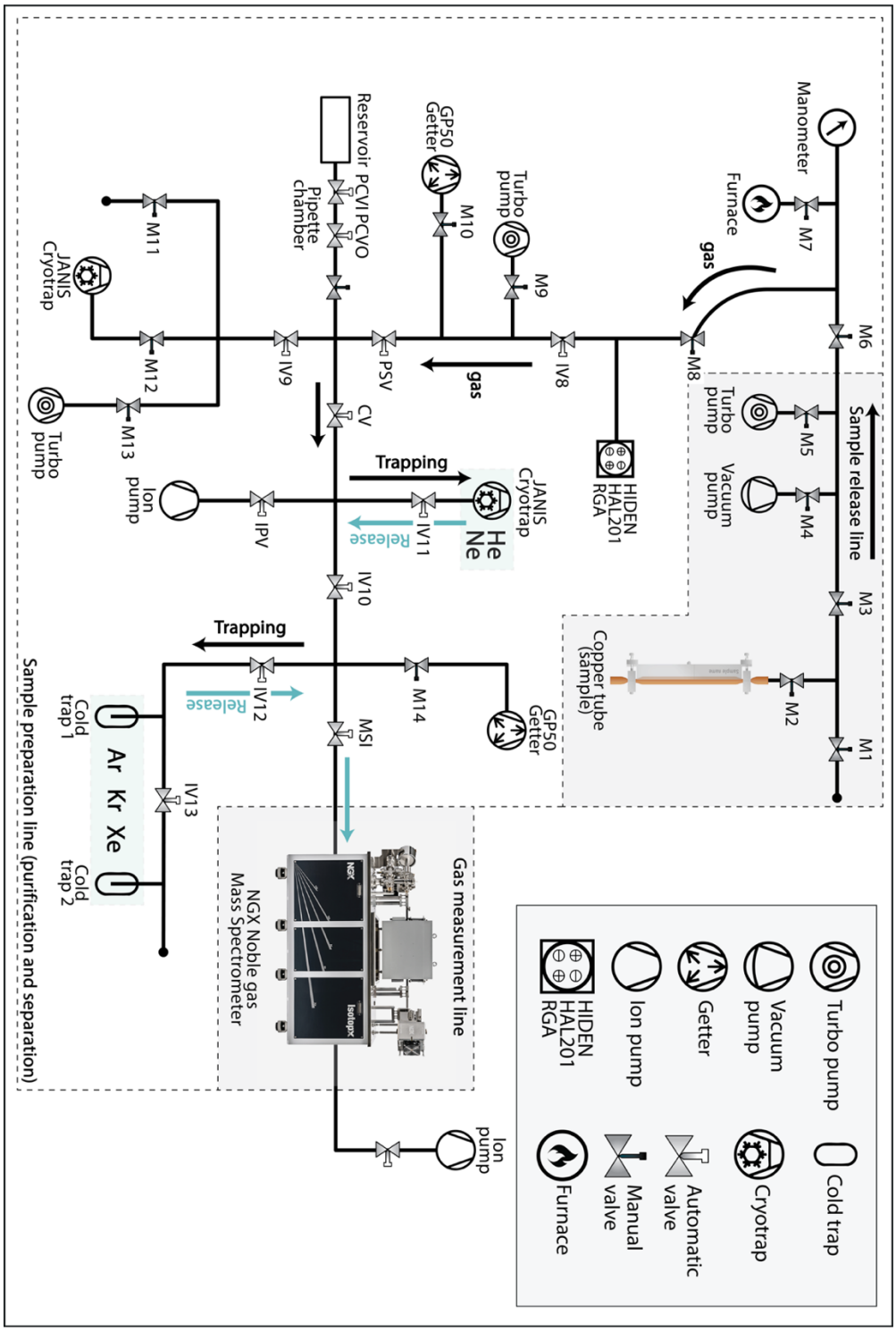

Figure 16 - Schematic diagram of the NGX noble gas mass analytical system. The system comprises similar elements detailed in Zhang et al., 2019a; which can be divided into the main units for sample introduction, purification, separation and analysis. Procedures are described in more detail in section 1.5.2.2. Nomenclature: IV = Inlet valves, PCV = Pipette chamber valves, IPV = Ion pump valves, MSI = Mass spec inlet

1.5.2.1 Sample preparation, release, and extraction

Noble gases have a comparably low abundance compared to most elements of interest in geosciences. Their presence, therefore, requires a high detection efficiency, and a 'static' mass spectrometric analysis, usually in isolation, where all valves to vacuum pumps in the cleaning line need to be closed, under ultra-high vacuum (UHV). In contrast, the stable isotopes of various light elements (H, C, N, O and S) can usually be analysed through insertion into the mass spectrometer with valves open (Wieler, 2014). The UHV is maintained by an assembly of systems, which include turbo molecular pumps and ion pumps. Before commencing gas extraction to the purification line, it is necessary to expel any residual gases in the NGX by using a turbo-molecular pump for up to 6 hours to maintain a prep line vacuum of 2×10^{-7} mbar.

To prepare the crimped copper tube for analysis, a copper cutter is spun around the end of the cylinder, where a clean contact is made, and upon which an O-ring and cross nut are placed. The sample is then clamped and fastened to the NGX. The pinch-off clamp of the copper tube can then be opened, and using a special pair of pliers, the copper tube can be unsealed without breaking due to it being both malleable and ductile.

The preparation bench also includes a 0.2 cc pipette and 4000 cc reservoir tank, which permits the ability to admit air standards or spike aliquots. Before allowing the release of the sample from the copper tube, a quadrupole MS (Hiden Analytical HAL-201) was used for the detection of leaks and to prevent contamination of air in the sampling process. Once the gas was partly expelled from the copper tube and released and expanded into the initial preparation section, it is necessary to measure the pressure (Torr) using the MSK manometer before admittance to the rest of the prep line for purification and separation of the gases. Using a precisely known aliquot of gas, standardisation of the system could be accomplished (Stanley et al., 2009).

1.5.2.2 Noble gas purification and separation

The full gas purification line comprises various components under UHV (Figure 16). Initially, the gas sample was isolated between three manual valves (M6-M7-M8 - the sample inlet area), so that the pressure could be determined using a manometer pressure gauge. Using a titanium sponge, the sampled gas was heated to 800°C for a set period to remove reactive gases such as CH_4 (and other hydrocarbons), CO_2, O_2, CO, N_2, H_2S and H_2. The gas sample was then expanded onto the prep line, which is equipped with a GP-50 SAES hot getter (St101 alloy) with constant operating temperature. Residual unwanted

gases are removed using an 80 s^{-1} turbo molecular pump. Separation of the noble gases into measurable concentrations occurs through the use of a cryogenic trap, ion pump, a second GP-50 cold getter and liquid N_2 charcoal trap. Purification of the noble gases mixture is important as chemically reactive volatile species must be removed that would otherwise compromise the analysis. There is typically a significant difference, often several orders of magnitude, between the concentration of noble gases in air standards versus actual gas samples. After the chemically reactive volatile species have been removed, the mixture of pure noble gases, comprising He, Ne, Ar, Kr, and Xe must be separated prior to analysis. This can be accomplished using a series of cryogenic traps. Initially, heavier noble gases such as Ar, Kr, and Xe are captured onto a cold finger coated in activated charcoal, then immersed in liquid nitrogen for 15 minutes. Remaining gases, namely He and Ne, are collected onto a pre-cooled JANIS cryogenic trap that has been brought down to a temperature of 10 K, and this too is held for 15 minutes.

Table 16 – Magnitude and efficiency of noble gas trapping and release at a range of temperatures

He		Ne		Ar		Kr		Xe	
T [K]	%	T [K]	%	T [K]	%	T [K]	%	T [K]	%
11	0.0	27	0.0	95	0	130	0	140	0
12	0.0	32	0.0	99	0.1	140	0.3	150	0
13	0.0	35	0.2	105	0.1	150	1.6	160	0
15	0.1	38	1.6	115	0.3	160	5.7	170	0.1
17	0.9	41	7.4	125	10.7	170	15	180	0.3
19	6.7	42	11.1	135	37.4	180	33.6	190	0.9
21	27.8	44	23.2	145	74.5	190	64.9	200	2.5
23	60.9	45	31.1	155	93.3	200	87.5	210	6
25	84.2	46	40.0	165	99.6	210	100	220	12.2
27	94.1	47	49.7	175	100	220	100	230	26.6
29	97.9	48	59.0	179	100			240	45.3
31	99.3	49	67.4					250	69.1
33	99.8	50	74.0					260	84.1
35	100.0	51	79.8					270	90.7
37	100.0	52	84.3					280	96.9
		53	88.4					290	99.4
		54	91.1					300	100
		55	93.2						
		56	94.6						
		57	95.6						
		58	96.4						
		60	97.8						
		63	98.7						
		70	99.9						
		75	100.0						

Upon trapping of all the gases onto the cold traps, the cryogenic trap's temperature is elevated to 50 K for another 15-minute duration to release He into the line. Following a series of dilution and expansion processes, the now "pure" He is admitted into the NGX noble gas mass spectrometer to assess He abundance and isotopic composition.
Following this, the temperature of the cryogenic trap is increased to 95 K for a 15-minute interval to free Ne into the line. Adopting the same procedure as with He, Ne isotopes can subsequently be evaluated using the NGX mass spectrometer.
Upon the completion of Ne isotope measurement, the charcoal trap's temperature is raised to 210 K for another further 15 minutes. This initiates the release of the 'absorbed' Ar and Kr, which then expands into the preparation line. Following several rounds of expansion and dilution akin to the processes for He and Ne, a modest aliquot of Ar and Kr is isolated and introduced simultaneously into the NGX mass spectrometer to appraise both the abundance and isotopic characteristics of Ar and Kr. During this period of Ar-Kr measurement, it's crucial to deactivate the heater on the cold finger and then cool it down to the temperature of liquid nitrogen (T=77 K).
To effectively offset the impact of abundant Ar on Xe's release from the activated charcoal, three separation cycles are implemented as follows: Initially, the charcoal trap's temperature is elevated to 210 K for 15 minutes, causing the desorption of remaining Ar and Kr from the charcoal into the preparation line. Subsequently, these liberated gases are evacuated for an additional 15-minute period. At the same time, the temperature of the charcoal is warmed to 450 K to induce Xe release.

Table 17 – Important separation temperatures for noble gases during gas sample preparation and analysis

Noble gas	Separation temp (K)	Notes
He	50	Separation of He from He & Ne mixture
Ne	95	Total release of Ne from the cryotrap
Ar	210	Release of Ar & Kr, while Xe remains trapped on the
Kr	210	charcoal
Xe	195	Xe re-trapped on the charcoal, Ar & Kr remain in the line

Once the pumping concludes, the freed Xe in the cold finger is expanded into the line for a further 5 minutes. Afterwards, the gases in the line are reabsorbed onto the charcoal trap at 210 K. The second and third cycles replicate this procedure to ensure comprehensive separation of Xe from Ar and Kr, a vital step before Xe isotope measurement. Taking into account their associated partial pressures, the optimal release temperatures for the suite of noble gases are detailed in Table 17.

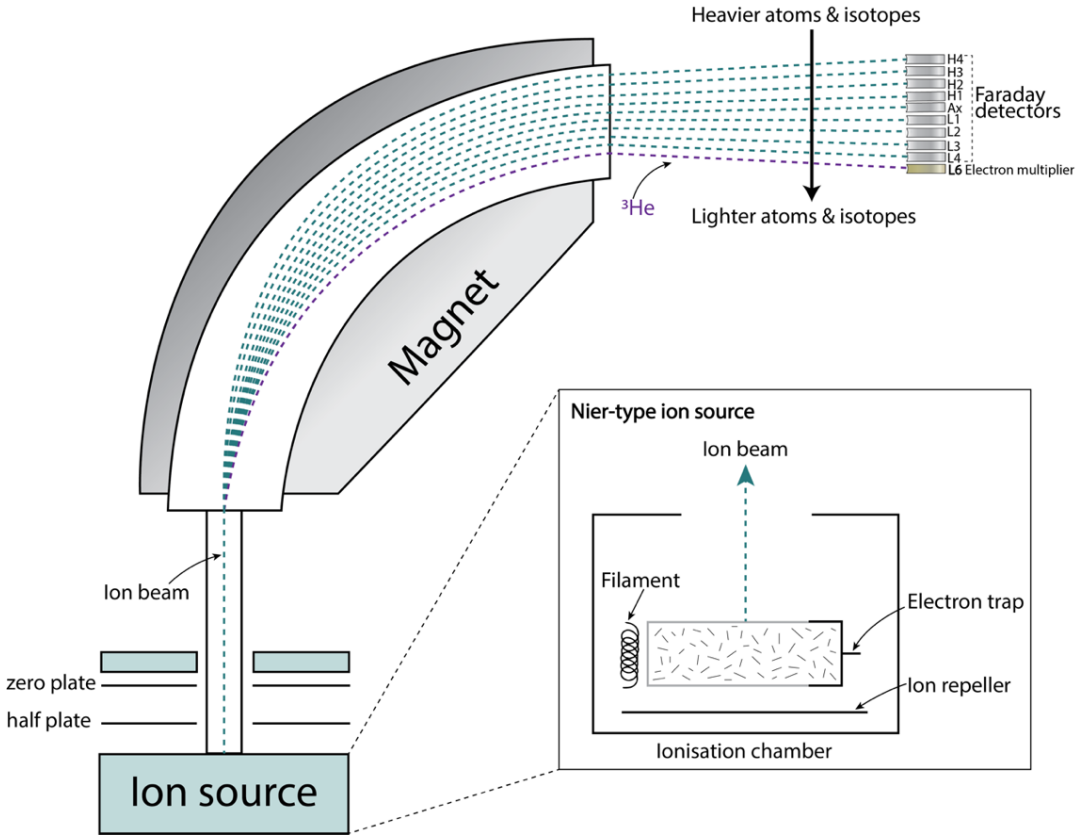

Figure 17 – Schematic diagram of the NGX mass spectrometer, including the magnet and collector configuration and cross-section of the Nier-type ion source. 9 Faraday collectors allow for the simultaneous measurement of all 9 isotopes of Xe. Implementing ATONA detector amplifiers also provides lower noise, a wider dynamic range and better stability.

1.5.2.3 Noble gas abundances and isotope measurement

The noble gas mass spectrometer is operated in 'static mode', which is a term that denotes a type of analysis whereby all the available gas is admitted to the spectrometer with the pumps isolated. The drawback of this technique is that the signal will decrease over time as gas is progressively consumed by ionisation. It does, however, allow for a more sensitive reading. The electron bombardment source makes use of a conceptually simple scheme, where a filament (a Nier-type ion source for the NGX) creates a well-defined electron beam which then excites atoms to metastable states (Gay, 1996) (Figure 17). Therefore, the gas molecules are ionised in an ionisation chamber by the bombardment of electrons. Important parameters include the electron beam energy and current. Ions are extracted from the source to the flight tube by a series of decreasing voltage focus-and-acceleration plates (Marrocchi et al., 2009). The voltage of electron acceleration is typically around 100 V; however, this is sometimes reduced to around 40 eV when mitigating the interference from double-charged species such as $^{40}Ar^{++}$ during the analysis of Ne (Wieler, 2014); still, these gases (^{40}Ar) were also measured to correct for the neon isotopes of ^{20}Ne and ^{22}Ne (Niedermann et al., 1993).

The large magnet provides sufficient mass dispersion for the static collection of Xe, Kr, Ne, and Ar. The NGX also has the unique capability of simultaneously measuring up to 9 isotopes of Xe on its Faraday collectors. This is because of its modified magnet exit poles, which can rotate the instrument's focal plane so that the collector focal plane is perpendicular to the ion trajectory.

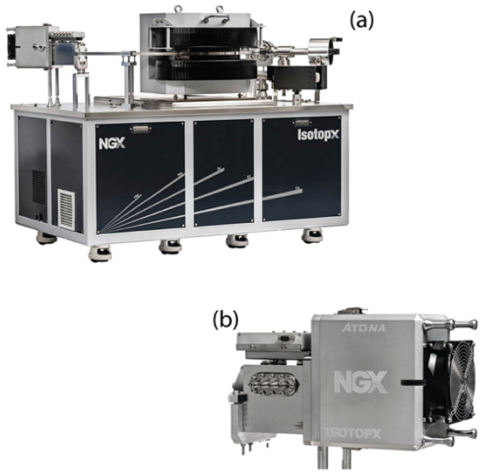

Figure 18 – (a) The NGX static multi-collector noble gas mass spectrometer and (b) the ATONA Faraday amplifier, which eliminates the need for a feedback resistor and significantly reduces amplifier noise

1.5.2.4 Blanks, air standards and Reproducibility

Blanks and air standards were measured at various intervals to continually assess the mass spectrometers' precision and maintain the reproducibility of results. Measurement uncertainty is introduced where an ion beam is considered small, i.e. for ^{36}Ar, when the ion beam is smaller than 1.0×10^{-15} moles (Mark et al., 2009). Equipment efficiency and the diminution of the cleaning procedure may affect each sample analysis, and therefore, a procedural blank was conducted following one to two sample runs. Besides validating system sensitivity and ensuring instrumental stability, they detect potential systemic anomalies, such as leaks or residual background gases that might have been retained from antecedent measurements within the sample preparation line or the mass spectrometer. To carry out a blank test, the mass spectrometer and preparation line were left isolated (typically overnight) to ensure the removal of any atmospheric air or previous sample remnants and to allow it to reach a stable condition. The NGX was then run under the same conditions and sample procedures without introducing any gas into the sample preparation line, and the signal measured under these conditions represented the blank. The results of the blank run indicate any residual gases or contamination in the system. A known aliquot of clean, dry, atmospheric air is used as the 'standard' for the air standard test. The purification and separation procedures are also carried out in the exact manner

employed during sample analysis. The quantification of noble gas elemental abundances and the respective isotopic ratios for each individual sample is calculated through comparison with established air standards and a blank correction factor. The magnitude of blank interference is negligible, typically at least three orders of magnitude less than measurements derived from air standards. Further mass spectrometer interferences can occur when ions of similar mass-to-charge ratios coalesce in a sample, which may lead to inaccurate measurements of the target ions. Common isobaric interferences occur with various species found in the region of the noble gases, and this is summarised in Table 18, i.e., ^{3}He interferences include $^{1}H^{2}D^{+}$ (mass/charge: 3.0215), tritium $^{3}H^{+}$ (mass/charge: 3.0161) and $^{1}H^{1}H^{1}H^{+}$ (mass/charge: 3.0238). ^{40}Ar++ (mass/charge: 19.981) and $^{1}H_{2}{}^{18}O^{+}$ (mass/charge: 20.015), too, are present during ^{20}Ne analysis, as is CO_2^{++} (mass/charge: 21.995) for ^{22}Ne measurement, and these need sufficient resolving power mass filters so that we may adequately distinguish the appropriate signal (Burnard et al., 2013). As the resolution (mass/peak width) of the NGX multiplier (600) exceeds the required resolution for resolving HD^{+} interference on $^{3}He^{+}$ (509), it is relatively straightforward to determine the appropriate peak accurately.

Table 18 - Common noble gas interferences as compiled by Burnard et al. (2013).

Noble gas	Interfering species	Mass/Charge (m/z)
^{3}He	$^{1}H^{2}D^{+}$	3.0215
^{3}He	$^{3}H^{+}$	3.0161
^{3}He	$^{1}H^{1}H^{1}H^{+}$	3.0238
^{4}He	$^{12}C^{+++}$	4.0000
^{20}Ne	$^{1}H_{2}{}^{18}O^{+}$	20.015
^{20}Ne	$^{1}H^{19}F^{+}$	20.006
^{20}Ne	$^{40}Ar^{++}$	19.981
^{21}Ne	$^{20}NeH^{+}$	21.0000
^{21}Ne	$^{12}C_{3}{}^{1}H_{6}{}^{++}$	21.023
^{21}Ne	$^{63}Cu^{+++}$	20.976
^{22}Ne	CO_2^{++}	21.995
^{22}Ne	$^{66}Zn^{+++}$	21.975
^{36}Ar	$^{12}C_{3}{}^{+}$	36.000
^{36}Ar	$^{1}H^{35}Cl^{+}$	35.977
^{40}Ar	$^{12}C_{3}{}^{1}H_{4}{}^{+}$	40.031
$^{78\text{-}86}Kr$	$^{12}C_{6}{}^{1}H_{6\text{-}12}{}^{+}$	78-86
$^{124\text{-}136}Xe$	$^{12}C_{10}{}^{1}H_{4\text{-}16}{}^{+}$	124-136

These common interferences and the overlap of each species within the spectra of noble gas isotopes is represented in Figure 19:

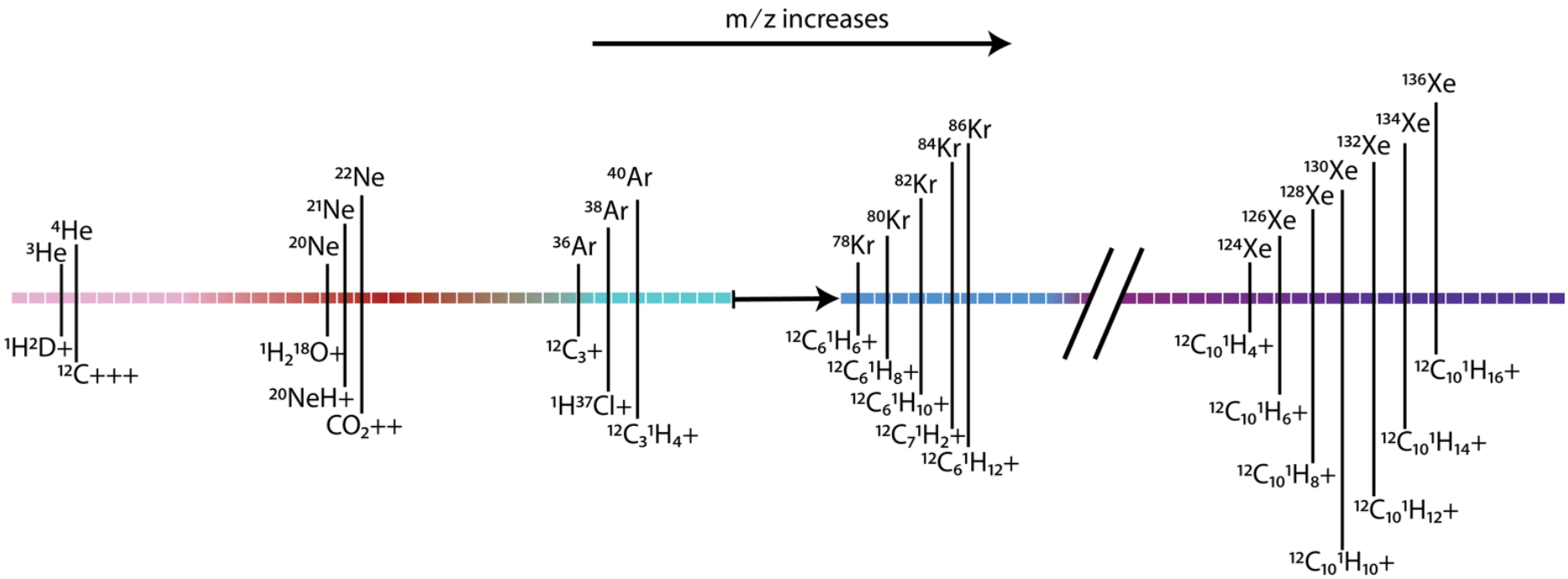

Figure 19 – Spectra for the noble gases and their common interferences during measurement, modified from Pinti and Marty (1998).

1.5.3 Bulk gas analysis: Major gas components and stable C/H isotopes

The quantification of major gaseous constituents such as CH_4, CO_2, N_2, and H_2, as well as the respective stable carbon and hydrogen isotopes, was carried out using established analytical methods on natural gas and formation water samples.

1.5.3.1 Sampling and analytical methods

For the 18 Bohai Bay Basin gas samples, natural gas samples were collected using a high-pressure steel cylinder at the wellhead. Just as described with the copper cylinders, no leakage or contamination was ensured by first pumping the cylinder to vacuum at the laboratory, then secondly flushing the pre-existing air contained within the cylinder for a set amount of time at the production well. Analysis of each sample's geochemical composition, including their C and H isotope signatures, and absolute hydrocarbon content was carried out using a combination of gas chromatography and mass spectrometry, and these procedures are described below.

1.5.3.2 Measurement of bulk gas abundance

For the primary gas component abundances (CH_4, CO_2, O_2, H_2, H_2S, N_2, He and Ar) and analyses were conducted at the Key Laboratory of Petroleum Resources Research, Institute of Geology and Geophysics, Chinese Academy of Sciences, situated in Lanzhou, China, utilising a MAT 271 mass spectrometer.

Subsequently, the abundances of hydrocarbons (CH_4, C_2H_6, and C_3H_8) were ascertained through an Agilent 6890N gas chromatograph (GC) furnished with a flame-ionisation detector (FID). He and N_2 were used as carrier gases and the GC setup included double thermal conductivity detectors (TCD). The chromatographic separation of individual hydrocarbon components from C_1 to C_3 was accomplished using a quartz capillary column (30m x 0.25mm x 0.25μm) of PLOT Al_2O_3 dimensions (50 m x 0.53 mm). The temperature parameters of the GC oven commenced at 30°C, maintained for an initial period of 10 minutes, and subsequently increased to 180°C at an increment rate of 10°C/min, sustaining this elevated temperature for a duration of 20 to 30 minutes, aligning with the methodologies specified in (Cao et al., 2016, 2018, 2020a).

1.5.3.3 Determining carbon ($\delta^{13}C$) and hydrogen (δH) isotopic compositions

The isotopic ratios of carbon and hydrogen were measured at the Key Laboratory of the Research Institute of Exploration and Development of PetroChina, in Beijing, China. Utilising a MAT 253 gas isotopic mass spectrometer, the stable isotopic compositions of

carbon, i.e., $\delta^{13}C$ of carbon-containing compounds such as carbon dioxide ($\delta^{13}C_{CO2}$), methane ($\delta^{13}C_{CH4}$) were ascertained, by firstly separating natural gas samples into methane, ethane, propane, butane and CO_2 through a chromatography column of an SRI 8610C gas chromatograph. These separated components were channelled into a combustion furnace by the He carrier gas, then oxidised into CO_2 by CuO at a temperature of 850°C. The resultant species, after conversion, were transported by the He carrier gas to the mass spectrometer for isotopic composition measurement. Dual inlet analysis was conducted, referencing the international NBS-19 CO_2 measurement standard. The analytical protocols were consistent with those outlined in Qin et al. (2018). Isotopic ratios of carbon ($\delta^{13}C_{CO2}$ and $\delta^{13}C_{C1\text{-}C5}$) are expressed in the delta (δ) notation in per mil (‰) and calibrated against the Vienna Pee Dee Belemnite (VPDB) standard ($\delta^{13}C_{VPDB}$ = 1.95 ± 0.04‰) (IAEA, 1995), where the ratio of C isotopes, $^{13}C/^{12}C$ = 0.011238. The δ notation is used as the differences between the D/H and $^{13}C/^{12}C$ values in natural substances are exceedingly small. Therefore, measurements of isotopic composition can be made in reference to a standard material, which can be conveniently expressed with "δ", which is determined using:

$$\delta^{13}C_{sample-standard} = 1000\left(\frac{\left(\frac{^{13}C}{^{12}C}\right)_{sample} - \left(\frac{^{13}C}{^{12}C}\right)_{standard}}{\left(\frac{^{13}C}{^{12}C}\right)_{standard}}\right) \quad (61)$$

and:

$$\delta D_{sample-standard} = 1000\left(\frac{\left(\frac{D}{H}\right)_{sample} - \left(\frac{D}{H}\right)_{standard}}{\left(\frac{D}{H}\right)_{standard}}\right) \quad (62)$$

Multiple analytical runs ensured precision of greater than 0.5‰ for carbon isotopes and approximately 3‰ for hydrogen isotopes. Repeat experiments and maintenance of inter-laboratory standards were also employed for validation. Reproducibility and accuracy are estimated to be ± 0.2‰ with respect to the VPDB standard. For δD, VSMOW (Vienna Standard Mean Ocean Water) notation is used (where the absolute deuterium content of VSMOW is approximately 155.76 ppm, which is the ratio between D/H = 0.00015576) as the reference material for isotope analysis, and values are also reported in per mil (‰) relative to this standard. The analytical precision and error for δD values is ± 2‰.

Chapter 2 The characterisation of noble gases in organic-rich Wufeng-Longmaxi shales, Sichuan Basin and the role of adsorption and solubility-controlled fractionation

(Manuscript 1)

Jamie Robert Beagle[a, b, c, *], Chunhui Cao[d], Shengfei Qin[e], Yunpeng Wang[c], Quanyou Liu[a, g], Greg Holland[f], Ben Surridge[b], Zheng Zhou[b, †]

[a]State Key Laboratory of Shale Oil and Gas Enrichment Mechanisms and Effective Development, Beijing 100083, China

[b]Lancaster Environment Centre, Lancaster University, Lancaster, LA1 4YQ, UK

[c]State Key Laboratory of Organic Geochemistry, Guangzhou Institute of Geochemistry, Chinese Academy of Sciences, Guangzhou, 510640, China

[d]Northwest Institute of Eco-Environment and Resources, Chinese Academy of Sciences, Lanzhou, 730000, China

[e]Research Institute of Petroleum Exploration & Development, PetroChina, Beijing, 100083 China

[f]Department of Earth and Environmental Sciences, The University of Manchester, M13 9PL, UK

[g]Institute of Energy, Peking University, Beijing, 100871, China

* Corresponding author. Email address: j.beagle@lancaster.ac.uk (Jamie Beagle)

† Corresponding author. Email address: z.zhou4@lancaster.ac.uk (Zheng Zhou)

2.1 Abstract

The Sichuan Basin, in the SW of China, is acknowledged to be the cradle and future of China's natural gas industry, having become one of the leading areas for unconventional shale gas exploration in recent years. The high-quality, organic-rich Upper Ordovician Wufeng and Lower Silurian Longmaxi marine shales (<98% methane) exhibit ideal characteristics such as stable vertical and lateral distribution. Understanding the storage mechanisms of shale through the adsorption of noble gases is crucial for evaluating gas retention and migration processes within unconventional reservoirs. Adsorption not only influences the distribution and concentration of noble gases but also serves as an indicator of the interaction between organic-rich shale and gas phases. This knowledge can help to predict the efficiency of gas recovery and the long-term stability of reservoirs, ultimately guiding the development of more effective extraction strategies and improving estimates of gas reserves. Noble gases are valuable geo-dynamic fluid flow tracers that can provide a set of conservative tools capable of defining the physical conditions that affect crustal fluid systems. In this study, we present noble gas isotopic data with the purpose of understanding the origin and accumulation mechanisms associated with 4 major gas fields within the Sichuan Basin, comprising the Upper Ordovician-Lower Silurian, Wufeng-Longmaxi shales in the Weiyuan, Fuling, Changning and Zhaotong gas fields. 24 gas samples were collected from producing wells within the central, eastern, and southern margins of the Sichuan Basin. $^{3}He/^{4}He$ ratios range between $0.0037R_a$ to $0.038R_a$ (R_a= atmospheric $^{3}He/^{4}He$), indicating a predominantly crustal radiogenic signature. We have resolved the non-atmospheric, crustal-derived excess ($^{40}Ar^{*}$) and $^{40}Ar^{*}/^{36}Ar$ ratios are far higher (≤5817) than air ($^{40}Ar/^{36}Ar_{air}$=298.56) which emphasises the long-term decay of ^{40}K in surrounding minerals. Water-derived $^{20}Ne/^{36}Ar$ ratios and radiogenic $^{4}He/^{40}Ar^{*}$ ratios reveal the distinctive accumulation and migratory mechanisms of shale gases and the role of groundwater. We assert that gas ratios have evolved in a closed system, where solubility-controlled phase interactions, accompanied by adsorption processes along the clay-rich matrix of the Wufeng-Longmaxi shale govern the geochemical characteristics within the pore volume, and explain the fractionation of air-derived ^{84}Kr and ^{132}Xe concentrations in these unconventional gas fields.

*Keywords: Noble gases, Unconventional reservoirs, Shale gas, Tight sandstone gas, Sichuan Basin, Adsorption, Exsolution

2.2 Introduction

Recent macroeconomic growth in China has given rise to increased utilisation of hydrocarbons, with total energy consumption rising from 5.7 x 10^8 tons of standard coal in 1978 to 4.49 x 10^9 tons of standard coal in 2017, albeit demand steadied at between 3.92 x 10^9 and 4.14 x 10^9 in 2020 (Mengshu et al., 2021). To meet the 2030 sustainable development goals set out by the United Nations General Assembly as part of Resolution 70/1 in 2015 and the CO_2 emissions targets addressed in the 'Energy Revolution Strategy' in 2016 (IEA, 2016), China is successfully decoupling its economic growth with the use of coal and improving the productivity of existing oil and gas systems by developing more efficient technologies such as high-volume hydraulic fracturing. China's total energy consumption (CTEC) is forecast to peak in 2035 (Zeng et al., 2018), with carbon neutrality being reached before 2060 by improving and diversifying the energy mix. In an effort to meet the rising demand, unconventional hydrocarbon resources, principally sourced from shale gas reservoirs, have been promoted as cleaner substitute fuel sources over coal and oil. Shale gases are forecast by 2040 to supersede oil as the world's leading energy source (Zhang and Lu, 2015), making up ~45% of the total global natural gas market (IEA, 2019).

In 2014, shale gas production in China totalled 13 x 10^8 m^3 (Dai et al., 2016); by the end of 2020, it had totalled 20 x 10^8 m^3 (Nie et al., 2021). Natural gas stored within in-situ shale reservoirs is seen as a less carbon-intensive alternative to coal. Sourced from organic-rich black shale deposited on continental shelves during the Late Ordovician and Early Silurian, these self-contained unconventional natural gas-bearing units are proven to have promising source-rock potential worldwide (Klemme and Ulmishek, 1991).

The Sichuan Basin is China's largest gas-producing region (Chen et al., 2017) and is the cradle and the future of China's natural gas industry (Ma, 2017b). It is a tectonically stable basin located in the SW of China, with known economic resources, particularly in its southern domain, where the Longmaxi marine shale has favourable characteristics (Dai et al., 2014) and an evaluated exploration and development area of 4.5 x10^4 km^2 (Zou et al., 2016). There are proven cumulative reserves of 3.69 x 10^{12} m^3, and by 2030, natural gas productivity is expected to exceed 5 x 10^{10} m^3 to 7 x 10^{10} m^3 (Ma, 2017a). Shale gas reservoirs with similar characteristics (3500-4500m deep water shelf environment, with high pressure and suitable preservation characteristics) are already proven in the Jiaoshiba field, in the Fuling area of the Sichuan Basin, where 5 x 10^{11} m^3 of reserves have been previously discovered (Guo, et al., 2016).

Noble gases provide researchers with a set of conservative, nonreactive geochemical tracers capable of defining the physical conditions that affect geological systems, including the determination of fluid origin, fluid interaction, permeability, temperature and fluid flow (Hunt et al., 2012), quantitative geological modelling of the migratory, trapping and extraction processes of hydrocarbon reserves (Prinzhofer, 2013) as well as the mass balance and surface-subsurface phase interactions that take place (Zhou et al., 2005). Isotopic fractionation of noble gases is common due to the way noble gases interact with other materials through processes such as diffusion, solution and adsorption. The solubility of the lighter noble gases (He and Ne) is relatively unaffected by temperature, while the solubility of the heavier noble gases (Kr and Xe) is largely governed by salinity and temperature conditions (Wood and Caputi, 1966, Mazor and Fournier, 1973, Benson and Krause, 1976, Potter and Clynne, 1978, Hamme and Emerson, 2004). Xe abundances are widely studied in Earth and planetary sciences and a commonly reported deficiency of Xe in the terrestrial noble gas inventory shows that Xe resides mostly in a reservoir other than air. This is thought to be attributed to the ubiquitous adsorption of a non-trivial quantity of atmospheric Xe on a sufficiently good adsorbent, such as shale (Bernatowicz and Podosek, 1986, Podosek et al., 1981). The complex set of conditions that control Kr and Xe adsorption on shales, as well as the timing and extent to which adsorption and desorption vary, is still a relatively unknown phenomenon. Understanding the role of He, Ne, Ar, Kr, Xe and their associated provenance is critical in constraining the nexus of geochemical information found within the shale gases of the Sichuan Basin. This study determines the requisite geological and geochemical characteristics, including the compositional variability of noble gas ratios, bulk chemistry and fluid migration processes, and attempts to understand the role of adsorption and desorption in association with solubility-controlled dissolution and exsolution in the evolution of noble gas isotope ratios in shale gases from heterogeneous gas fields distributed across a large extent of the Sichuan Basin (~300km^2).

Figure 20 - Map of the Sichuan Basin, highlighting sample locations and basin extent, as well as major tectono-structural features and major gas fields within the basin, including the (1) Fuling gas field within the Jiaoshiba anticline (Figure 21) in the East Sichuan Depression, (2) Weiyuan gas field in the Central Sichuan Uplift, (3) Changning and Zhaotong gas fields located in the South Sichuan Depression. The stratigraphic column (inset, top right) shows the main lithological units of the Sichuan Basin and the location of source rock (S) and reservoir (R) intervals for the relevant formations in this study. The gas fields sampled are denoted by a star symbol next to their associated target reservoir in the stratigraphic column (modified after Ni et al. (2014) and Wang et al. (2020b).

2.3 Regional geology and tectonic evolution

The Sichuan Basin, in eastern Sichuan Province, China, is situated within the north-western domain of the Yangtze Plate. It covers a total area of approximately 1.8 x 10^5 km^2, making it one of the four largest basins in China (Li et al., 2016b) and one of the most tectonically stable sedimentary basins in China, making it particularly favourable for developing and preserving large gas fields. It is geographically bounded in the north by the Micang (N) and Daba (NE) mountains, in the south by the Daliang (SW) and Dalou (SE) Mountains, in the west by the Longmen Mountains and flanked on its eastern side by the Qiyao Dalou Mountains (Figure 20). Tectonic features generally align along two planes, trending NE-SW and NW-SE, amongst a diamond-shaped basin (Huang et al., 2018). The basin can be partitioned into East (east of the Huayingshan fault), South (South and Southwest), West (West of the Longquanshan fault), and Central Sichuan (between the Longquanshan fault and the Huayingshan fault) gas-oil accumulation zones (Ni et al., 2014) with an average basinal geothermal gradient of 22.8°C/km (Dai et al., 2018). Gas fields have formed across all 4 of these partitioned domains, notably in the Weiyuan, Fuling, Changning and Zhaotong plays. Due to the relatively close distances between the Changning and Zhaotong shale gas research and exploration areas, these are referred to as 'CZ' (Dai et al., 2016). The CZ blocks are located within the eastern extent of the Dianqianbei Depression, along the southern periphery of the Sichuan Basin in the Yangtze tectonic region.

The South China plate comprises the Yangtze and Cathaysia blocks. Several distinct tectonic movements have contributed to the development of the Sichuan basin; these include the Caledonian (late Sinian-Silurian), Hercynian (Devonian-Permian), Indosinian (Triassic), Yanshanian (Jurassic-Late Cretaceous) and Himalayan (Paleo-Quaternary) (Zhang et al., 2013), the latter of these two events having the strongest influence on the overall structural morphology of the Sichuan Basin (Fan et al., 2020). During the transition between the Late Ordovician and Early Silurian, the South China plate was located in the tropics, with climate altering from cold and arid to warm and humid (Xiao et al., 2021); high-productivity marine organisms dominated whilst the region was still part of the north-western margins of Gondwana (Zhou et al., 2015). Subsequently, vast oceanographic changes took place with a distinct alteration in palaeogeography, evidenced by three major intervals: the Mid-late Ashgill, Hirnantian, and early Rhuddanian, with an overall shift from passive margin to foreland marine tectonic environment. The Caledonian orogeny resulted in the widespread uplift of basinal highs

such as the western Chuanzhong uplift and favourable deep-sea, dysoxic-anoxic conditions that can be attributed to a rapid early Silurian transgression, a landward movement of the paleogeographic shoreline due to global-warming driven melting of Gondwana glaciation (Xu et al., 2004). This resulted in a change in the distribution of litho- and bio-facies whereby organic-rich black shales occupied a large extent of the Yangtze platform deposited atop a relatively stable Yangtze interior craton under strong anoxic to euxinic conditions (Li et al., 2017a). Uplift during the Late Silurian eroded a large extent of Upper Silurian units, preserving mostly only Lower Silurian strata, principally the Lower Silurian Longmaxi Marine shales (445.6-550.8 Ma, Figure 20), which are mainly composed of high amounts of methane (~98.8%) (Feng et al., 2019), with the highest recorded CH_4 content (99.59%) for shale gases in the world (Dai et al., 2016) sourced from a 100-600m thick formation with favourable types of organic matter. The bottom 20-70m of the formation is considered the sweet spot, with TOC >2% (Jin et al., 2018). The Longmaxi shale is a relatively porous and permeable unit, with porosity ranging from 1.2-10.8% and permeability ranging from 0.25 μD to 1.737 mD (Dai et al., 2016). Shale enrichment has also occurred within the former deep-water shelf, and the craton depression in the upper Yangtze plate is where most of the thickest shale was deposited. The relative stability and resistance to structural deformation is due to gases having accumulated far from regional faults (Nie et al., 2021).

Marine shales, such as the Wufeng-Longmaxi shale, are predominantly thought to have a greater shale gas potential (Pu et al., 2010, Zou et al., 2010, Stevens et al., 2013), while lacustrine and transitional shales have been considered less prospective due to their more clay-rich nature (De Silva et al., 2015; Jiang et al., 2016). The thickness of Wufeng-Longmaxi shale increases southwards throughout the Sichuan Basin (Chen et al., 2021b). The Precambrian to Lower Silurian marine shales demonstrate lower permeability, with more micro to nano-scale pores when compared to the younger transitional-lacustrine shales. These are the best gas prospects, especially in the Longmaxi shales of the Lower Silurian, where shale gas has been produced due to stable vertical and lateral distribution, good reservoir quality and high gas content.

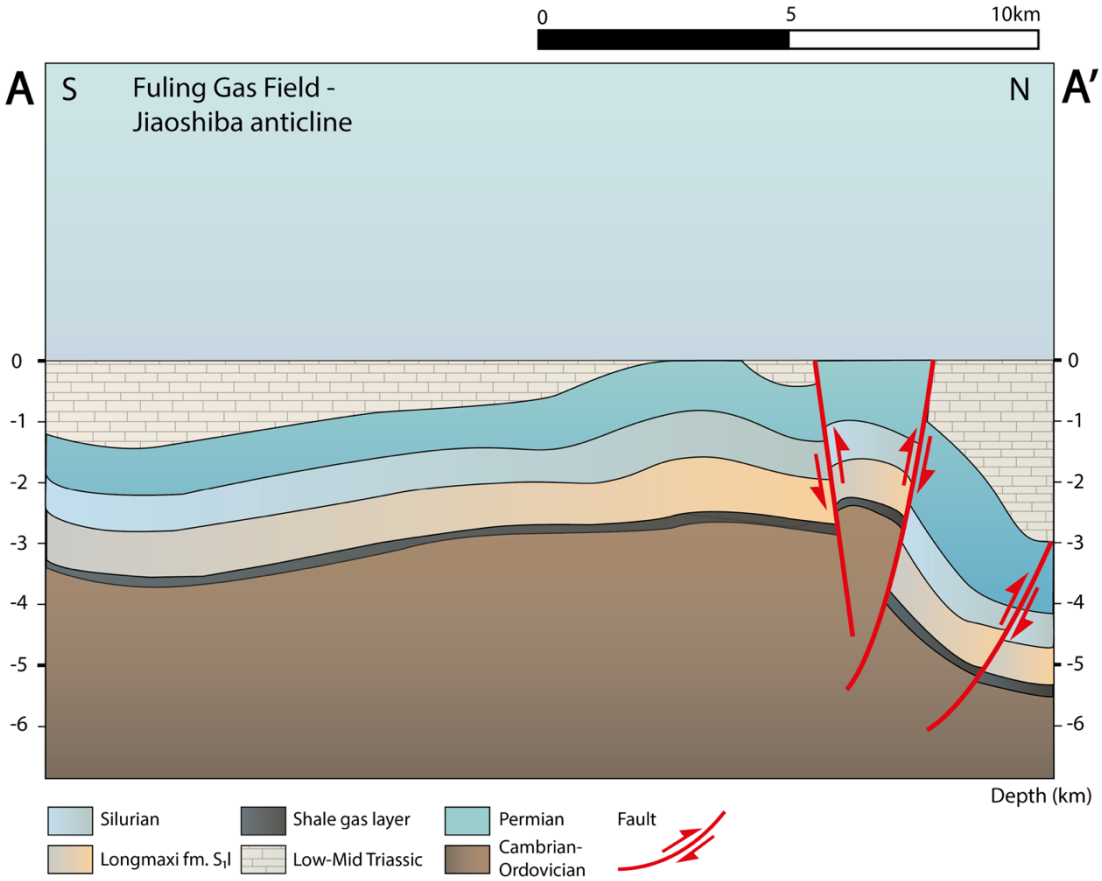

Figure 21 – An illustration of the subsurface geological structure of the Jiaoshiba anticline, focusing on the stratigraphic and structural framework relevant to the unconventional Fuling shale gas field. This diagram highlights key lithological units, including Silurian units, the Longmaxi Formation, Permian, Low-Mid Triassic, and Cambrian-Ordovician. Modified from Nie et al. (2020).

2.4 Sampling and Analytical Methods

2.4.1 Sampling procedures

Gas samples (n = 24) were collected in standard refrigeration grade, internally polished, 10 mm diameter copper tubes (50cm long), affixed to a stainless-steel pressure regulator on the well-head via a high-pressure hose. Residual air contamination was removed by allowing gas to flow freely through the collection system for at least 10 minutes. The copper tubes were then cold-welded shut at their downstream end by a steel pinch-off clamp, then sealed at their upstream end while still over-pressured to avoid degassing by steel pinch-off clamps, with internal pressures regulated to around 1 bar above atmospheric pressure. The sample can then be stored without significant interference. Despite being the most mobile noble gas, Helium only has a maximum leak rate to a vacuum of less than 10^{-9} cm^3 STP yr^{-1}. Collection methods for the gas samples were carried out following Zhou et al. (2005).

2.4.2 Analytical methods

The procedural extraction and analyses of the noble gases were carried out on the NGX Static Multicollector Noble Gas Mass Spectrometer (Isotopx) at the Subsurface Fluid Isotope Geochemistry Laboratory at the Lancaster Environment Centre, Lancaster University, using the methods described in Li et al. (2021b). A blank and an air standard, (diluted from a 2L volume using a pipette of 5.7cc air) were measured at equal intervals throughout the analysis. The precision of the noble gas analysis is governed by the sample size, including this blank correction. Common interferences occur with various species found in the region of noble gases. During Ne abundance and isotope analyses, appropriate mass peaks were monitored to correct for interferences caused by doubly charged ions of $^{40}Ar^{2+}$ and $^{44}CO_2^{2++}$ on ^{20}Ne and ^{22}Ne, respectively. All uncertainties have been considered, including statistical analytical error, blank error, air standard reproducibility, expansion volume uncertainty and mass spectrometer sensitivity stability.

2.5 Results

2.5.1 Gas composition and geochemistry

A total of 24 gas samples were gathered from unconventional shale gas wells within the Sichuan Basin and were analysed for their noble gas abundance and isotopic composition, bulk chemistry and stable carbon isotope chemistry. Sample name, reservoir strata, burial depth and major gas component (%) information are given (Table 19), along with noble gas concentrations and isotopic ratios for He, Ne, Ar, Kr and Xe (Table 20). Corresponding air-derived elemental ratios ($^{20}Ne/^{36}Ar$, $^{84}Kr/^{36}Ar$ and $^{132}Xe/^{36}Ar$) are also published in conjunction for reference (Table 21). The study area comprises 4 shale gas fields: the Zhaotong gas field, n = 5 (sample prefix YS and YH), and Changning gas field n = 5 (sample prefix NH), both located in the Southern domain, the Weiyuan gas field, n = 3 (sample prefix W), in the Central-Southern Sichuan gas domain, and the Fuling gas field, n = 11 (sample prefix JY), situated in the Eastern Sichuan Basin gas domain. All of these gas fields target the Late Ordovician-Early Silurian Wufeng-Longmaxi formation (O_3w-S_1l - Figure 20).

Gas samples are predominantly comprised of CH_4 (97.00-99.36%) with minor contributions of C_2H_6 (0.32-0.56%) and C_3H_8 (~0.01%) as well as a minor abundance of elements, including CO_2 (0.01-1.06%) and N_2 (0.04-4.44%). While stable carbon isotope ratios ($\delta^{13}C$, VPDB) for CH_4, C_2H_6. C_3H_8 and CO_2 range between -37.30 to -26.93‰, -40.30 to -33.70‰, -37.96 to -33.60‰ and -8.3 to 10.42‰, respectively. Gas dryness ($\frac{C_1}{C_2+C_3}$), which describes the ratio of CH_4 to heavier hydrocarbons (C_2H_6 and C_3H_8) highlights that sampled gases are extremely dry (173.33-295.36) and indicates that the Wufeng-Longmaxi shale is a mature unconventional reservoir at a later stage of thermal maturity.

Table 19 - Gas composition data from different wells across various gas fields in the Sichuan Basin are presented. Major gas components, including methane (CH_4), ethane (C_2H_6), and propane (C_3H_8), are quantified as percentages. The table also includes concentrations of carbon dioxide (CO_2) and nitrogen (N_2), along with the isotopic compositions ($\delta^{13}C$, ‰ VPDB) of CH_4, C_2H_6, C_3H_8, and CO_2. This dataset provides insights into the geochemical characteristics of gases within the Zhaotong, Weiyuan, Changning, and Fuling gas fields, highlighting variations in gas compositions and isotopic signatures across different stratigraphic units (O_3w-S_1l).

Well	Strata	Major gas components (%)					$\delta^{13}C$ (‰), VPDB			
		CH_4	C_2H_6	C_3H_8	CO_2	N_2	CH_4	C_2H_6	C_3H_8	CO_2
Zhaotong gas field										
YS108 H4-3	O_3w-S_1l	-	-	-	-	-	-	-	-	-
YS108-H4-1	O_3w-S_1l	-	-	-	-	-	-	-	-	-
YS108 H6-1	O_3w-S_1l	-	-	-	-	-	-	-	-	-
YH6-6	O_3w-S_1l	99.08	0.43	0.01	0.18	0.30	-26.93	-33.71	-33.70	-
YH7-5	O_3w-S_1l	99.11	0.50	0.01	0.15	0.23	-27.29	-34.36	-35.18	-8.30
Weiyuan gas field										
W201H1	O_3w-S_1l	98.56	0.37	0.01	1.06	4.44	-35.20	-38.70	-35.90	-7.10
W201	O_3w-S_1l	99.09	0.48	0.01	0.42	1.13	-37.30	-38.30	-33.60	-7.30
W201H3	O_3w-S_1l	97.00	0.32	0.01	0.87	2.81	-35.30	-40.30	-37.50	-5.80
Changning gas field										
NH13-3	O_3w-S_1l	98.72	0.41	0.01	0.36	-	-28.10	-33.70	-	-1.50
NH13-1	O_3w-S_1l	99.35	0.42	0.01	0.01	-	-27.91	-33.87	-35.52	-1.03
NH13-2	O_3w-S_1l	99.09	0.41	0.01	0.28	0.22	-28.29	-34.52	-35.86	1.90
NH8-2	O_3w-S_1l	98.98	0.46	0.01	0.58	-	-27.20	-34.49	-35.27	-1.34
NH8-1	O_3w-S_1l	99.36	0.48	0.01	0.68	0.04	-27.65	-33.76	-37.24	1.94
Fuling gas field										
JY57-3	O_3w-S_1l	99.42	0.52	0.01	-	0.05	-31.29	-37.29		
JY59-4	O_3w-S_1l	98.67	0.47	0.01	-	0.85	-30.47	-37.17	-37.17	
JY56-4	O_3w-S_1l	98.79	0.49	0.01	-	0.70	-30.60	-37.30	-37.96	
JY63-3	O_3w-S_1l	98.76	0.46	0.01	-	0.77	-29.43	-35.44	-37.41	-2.09
JY47-3	O_3w-S_1l	98.82	0.40	0.01	0.06	0.71	-30.48	-35.40	-36.54	10.42
JY47-6	O_3w-S_1l	98.75	0.36	0.01	0.08	0.80	-30.99	-35.50	-	-
JY52-2	O_3w-S_1l	98.13	0.38	0.01	0.61	0.87	-30.48	-36.10	-36.74	3.76
JY52-1	O_3w-S_1l	98.42	0.37	0.01	0.46	0.74	-31.09	-36.42	-36.93	2.70
JY57-1	O_3w-S_1l	98.80	0.56	0.01	-	0.63	-30.79	-36.69	-37.68	-
JY36-5	O_3w-S_1l	98.77	0.53	0.01	0.17	0.52	-30.56	-36.53	-37.54	1.38
JY56-6	O_3w-S_1l	98.10	0.46	0.01	0.44	0.99	-30.04	-36.45	-	5.00

Table 20 – Noble gas isotope concentrations and ratios for helium (^{4}He), neon (^{20}Ne, ^{21}Ne, and ^{22}Ne), argon (^{36}Ar and ^{40}Ar), krypton (^{84}Kr and ^{86}Kr), and xenon (^{130}Xe and ^{132}Xe). Concentrations are provided in standard temperature and pressure (STP) units (cm^3 STP/cm^3). ^{21}Ne* and ^{40}Ar* represent the values for purely nucleogenic ^{21}Ne and radiogenic ^{40}Ar, corrected for an atmospheric excess (Equations 1 and 2). ^{3}He/^{4}He (R) ratios are normalised to the air value R_a = 1.39 x 10^{-6}. 1σ errors are shown in the table following a '±' sign.

Sample	^{4}He x 10^{-6} cm^3 STP/cm^3	^{20}Ne x 10^{-11} cm^3 STP/cm^3	^{36}Ar x 10^{-10} cm^3 STP/cm^3	^{84}Kr x 10^{-11} cm^3 STP/cm^3	^{132}Xe x 10^{-12} cm^3 STP/cm^3	^{3}He/^{4}He (R/R$_a$)	^{20}Ne/^{22}Ne	^{21}Ne*/^{22}Ne	^{40}Ar*/^{36}Ar	^{86}Kr/^{84}Kr	^{132}Xe/^{130}Xe
Air						1	9.81	0.029	298.6	0.31	6.61
Zhaotong gas field											
YS108 H4-3	n/a	16.6 ± 1.4	0.57 ± 0.03	5.65 ± 0.07	16.27 ± 7.76	n/a	7.87 ± 0.7	0.0922 ± 0.02	595.5 ± 27.3	0.31 ± 0.07	n/a
YS108-H4-1	36.36 ± 0.4	39.72 ± 3.4	16.46 ± 0.41	4.77 ± 0.07	4.49 ± 0.72	0.004 ± 0.0001	8.40 ± 0.77	0.03 ± 0.01	2465 ± 66.2	0.31 ± 0.007	n/a
YS108 H6-1	149.67 ± 17.6	n/a	932.13 ± 58.3	37.90 ± 12.2	47.49 ± 1.24	0.006 ± 0.002	n/a	n/a	n/a	0.32 ± 0.18	6.70 ± 0.45
YH6-6	202 ± 2.9	16.1 ± 1	13.27 ± 0.51	5.35 ± 0.09	6.13 ± 0.11	0.006 ± 0.0001	12.32 ± 0.62	0.0351 ± 0.0005	1437 ± 59.1	0.32 ± 0.005	6.49 ± 0.1
YH7-5	173 ± 2.4	13.8 ± 1.5	13.8± 0.31	5.48 ± 0.09	6.00 ± 0.11	0.005 ± 0.0001	14.26 ± 0.71	0.0321 ± 0.0005	1284 ± 34.4	0.31 ± 0.003	6.44 ± 0.1
Weiyuan gas field											
W201H1	77.09 ± 7.5	880.07 ± 9.5	324.23 ± 14.6	1.03 ± 0.01	6.93 ± 0.13	0.033 ± 0.004	9.48 ± 0.15	0.002 ± 0.0001	944.5 ± 44.2	0.30 ± 0.007	6.46 ± 0.28
W201	86.82 ± 11.2	68.84 ± 1.9	30.74 ± 2.34	2.96 ± 0.03	14.64 ± 0.36	0.038 ± 0.005	9.25 ± 0.28	0.0444 ± 0.002	2223 ± 171.1	0.31 ± 0.005	6.34 ± 0.43
W201H3	393.73 ±49.7	90.72 ± 4	2.73 ± 0.18	11.70 ± 0.19	11.58 ± 0.25	0.017 ± 0.002	9.44 ± 0.44	0.07 ± 0.003	2327 ± 152.5	0.33 ± 0.009	6.62 ± 0.39
Changning gas field											
NH13-3	6.68 ± 0.2	33.09 ± 0.8	0.56 ± 0.46	2.67 ± 0.04	0.43 ± 0.01	n/a	10.74 ± 0.29	0.04 ± 0.002	n/a	0.31 ± 0.008	6.70 ± 0.52
NH13-1	38.6 ± 5.1	4008.57 ± 58.5	742.75 ± 9.65	105.67 ± 1.47	74.94 ± 1.38	0.009 ± 0.0001	9.94 ± 0.58	n/a	n/a	0.31 ± 0.007	6.60 ± 0.36
NH13-2	43.13 ± 5.8	37.42 ± 1.2	14.19 ± 2.23	6.91 ± 0.10	8.43 ± 0.17	0.009 ± 0.001	10.24 ± 0.36	0.0379 ± 0.002	2077 ± 327	0.31 ± 0.008	6.54 ± 0.37
NH8-2	37.63 ± 5.1	34.55 ± 1.2	5.39 ± 1.82	12.03 ± 0.17	8.56 ± 0.17	0.009 ± 0.001	9.92 ± 0.37	0.0364 ± 0.002	5522 ± 1867	0.31 ± 0.007	6.59 ± 0.38
NH8-1	35.71 ± 2.3	224.48 ± 3.7	32.22 ± 2.73	9.53 ± 0.14	9.52 ± 0.19	0.010 ± 0.001	10.29 ± 0.21	0.0059 ± 0.0002	874.1 ± 74.6	0.30 ± 0.008	6.55 ± 0.37
Fuling gas field											
JY57-3	337 ± 4.8	19.5 ± 0.4	13.76 ± 0.2	6.57 ± 0.11	6.39 ± 0.11	0.013 ± 0.0002	9.88 ± 0.21	0.0361 ± 0.0005	1566 ± 31.4	0.31 ± 0.004	6.48 ± 0.08
JY59-4	293 ± 4.2	22.7 ± 0.5	15.92 ± 0.51	7.59 ± 0.12	8.70 ± 0.15	0.009 ± 0.0001	9.35 ± 0.19	0.0381 ± 0.0005	1520 ± 53.3	0.30 ± 0.003	6.50 ± 0.08
JY56-4	199 ± 2.8	85.2 ± 1.2	19.07 ± 0.37	8.64 ± 0.14	8.37 ± 0.14	0.007 ± 0.0001	9.90 ± 0.06	0.0091 ± 0.0002	1172 ± 28.3	0.30 ± 0.002	6.65 ± 0.09
JY63-3	224 ± 3.2	24.9 ± 0.6	15.45 ± 0.41	6.82 ± 0.11	7.97 ± 0.13	0.008 ± 0.0001	10.06 ± 0.23	0.0341 ± 0.0005	1601 ± 47.7	0.31 ± 0.004	6.53 ± 0.08
JY47-3	238 ± 3.4	31.1 ± 0.9	19.01 ± 0.39	8.33 ± 0.13	10.30 ± 0.17	0.008 ± 0.0001	9.92 ± 0.23	0.0311 ± 0.0005	1388 ± 34.7	0.32 ± 0.004	6.60 ± 0.08
JY47-6	327 ± 4.6	26 ± 0.5	16.62 ± 0.45	5.81 ± 0.10	7.65 ± 0.13	0.010 ± 0.0001	9.88 ± 0.18	0.0401 ± 0.0005	1690 ± 51.8	0.32 ± 0.005	6.27 ± 0.08
JY52-2	286 ± 4	25.1 ± 0.6	35.91 ± 0.41	16.20 ± 0.26	10.80 ± 0.18	0.008 ± 0.0001	9.54 ± 0.23	0.0371 ± 0.0005	812.7 ± 14.7	0.31 ± 0.002	6.54 ± 0.09
JY52-1	233 ± 3.3	36.2 ± 1	24.84 ± 0.59	8.45 ± 0.14	10.40 ± 0.18	0.010 ± 0.0001	9.62 ± 0.74	0.0281 ± 0.0004	1142 ± 31.7	0.32 ± 0.004	6.46 ± 0.08
JY57-1	172 ± 2.4	18.8 ± 1.4	7.08 ± 0.35	7.08 ± 0.12	8.32 ± 0.14	0.007 ± 0.0001	10.40 ± 0.67	0.0351 ± 0.0005	3266 ± 167.2	0.31 ± 0.003	6.43 ± 0.08
JY36-5	200 ± 2.8	22.1 ± 0.6	22.92 ± 2.5	6.66 ± 0.11	8.86 ± 0.16	0.006 ± 0.0001	14.23 ± 1.34	0.0321 ± 0.0005	812.6 ± 89.3	0.31 ± 0.004	6.46 ± 0.09
JY56-6	158 ± 2.2	23.50 ± 1.4	16.47 ± 0.34	7.32 ± 0.13	8.09 ± 0.14	0.007 ± 0.0001	10.62 ± 0.47	0.0381 ± 0.0005	1466 ± 36.7	0.31 ± 0.005	6.49 ± 0.09

Table 21 – Elemental ratios for air-derived isotopes of Ne (^{20}Ne), Ar (^{36}Ar), Kr (^{84}Kr) and Xe (^{132}Xe) from the Zhaotong, Weiyuan, Changning and Fuling gas fields. 1σ errors are shown in the table. These ratios are crucial for understanding noble gases' geochemical behaviour and origins in these shale gas reservoirs.

Sample	$^{20}Ne/^{36}Ar$		$^{84}Kr/^{36}Ar$		$^{132}Xe/^{36}Ar$		$^{132}Xe/^{84}Kr$	
	x 10^{-2}	error (1σ)	x 10^{-2}	error (1σ)	x 10^{-3}	error (1σ)		error (1σ)
Zhaotong gas field								
YS108 H4-3	n/a	n/a	n/a	n/a	n/a	n/a	0.29	0.138
YS108-H4-1	24.13	2.15	2.90	0.08	2.73	0.44	0.09	0.015
YS108 H6-1	n/a	n/a	0.41	0.13	0.51	0.03	0.13	0.041
YH6-6	12.13	0.9	4.03	0.17	4.62	0.19	0.11	0.003
YH7-5	10.00	1.1	3.97	0.11	4.35	0.13	0.11	0.003
Weiyuan gas field								
W201H1	27.14	1.26	0.03	0.01	0.21	0.01	0.67	0.015
W201	22.39	1.82	0.96	0.07	4.76	0.38	0.50	0.014
W201H3	n/a	n/a	42.92	2.85	42.47	2.88	0.10	0.003
Changning gas field								
NH13-3	n/a	n/a	47.40	39.98	7.67	6.31	0.02	0.001
NH13-1	53.97	1.05	1.42	0.03	1.01	0.02	0.07	0.002
NH13-2	26.37	4.22	4.87	0.77	5.94	0.94	0.12	0.003
NH8-2	64.13	21.8	22.32	7.55	15.89	5.38	0.07	0.002
NH8-1	69.67	6.01	2.96	0.25	2.96	0.26	0.10	0.002
Fuling gas field								
JY57-3	14.18	0.35	4.78	0.11	4.65	0.11	0.10	0.002
JY59-4	14.26	0.55	4.77	0.17	5.46	0.2	0.11	0.003
JY56-4	44.67	1.08	4.53	0.11	4.39	0.11	0.10	0.002
JY63-3	16.11	0.59	4.41	0.14	5.16	0.16	0.12	0.003
JY47-3	16.36	0.57	4.38	0.11	5.42	0.14	0.12	0.003
JY47-6	15.64	0.51	3.50	0.11	4.60	0.15	0.13	0.003
JY52-2	6.99	0.19	4.51	0.09	3.01	0.06	0.07	0.002
JY52-1	14.57	0.54	3.40	0.1	4.19	0.12	0.12	0.003
JY57-1	26.57	2.36	10.01	0.52	11.76	0.61	0.12	0.003
JY36-5	9.64	1.08	2.91	0.32	3.87	0.43	0.13	0.003
JY56-6	14.27	0.91	4.45	0.12	4.91	0.13	0.11	0.003

2.5.2 Noble gas isotopic signatures

2.5.2.1 Helium

Helium (^{4}He) concentrations range from 6.68 to 393.73 x 10^{-6} cm^3 STPcm^{-3}, with ^{4}He concentrations particularly high in the Fuling gas field. Helium isotope ratios (^{3}He/^{4}He) are reported relative to the atmospheric ^{3}He/^{4}He ratio; R_a = 1.39 x 10^{-6} (Porcelli et al., 2002) and range from 0.0037R_a to 0.038R_a (Table 20), highlighting a strongly crustal radiogenic signature. Geospatial disparities are clear, with Weiyuan sample ratios exhibiting ratios that are an order of magnitude larger (0.017R_a-0.038R_a) compared to samples from Zhaotong (0.0037R_a-0.0062R_a), Fuling (0.0062R_a-0.0126R_a), and Changning (0.0088R_a - 0.009R_a). Variations in the ^{3}He/^{4}He ratio could result from ^{4}He ingrowth rather than minor perturbations of mantle signature ^{3}He, as the dominant radiogenic signature in these gas samples indicates that there is little atmospheric or mantle helium input, and the contribution exhibited across all samples is negligible. ^{4}He/^{20}Ne ratios are all far in excess of the air value (0.003), but values are elevated in the Fuling gas field, where they range from 2 to 20 x 10^5, which also far exceeds the ^{4}He/^{20}Ne ASW (air-saturated water) value of 0.288, thus the input of atmospheric He is similarly minimal. Sample YS108 H4-3 from the Zhaotong area is likely to be air contaminated, with its composition variably altered from either contamination during sampling, storage, or analysis, as its ^{4}He/^{20}Ne value is noticeably lower (665). Hence, it has been excluded from further description.

2.5.2.2 Neon

Neon (^{20}Ne) concentrations range from 0.13 to 8.8 x $10^{-9}$$cm^3$ STP cm^{-3}. ^{20}Ne is attributed to the recharge of meteoric groundwaters, and concentrations are affected by gas production, with wells at a later stage of production (and degassing) exhibiting lower concentrations of ^{20}Ne (Zhou et al., 2005). ^{20}Ne in shale gas samples has also previously been shown to correlate well with maturity, with lower Ne concentrations in samples indicative of greater thermal maturity (Byrne et al., 2020).

Both ^{20}Ne/^{22}Ne and ^{21}Ne/^{22}Ne (Table 20) ratios highlight an excess of ^{21}Ne and ^{22}Ne relative to air, where ^{20}Ne/^{22}Ne_{air} and ^{21}Ne/^{22}Ne_{air} ratios are 9.81 and 0.029 respectively (Porcelli et al., 2002). ^{20}Ne/^{22}Ne ratios are typically lower at between 9.25 - 9.48 in the central Weiyuan area, whereas ^{20}Ne/^{22}Ne ratios are as high as 14.23 and 14.26 in the eastern Fuling area and Zhaotong area, respectively. These values fall far outside the atmospheric ^{20}Ne/^{22}Ne range and potentially result from a process related to mass-

dependent fractionation, as the contribution of $^{40}Ar^{++}$ has been excluded. $^{21}Ne/^{22}Ne$ ratios are similarly in excess of this atmospheric value and range from 0.031 (W201H1) to 0.982 (NH13-1). To distinguish between exclusively crustal nucleogenic and radiogenic (corrected for atmospheric contributions) derived noble gases ($^{21}Ne_{rad}$ and $^{40}Ar_{rad}$), the notations $^{21}Ne^*$ and $^{40}Ar^*$ are used herein. Ballentine and Burnard (2002) outline the method for quantifying these resolved components whereby we calculate the contribution of purely nucleogenic $^{21}Ne^*$ and radiogenic $^{40}Ar^*$:

$$[i]_{\mathrm{rad}} = [i]_{\mathrm{meas}} \times [1 - \frac{(i/j)_{\mathrm{air}}}{(i/j)_{\mathrm{meas}}}] \quad (63)$$

Where the concentration of isotope '*i*' is considered purely radiogenic or excess, $[i]_{rad}$, when isotope '*i*' denotes ^{21}Ne, isotope '*j*' refers to ^{22}Ne, and when '*i*'=^{40}Ar, '*j*'=^{36}Ar. Using the measured concentrations of isotope '*i*', $[i]_{meas}$, and the measured ratio of isotopes '*i*' and '*j*' in the sample, $(i/j)_{meas}$, while $^{21}Ne/^{22}Ne_{air}$ = 0.029 and $^{40}Ar/^{36}Ar_{air}$ = 298.56 (Lee et al., 2006).

2.5.2.3 Argon

^{36}Ar concentrations range between 0.056 to 93.213 x 10^{-9} cm^3 STPcm^{-3}. Argon isotope ratios ($^{40}Ar^*/^{36}Ar$) are up to 2465 in the Zhaotong field and up to 5522 in the Changning field, showing elevated radiogenic $^{40}Ar^*/^{36}Ar$, compared to the atmospheric $^{40}Ar/^{36}Ar$ ratio of 298.6 (Lee et al., 2006). This variation is attributed to an excess of ^{40}Ar derived from crustal material produced by ^{40}K decay.

2.5.2.4 Krypton and Xenon

In the shale gas samples, ^{84}Kr and ^{132}Xe concentrations range from 0.103 to 10.567 x 10^{-10} cm^3 STPcm^{-3}, and 0.43 to 74.94 x 10^{-12} cm^3 STPcm^{-3}, respectively. Isotope ratios of Krypton and Xenon are indistinguishable from corresponding air values; $^{86}Kr/^{84}Kr$ ranges from 0.301 to 0.326, where the air value = 0.305 (Aregbe et al., 1996), whilst $^{132}Xe/^{130}Xe$ values vary between 6.27 to 6.7, where the air value = 6.607 (Pepin, 2000). Gas samples show an overall slight enrichment of ^{84}Kr and a depletion of ^{132}Xe with respect to initial ASW values introduced at recharge. $^{84}Kr_{meas}/^{84}Kr_{asw}$ = 1.29, whilst $^{132}Xe_{meas}/^{132}Xe_{asw}$ = 0.69. However, $(^{84}Kr/^{36}Ar)_{meas}/(^{84}Kr/^{36}Ar)_{asw}$ and $(^{132}Xe/^{36}Ar)_{meas}/(^{132}Xe/^{36}Ar)_{asw}$ are on average 0.77 and 1.8 times higher in gas samples than the calculated ASW ratios, respectively.

2.6 Discussion

2.6.1 Origins of atmosphere-derived noble gases

The atmosphere-derived noble gases (^{20}Ne, ^{36}Ar, ^{84}Kr and ^{132}Xe) are introduced during aquifer recharge of meteoric waters at surface conditions and have no significant subsurface source. The groundwater equilibrated with this atmospheric component is termed air-saturated water (ASW). Noble gases that have been transported in the subsurface and have consequently accumulated within a reservoir represent a singular, binary, or ternary mixture of noble gases that can be ascribed to an atmospheric, radiogenic, or mantle-derived end-member source. An estimate of the initial inventory of ASW noble gases in pore fluids (the noble gas isotopic ratios of groundwater) and the ratios of gases that phase change from a liquid phase groundwater component into the gas phase via exsolution are variably altered by solubility, which can be quantified using Henry's Law.

2.6.2 Processes affecting noble gas abundances

Measured noble gas isotope ratios reflect the extent of end-member contributions, and the degree of interaction between the shale gas-bearing reservoir interval and adjacent groundwaters can be more clearly understood, as well as whether the system is open or closed to gas loss. Besides the exchange of gases with an aqueous phase outlined above, other studies have determined the importance of a solid phase influence, such as the process of adsorption that similarly affects heavy noble gases (Zhou et al., 2005, Torgersen and Kennedy, 1999). Using coefficients for adsorption (Henry's constant, K – Table 22), we can quantify the degree to which heavy noble gases present are partitioned due to a 'solid phase' component following migration to a trapping structure. We then calculate the altered remaining noble gas ratio in a free gas phase, which is depleted in Kr and Xe resulting from the in-situ removal of these noble gases due to adsorption.

Table 22 - Henry's constants (atm kg/mol) for gas-water phase and water-solid (shale interface) phase interactions. Henry's constants for solubility-controlled exsolution calculated from Ballentine et al. (2002), Crovetto et al. (1982) and dimensionless constants calculated from Sander (2015) Henry's constants for adsorption-controlled processes are collated from average Mt McRae samples from Podosek et al. (1981). K units are converted from cc (STP)/g atm where 1 ccSTP = 4.465 x 10^{-5} mol (Ozima and Podosek, 2002).

Process	He	Ne	Ar	Kr	Xe	Depth (m)	Temp (°C)	Salinity (MNaCl)
Recharge	2456.03	1978.70	529.14	273.75	144.59	-750	10	0.1
Reservoir	2000.37	2104.57	1152.88	785.83	563.31	2800	100	2
Adsorption	-	-	-	248.65	289.48	-	-	-

In water, noble gas solubility is principally determined by both temperature and salinity. Solubility (S) is proportional atomic mass (M), S∝M, where $(\frac{1}{K_{Ne}} < \frac{1}{K_{Ar}} < \frac{1}{K_{Kr}} < \frac{1}{K_{Xe}})$, and therefore, under recharge conditions accounting for local elevation (750m, where air pressure is ~0.9atm once adjusted for relative humidity), temperature (10°C), and salinity (0.1M NaCl), Ne is determined to be the least soluble of the ASW-derived noble gases in water, with Ne first being apportioned into the gas phase, while Kr and Xe remain dissolved in groundwater during initial degassing due to their higher atomic mass. At reservoir conditions, considering an average geothermal gradient across the Sichuan basin of between 20-25°C km^{-1} (Chen et al., 2017) and 23°C km^{-1} (Liu et al., 2021a), we model using a temperature of 100°C and 2M NaCl. Ne is calculated to be slightly less soluble at reservoir conditions than at recharge, whereas Ar, Kr and Xe are approximately 2,3 and 4 times less soluble, respectively, than at recharge conditions (Table 22).

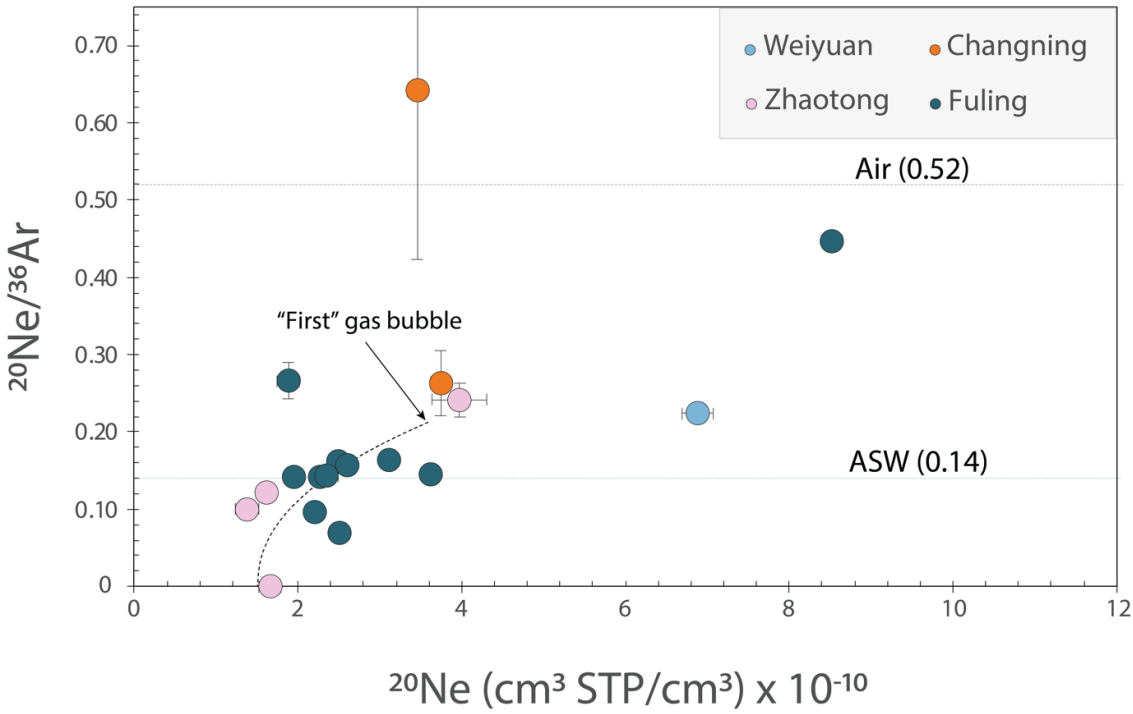

Figure 22 – Air-derived noble gases $^{20}Ne/^{36}Ar$ fractionate due to mass-dependent solubility processes. Each increment of the predicted solubility-controlled exsolution line signifies the predicted $^{20}Ne/^{36}Ar$ ratio with a corresponding amount (%) of Ar exsolved from groundwater into a gas phase. Most gas samples are far from the influence of air (0.52) but have values approaching ASW (0.14). Unconventional shale gases from the Fuling field have $^{20}Ne/^{36}Ar$ values closest to ASW, which indicates possible closed system equilibration with a groundwater component. Weiyuan W201H3 $^{20}Ne/^{36}Ar$ values are outside of the graph range (>0.72), while W201H1 ^{20}Ne values are also higher than 1.2 x 10^{-9}. ^{20}Ne concentrations for air (1645 x 10^{-8}) and ASW (19.2 x 10^{-8}) fall outside the plotted range and are represented by their respective $^{20}Ne/^{36}Ar$ ratios,

As no radiogenic or nucleogenic sources of ^{20}Ne or ^{36}Ar exist, the isotopic ratio ($^{20}Ne/^{36}Ar$) reflects the degree of fractionation between a gas-liquid phase (Hunt et al.,

2012) and the extent of mixing with groundwater (Kipfer et al., 2002). Due to lower solubility in water, Ne begins to degas prior to Ar, resulting in early gas bubbles that carry a higher concentration of Ne than Ar and a signature of $^{20}Ne/^{36}Ar$ that initially exceeds the value of ASW. Samples with elevated $^{20}Ne/^{36}Ar$ values indicate they are at an earlier stage of degassing and elemental fractionation, while possibly in contact with a liquid phase, whereby a greater proportion of Ar remains dissolved in groundwater ($V_g/V_w \rightarrow 0$). As progressive degassing of this groundwater component occurs, defined by the modelled solubility-controlled exsolution curve in Figure 22, gas bubbles that follow contain progressively higher concentrations of the more soluble, heavier noble gases, resulting in increasingly lower $^{20}Ne/^{36}Ar$ ratios in the gas phase, until the groundwater component becomes fully degassed, $V_g/V_w \rightarrow \infty$. Gas samples exhibit $^{20}Ne/^{36}Ar$ ratios that are significantly less than the air value (0.52), and close to, but slightly greater than the ASW value (0.14), and we therefore infer that the shale gas bearing unit is potentially closed to gas loss, at equilibrium, or at a very early stage of degassing.

2.6.3 In-situ open vs. closed system behaviour

Normalising the measured air-derived noble gas isotope ratios (^{20}Ne, ^{36}Ar, ^{84}Kr, ^{132}Xe) to initial ASW values (Figure 23) reveals the extent of fractionation relative to the 'original' isotope ratio that was present during the introduction of noble gases at recharge. These corrected elemental ratios show whether the system is either open or closed to gas loss. Where $^{20}Ne/^{36}Ar$ values have evolved to exceed the value of ASW, we conclude that closed system behaviour where equilibrium, or only partial degassing has occurred. Due to adsorption and desorption, Kr and Xe ratios are unreliable when determining open or closed system behaviour using this method, as measured $^{84}Kr/^{36}Ar$ and $^{132}Xe/^{36}Ar$ ratios, which, after excluding sample NH8-2, have values of 0.91 (depleted relative to ASW) and 1.6 (enriched relative to ASW), respectively. Typically, $^{84}Kr/^{36}Ar$ and $^{132}Xe/^{36}Ar$ values which are enriched relative to ASW are thought to arise following interaction with an oil phase (Barry et al., 2016). However, the Wufeng-Longmaxi shale is high to over-mature and in the dry gas window (Jiang et al., 2017). The data is interpreted to be representative of at least a two-process system that potentially alters heavier noble gas species, understood to be a binary mechanism comprising of solubility-controlled exsolution and adsorption of noble gases in a closed system (both governed by Henry's Law). The extent of adsorption is variably modified by the reservoir lithology, but it is particularly significant in altering heavy noble gas abundances in organic-rich shales, where the presence of clays can increase the affinity for Kr and Xe (Podosek et al., 1981).

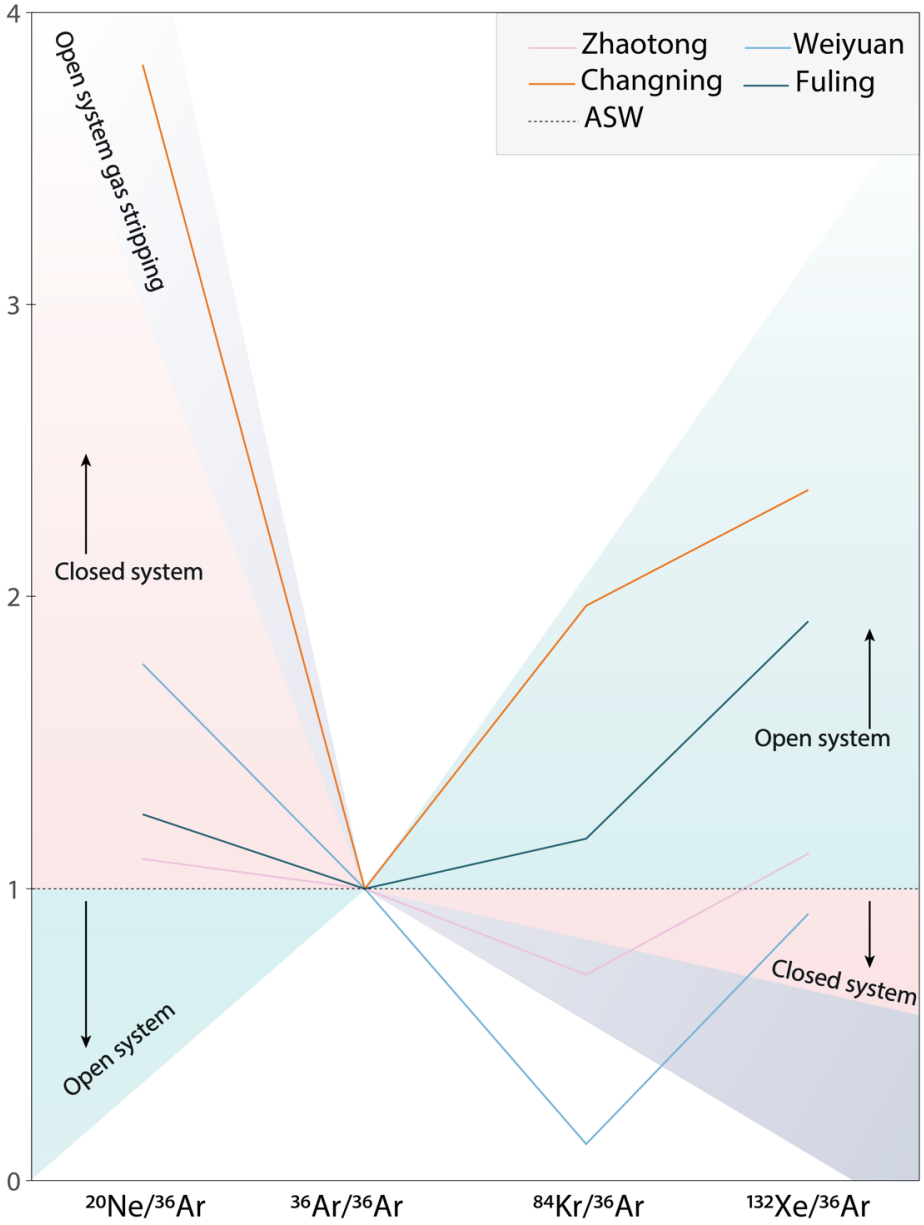

Figure 23 - Mean air-derived noble gas isotope abundances (^{20}Ne, ^{36}Ar, ^{84}Kr and ^{132}Xe – with outliers removed) plotted relative to ^{36}Ar (normalised to ASW at 10°C, where ASW = 1). The plot represents average abundances across each gas field. Most tight sandstone gas samples indicate open-system behaviour (^{20}Ne/^{36}Ar < 1) with possible enrichment of ^{84}Kr and ^{132}Xe. Except for Changning shale gases, for which all noble gas ratios > 1, the remaining unconventional shale gas samples plot close to or below the ASW line for the suite of heavy noble gases (^{84}Kr and ^{132}Xe).

2.6.4 Ne signatures in shale gases

Purely nucleogenic ^{21}Ne* represents ~50-60% of the total measured ^{21}Ne in Fuling, Zhaotong and Changning shale gas samples. In the Weiyuan shale gas samples, ^{21}Ne* accounts for ~60-70% of total measured ^{21}Ne, underscoring a lower atmospheric input in gases from the central Sichuan Basin. ^{21}Ne/^{22}Ne isotope ratios correlate well with the relative ages of gas generation and the timing of contact with fluids that transport these crustal-derived noble gases. These values are nominally higher than the empirically

derived crustal neon radiogenic production line trending downwards to a lower $^{20}Ne/^{22}Ne$ vs $^{21}Ne/^{22}Ne$ value (Figure 24), which represents the mixing line between crustal and air endmembers.

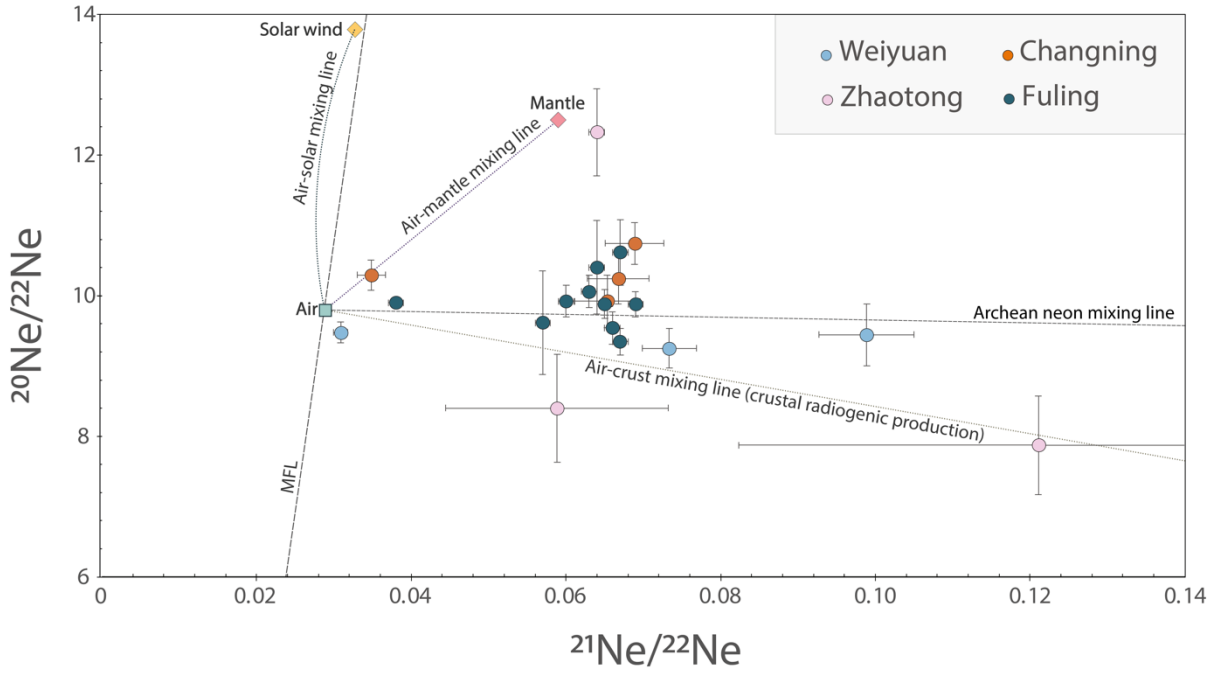

Figure 24 - Neon isotope plot that shows $^{20}Ne/^{22}Ne$ vs $^{21}Ne/^{22}Ne$ ratios in samples relative to air, mantle and crustal endmembers. Values are indicative of a two-component mixture between air and crust, with negligible mantle influence. Enrichment of $^{21}Ne/^{22}Ne$ in these unconventional gas samples may arise from the lack of gas migration as other gas fields such as the shallower, younger late Triassic tight-sandstone Xujiahe sourced gases, which have undergone gas migration, have a significantly lesser contribution of radiogenic $^{21}Ne/^{22}Ne$. An Archean crustal endmember has a higher $^{21}Ne/^{22}Ne$ intercept (Holland et al., 2013), which is consistent with the average crustal O/F ratio (Ballentine and Burnard, 2002). Zhaotong gas samples exhibit large $^{21}Ne/^{22}Ne$ error margins due to their low measured concentrations, which limits their reliability.

To model the reservoir behaviour of air-derived Ne (^{20}Ne) following the recharge of groundwaters in contact with the atmosphere, we use non-ideal Henry's constants to define the expected solubility-controlled exsolution of Ne associated with fractionation. According to this model, lighter air-derived isotopes ($^{20}Ne/^{36}Ar$) should evolve from an 'initial gas bubble' value of around 0.21 to a value approaching zero as Ne becomes almost fully degassed from groundwater. Ne has low solubility in water, and any increase or decrease in pressure and/or temperature may result in fluids enriched in noble gases, such as a gas component with an elevated $^{20}Ne/^{36}Ar$ ratio relative to ASW. When considering the role of groundwater in the evolution of noble gas ratios, we observe that air-derived $^{20}Ne/^{36}Ar$ ratios correlate poorly with radiogenic $^{4}He/^{40}Ar$ ratios in the shale gas samples. This shows that mixing with air-saturated groundwaters is not the primary mechanism for the introduction of crustal He and the He signatures have accumulated

independent of a well-mixed liquid phase. The perceived excess of radiogenic $^{4}He/^{40}Ar$ is primarily controlled by the amount of U, Th and K. This results in values of $^{4}He/^{40}Ar$ outside of the range for a predicted solubility-controlled exsolution curve. Changning shale gas samples, which appear to indicate open gas stripping all have $^{20}Ne/^{36}Ar$ values that are in excess of the calculated ASW value, and low $^{4}He/^{40}Ar$ concentrations, which could be as a result of multi-stage fractionation but could also be due to a process such as subsequent re-solution and effervescence of Ne.

2.6.5 Crustal-sourced radiogenic and nucleogenic noble gases

Whilst helium is known to exist alongside natural gas in hydrocarbon-bearing formations, natural gases are formed through the thermal decomposition of sedimentary organic matter, while He is carried via a mobile fluid phase (groundwater, oil-gas, or magma) following its release from adjacent minerals. ^{4}He accumulates over periods of geologic time through radiogenic production, with the decay of U and Th in the crust, and ^{4}He concentration is, therefore, a function of both residence time and the initial U and Th concentration. Typical crustal $^{3}He/^{4}He$ values are $0.01R_a$, whilst mantle $^{3}He/^{4}He$ values are $8R_a$ (Ballentine and Burnard, 2002). Evidence of a stronger crustal radiogenic signature in the Fuling shale gas samples (higher concentrations of $^{40}Ar^{*}$), with less interaction with surrounding atmosphere-derived waters, is also an observable feature of these shale gases. The highly productive Fuling gas field features a highly clay rich mineralogy, with high high quantities of illite and smectite, which have significant amounts of ^{40}K in their structure, which readily decays into ^{40}Ar.

2.6.5.1 Quantifying crustal neon and argon abundances

The isotopes ^{21}Ne and ^{40}Ar are produced via radioactive decay in the crust. However, they are also found abundantly in the atmosphere, and therefore, their contributions require resolving by subtracting the known atmospheric ^{21}Ne and ^{40}Ar values from the measured values to quantify the crustal excess (Equation (63) in a two-component mixing system with air (Ballentine et al., 2002, Hunt et al., 2012). ^{40}Ar in samples is predominantly crustal radiogenic in origin, where $^{40}Ar^{*}$ equals 80-90% of the total measured ^{40}Ar in shale gases. Resolved, purely radiogenic $^{40}Ar^{*}/^{36}Ar$ ratios that are less than the air value might arise from a much lower contribution of K ingrowth, however since $^{40}Ar^{*}$ represents the resolved excess from a crustal source, some values are indeed expected to be lower than this air value, which is true of samples NH13-3 ($^{40}Ar^{*}/^{36}Ar$ =

22.09), however all non-resolved $^{40}Ar/^{36}Ar$ values >298.6; NH13-3 ($^{40}Ar/^{36}Ar$ = 317.59), which shows that an air component has significantly influenced this sample.

In a system whereby the shale gases have not undergone migration from a separate source rock to reservoir unit. Figure 25 shows Ar isotope fractionation ($^{40}Ar^*/^{36}Ar$ ratios vs. $1/^{36}Ar$). $^{40}Ar^*$ is a useful tool in geochronology and high concentrations in shale gases can be attributed to a greater accumulation time for the decay of ^{40}K, which is found in high concentrations in shale (26,000 ppm). Marginally lower $^{40}Ar^*/^{36}Ar$ values in gases are due to a localised depletion of K-rich minerals that decay into $^{40}Ar^*$. A linear trend of increasing $^{40}Ar^*/^{36}Ar$ with $1/^{36}Ar$, and mixing between air-crustal end-members has been observed in other geochemical studies on shale gases within the Sichuan basin (Liu et al., 2021a).

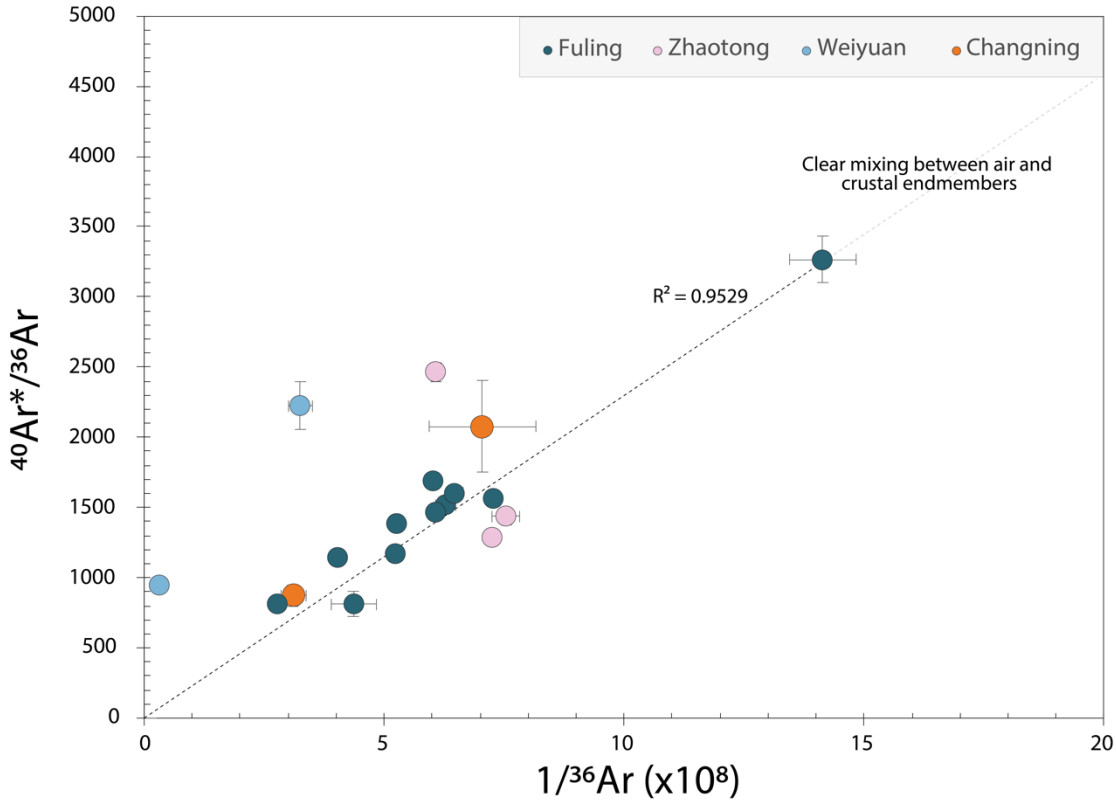

Figure 25 – Argon isotope ratios and concentrations. $^{40}Ar/^{36}Ar_{air}$ value: 298.6 (Lee et al., 2006) which when corrected: $^{40}Ar^*/^{36}Ar_{air}$ = 0; any ratios in excess of this value underline the input of the radiogenic isotope ^{40}Ar due to the decay of crustal ^{40}K. Unconventional shale gases contain $^{40}Ar^*$ concentrations that are higher than unconventional tight sandstone and conventional gas reservoirs, however, $1/^{36}Ar$ ratios are not too dissimilar between both the unconventional shale gas reservoirs and other published noble gas data from the Sichuan Basin. We infer that the extent of migration is also likely not a major control on ^{40}Ar or $1/^{36}Ar$ concentrations. Dotted trendlines signify mixing between air and crust endmembers which describes the evolution of gas ratios between the known air value and crustal endmember.

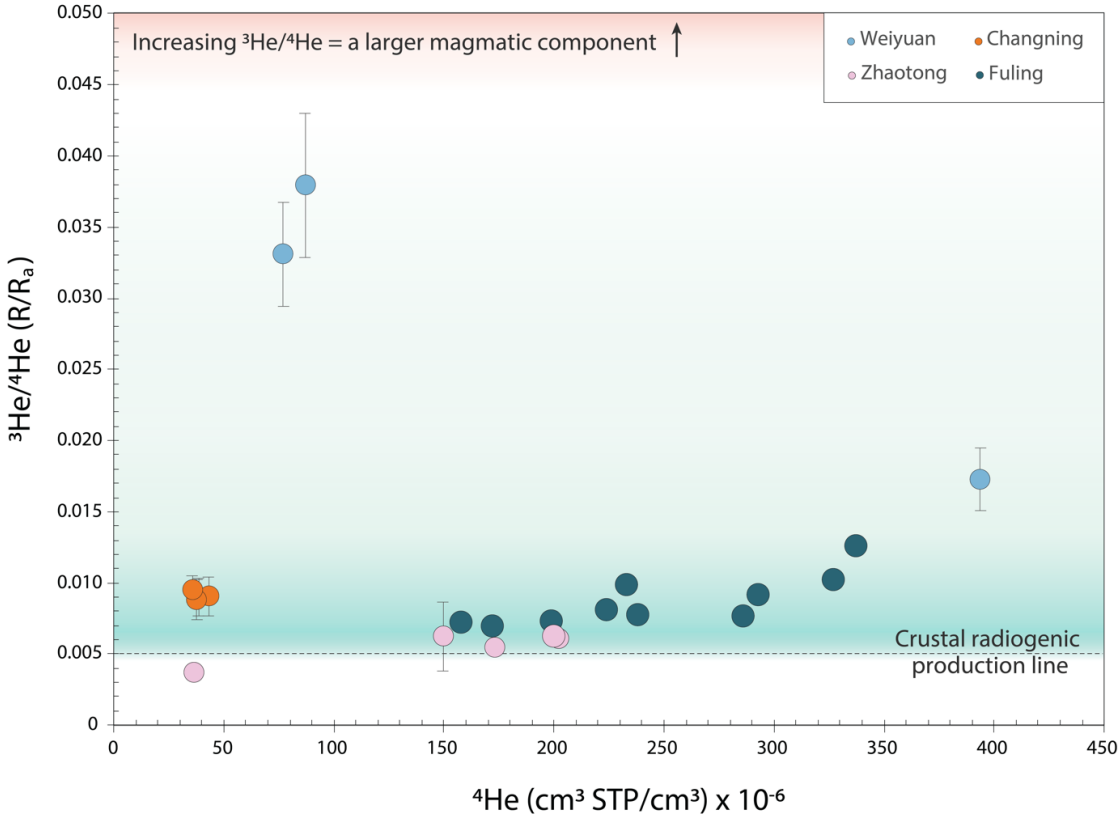

Figure 26 – Helium concentrations and isotope ratios for the Sichuan Basin. R/R_a denotes $^3He/^4He$ relative to atmosphere, where R_a = 1.39 x 10^{-6} (Porcelli et al., 2002). Ratios for all samples have a highly uniform radiogenic signature and indicate derivation from a singular source, despite the late Triassic tight-sands gases being generated much later than the early Silurian shale gases. Once again, there is only minor variation between both conventional and unconventional sample ratios, and therefore, accumulation of radiogenic ^4He is likely to have occurred more recently, in situ following migration.

2.6.5.2 Resolving crustal and mantle derived He

Helium rich gas pools are proven to exist in the older, deeply buried Cambrian marine shales of the Qiongzhusi formation in the Weiyuan area of the Sichuan Basin, where in-situ minerals have had longer to decay into their respective daughter isotopes (Wang et al., 2020b). In the Wufeng-Longmaxi shale, these radiogenic noble gases ($^4He_{rad}$, $^{21}Ne^*$, $^{22}Ne_{rad}$, $^{40}Ar^*$), are also sourced from the deeper crust where there exist high levels of K, U and Th that have radioactively decayed. The production ratio of ^4He is also altered due to the enrichment of U and Th in shales (U = 1-30 ppm, Th = 1-25 ppm) (Hannigan and Basu, 1998, Peucker-Ehrenbrink and Hannigan, 2000).

^4He concentrations are altered due to variable uranium abundances adjacent to the area of gas accumulation. In Figure 26, a large crustal component can be observed across all gas samples, as R/R_a ratios are low (0.004-0.04R_a), and plot close to the typical crustal radiogenic production line. Weiyuan shale gas samples exhibit larger error bars as a result of lower measured concentrations of He, and these gas samples have higher R/R_a values

approaching 0.02-0.04R_a. ^{4}He enrichment can also occur from ^{4}He dissolved and transported via groundwater or via influence from an additional flux of ^{4}He from an adjacent granitic body (Zhang et al., 2019c). ^{3}He/^{4}He (R/R_a) ratios range between 0.0037R_a to 0.038R_a across all gas fields, and this indicates a principally crustal radiogenic signature. Using the following mass balance equation allows us to resolve the amount of helium derived from the crust and upper mantle (Jenden et al., 1993):

$$He_{mantle}(\%) = \frac{(R_{sample} - R_{crust})}{(R_{mantle} - R_{crust})} \times 100\% \quad (64)$$

Where R represents the ^{3}He/^{4}He ratio, and using a crustal ^{3}He/^{4}He value of 0.007R_a and a mantle ^{3}He/^{4}He value of 8R_a (Ballentine and Burnard, 2002) we have determined that the fraction of mantle derived He is insignificant in all gas samples, only accounting for 0.1-0.35% of He in Weiyuan shale gas samples, and negligible (0-0.001%) for all other shale gas samples ($^4He_{rad}/^4He_{mantle} > 0.99$).

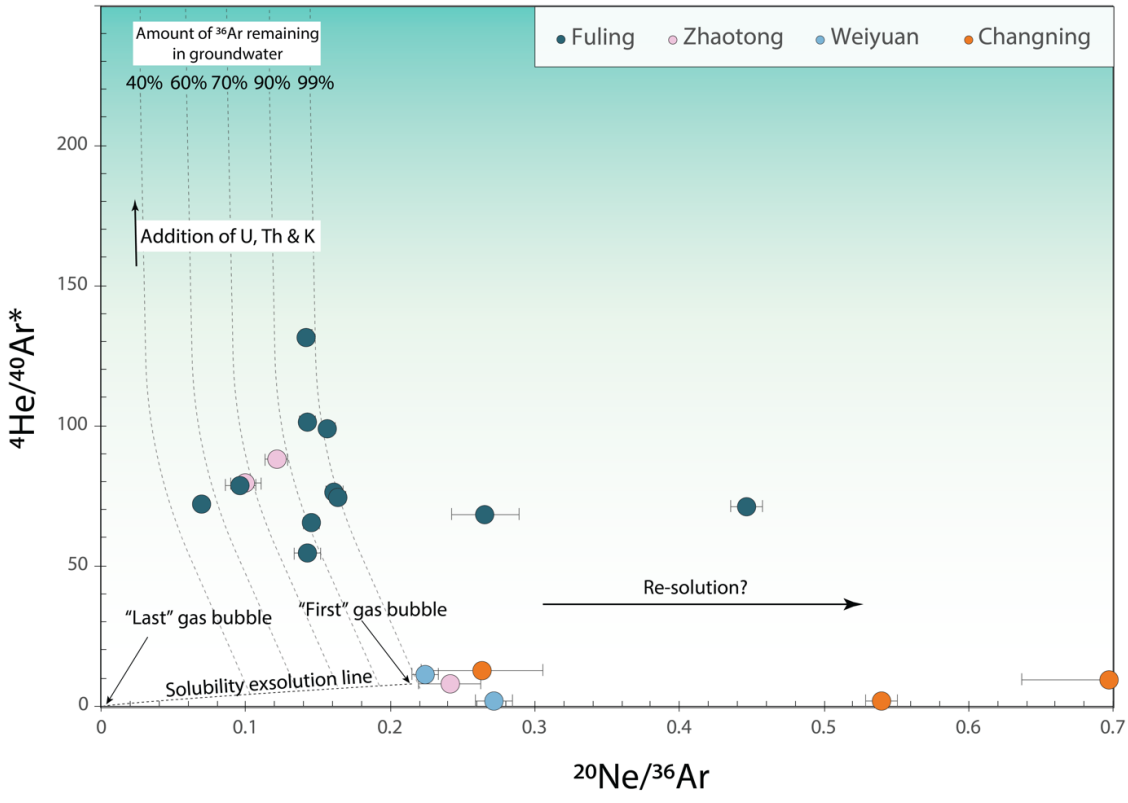

Figure 27 – Radiogenic ^{4}He/^{40}Ar* vs air-derived ^{20}Ne/^{36}Ar plots (^{40}Ar* = air corrected radiogenic Ar). Effervescence or re-solution of gases back into the liquid phase from the gas phase could explain ^{20}Ne/^{36}Ar values that exceed ASW. ^{4}He/^{40}Ar* is dependent on the amount of localised U, Th and K. Fuling gas samples are clearly enriched in radiogenic ^{4}He/^{40}Ar*, while Changning gas samples are enriched in air-derived ^{20}Ne/^{36}Ar. The solubility exsolution line represents the modification of dissolved Ar as it steadily exsolves from a liquid phase into a gas phase and the corresponding ^{20}Ne/^{36}Ar gas bubble signature at the time of degassing.

2.6.5.3 ^{4}He accumulation rates and inference on the ages of H_2O fluid residence

To assess the in-situ production rates and flux of reservoir ^{4}He in the Longmaxi shale, we use the following equations (Torgersen, 1980):

$$^4He_{in\ situ\ production} = \frac{\rho \Lambda J_4 (1-\phi)}{\phi} t \quad (65)$$

where 'ρ' is rock density in g/cm^3 (2.65 g/cm^3), 'Λ' is a parameter that defines the efficiency of transfer from the rock matrix into the gas phase, which is fast on geological timescales (→1), 'ϕ' is the reservoir porosity (0.0447), and 't' describes the residence time of groundwaters (years). J_4, which relates to the decay of Uranium (U) and Thorium (Th), can be expressed as (Craig and Lupton, 1976):

$$J_4 = 0.2355 \times 10^{-12}(\mathrm{U})(1 + 0.123(\mathrm{Th/U}) - 4)) \quad (66)$$

U and Th concentrations (Table 23) are measured by spectral gamma ray and inferred from wireline logging data. ^{4}He ages can then be determined:

$$^4He\ age = \frac{^4He_{meas} - {}^4He_{initial}}{4He_{in\ situ\ production}} \quad (67)$$

U is a redox-sensitive element, and as a result, it is preferentially enriched in sediments deposited under anoxic conditions (Kimura and Watanabe, 2001). It is well understood that high TOC content in shale is known to correlate with high uranium concentrations and a greater in-situ production rate of ^{4}He. This is consistent with Wufeng-Longmaxi shale logging characteristics at well JY1, where U concentrations reach 30 ppm within the black shale sweet spots at an average of 26 ppm along these intervals (Wang et al., 2020a). U concentrations for the Wufeng-Longmaxi formation (including the underlying grey-black interval) at well W201 are 9 ppm (Zhao et al., 2016a), and average U concentrations are 15 ppm. Th concentrations for Wufeng-Longmaxi shales in well JY1 measure close to the crustal value at 7.85 ppm and are, on average, 12 ppm.

Table 23 – Crustal derived radiogenic ^{4}He groundwater ages using U (ppm), Th (ppm) concentrations. (1) U and Th concentrations in the Wufeng-Longmaxi fm. (Wang et al., 2020a). ^{4}He ages and ^{4}He in-situ production rates for the Weiyuan, Changning and Fuling gas fields are calculated using available data from the Zhaotong gas field.

	U (ppm)	Th (ppm)	^{4}He in-situ production rate (cm^3 STP ^{4}He/cm^3 H_2O year) x 10^{-10}	Initial ^{4}He in groundwater (cm^3 STP ^{4}He/cm^3 H_2O)	^{4}He age (year) x 10^6
Zhaotong	15[1]	12[1]	2.27	0.03	1.01
Weiyuan	""	""	""	0.22	11.85
Changning	""	""	""	0.005	1.11
Fuling	""	""	""	0.07	3.51

Using a simple partitioning model between a gas (g) and liquid phase (w), ^{4}He concentrations in the liquid phase can be backcalculated, as ^4He_w is a function of dimensionless Henry's constant (K_{He}^d), which accounts for non-ideality in the gas phase, reservoir pressure, and temperature:

$$^4He_w = \left[\left(\frac{^4He}{Ar_g} \right) \Big/ \left(\frac{K_{He}^d}{K_{Ar}^d} \right) \right] Ar_w \quad (68)$$

Erroneous ^{4}He ages in the Weiyuan gas field, that exceed the limits of a reasonable accumulation timescale, are likely due to large quantities of He (as high as 18770 ppm) which are highly localised and are derived from pre-sinian granite in the Weiyuan gas field (Wang et al., 2020b). ^{4}He values can be accounted for by this in-situ production, and consequently, the volume of rock, and quantity of U, K and Th required to produce the measured radiogenic ^{4}He concentrations are considered sufficient.

2.6.6 Closed system volumetric gas-groundwater estimates

Considering a closed system governs the majority of gas samples in this study, we adopt the use of conceptual models (zero order total degassing and first order equilibrium) developed by Barry et al. (2016) to quantify the extent of the gas-groundwater interaction via solubility controlled processes, in accordance with Henry's law. These models help expand upon our understanding of the complex reservoir conditions and potential storage mechanisms. Wufeng-Longmaxi shales have low preserved porosity (

Table 24, <6%), and therefore held formation waters are expected to be low. When there is a large quantity of formation waters (in lithologies where porosity is higher), it is probable that a more significant exchange of noble gases between water and

hydrocarbons will take place. Second order models (open system gas-stripping and closed system gas stripping) have not been considered for the unconventional shale gases, as migration is negligible in the accumulation stage. The Wufeng-Longmaxi black shales are well sealed both laterally and vertically (Hu et al., 2014), and the measured $^{3}He/^{4}He$ contents in all samples reaffirms past observations that there has been a lack of intense faulting within the area, and therefore relative stability has prevented large scale migration or an escape mechanism for gases (Borjigin et al., 2017). These models assume gas phase ideality, although these systems may invariably deviate from this ideal behaviour. Furthermore, due to the fractionation of heavy noble gases due to adsorption and desorption, the solubility models we employ here will not be appropriate for determining accurate volumetric gas-water ratios for Kr and Xe, and therefore they have been excluded. Using a preliminary zero-order model, termed TGS (total gas stripping), we assume that an initial water body has been wholly degassed, representing an endmember like scenario whereby the complete exsolution of noble gas '*i*' from the water phase into the gas phase has occurred, leading to the highest gas-to-water volumetric ratios compared to the other models:

$$\frac{V_g}{V_w}(\boldsymbol{TGS}) = \frac{[C_i^{asw}]}{Z\left[C_{i(meas)}^{g}\right]} \tag{69}$$

C_i^{asw} represents concentrations of noble gas species '*i*' in the initial ASW, while $C_{i(meas)}^{g}$ is the concentration of measured gas in samples. $\frac{V_g}{V_w}$ is the minimum volume of water necessary to produce the measured gas concentrations at reservoir temperature and pressure (RTP). We use 'Z', the compression factor to modify our standard temperature and pressure (STP) measured gas concentrations into RTP at 295 bar (Nie et al., 2020) with a temperature of 10°C, where STP = 273.15 K at 1 bar:

$$Z = \frac{[273.15P_R]}{T_R} \tag{70}$$

To produce the measured abundances of ^{20}Ne in 1 cm^3 of gas requires an approximate volume of water to be completely stripped of its initial noble gas inventory and where measured gas abundances are low, a larger volume of water is required. V_g/V_w for the gas samples shows A first order equilibrium partitioning and redissolution model (EPR) is employed to calculate the V_g/V_w resulting from an apportioned noble gas remaining dissolved in water, assuming direct contact between the hydrocarbon phase and water,

where equilibrium is achieved under reservoir conditions. In this scenario, hydrocarbons displace formation water, reaching equilibrium at the gas-water interface:

$$\frac{V_g}{V_w}(\boldsymbol{EPR}) = \frac{[C_i^{asw}]}{Z\left[C_{i(meas)}^{g}\right]} - H \tag{71}$$

where:

$$H = \frac{22400 T_R \rho_w}{1000 \times 273.15\, K_i^M} \tag{72}$$

The EPR model represents a second endmember-like scenario, which assumes that under reservoir conditions, the gas and groundwater phases are in equilibrium. As some noble gases will remain dissolved in the water, theoretically, a larger volume of water should be required than the previous zero-order model to produce the measured concentrations of gas in samples. The minimum volume of water required to produce the measured gas concentrations yields a similar volume in the zero (TGS) and first-order (EPR) models. With both the formation porosity and known proven gas reserves for each field, and the calculated gas-water volumetric ratio, we can estimate the total formation water volume and rock volume. In the Zhaotong gas field, 10^{11} m^3 of gas requires 2.05 x 10^{10} m^3 of water, and a formation with 2.6% porosity would yield a gas-bearing rock volume of 3.85 x 10^{12} m^3. The observed V_g/V_w ratios for these gas samples indicate that, depending on the volume of available water, the system fluctuates between conditions of near-complete gas stripping and equilibrium. Samples demonstrate that ~85%±10% Ar has exsolved from a liquid phase into the gas phase (i.e., only 15%±10% remains in the groundwater phase. This suggests that the noble gas content reflects varying extents of degassing, with some samples approaching equilibrium while others exhibit characteristics of gas stripping, highlighting a dynamic interaction between gas and water phases in the reservoir.

Table 24 – Rock formation volume estimates using average G/W volume ratio estimates for the Sichuan Basin. (1) Liang et al. (2020) (2) Jiao (2019) (3) Wei et al. (2008) and Zhu et al. (2015) (4) Wang (2018) (5)(6) Xu et al. (2020b) (7)(8) Zhang et al. (2021b)

Gas field		Proven gas reserves (m^3)	Porosity (%)	G/W volume ratio	Total water volume (m^3)	Total rock volume (m^3)
Zhaotong	South	1.00 x 10^{11} (1)	2.60(5)	4.87	2.05 x 10^{10}	3.85 x 10^{12}
Changning	South	2.83 x 10^{11} (2)	5.10(6)	0.78	3.63 x 10^{11}	5.55 x 10^{12}
Weiyuan	Central	4.09 x 10^{10} (3)	5.40(7)	1.99	2.06 x 10^{10}	7.57 x 10^{11}
Fuling	East	6.01 x 10^{11} (4)	4.78(8)	3.43	1.75 x 10^{11}	1.26 x 10^{13}

Table 25 – Gas-groundwater volume ratios for zero (TGS) and first-order (EPR) models

.	^{20}Ne		^{36}Ar	
	V_g/V_w (TGS)	V_g/V_w (EPR)	V_g/V_w (TGS)	V_g/V_w (EPR)
Zhaotong gas field				
YS108 H4-3	5.35	5.34	-	-
YS108-H4-1	2.24	2.22	3.86	3.83
YH6-6	5.52	5.51	4.78	4.76
YH7-5	6.44	6.43	4.60	4.57
Weiyuan gas field				
W201H1	0.10	0.09	0.20	0.17
W201	1.29	1.28	2.07	2.04
W201H3	0.98	0.97	23.28	23.25
Changning gas field				
NH13-3	2.69	2.67	-	-
NH13-2	2.38	2.36	4.47	4.45
NH8-2	2.57	2.56	11.78	11.76
NH8-1	0.40	0.38	1.97	1.94
Fuling gas field				
JY57-3	4.56	4.54	4.61	4.59
JY59-4	3.92	3.90	3.99	3.96
JY56-4	1.04	1.03	3.33	3.30
JY63-3	3.57	3.56	4.11	4.08
JY47-3	2.86	2.84	3.34	3.31
JY47-6	3.42	3.40	3.82	3.79
JY52-2	3.54	3.53	1.77	1.74
JY52-1	2.46	2.44	2.56	2.53
JY57-1	4.73	4.71	8.97	8.94
JY36-5	4.02	4.01	2.77	2.74
JY56-6	3.78	3.77	3.85	3.83

2.6.7 Adsorption of noble gases

Investigations into the governing factors that determine the adsorption of methane on shales are ongoing (Hu et al., 2022) and the physical adsorption mechanisms of noble gases in shales and other geological media require further scientific inquiry, owing to growth in shale gas exploration worldwide. Noble gas fractionation that arises due to adsorption is understood to be non-trivial (Paul et al., 2018); as is the magnitude to which adsorption may alter the elemental abundances of Kr and Xe in the subsurface (Phinney, 1972). Similarly, Earth's depletion of atmospheric Xe may be a result of a terrestrial Xe reservoir, due to the potential widespread adsorption of Xe onto sediments (Fanale and Cannon, 1971, Podosek et al., 1981, Bernatowicz and Podosek, 1986, Tolstikhin and O'Nions, 1994, Marrocchi and Marty, 2013). A significant fraction of the heavy noble gases (Kr and Xe) in gas samples is feasibly derived from the desorption of an excess component currently adsorbed and trapped along the surface of hydrocarbon-bearing strata, including shale (Torgersen and Kennedy, 1999).

2.6.7.1 Gas-solid phase interactions due to adsorption

Adsorption, as a type of phase change, has the capacity to dictate the signatures of various noble gas ratios (Ozima and Podosek, 2002). In shales, light and heavy noble gases are more fractionated than in ASW, where solubility is the singular control on noble gas concentrations (Prinzhofer, 2013). The exchange between a solid phase and gas phase occurs when a noble gas collides with a solid substrate and is held by weak molecular forces, thereby being adsorbed. Conversely, desorption occurs when a molecule attains sufficient thermal energy to leave the solid surface of the substrate and return to the gas phase (Ciesla et al., 2018). It is essential to model the influence of adsorption in partitioning noble gases in a residual free-gas phase mixture. We derive a simple model that involves a fixation mechanism to hold free gas along a geological interface, converting it to adsorbed, or 'trapped gas', in a 'solid phase' whereby its contents are proportional to Henry's constants for adsorption. Hereafter, residual noble gas ratios in the remaining free gas phase can be estimated following the removal of these trapped gas particles. The parameters that describe the equilibrium between the sorbent, or the interface of geochemical importance (i.e. shales) and the temporary residence of the noble gas sorbate are well defined by Henry's law, and Henry's constant $\mathcal{K}$, as a function of temperature '*T*' and partial pressure (fugacity) '*P*' in the gas phase. At

sufficiently low pressures, the concentration of gas '*N*', which is adsorbed on a solid surface, follows the linear relationship:

$$N = \mathcal{K}_i P \tag{73}$$

The adsorption behaviour of the noble gases is in accordance with Henry's law for a corresponding set of solubility coefficients, such that Ne, Ar, Kr and Xe can be assigned a constant, $\mathcal{K}_i^{adsorbed}$ value (see Henry's constants, Table 22). Adsorption isotherms for Kr and Xe have been shown to obey Henry's law under experimental conditions (Ianovski et al., 2002) and on various shale samples at relevant temperatures (Fanale and Cannon, 1971, Phinney, 1972) and between a free and sorbed phase (Zhang et al., 2021a). In the subsurface, Henry's law is also likely to be obeyed, as the concentrations of measured Kr and Xe are relatively minor compared to those concentrations of Kr and Xe used in theoretical isothermal lab-based models. Nonetheless, the role of adsorption is still significant, as its effect may be amplified by that of distillation (Marrocchi and Marty, 2013). Subsequently, it is possible to determine the fractionation of the residual isotopic ratios ($^{84}Kr/^{36}Ar$ and $^{132}Xe/^{36}Ar$) in the system, as Kr and Xe are progressively adsorbed, which is a function of the remaining fraction of Ar (^{36}Ar) in the free gas phase, at reservoir conditions:

$$\left({}^{i}/_{[Ar]}\right)_{adsorbed} = \left({}^{i}/_{[Ar]}\right)_{asw} P^{(\alpha-1)} \tag{74}$$

Where '*i*' represents the concentration of a chosen noble gas species (i.e. Ne, Kr or Xe), '*P*' is the fraction of Ar remaining in the free gas phase and 'α' is the fractionation coefficient for an adsorbed gas phase (the ratio between both Henry's adsorption constants), which is given by:

$$\alpha = \left(K_i^{adsorbed} \Big/ K_{Ar}^{adsorbed}\right) \tag{75}$$

Several elemental isotope ratios in the gas phase are considered, which have fractionated from an initial ASW value due to solubility-controlled processes. In principle, adsorption, and the stripping of noble gases from groundwater through batch or Rayleigh fractionation will occur simultaneously, resulting in the potential for a wide range of elemental ratios to be measured. Therefore, we have calculated 'initial' ratios, that mark the starting point from which the heavy noble gases begin to phase change due to adsorption, signifying their removal from a free-gas phase and subsequent partitioning

into a solid phase. These ratios are determined by the extent of prior Ar degassing (% Ar exsolved from the liquid phase) between two distinctive endmember scenarios: 1) a preliminary Ar-depleted gas phase and 2) an Ar-rich gas state (full degassing of water).

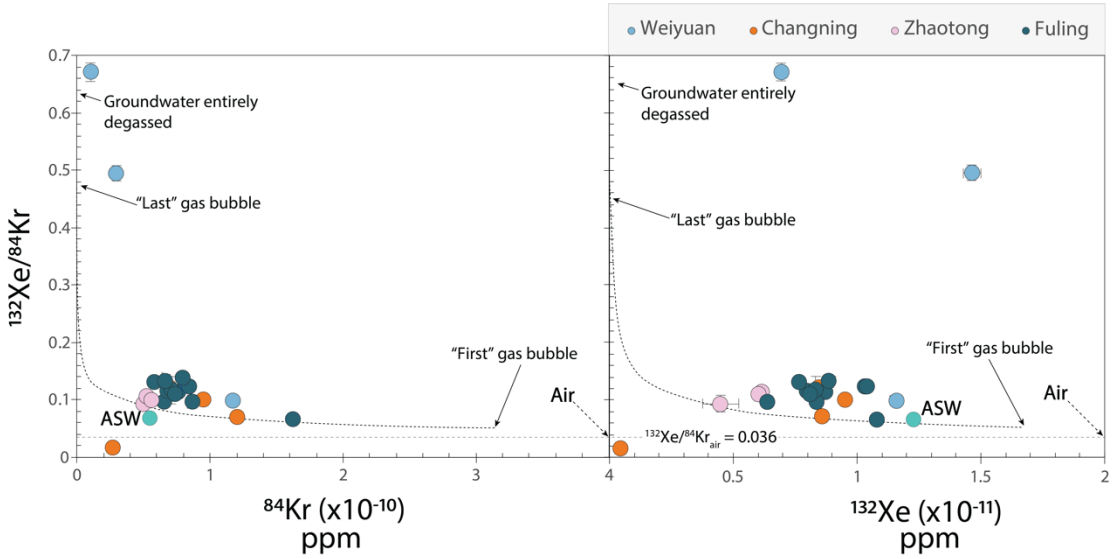

Figure 28 – Air-derived heavy noble gases $^{132}Xe/^{84}Kr$ vs ^{84}Kr concentrations. Weiyuan shale gas samples are highly enriched in Xe and are more fractionated. Air-derived heavy noble gases $^{132}Xe/^{84}Kr$ vs ^{132}Xe concentrations. Almost all of the measured $^{132}Xe/^{84}Kr$ values plot slightly above the predicted values from the solubility-controlled batch fractionation model, however, Weiyuan shale gas samples plot much higher and are more fractionated, potentially due to desorption of Xe back into the gas phase. Concentrations of ^{84}Kr and ^{132}Xe are depleted relative to concentrations in air, where $^{84}Kr_{air}$ = 650 x 10^{-9} and $^{132}Xe_{air}$ = 2.42 x 10^{-8}, and $^{132}Xe/^{84}Kr_{air}$ = 0.036.

2.6.7.2 Fractionation of Kr and Xe due to adsorption

Physical adsorption of Xe onto geological media, the quantity adsorbed and the extent to which these processes may alter Xe signatures is recognised to be non-trivial (Paul et al., 2018). Tight sandstone gas samples show considerable variation in ^{84}Kr and ^{132}Xe concentrations, but very little overall fractionation of $^{132}Xe/^{84}Kr$ ratios (Figure 28). Any linear increase or decrease in ^{84}Kr concentration is accompanied by a similar modification of ^{132}Xe, and paired with the lack of overall variability in $^{132}Xe/^{84}Kr$ ratios reveals the addition and removal of Kr and Xe in these samples occurs due to a common process that is likely adsorption.

The extent solubility-controlled processes, which heavily alter the noble gas isotope signatures in response to reservoir fluxes, implies that it is difficult to resolve the extent to which adsorption and desorption (occurring later, but also primarily due to major changes in reservoir conditions, i.e. gas extraction) has played a role in altering the observable noble gas ratios. The variability of isotopic values due to the adsorption of the heavier noble gases is expected to be comparably minor than the process of Rayleigh and batch fractionation; therefore, if we consider our solubility controlled exsolution ratios as

a starting point for the evolution of an elemental fraction, we expect elemental ratios that deviate slightly towards or away from the solubility controlled exsolution line, which is dependent on the magnitude of subsequent adsorption and desorption. When modelling the adsorption behaviour of noble gases, the lighter species (He and Ne) are known to be much poorer sorbates (Ozima and Podosek, 2002), whilst efficient adsorption of the heavier noble gases is possible due to the molecular size and higher polarisation of Kr and Xe compared to the lighter noble gases. It is therefore more valuable to consider the concentrations of noble gases with a higher mass, namely Kr and more so Xe, which has a higher affinity for adsorption than He, Ne or even Ar.

Henry's constants $(\mathcal{K})$ for adsorption, which are noted in Table 22 can be used to consider the wider geological implications on the flux of heavy noble gases in the subsurface, although there is a distinct lack of study in the literature from which we can draw relevant adsorption coefficients (laboratory sorption experiments, such as Wacker (1989) have shown to include high error margins, Ne 35%, Ar 40%, Kr 16% and Xe 20%). It is possible that the effect of adsorption of Kr and Xe is stronger in nature than what is observed in both the laboratory and in simulations. We should also consider other sediments beside shales (i.e., sandstones) as potential, or even prevalent adsorption interfaces for the removal or addition (desorption) of these noble gases.

2.6.7.3 Adsorption of noble gases in unconventional shale reservoirs

The gas storage capacity resulting from physical adsorption is similarly important to consider. Unconventional reservoirs such as shales describe in-situ petroleum accumulations in low porosity, low permeability, fine-grained, organic rich formations whereby the shale is both the source of and the trap for the natural gas i.e. little to no migration has occurred whilst the drainage radius is also typically minimal in extent. Unconventional shale require significant well stimulation such as hydraulic fracturing to boost productivity and become economically viable, although when water is present, adsorption capacity may be significantly reduced as H_2O molecules occupy adsorption sites. Some considerations and generalisations have been made in our model insofar as; we assume that the shale is uniformly efficient at trapping gas with a finite adsorption capacity (Langmuir, 1918), and factors such as TOC variability, clay mineralogy and variation in organic matter, which play an important role in the distribution and trapping of noble gases adsorbed on nanopore scales are laterally homogenous across the extent of the sampled wells. Therefore, this model represents an ideal scenario, which attempts to describe the variable partitioning of noble gases due to adsorption.

2.6.7.4 Efficiency of noble gas adsorption due to shale characteristics

Noble gas adsorption occurs much more rapidly than gas diffusion over macroscopic distances (Paul et al., 2018), while laboratory-based observations have shown rates of desorption (τ) for noble gases to increase with temperature, a function of depth. Fractionation of noble gases due to adsorption are therefore unlikely to be indicative of fluid or gas residence time due to the rapid rate at which it occurs on geological timescales. Efficiency of adsorption and desorption is also dependent on rock mineralogy with which clay minerals and organic matter constitute the primary adsorbents. Total organic carbon (TOC) is a key parameter that affects adsorption rate and the total adsorption capacity of shale, as surface area and micropore volume is intrinsically linked to the presence of organic matter (Tian et al., 2016). The Wufeng-Longmaxi shales are mainly composed of quartz, clay, calcite, dolomite, plagioclase and pyrite (Qiu and Zou, 2019) and have the requisite qualities to efficiently trap a large proportion of Kr and Xe, as well as TOC of up between 6-8 wt% (Liu et al., 2020b). In high pressure environments, prominent desorption has been shown to stimulate an increase in shale permeability (Guo et al., 2017), which is conducive to economic shale gas development and enhancing overall recovery. Therefore, resolving the magnitude of noble gas desorption, by calculating the extent to which Xe is measured in excess of ASW, could reveal potential targets where shale permeability has variably improved.

Following drilling, pumping of water and expulsion of natural gas reserves, a previously trapped adsorbed 'solid phase' gas could desorb leading to a perceived enrichment of heavy noble gases in the production well, and this could explain the relative excess observed in some gas samples. Increased desorption efficiency will lead to an almost immediate, measurable excess of Xe relative to ASW. There is a clear enrichment in Xe, as the $^{132}Xe/^{84}Kr$ ratios in samples are in excess (~200%) of the predicted range defined by the solubility controlled exsolution line, with the initial value determined by the volume of Kr and Xe introduced into the system at recharge (Figure 29).

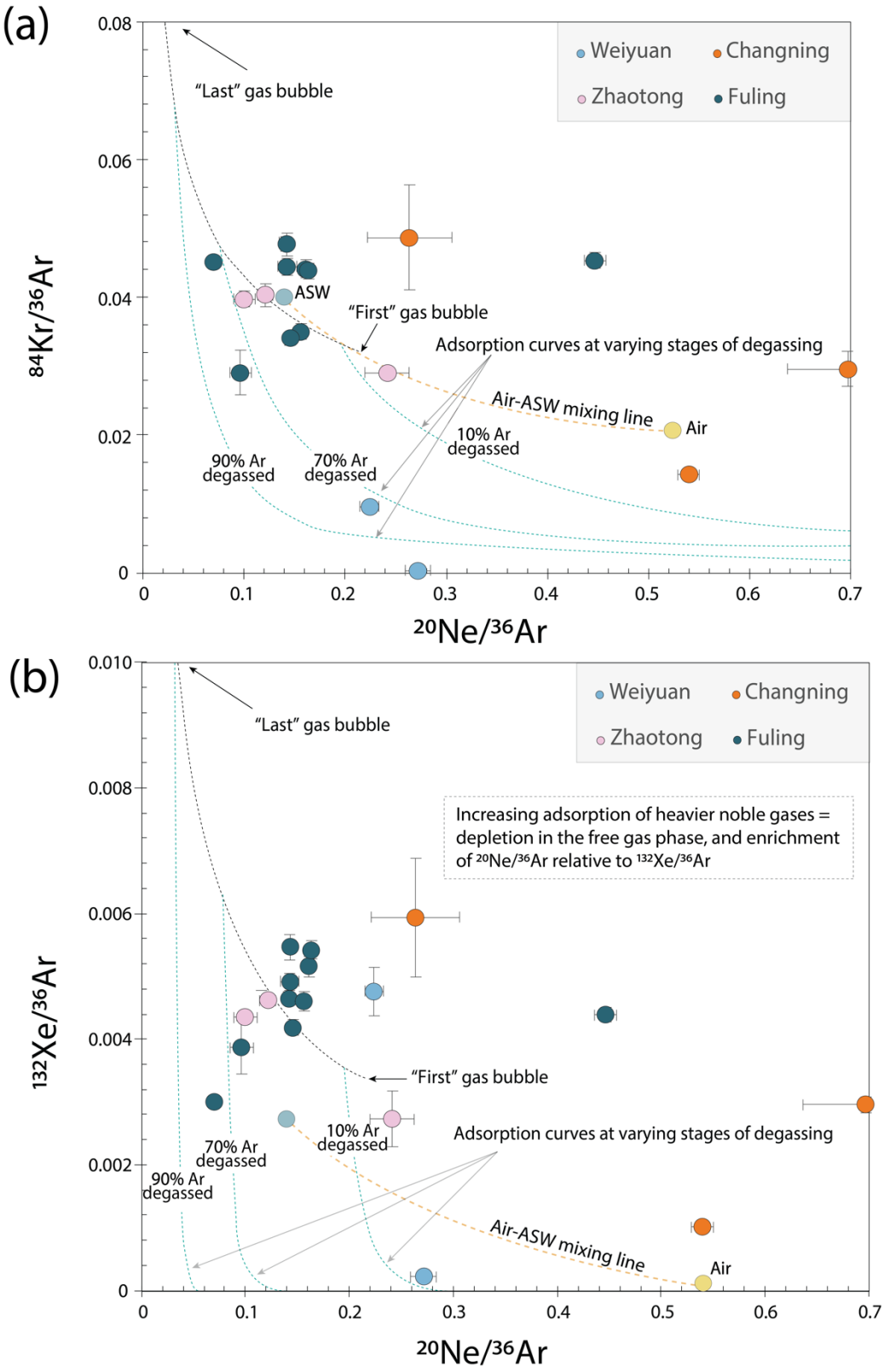

Figure 29 - Evolution of atmosphere-derived noble gases $^{20}Ne/^{36}Ar$ vs (a) $^{84}Kr/^{36}Ar$ and (b) $^{132}Xe/^{36}Ar$. The dotted line (black) represents the expected solubility-dependent fractionation in the gas phase. The Air-ASW mixing line (yellow) signifies mixing between air and ASW endmembers. Modelled adsorption lines (blue) and associated noble gas elemental ratios evolve dependent on the extent of prior Ar degassing (10%, 70% and 90% for this model). The 'first' and 'last' gas bubbles reflect the expected isotope ratios during 'early' and 'late' degassing, and at each intermediary stage of gas loss. Initial gas bubbles are enriched in lighter, less soluble noble gases and final gas bubbles are depleted in Ne, and Kr/Xe enriched.

2.6.7.5 Excess Kr and Xe

Due to this measured enrichment of Kr and Xe, it is thereby possible to modify the fractionation curve to account for this 200% Xe excess, and gas samples appear to fit this adjustment to the batch fractionation model reasonably well (Figure 30). As Xe is the most soluble and has the highest affinity for adsorption of the noble gases, it tends to remain in solution or become adsorbed, and therefore only an insignificant volume will remain in a free gas phase until the requisite conditions for desorption occur. If Kr and Xe are in excess, or their elemental ratios are altered due to adsorption, the volumetric gas-water ratios (V_g/V_w) calculated will be unreliable for both noble gases and as a result the extent of gas-water interaction in the volumetric groundwater-gas models (TGS and EPR) described above only consider He and Ne. It has been posited the interaction of noble gases with an oil phase can result in the perceived enrichments of these heavy noble gas species, however the Wufeng-Longmaxi black shale gases are overly mature and are less likely to have come into direct contact with an oil phase having already undergone secondary cracking.

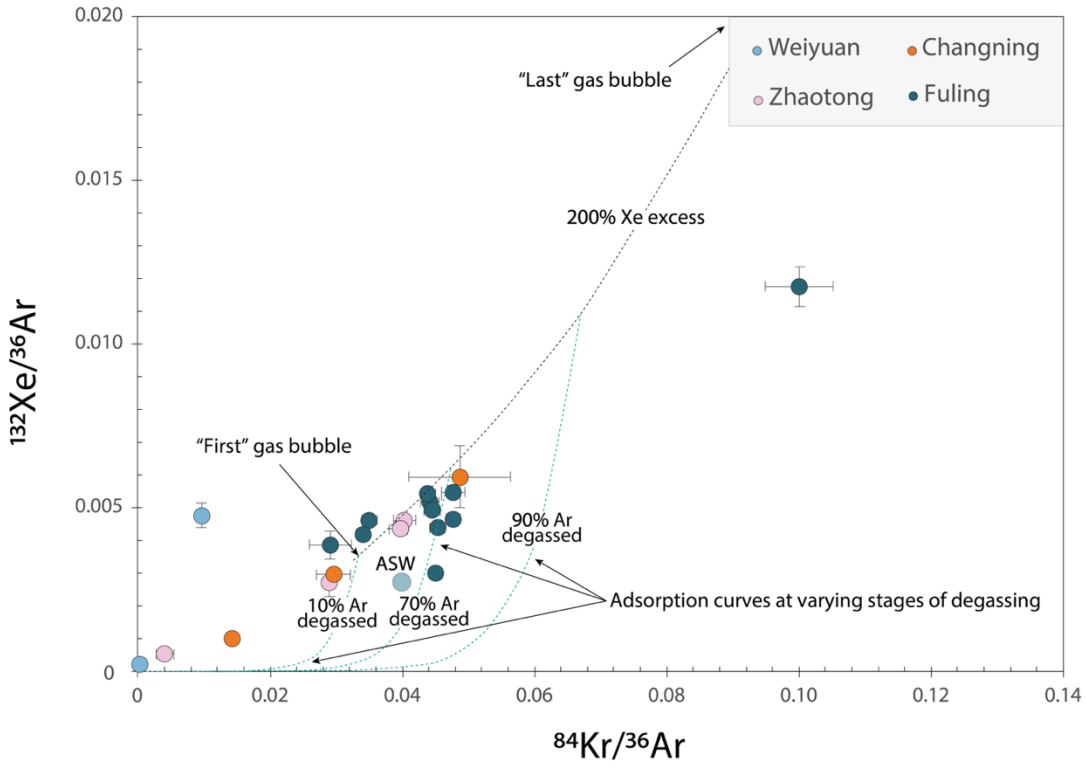

Figure 30 – Air-derived heavy noble gas ratios $^{132}Xe/^{36}Ar$ vs $^{84}Kr/^{36}Ar$. The data fits a batch fractionation curve, modified for a 200% excess Xe component. Representing remaining elemental ratios in the free gas phase. As progressive degassing of Ar ensues, elemental ratios of the heavier ^{84}Kr and ^{132}Xe increase exponentially as more is partitioned into the gas phase. A linear increase in ^{132}Xe and ^{84}Kr concentrations in tight sandstone gas samples occurs at a different rate from shale gas samples.

2.6.7.6 Three-phase volume model for describing noble gas partitioning

While adsorption alone likely does not account for the entire abundance of xenon, even using conservative estimates, at least one-third of Xe along the pore matrix can be considered to be in the adsorbed phase (Paul et al., 2018). These noble gases exist between three thermodynamic states in geological reservoirs: adsorbed gas, free gas and gas in solution. The contribution of water, oil and various other gas species (C_2H_6, C_3H_8, CO_2, N_2, etc.) affect overall adsorption behaviour (Chen et al., 2021a). Nonetheless, equilibration with water is a primary control on the impact of adsorption on noble gas ratios, as water content generally reduces the adsorption capacity of shale. This idea can be represented in a simple mass balance equation comprising these three-phases:

$$\boldsymbol{G_{total} = G_{adsorbed} + G_{free} + G_{solution}} \quad (76)$$

The isotope ratios of the noble gases sampled reflects the partitioning of gases remaining in the free gas phase (G_{free}), whereby its isotopic signature has been partially altered by a dissolved component ($G_{solution}$), which is a function of solubility, and by a variable amount of heavy noble gases adsorbed onto a substrate, i.e., a geological interface such as shale ($G_{adsorbed}$). We consider the low porosity-permeability Wufeng-Longmaxi shale a closed batch system, where there is very little to no gas loss, and limited water availability ($V_g > V_w$). It is reasonable to assume that these noble gases remain in a steady-state equilibrium between these three phases (Figure 31). Therefore, in the Changning, Zhaotong, Weiyuan and Fuling gas fields, the total volume of noble gases in the system remains constant (G_{total}). Within a singular pore cavity, where there exists a gas-liquid contact, the noble gases fractionate, successively degassing the lighter, less soluble noble gases until an equilibrium is reached. Heavier noble gases (Kr and Xe) in the free gas phase will preferentially adsorb due to their ionisation energies. Kr and Xe sorbate molecules are then bound to the sorbent surface until the energy required to overcome these forces is reached, which then commences desorption back into a free gas phase or dissolution back into water. The exchange between this free gas phase and 'solid' adsorbed phase, and the extent of pore-water degassing is illustrated by determining how much dissolved Ar remains in the liquid phase, i.e., when 50% Ar is remaining in water, what is the resulting modification of Kr and Xe concentrations due to adsorption.

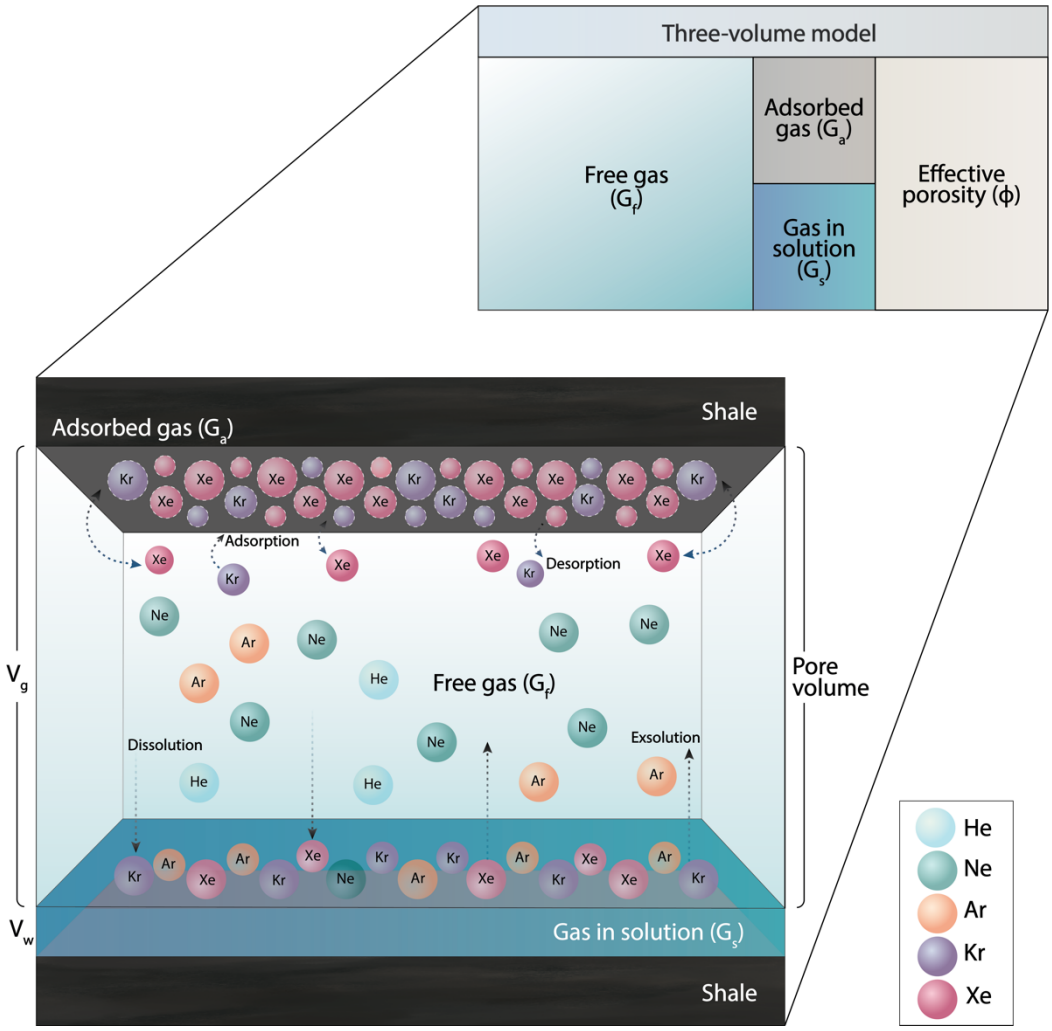

Figure 31 – Conceptual model of a closed system showing the nano-scale equilibrium between the three phases; an adsorbed 'solid phase' gas, free gas, and a dissolved component (gas in solution).

The rate of adsorption between Kr and Xe differs greatly; $^{84}Kr/^{36}Ar$ adsorption is more gradual, and has a mass closer to that of Ar, $^{84}Kr/^{36}Ar$ partitions more slowly into an adsorbed phase, adsorption of Kr begins when ~30% of Ar has exsolved. ^{132}Xe adsorption commences when more than 90% of Ar has exsolved and reaches maximum saturation during the final 10% of Ar gas stripping, and around 20% of $^{132}Xe/^{36}Ar$ and $^{84}Kr/^{36}Ar$ is comprised of an adsorbed component by the time Ar is fully degassed.

2.7 Concluding remarks

Unconventional shale gases have proven to be valuable economic resources worldwide, and the pioneering application of noble gas isotope geochemistry in these areas has improved our understanding of the complex factors that control subsurface fluid interactions and the fluxes between gases sourced from air and crustal endmembers.

We investigate noble gas signatures across four unique gas fields within the Sichuan basin with distinct generation, migration, and accumulation histories. Open (via Rayleigh fractionation) vs. closed (via batch fractionation) system behaviour has been assessed, quantification of gas-groundwater volume ratios, and evaluation of the principal factors governing noble gas isotope fractionation in these unconventional gas reservoirs has been carried out. In unconventional shale gases, where the gas has been generated in-situ, there exists a variable mixture of ASW and crustal derived noble gases. Shale gas reservoirs have R/R_a values that are strongly crustal (0.0037-0.038 R_a). There appears to be agreement with solubility-based batch fractionation models to justify the extent of fractionation in the lighter noble gases (Ne and Ar). Air-derived $^{20}Ne/^{36}Ar$ ratios that have values in excess of the model line for solubility-controlled exsolution and are enriched in lighter Ne with respect to ASW, are likely to have undergone redissolution or effervescence of noble gases back into water, potentially due to a change in physical conditions such as an increase in pressure during burial. We believe at least two processes are responsible for the measured heavy noble gas inventory, as air-derived $^{20}Ne/^{36}Ar$ ratios do not correlate strongly with air-derived $^{132}Xe/^{36}Ar$ ratios and therefore migration and the influence of atmosphere-equilibrated groundwaters is not likely to be the primary control on the amount of residual Xe. Using a model derived from Henry's law which utilises Henry's constants for Kr and Xe adsorption, this mode of fractionation and the perceived excess can indeed be attributed to adsorption and trapping of heavy noble gases, which cannot be accounted for by solubility-controlled processes alone. Due to the burial history and organic matter type, we also disregard interaction with an oil phase as a possible Kr and Xe enrichment mechanism.

There are implications for gas exploration in China as burgeoning new technologies increase the production efficiency of previously unreachable gas reserves in low porosity, low permeability shales. Modelling noble gas adsorption behaviour still has many uncertainties due to larger-scale formation heterogeneities and nanoscale pore differences; however, further study into this field may indeed aid in defining the extent of previously unattainable shale gas reserves and to better understand how their abundances are altered by an adsorbed 'solid phase'. The extent to which formation heterogeneity modifies adsorption capacity cannot be accounted for until better adsorption models are developed (Babatunde et al., 2022). Gas samples V_g/V_w ratios define the extent of interaction with groundwaters, and as the amount of available water increases, the

adsorption capacity of Xe onto shale is hindered, indicating that contact with a water volume plays a critical role in controlling the degree of Xe adsorption in the system. By better constraining the genetic source and phase interactions amongst groundwater, gas and adsorbed gas components, this dataset yields a valuable tool to effectively guide the exploration and development of further unconventional resources in the region.

MANUSCRIPT 1 REFERENCES

Aregbe, Y., Valkiers, S., Mayer, K., De Bièvre, P., 1996. Comparative isotopic measurements on xenon and krypton. International Journal of Mass Spectrometry and Ion Processes 153(1), L1-L5. doi.org/https://doi.org/10.1016/0168-1176(96)04368-6.

Babatunde, K.A., Negash, B.M., Jufar, S.R., Ahmed, T.Y., Mojid, M.R., 2022. Adsorption of gases on heterogeneous shale surfaces: A review. Journal of Petroleum Science and Engineering 208, 109466. doi.org/https://doi.org/10.1016/j.petrol.2021.109466.

Ballentine, C.J., Burgess, R., Marty, B., 2002. Tracing Fluid Origin, Transport and Interaction in the Crust. Reviews in Mineralogy and Geochemistry 47(1), 539-614. doi.org/10.2138/rmg.2002.47.13.

Ballentine, C.J., Burnard, P.G., 2002. Production, Release and Transport of Noble Gases in the Continental Crust. Reviews in Mineralogy and Geochemistry 47(1), 481-538. doi.org/10.2138/rmg.2002.47.12.

Barry, P.H., Lawson, M., Meurer, W.P., Warr, O., Mabry, J.C., Byrne, D.J., Ballentine, C.J., 2016. Noble gases solubility models of hydrocarbon charge mechanism in the Sleipner Vest gas field. Geochimica et Cosmochimica Acta 194, 291-309. doi.org/https://doi.org/10.1016/j.gca.2016.08.021.

Benson, B.B., Krause, D., Jr., 1976. Empirical laws for dilute aqueous solutions of nonpolar gases. The Journal of Chemical Physics 64(2), 689-709. doi.org/10.1063/1.432215.

Bernatowicz, T.J., Podosek, F.A., 1986. Adsorption and isotopic fractionation of Xe. Geochimica et Cosmochimica Acta 50(7), 1503-1507. doi.org/https://doi.org/10.1016/0016-7037(86)90324-8.

Borjigin, T., Shen, B., Yu, L., Yunfeng, Y., Zhang, W., Cheng, T., Xi, B., Zhang, Q., Bao, F., Qin, J., 2017. Mechanisms of shale gas generation and accumulation in the Ordovician Wufeng-Longmaxi Formation, Sichuan Basin, SW China. Petroleum Exploration and Development 44, 69-78.

Byrne, D.J., Barry, P.H., Lawson, M., Ballentine, C.J., 2020. The use of noble gas isotopes to constrain subsurface fluid flow and hydrocarbon migration in the East Texas Basin. Geochimica et Cosmochimica Acta 268, 186-208. doi.org/https://doi.org/10.1016/j.gca.2019.10.001.

Chen, G., Li, C., Lu, S., Guo, T., Wang, M., Xue, Q., Zhang, T., Li, Z., Sun, Y., Liu, J., Jiang, S., 2021. Critical factors controlling adsorption capacity of shale gas in Wufeng-Longmaxi formation, Sichuan Basin: Evidences from both experiments and molecular simulations. Journal of Natural Gas Science and Engineering 88, 103774. doi.org/https://doi.org/10.1016/j.jngse.2020.103774.

Chen, K., Li, J., Tang, X., Shen, J., Wang, P., Peng, J., Meng, J., 2021. Key geological factors for shale gas accumulation in the Wufeng–Longmaxi Fms in the central Yangtze area. Natural Gas Industry B 8(1), 1-12. doi.org/https://doi.org/10.1016/j.ngib.2020.06.001.

Ciesla, F.J., Krijt, S., Yokochi, R., Sandford, S., 2018. The Efficiency of Noble Gas Trapping in Astrophysical Environments. The Astrophysical Journal 867(2), 146.

Craig, H., Lupton, J.E., 1976. Primordial neon, helium, and hydrogen in oceanic basalts. Earth and Planetary Science Letters 31(3), 369-385. doi.org/https://doi.org/10.1016/0012-821X(76)90118-7.

Crovetto, R., Fernández-Prini, R., Japas, M.L., 1982. Solubilities of inert gases and methane in H2O and in D2O in the temperature range of 300 to 600 K. The Journal of Chemical Physics 76(2), 1077-1086. doi.org/10.1063/1.443074.

Dai, J., Ni, Y., Qin, S., Huang, S., Peng, W., Han, W., 2018. Geochemical characteristics of ultra-deep natural gas in the Sichuan Basin, SW China. Petroleum Exploration and Development 45(4), 619-628. doi.org/https://doi.org/10.1016/S1876-3804(18)30067-3.

Dai, J., Zou, C., Dong, D., Ni, Y., Wu, W., Gong, D., Wang, Y., Huang, S., Huang, J., Fang, C., Liu, D., 2016. Geochemical characteristics of marine and terrestrial shale gas in China. Marine and Petroleum Geology 76, 444-463. doi.org/https://doi.org/10.1016/j.marpetgeo.2016.04.027.

Dai, J., Zou, C., Liao, S., Dong, D., Ni, Y., Huang, J., Wu, W., Gong, D., Huang, S., Hu, G., 2014. Geochemistry of the extremely high thermal maturity Longmaxi shale gas, southern Sichuan Basin. Organic Geochemistry 74, 3-12. doi.org/https://doi.org/10.1016/j.orggeochem.2014.01.018.

Fan, C., Li, H., Qin, Q., He, S., Zhong, C., 2020. Geological conditions and exploration potential of shale gas reservoir in Wufeng and Longmaxi Formation of southeastern Sichuan Basin, China. Journal of Petroleum Science and Engineering 191, 107138. doi.org/https://doi.org/10.1016/j.petrol.2020.107138.

Fanale, F.P., Cannon, W.A., 1971. Physical adsorption of rare gas on terrigenous sediments. Earth and Planetary Science Letters 11, 362-368. doi.org/10.1016/0012-821x(71)90195-6.

Feng, Z., Dong, D., Tian, J., Wu, W., Cai, Y., Shi, Z., Peng, W., 2019. Geochemical characteristics of Lower Silurian shale gas in the Changning-Zhaotong exploration blocks, southern periphery of the Sichuan Basin. Journal of Petroleum Science and Engineering 174, 281-290. doi.org/https://doi.org/10.1016/j.petrol.2018.11.022.

Guo, W., Hu, Z., Zhang, X., Yu, R., Wang, L., 2017. Shale gas adsorption and desorption characteristics and its effects on shale permeability. Energy Exploration & Exploitation 35(4), 463-481.

Hamme, R.C., Emerson, S.R., 2004. The solubility of neon, nitrogen and argon in distilled water and seawater. Deep Sea Research Part I: Oceanographic Research Papers 51(11), 1517-1528.

Hannigan, R.E., Basu, A.R., 1998. Late diagenetic trace element remobilization in organic-rich black shales of the taconic foreland basin of Quebec, Ontario and New York.

Hu, D., Zhang, H., Ni, K., Yu, G., 2014. Main controlling factors for gas preservation conditions of marine shales in southeastern margins of the Sichuan Basin. Natural Gas Industry 34, 17-23. doi.org/10.3787/j.issn.1000-0976.2014.06.003.

Hu, X., Li, R., Ming, Y., Deng, H., 2022. Insights into shale gas adsorption and an improved method for characterizing adsorption isotherm from molecular perspectives. Chemical Engineering Journal 431, 134183. doi.org/https://doi.org/10.1016/j.cej.2021.134183.

Huang, H., He, D., Li, Y., Li, J., Zhang, L., 2018. Silurian tectonic-sedimentary setting and basin evolution in the Sichuan area, southwest China: Implications for palaeogeographic reconstructions. Marine and Petroleum Geology 92, 403-423. doi.org/https://doi.org/10.1016/j.marpetgeo.2017.11.006.

Hunt, A., Darrah, T., J. Poreda, R., 2012. Determining the source and genetic fingerprint of natural gases using noble gas geochemistry: A northern Appalachian Basin case study. AAPG Bulletin 96, 1785-1811. doi.org/10.1306/03161211093.

Ianovski, D., Munakata, K., Kanjo, S., Yokoyama, Y., Koga, A., Yamatsuki, S., Tanaka, K., Fukumatsu, T., Nishikawa, M., Igarashi, Y., 2002. Adsorption of Noble Gases on H-Mordenite. Journal of Nuclear Science and Technology - J NUCL SCI TECHNOL 39, 1213-1218. doi.org/10.1080/18811248.2002.9715313.

IEA, 2016. Energy Supply and Consumption Revolution Strategy (2016-2030). International Energy Agency.

IEA, 2019. Global Gas Security Review 2019, International Energy Agency, Paris.

Jenden, P.D., Hilton, D., Kaplan, I., Craig, H., Howell, D., 1993. Abiogenic hydrocarbons and mantle helium in oil and gas fields. US Geological survey professional paper 1570(1), 31-56.

Jiang, S., Tang, X., Cai, D., Xue, G., He, Z., Long, S., Peng, Y., Gao, B., Xu, Z., Dahdah, N., 2017. Comparison of marine, transitional, and lacustrine shales: A case study from the Sichuan Basin in China. Journal of Petroleum Science and Engineering 150, 334-347. doi.org/https://doi.org/10.1016/j.petrol.2016.12.014.

Jiao, F., 2019. Theoretical insights, core technologies and practices concerning "volume development" of shale gas in China. Natural Gas Industry B 6(6), 525-538. doi.org/https://doi.org/10.1016/j.ngib.2019.05.001.

Jin, Z., Nie, H., Liu, Q., Zhao, J., Jiang, T., 2018. Source and seal coupling mechanism for shale gas enrichment in upper Ordovician Wufeng Formation - Lower Silurian Longmaxi Formation in Sichuan Basin and its periphery. Marine and Petroleum Geology 97, 78-93. doi.org/https://doi.org/10.1016/j.marpetgeo.2018.06.009.

Kimura, H., Watanabe, Y., 2001. Oceanic anoxia at the Precambrian-Cambrian boundary. Geology 29(11), 995-998.

Kipfer, R., Aeschbach-Hertig, W., Peeters, F., Stute, M., 2002. Noble Gases in Lakes and Ground Waters. Reviews in Mineralogy and Geochemistry 47(1), 615-700. doi.org/10.2138/rmg.2002.47.14.

Klemme, H., Ulmishek, G., 1991. Effective Petroleum Source Rocks of the World: Stratigraphic Distribution and Controlling Depositional Factors. Aapg Bulletin - AAPG BULL 75, 1809-1851. doi.org/10.1306/0C9B2A47-1710-11D7-8645000102C1865D.

Lee, J.-Y., Marti, K., Severinghaus, J.P., Kawamura, K., Yoo, H.-S., Lee, J.B., Kim, J.S., 2006. A redetermination of the isotopic abundances of atmospheric Ar. Geochimica et Cosmochimica Acta 70(17), 4507-4512. doi.org/https://doi.org/10.1016/j.gca.2006.06.1563.

Li, Y., He, D., Chen, L., Mei, Q., Li, C., Zhang, L., 2016. Cretaceous sedimentary basins in Sichuan, SW China: Restoration of tectonic and depositional environments. Cretaceous Research 57, 50-65. doi.org/https://doi.org/10.1016/j.cretres.2015.07.013.

Li, Y., Tootell, D., Holland, G., Zhou, Z., 2021. Performance of the NGX High-Resolution Multiple Collector Noble Gas Mass Spectrometer. Geochemistry, Geophysics, Geosystems 22(11), e2021GC009997. doi.org/https://doi.org/10.1029/2021GC009997.

Li, Y., Zhang, T., Ellis, G.S., Shao, D., 2017. Depositional environment and organic matter accumulation of Upper Ordovician–Lower Silurian marine shale in the Upper Yangtze Platform, South China. Palaeogeography, Palaeoclimatology, Palaeoecology 466, 252-264. doi.org/https://doi.org/10.1016/j.palaeo.2016.11.037.

Liang, X., Xu, Z., Zhang, Z., Wang, W., Zhang, J., Lu, H., Zhang, L., Zou, C., Wang, G., Mei, J., Rui, Y., 2020. Breakthrough of shallow shale gas exploration in Taiyang anticline area and its significance for resource development in Zhaotong, Yunnan Province, China. Petroleum Exploration and Development 47(1), 12-29. doi.org/https://doi.org/10.1016/S1876-3804(20)60002-7.

Liu, R., Wen, T., Amalberti, J., Zheng, J., Hao, F., Jiang, D., 2021. The dichotomy in noble gas signatures linked to tectonic deformation in Wufeng-Longmaxi Shale, Sichuan Basin. Chemical Geology 581, 120412. doi.org/https://doi.org/10.1016/j.chemgeo.2021.120412.

Ma, X., 2017a. A golden era for natural gas development in the Sichuan Basin. Natural Gas Industry B 4(3), 163-173. doi.org/10.1016/j.ngib.2017.08.001.

Ma, X., 2017b. Natural gas and energy revolution: A case study of Sichuan–Chongqing gas province. Natural Gas Industry B 4(2), 91-99. doi.org/https://doi.org/10.1016/j.ngib.2017.07.014.

Marrocchi, Y., Marty, B., 2013. Experimental determination of the xenon isotopic fractionation during adsorption. Geophysical Research Letters 40, 4165-4170. doi.org/10.1002/grl.50845.

Mazor, E., Fournier, R., 1973. More on noble gases in Yellowstone National Park hot waters. Geochimica et Cosmochimica Acta 37(3), 515-525.

Mengshu, S., Yuansheng, H., Xiaofeng, X., Dunnan, L., 2021. China's coal consumption forecasting using adaptive differential evolution algorithm and support vector machine. Resources Policy 74, 102287. doi.org/https://doi.org/10.1016/j.resourpol.2021.102287.

Ni, Y., Dai, J., Tao, S., Wu, X., Liao, F., Wu, W., Zhang, D., 2014. Helium signatures of gases from the Sichuan Basin, China. Organic Geochemistry 74, 33-43. doi.org/https://doi.org/10.1016/j.orggeochem.2014.03.007.

Nie, H., Chen, Q., Zhang, G., Sun, C., Wang, P., Lu, Z., 2021. An overview of the characteristic of typical Wufeng–Longmaxi shale gas fields in the Sichuan Basin, China. Natural Gas Industry B. doi.org/https://doi.org/10.1016/j.ngib.2021.04.001.

Nie, H., Li, D., Liu, G., Lu, Z., Hu, W., Wang, R., Zhang, G., 2020. An overview of the geology and production of the Fuling shale gas field, Sichuan Basin, China. Energy Geoscience 1(3), 147-164. doi.org/https://doi.org/10.1016/j.engeos.2020.06.005.

Ozima, M., Podosek, F., 2002. Noble Gas Geochemistry. Noble Gas Geochemistry, by Minoru Ozima and Frank A. Podosek, pp. 300. ISBN 0521803667. Cambridge, UK: Cambridge University Press, December 2001. 367.

Paul, M.J., Biegalski, S.R., Haas, D.A., Jiang, H., Daigle, H., Lowrey, J.D., 2018. Xenon adsorption on geological media and implications for radionuclide signatures. Journal of Environmental Radioactivity 187, 65-72. doi.org/https://doi.org/10.1016/j.jenvrad.2018.01.029.

Pepin, R.O., 2000. On the Isotopic Composition of Primordial Xenon in Terrestrial Planet Atmospheres, in: Benz, W., Kallenbach, R., Lugmair, G.W. (Eds.), From Dust to Terrestrial Planets. Springer Netherlands, Dordrecht, pp. 371-395.

Peucker-Ehrenbrink, B., Hannigan, R., 2000. Effects of black shale weathering on the mobility of rhenium and platinum group elements. Geology 28. doi.org/10.1130/0091-7613(2000)28<475:EOBSWO>2.0.CO.

Phinney, D., 1972. 36Ar, Kr, and Xe in terrestrial materials. Earth and Planetary Science Letters 16(3), 413-420.

Podosek, F.A., Bernatowicz, T.J., Kramer, F.E., 1981. Adsorption of xenon and krypton on shales. Geochimica et Cosmochimica Acta 45(12), 2401-2415. doi.org/https://doi.org/10.1016/0016-7037(81)90094-6.

Porcelli, D., Ballentine, C., Wieler, R., 2002. An Overview of Noble Gas Geochemistry and Cosmochemistry. Reviews in Mineralogy & Geochemistry - REV MINERAL GEOCHEM 47, 1-19. doi.org/10.2138/rmg.2002.47.1.

Potter, R.W., Clynne, M.A., 1978. The solubility of the noble gases He, Ne, Ar, Kr, and Xe in water up to the critical point. Journal of Solution Chemistry 7(11), 837-844. doi.org/10.1007/BF00650811.

Prinzhofer, A., 2013. Noble Gases in Oil and Gas Accumulations, in: Burnard, P. (Ed.) The Noble Gases as Geochemical Tracers. Springer Berlin Heidelberg, Berlin, Heidelberg, pp. 225-247. doi.org/10.1007/978-3-642-28836-4_9.

Pu, B., Jiang, Y., Wang, Y., Bao, S., Liu, X., 2010. Reservoir-forming conditions and favorable exploration zones of shale gas in Lower Silurian Longmaxi Formation of Sichuan Basin. Acta Petrolei Sinica 31(2), 225-230. doi.org/10.7623/syxb201002008.

Qiu, Z., Zou, C., 2019. Controlling factors on the formation and distribution of "sweet-spot areas" of marine gas shales in South China and a preliminary discussion on unconventional petroleum sedimentology. Journal of Asian Earth Sciences, 103989. doi.org/https://doi.org/10.1016/j.jseaes.2019.103989.

Sander, R., 2015. Compilation of Henry's law constants (version 4.0) for water as solvent. Atmos. Chem. Phys. 15(8), 4399-4981. doi.org/10.5194/acp-15-4399-2015.

Shangbin, C., Yanming, Z., Si, C., Yufu, H., Changqing, F., Junhua, F., 2017. Hydrocarbon generation and shale gas accumulation in the Longmaxi Formation, Southern Sichuan Basin, China. Marine and Petroleum Geology 86, 248-258. doi.org/https://doi.org/10.1016/j.marpetgeo.2017.05.017.

Stevens, S.H., Moodhe, K.D., Kuuskraa, V.A., 2013. China shale gas and shale oil resource evaluation and technical challenges, SPE Asia Pacific Oil and Gas Conference and Exhibition. SPE, pp. SPE-165832-MS.

Tian, H., Li, T., Zhang, T., Xiao, X., 2016. Characterization of methane adsorption on overmature Lower Silurian–Upper Ordovician shales in Sichuan Basin, southwest China: Experimental results and geological implications. International Journal of Coal Geology 156, 36-49. doi.org/https://doi.org/10.1016/j.coal.2016.01.013.

Tolstikhin, I.N., O'Nions, R.K., 1994. The Earth's missing xenon: A combination of early degassing and of rare gas loss from the atmosphere. Chemical Geology 115(1), 1-6. doi.org/https://doi.org/10.1016/0009-2541(94)90142-2.

Torgersen, T., 1980. Controls on pore-fluid concentration of 4He and 222Rn and the calculation of 4He/222Rn ages. Journal of Geochemical Exploration 13(1), 57-75. doi.org/https://doi.org/10.1016/0375-6742(80)90021-7.

Torgersen, T., Kennedy, B.M., 1999. Air-Xe enrichments in Elk Hills oil field gases: role of water in migration and storage. Earth and Planetary Science Letters 167(3), 239-253. doi.org/https://doi.org/10.1016/S0012-821X(99)00021-7.

Wacker, J.F., 1989. Laboratory simulation of meteoritic noble gases. III. Sorption of neon, argon, krypton, and xenon on carbon: Elemental fractionation. Geochimica et Cosmochimica Acta 53(6), 1421-1433.

Wang, G., Jin, Z., Liu, G., Liu, Q., Liu, Z., Wang, H., Liang, X., Jiang, T., Wang, R., 2020. Geological implications of gamma ray (GR) anomalies in marine shales: A case study of the Ordovician-Silurian Wufeng-Longmaxi succession in the Sichuan Basin and its periphery, Southwest China. Journal of Asian Earth Sciences 199, 104359. doi.org/https://doi.org/10.1016/j.jseaes.2020.104359.

Wang, X., Liu, W., Li, X., Liu, Q., Tao, C., Xu, Y., 2020. Radiogenic helium concentration and isotope variations in crustal gas pools from Sichuan Basin, China. Applied Geochemistry 117, 104586. doi.org/https://doi.org/10.1016/j.apgeochem.2020.104586.

Wang, Z., 2018. Reservoir forming conditions and key exploration and development technologies for marine shale gas fields in Fuling area, South China. Petroleum Research 3(3), 197-209. doi.org/https://doi.org/10.1016/j.ptlrs.2018.06.008.

Wang, Z.-c., Zhao, W.-z., Li, Z.-y., Jiang, X.-f., Li, J., 2008. Role of basement faults in gas accumulation of Xujiahe Formation, Sichuan Basin. Petroleum Exploration and Development 35(5), 541-547. doi.org/https://doi.org/10.1016/S1876-3804(09)60087-2.

Wei, G., Chen, G., Du, S., Zhang, L., Yang, W., 2008. Petroleum systems of the oldest gas field in China: Neoproterozoic gas pools in the Weiyuan gas field, Sichuan Basin. Marine and Petroleum Geology 25(4), 371-386. doi.org/https://doi.org/10.1016/j.marpetgeo.2008.01.009.

Wood, D., Caputi, R., 1966. Solubilities of Kr and Xe in fresh and sea water. (No Title).

Xiao, B., Liu, S., Li, Z., Ran, B., Ye, Y., Yang, D., Li, J., 2021. Geochemical characteristics of marine shale in the Wufeng Formation–Longmaxi Formation in the northern Sichuan Basin, South China and its implications for depositional controls on organic matter. Journal of Petroleum Science and Engineering 203, 108618. doi.org/https://doi.org/10.1016/j.petrol.2021.108618.

Xu, C., Jia-yu, R., Yue, L., Boucot, A.J., 2004. Facies patterns and geography of the Yangtze region, South China, through the Ordovician and Silurian transition. Palaeogeography, Palaeoclimatology, Palaeoecology 204(3), 353-372. doi.org/https://doi.org/10.1016/S0031-0182(03)00736-3.

Xu, Z., Liang, X., Lu, H., Zhang, J., Shu, H., Xu, Y., Wu, J., Wang, G., Lu, W., Tang, X., Shi, W., 2020. Structural deformation characteristics and shale gas preservation conditions in the Zhaotong National Shale Gas Demonstration Area along the southern margin of the Sichuan Basin. Natural Gas Industry B 7(3), 224-233. doi.org/https://doi.org/10.1016/j.ngib.2019.10.004.

Zeng, B., Duan, H., Bai, Y., Meng, W., 2018. Forecasting the output of shale gas in China using an unbiased grey model and weakening buffer operator. Energy 151, 238-249. doi.org/https://doi.org/10.1016/j.energy.2018.03.045.

Zhang, G., Guo, A., Wang, Y., Li, S., Dong, Y., Liu, S., He, D., Cheng, S., Lu, R., Yao, A., 2013. Tectonics of South China continent and its implications. Science China Earth Sciences 56(11), 1804-1828. doi.org/10.1007/s11430-013-4679-1.

Zhang, M., Chakraborty, N., Karpyn, Z.T., Emami-Meybodi, H., Ayala, L.F., 2021. Experimental and numerical study of gas diffusion and sorption kinetics in ultratight rocks. Fuel 286, 119300. doi.org/https://doi.org/10.1016/j.fuel.2020.119300.

Zhang, W., Li, Y., Zhao, F., Han, W., Zhou, J., Holland, G., Zhou, Z., 2019. Quantifying the helium and hydrocarbon accumulation processes using noble gases in the North Qaidam Basin, China. Chemical Geology 525, 368-379. doi.org/https://doi.org/10.1016/j.chemgeo.2019.07.020.

Zhang, Y., Jiang, S., He, Z., Li, Y., Xiao, D., Chen, G., Zhao, J., 2021. Coupling between Source Rock and Reservoir of Shale Gas in Wufeng-Longmaxi Formation in Sichuan Basin, South China. Energies 14(9). doi.org/10.3390/en14092679.

Zhang, Y., Lu, B., 2015. Prediction of global energy trend and analysis on energy technology innovation characteristics. 35, 1-10. doi.org/10.3787/j.issn.1000-0976.2015.10.001.

Zhao, W., Li, J., Yang, T., Wang, S., Huang, J., 2016. Geological difference and its significance of marine shale gases in South China. Petroleum Exploration and Development 43(4), 547-559. doi.org/https://doi.org/10.1016/S1876-3804(16)30065-9.

Zhou, L., Algeo, T.J., Shen, J., Hu, Z., Gong, H., Xie, S., Huang, J., Gao, S., 2015. Changes in marine productivity and redox conditions during the Late Ordovician Hirnantian glaciation. Palaeogeography, Palaeoclimatology, Palaeoecology 420, 223-234. doi.org/https://doi.org/10.1016/j.palaeo.2014.12.012.

Zhou, Z., Ballentine, C.J., Kipfer, R., Schoell, M., Thibodeaux, S., 2005. Noble gas tracing of groundwater/coalbed methane interaction in the San Juan Basin, USA. Geochimica et Cosmochimica Acta 69(23), 5413-5428. doi.org/https://doi.org/10.1016/j.gca.2005.06.027.

Zhu, G., Wang, T., Xie, Z., Xie, B., Liu, K., 2015. Giant gas discovery in the Precambrian deeply buried reservoirs in the Sichuan Basin, China: Implications for gas exploration in old cratonic basins. Precambrian Research 262, 45-66. doi.org/https://doi.org/10.1016/j.precamres.2015.02.023.

Zou, C., Dong, D., Wang, Y., Li, X., Huang, J., Wang, S., Guan, Q., Zhang, C., Wang, H., Liu, H., Bai, W., Liang, F., Lin, W., Zhao, Q., Liu, D., Yang, Z., Liang, P., Sun, S., Qiu, Z., 2016. Shale gas in China: Characteristics, challenges and prospects (II). Petroleum Exploration and Development 43(2), 182-196. doi.org/https://doi.org/10.1016/S1876-3804(16)30022-2.

Zou, C., Zhang, G., Tao, S., Hu, S., Li, X., Li, J., Dong, D., Zhu, R., 2010. Geological features and exploration discoveries of unconventional resources and the petroleum geological theory. Petroleum Exploration and Development 37, 641-653.

Chapter 3 Noble gas signatures, insights into methanogenesis and CO_2 generation linked to the geodynamic setting of the Huanghua Depression, Bohai Bay Basin, China

(Manuscript 2)

Beagle, J.R.[23], Cao, C.[4], Qin, S.[5] Wang, Y.[3], Liu, Q.[17], Zhong, W.[6], Holland, G.[6], Zhou, Z.[2]

[1]State Key Laboratory of Shale Oil and Gas Enrichment Mechanisms and Effective Development, Beijing 100083, China

[2]LEC, Lancaster University, Lancaster, LA1 4YQ, UK

[3]Guangzhou Institute of Geochemistry, Chinese Academy of Sciences, Guangzhou, 510640, China

[4]Key Laboratory of Petroleum Resources, Institute of Geology and Geophysics, Chinese Academy of Sciences, Lanzhou, 730000, China

[5]Research Institute of Petroleum Exploration & Development (RIPED), PetroChina, Beijing, 100083 China

[6]Department of Earth and Environmental Sciences, The University of Manchester, M13 9PL, UK

[7]Institute of Energy, Peking University, China

3.1 Abstract

The Bohai Bay Basin (BBB), a significant oil and gas-producing region in north-eastern China offers a unique setting to explore the mechanisms and thermal dynamics related to hydrocarbon formation during rifting.

Within the Huanghua Depression (HHD) in the central BBB, 18 natural gas samples were measured for their noble gas (He, Ne, Ar, Kr, Xe), bulk chemical composition (CO_2, N_2, H_2) and stable carbon and hydrogen isotopic compositions ($\delta^{13}C_{C1-C4}$ and δD_{C1-C2}). $^3He/^4He$ (R/R_a) ratios range from a crustal radiogenic signature of $0.22R_a$ in the southern HHD to a more magmatic-influenced ratio of $2.17R_a$ in the central Gangxi buried hill. Atmosphere derived noble gas ratios ($^{20}Ne/^{36}Ar$) appear to have evolved in a predominantly open system, with values that fall below ASW. High concentrations of H_2 are found across all gas samples (<22.01%), particularly in the Banqiao subsag, while δD_{C1} ratios are highly fractionated (-233.855‰ to -170.057‰). The results of this paper reveal a distinct generational history that relates to the geodynamic setting of the BBB, the dehydration of a deeply subducted stagnant slab and a complex mixing history with groundwater that has also influenced H_2 and CO_2 concentrations. We reveal the distinct end-member contributions to methane (CH_4) generation, with most gas being derived from a combination of abiotic, thermogenic, and microbial methanogenesis. Fault proximity governs the extent of fluid movement and provides a conduit for the mobilisation of CO_2, while samples isolated from major faults contain lower abundances of atmospheric noble gases. The timing of CO_2 generation is linked to intense Mesozoic volcanism; however, CO_2 concentrations increase with $C_1/(C_2+C_3)$, indicating the displacement of CH_4 by CO_2. Coupled with an exceptionally high degree of $\delta^{13}C_{CO2}$ fractionation (-13.695‰-6.390‰), the relative timing of CO_2 injection occurred following hydrocarbon maturation.

Keywords: Noble gas signatures, stable isotopes, methanogenesis, CO2, hydrogen, fluid flow, stagnant slab

3.2 Introduction

The coastal Bohai Bay basin (BBB) is a Meso-Cenozoic rift basin situated in northeastern China, with a total area of 2 x 10^5 km^2 (Yang and Xu, 2004). The Dagang Oil Field, located within the central Huanghua Depression (HHD) of the Bohai Bay Basin, has undergone continuous exploration and development since the latter part of the 20th century (Lu et al., 2019). Developmental effectiveness is waning after many years of production, and a better understanding of the geological complexities is key to ensuring future longevity (Yang et al., 2016a). Complex faulting associated with widespread rifting, as well as the unpredictability and variability in reservoir distribution, porosity, and permeability, present serious developmental challenges; however, utilising noble gas and stable isotopes provides a valuable opportunity to trace subsurface gas and fluid migration and characterise the basins' geochemical evolution. The suite of noble gases (He, Ne, Ar, Kr and Xe) are useful fluid tracers, as they do not readily form compounds with other elements due to their chemical inertness (Ballentine and Burnard, 2002). Furthermore, noble gases exhibit a wide range of solubilities in water, with He being the least soluble and Xe the most soluble (Aeschbach-Hertig and Solomon, 2013). The behaviour of noble gases offers detailed information about the fluid mixing and phase separation processes that occur in the subsurface. Fluid residence ages and the timing of fluid-rock interactions are determined by ascertaining the initial abundance and subsequent accumulation of radiogenic and nucleogenic noble gas isotopes, ^{4}He, ^{21}Ne, ^{40}Ar (Porcelli et al., 2002).

This paper presents a detailed investigation of noble gas and stable isotope signatures from natural gas (CH_4) samples across the Huanghua depression, enabling us to reveal the complex mixing history, thermal regime, and processes involved in the generation and migration of hydrocarbon fluids, alongside gases derived from magmatic and air-derived sources. This study applies unique insights provided by noble gas and stable isotope signatures to unravel the intricate history of methanogenesis and CO_2 generation in the basin. By focusing on the role of faulting, magma kinematics, and the thermal regime, this research not only enhances our understanding of the BBB but also provides broader implications for similar rift basins globally. We have determined significant contributions from abiotic, thermogenic, and microbial sources in methane generation and highlight the critical role of fault proximity in fluid migration. We have constrained the isotopic compositions ($\delta^{13}C_{C1}$, $CH_4/^3He$ and C_1/C_2+C_3) of gas endmembers to decipher the relative contributions of different methanogenic pathways and examine the

timing of CO_2 generation with relation to Eocene Shahejie fm. gas generation and migration. Such insights are essential for improving exploration strategies and resource management in mature basins worldwide.

[Figure from Section 1.2.2 (Figure 3) to be inserted here upon manuscript submission, but has been omitted in this thesis to avoid repetition. Refer to Section 1.2.2, Page 13 for the full stratigraphic column.]

3.3 Geological setting

The Bohai Bay Basin, which lies entirely within the North China Block, represents a complex extensional rift system that developed during the Late Mesozoic and Cenozoic along an NNE-SSW striking fault system (Chang, 1991, Allen et al., 1997). Tectonic stresses have led to widespread deformation, lithospheric stretching and large-scale strike-slip faults, which play a large part in oil and gas migration (Yuan et al., 2022). Thrusting due to the convergence of the North and South China blocks took place between the Late Jurassic and Early Cretaceous. This Mesozoic rifting episode is associated with extensive volcanism along the Daxing'anling tectonic-magmatic belt (Ren et al., 2002). Considerable sedimentation of pre-Cenozoic non-marine clastic material also accompanied this period, which underlies the later syn-rift Bohai sediments. Growth of the Cenozoic rift basin commenced during the Paleogene (Palaeocene to early Eocene) and is thought to be caused by crust-mantle processes triggered by prior subduction of the stagnant Izanagi slab, associated with the westward-moving Pacific plate (Wang et al., 2022a) and horizontal tension caused by the upwelling of buoyant heated mantle material (Qi and Yang, 2010). This widespread extension led to the syn-rift deposition of the Kongdian formation (Ek, ~65-48.1 Ma) and the Shahejie formation (Es, ~48.1-31.8 Ma), which was controlled mainly by large strike-slip faults within a series of continued half-graben segments (Allen et al., 1998).

Following a stable rifting period, the BBB evolved to a rifting-depressed conversion period during the Oligocene, and the Dongying formation (Ed, ~31.8-23 Ma) was deposited. Subsequent further evolution of the BBB resulted in a post-rift degeneration stage in the Neogene, whereby broad crustal subsidence occurred (Chen et al., 1984). Thermal subsidence during the Miocene was accompanied by post-rift deposition of the Guantao (Ng, ~23-11.1 Ma), Minghuazhen (Nm, ~11.1-1.8 Ma) and Pingyuan formations (Yang and Xu, 2004) in a braided and meandering river paleoenvironment (Chen et al., 2014). These formations cover the earlier syn-rift successions and are up to 4000-5000m thick (Yu and Koyi, 2016).

As a result of this subsidence, various depressions exist with complex superpositions (Figure 32), the largest of which is the Bozhong depression in the north-east part of the HHD (Hellinger et al., 1985), an important petroliferous tectonic unit within the central BBB (Pu et al., 2018). Within this major depression are several structural units and sub-basins, or sags (Figure 33). The Qikou sag, elongated in a NE-SW orientation, is the largest half-graben to have developed since the Paleogene (Pu et al., 2011). Besides the

Qikou sag, the central-northern area comprises further sub-units and secondary structures, including the Banqiao sub-sag, bounded by the Cangxian uplifted structural belt, the Qibei sub-sag and the Qinan sub-sag.

The Gangxi and Kongdian 'bulges' or 'highs' were also vital depocenters for detrital material from the Qibei, Qinan and Chengbei slopes, where fan-delta and sand-bodies were distributed during Paleogene Shahejie formation deposition (Pu et al., 2013) , and these zones represent significant target areas for hydrocarbon exploration. The main sedimentary reservoirs comprise these interbedded sand and shale intervals (Guofa et al., 2010) within the Shahejie formation; however, Carboniferous-Permian strata represent novel petroleum system targets and other exploration targets include the less well-constrained Ordovician carbonate reservoirs within the Qianmiqiao buried hill, close to the Banqiao sag (sample DG-8). The charging mechanisms are not clearly understood, although it has been proposed that hydrocarbons could have migrated from a Carboniferous source kitchen via active faults into the upper Ordovician unit (Yang et al., 2020).

Other older pre-rift sediments also signify new, emerging targets for hydrocarbon exploration within the Huanghua depression. The Wumaying buried hill is situated in the south of the HHD (samples YG-2 and Y101X1), with its NNE striking, broad anticlinal structure; it denotes a deeply buried (<4000m) Permian reservoir unit in the Lower Shihezi formation that is thought to be charged by Upper Paleozoic coil-measure source rocks (Jin et al., 2019). This buried hill has experienced multiple episodes of tectonic deformation, including the middle-late Triassic Indosinian movement, the Jurassic-Cretaceous Yanshanian movement and the Himalayan movement during the Eocene. The resultant structural deformation would have largely impacted the multistage hydrocarbon migration and the conditions for accumulation.

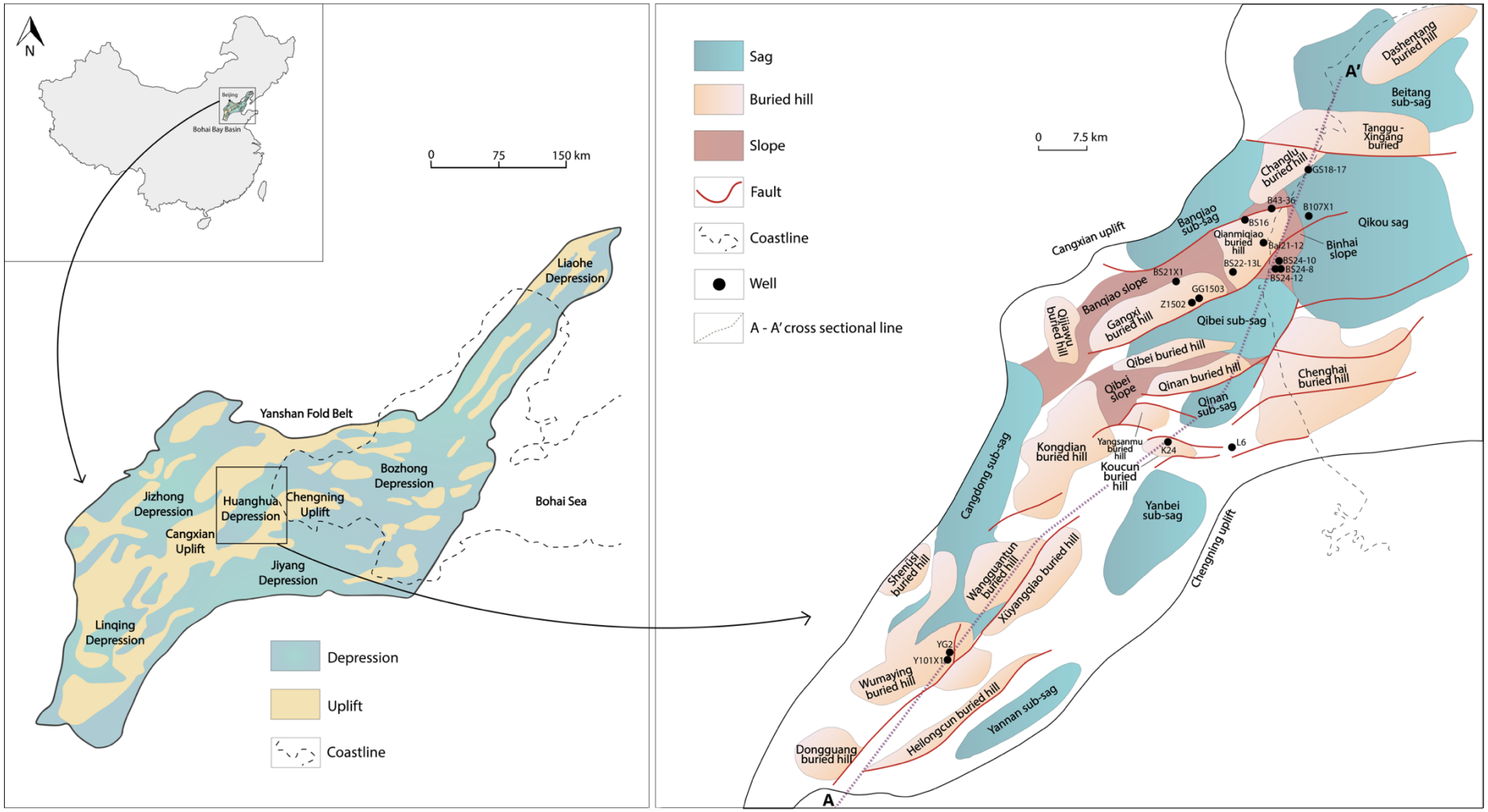

Figure 32 - Map of the Bohai Bay Basin (A) and the study area within the Huanghua depression, showing the major structural features, including sags, buried hills and regional faults. An A-A' cross-sectional line which represents a SW-NE stratigraphic cross section, is also denoted by a dashed line; modified after Zhao et al. (2019).

Figure 33 – SW-NE stratigraphic cross section showing the main structural units and sequence boundaries in the Huanghua Depression, denoted by A-A' in the previous figure; modified after (Zhou et al., 2021) & (Yuan et al., 2021). Sample locations are grouped and are given in the accompanying table.

Table 26 - Bohai Bay Basin gas samples and their group numbers based on their locations and fault proximity

Group	Major proximal faults	Sample numbers
1	Wumaying fault	Y101X1 & YG2
2	Koucun and Yangerzhuang faults	DG15, DG12
3	Gangxi fault	DG10, DG17, DG18
4	Gangdong, Binhai and Tangjiahe faults	DG1, DG2, DG3, DG4, DG5, DG6, DG11, DG16
5	Banqiao and Dazhangtuo faults	DG7, DG8, DG9

3.4 Sampling and Experimental Methods

3.4.1 Sampling

Eighteen free gas samples were taken from producing exploratory wells within the Gangdong, Madong, Maxi, Gangzhong, Banqiao, Gangxi, Liujianfang, Liuguanzhuang, Yangerzhuang, Wumaying, Qianmiqiao and Koucun oil and gas fields in the Bohai Bay Basin. Gas samples were collected from different formations, such as the Eocene Shahejie (Es) and Kongdian (Ek) formations, the Oligocene Dongying (Ed) formation, as well as Upper Paleozoic Carboniferous-Permian strata and the Ordovician Qianmiqiao buried hill (Figure 32). The locations of the sampling areas are also disclosed in Figure 33, and the respective group numbers given to each sample, based on their geographic location are shown in Table 26.

Noble gas samples were collected from producing wellheads in 9.8mm diameter, 1000mL volume, standard refrigeration grade internally polished copper cylinders. To lessen any potential air contamination before closure and sealing of the cylinder using stainless steel pinch-off clamps, gas was allowed to flush through for 10 minutes. Additional gas samples were taken at each wellhead using steel cylinders and filled with natural gas equilibrated to the wellhead pressure (Qin et al., 2018). Each sample was analysed to determine its molecular noble gas (copper cylinders), stable isotope gas composition, and carbon and hydrogen isotope abundances (steel cylinders).

3.4.2 Experimental methods

3.4.2.1 Major gas components and carbon isotopes

CH_4, CO_2, N_2, H_2 and other major gas and carbon isotope abundances were analysed using a MAT 271 mass spectrometer at the Key Laboratory of Petroleum Resources Research, Institute of Geology and Geophysics, Chinese Academy of Sciences in Lanzhou, China. Hydrocarbon (CH_4, C_2H_6 and C_3H_8) abundances were determined using an Agilent 6890N gas chromatograph (GC) equipped with a fluid-ionization detector (FID). A capillary column (PLOT Al2O3, 50 m x 0.53 mm) was utilised to divide the individual hydrocarbon gas components (C_1-C_3). The GC oven temperature was initially placed at 30°C for 10 min and ramped up to 180 °C at a rate of 10°C/min, and kept at 180°C for 20-30 min (Cao et al., 2016, Cao et al., 2018, Cao et al., 2020a).

Carbon and hydrogen isotopic compositions were analysed at the Key Laboratory of the Research Institute of Exploration and Development of PetroChina using a MAT 253 gas

isotopic mass spectrometer. The carbon isotopes of CH_4 and CO_2 were measured following the analytical procedures outlined in Qin et al. (2018). Stable carbon isotopic ($\delta^{13}C$) values are stated in the δ notation in per mil (‰) relative to the Vienna Pee Dee Belemnite standard (VPBD).

3.4.2.2 Noble gases

Noble gases were also analysed for their abundances and isotopic ratios. These were determined using an Isotopx NGX noble gas mass spectrometer with an ATONA Faraday cup detector amplifier and an electron multiplier at the Subsurface Fluid Isotope Geochemistry Laboratory at the Lancaster Environment Centre, Lancaster University. Subsequently, we employ a specially designed procedure that firstly involves mounting the sample copper tube to a system maintained at an ultra-high vacuum (UHV). Once the steel clamp at one end of the copper tube is unfastened, the transference of a known gas volume takes place following the manual opening and closing of the appropriate valve to an MKS dual capacitance manometer pressure gauge. Then, the gases can be isolated and introduced to a Ti-sponge furnace, preheated to 800°C, and later cooled to room temperature. In addition to two SAES GP-50 Ti-Zr alloy getters, these instruments act to break down and remove reactive gases (H_2S, N_2, CO_2, CO, C_1-C_4, H_2O) that would otherwise be harmful to both the preparation and analysis. The remaining 'purified' gas mixture of noble gases (He, Ne, Ar, Kr and Xe) can then be sequentially separated and trapped using cryogenic traps at 77K and 9.5K for heavy (Ar, Kr and Xe) and light (He and Ne) noble gases, respectively. The admittance of these gases into the mass spectrometer was then controlled by heating the appropriate cryogenic trap to the desired temperature (50K for Helium, 95K for Ne and 210K for Ar and Kr) for a set time interval. Xe, was released and expanded into the preparation line when the charcoal trap was heated to 450K; its isotopic concentrations were then determined using an electron multiplier. In contrast, ^{4}He, ^{20}Ne and ^{40}Ar isotopic concentrations were determined using the Faraday cup. Corrections were made to concentrations by periodically carrying out blank and air standard measurements. Interference of $^{40}Ar^{++}$ and $^{44}CO_2^{++}$ on ^{20}Ne and ^{22}Ne was also mitigated following the methods described in Niedermann et al. (1993).

3.5 Results

3.5.1 Major gas species abundances

Gases from the Huanghua depression in the Bohai Bay Basin contain variable amounts of methane (52.69%-83.08%). The highest CH_4 content can be found in the southeast between the Chenghai and Koucun buried hills (samples DG-12 and DG-15). The remaining gas fraction predominantly comprises a high concentration of H_2 (13.77%-22.01%), as well as N_2 (2.78%-8.90%), C_2H_6 (0.09%-6.77%) and C_3H_8 (0.02%-6.93%). The H_2 concentrations observed in these samples are notably high, we consider the potential for minor overestimation of these concentrations due to the presence of ionization fragments from heavier hydrocarbons in the quadrupole mass spectrometer. The dryness coefficient corresponds to the ratio of CH_4 (C_1) to the sum of heavier hydrocarbons ($D = C_1/C_{1-4}$). It indicates the degree of thermal maturation, potential accumulation, and migration gas samples have undergone (Zhang et al., 2022a). The dryness coefficient is approaching 1 in samples DG-10 (0.999) from well X59 in the Gangxi uplift, DG-12 (0.998) from well L6 in the Liuguanzhuang gas field in the Chengbei slope, DG-15 (0.993) from well K24 within the Koucun buried hill, DG-8 (0.944) from well B21 in the Banqiao sub-sag, and also in the two wells situated within the Wumaying buried hill, Y101X1 (0.940) and YG2 (0.942). The overall correlation coefficient that shows the strength of the relationship between the dryness coefficient and depth of the gas sample is moderately strong (r=0.534), demonstrating that gas dryness is generally higher in samples at greater depths, where gases are more mature as a result of higher temperature and pressure. CH_4 content (%) is higher in gas samples at shallower depths; conversely, CO_2 content (%) largely increases with depth.
The CO_2 content in gas samples ranges from 0.06% (DG-12) and 0.09% (DG-15) to 2.36% (DG-7) and 3.10% (DG-17), while H_2 content ranges from between 13.77% in sample DG-12 to 22.01% in sample DG-9.

3.5.2 Stable isotope compositions ($\delta^{13}C_{C1-5}$, $\delta^{13}C_{CO2}$ and δD)

Carbon VPDB (Vienna Pee Dee Belemnite) and Hydrogen VSMOW (Vienna Standard Mean Ocean Water) are used here as reference materials for stable isotope analysis, and values are reported in per mil (‰) relative to these standards (Table 28). Variations in $\delta^{13}C$, $\delta^{13}C_{CO2}$ and δD provide valuable insights into the origins, source and geological conditions that led to the formation of these natural gases within the Huanghua depression.

Gas samples $\delta^{13}C$ values of methane (C_1), ethane (C_2) and propane (C_3) range from between -45.4‰ to -31.8‰, -30.2‰ to -18.8‰ and -27.7‰ to -12.1‰, respectively. Sample DG-12, from well L6, exhibits a relatively isotopically light $\delta^{13}C(C_1)$ = -45.4‰ of all the sampled gases, while the highest $\delta^{13}C$ is found in the south of the Huanghua depression along the Wumaying fault in samples YG2 and Y101X1 (-31.802‰ and -32.008‰, respectively).

Upon inspection of δD_1, the deuterium composition of methane (C_1) and δD_2, the deuterium composition of ethane (C_1); samples DG-12 and DG-15 are also distinctively different from the remaining samples, too, being more enriched in the isotopically light protium isotope (1H) with δD_1 (-232.295‰ and -233.855‰) and δD_2 (-182.617‰ and -174.746‰).

DG-10 and DG-11 samples similarly indicate that they too have a lower 2H/1H ratio compared to the standard, (δD_1 = -209.615‰ and -221.403‰, δD_2 = -169.65‰ and -176.885‰, respectively). Other gas samples exhibit δD_1 values that are relatively enriched in the heavier deuterium isotope (2H) of between -170.057‰ and -192.911‰, and δD_2 values of between -115.423‰ and -149.883‰.

$\delta 13C_{CO2}$ values representing the carbon isotopic composition of CO_2 are reported for 9 gas samples. These values help assess the source of CO_2 from a crustal, mantle or organic origin and range between -13.695‰ (DG-10) and 6.390‰ (DG-11). DG-7 and DG-17, which contain the highest abundance of CO_2, exhibit $\delta^{13}C_{CO2}$ values that are both positive (3.020‰ and 2.885‰, respectively).

Table 27 - Significant gas species contributions in Bohai Bay Basin gas samples. Errors are ±0.1%.

Gas field	Sample name	Well name	Depth (m)	Chemical composition (%)						
				CH_4	C_2H_6	C_3H_8	C_4H_{10}	CO_2	N_2	H_2
Madong	DG-1	GS18-17	4218.1-4306	64.02	4.02	4.85	1.19	1.54	5.13	19.24
Gangdong	DG-2	B107X1	3054.7-3116.3	-	-	-	-	-	-	-
Madong	DG-3	B107-17	2968-2973	74.62	3.53	1.03	0.16	1.16	4.58	14.88
Maxi	DG-4	BS24-8	4492-4542.6	73.84	4.26	1.03	0.23	1.58	3.07	15.97
Maxi	DG-5	BS24-10	4305-4424.5	-	-	-	-	-	-	-
Maxi	DG-6	BS24-12	4395.7-4471.2	69.85	4.13	0.92	0.13	1.35	4.46	19.15
Qianmiqiao	DG-7	BS16	4631-4652	72.67	3.20	0.86	0.19	2.36	2.78	17.94
Banqiao	DG-8	Bai21	2644.4-3501.1	75.15	1.59	0.65	0.14	0.30	3.21	18.86
Banqiao	DG-9	B43-36	3918.6-3929.2	52.69	6.77	6.93	1.42	1.28	8.90	22.01
Gangxi	DG-10	X59	1057.58-1060.58	-	-	-	-	-	-	-
Liujianfang	DG-11	BS21X1	3314.1-3333.6	67.77	3.41	1.25	0.17	1.31	8.45	17.62
Liuguanzhuang	DG-12	L6	1138-1196	83.08	0.09	0.02	0.02	0.06	2.36	14.30
Koucun	DG-15	K24	1357.8-1368.5	82.42	0.16	0.34	0.14	0.09	3.01	13.77
Maxi	DG-16	BS22-13L	4921-5188	77.01	3.86	0.43	0.11	1.64	2.03	14.91
Gangbei	DG-17	Z1502	2477.7-2536.3	71.93	2.40	0.90	0.12	3.10	3.83	17.67
Gangzhong	DG-18	GG1503	1991.5-2172	73.62	3.77	1.34	0.17	0.62	3.22	17.25
Wumaying	YG-2	YG2	4702.8-4734.2	78.43	2.01	0.32	0.08	0.10	2.76	16.26
Wumaying	Y101X1	Y101X1	3425.5-3470.2	78.62	2.20	0.43	0.10	0.17	2.32	16.13

Table 28 - Carbon (‰, VPDB) and hydrogen (‰, VSMOW) isotopic composition of gases from the Bohai Bay Basin, China. Errors are ±0.1‰.

Gas field	Sample name	Well name	δ13C (‰VPDB)				δD (‰VSMOW)	
			$\delta^{13}C_{CO2}$	$\delta^{13}C_{C1}$	$\delta^{13}C_{C2}$	$\delta^{13}C_{C3}$	δD_1	δD_2
Madong	DG-1	GS18-17	-	-36.861	-	-	-	-
Gangdong	DG-2	B107X1	-	-40.433	-27.117	-25.837	-183.044	-144.945
Madong	DG-3	B107-17	-7.756	-38.954	-27.102	-26.175	-172.978	-115.423
Maxi	DG-4	BS24-8	-8.275	-37.298	-25.960	-21.941	-171.348	-128.369
Maxi	DG-5	BS24-10	-9.741	-40.672	-26.178	-22.746	-170.057	-141.581
Maxi	DG-6	BS24-12	-8.788	-41.623	-27.067	-23.197	-179.202	-125.781
Qianmiqiao	DG-7	BS16	3.020	-31.637	-28.700	-22.090	-175.2450	-132.927
Banqiao	DG-8	Bai21	-	-40.633	-26.957	-21.904	-171.548	-135.162
Banqiao	DG-9	B43-36	-	-40.917	-25.609	-23.649	-181.097	-146.701
Gangxi	DG-10	X59	-13.695	-44.740	-21.607	-	-221.403	-176.885
Liujianfang	DG-11	BS21X1	6.390	-45.050	-28.465	-27.695	-209.615	-169.65
Liuguanzhuang	DG-12	L6	-	-45.401	-18.790	-12.144	-232.295	-182.617
Koucun	DG-15	K24	-	-43.457	-30.203	-23.815	-233.855	-174.746
Maxi	DG-16	BS22-13L	5.390	-39.593	-25.270	-21.783	-181.583	-126.816
Gangbei	DG-17	Z1502	2.885	-38.029	-27.597	-27.482	-192.911	-142.514
Gangzhong	DG-18	GG1503	-	-39.117	-27.752	-26.502	-191.393	-143.105
Wumaying	YG-2	YG2	-	-31.802	-21.925	-20.466	-191.413	-149.883
Wumaying	Y101X1	Y101X1	-	-32.008	-21.890	-20.318	-186.055	-146.765

3.5.3 Noble gases

Table 29 and **Error! Reference source not found.** summarise the abundances and isotopic ratios of noble gas species (He, Ne, Ar, Kr, and Xe) in the BBB.

3.5.3.1 Helium

Helium (^{4}He) concentrations vary by more than a factor of 10, from 4.92 x 10^6 to 180 x 10^6 cm^3 STP/cm^3. Measured ^{3}He/^{4}He (R/R_a) ratios have been normalised and are reported relative to the atmospheric ratio, R_a = 1.384 x 10^{-6} (Ozima and Podosek, 2002). Sample values range between 0.22 R_a - 0.28 R_a in the deeply buried Ordovician reservoir rocks of the Wumaying buried hill to 2.17 R_a in the Permian Shihezi sandstones of the Gangbei buried hill. ^{4}He/^{20}Ne ratios range between 9447.79 to 1.19 x 10^7, and the contribution of He from atmospheric sources is therefore negligible, as these measured values are several orders of magnitude greater than the reported atmospheric ratio of ^{4}He/^{20}Ne in groundwater, which is 0.288 (Kipfer et al., 2002). He is, therefore, likely derived from a mixed mantle & crustal source, which can be deconvoluted using the equation:

$$He_{mantle}(\%) = (R_{sample} - R_{crust})/(R_{mantle} - R_{crust}) \text{ x } 100\% \qquad (77)$$

Using a crustal ^{3}He/^{4}He (R_{crust}) value of 0.01 R_a and a mantle ^{3}He/^{4}He (R_{mantle}) value of 8 R_a (Ballentine and Burnard, 2002), where R_{sample} corresponds to the resolved R/R_a in samples, using a simple two-component mixing model, we determine that the contribution of mantle He in sample DG-17 within the Gangbei buried hill, where the highest R/R_a value was measured (2.17 R_a) to be 26.98%, while there is only 2.66% to 3.33% mantle He contribution in the Wumaying buried hill samples, for samples YG-2 and YG-101X1, respectively, where R_a values were closest to the crustal value of 0.01. The average mantle He contribution across the rest of the sampled gases is 11.37%.

3.5.3.2 Neon

Neon (^{20}Ne) concentrations range from 0.77 x 10^{-12} to 98.68 x 10^{-10} cm^3 STP/cm^3. ^{20}Ne/^{22}Ne ratios range from 8.56 to 10.59, the highest value was measured in sample DG-11 from well BS21X1 in the Liujianfang gas field, slightly SE of the Gangxi uplift. The average ^{20}Ne/^{22}Ne value is 8.93 across all samples, which is lower than the reported atmospheric ^{20}Ne/^{22}Ne value of 9.80 (Bottomley et al., 1984). ^{21}Ne/^{22}Ne ratios show little

variation, ranging between 0.03 and 0.06, where all gas samples exceed the air value of 0.02959 (Györe et al., 2019).

$$^{21}Ne^{*} = {}^{22}Ne_{meas} \times [(^{21}Ne/^{22}Ne_{meas}) - (^{21}Ne/^{22}Ne_{air})] \quad (78)$$

$$^{40}Ar^{*} = {}^{36}Ar_{meas} \times [(^{40}Ar/^{36}Ar_{meas}) - (^{40}Ar/^{36}Ar_{air})] \quad (79)$$

In assessing the crustal component of Ne, the excess ^{21}Ne (^{21}Ne*) derived from nucleogenic reactions can be determined (Hunt et al., 2012). In sample DG-12 from well L6 in the Liuguanzhuang gas field, along the Chengbei slope, this excess only represents 2.35% of total ^{21}Ne, and similarly, in sample DG-18 from well GG1503, this excess only accounts for 0.06% of total ^{21}Ne. In contrast, most other gas samples have a variable contribution of crustal-derived ^{21}Ne of between 13.75% to 48.14%.

3.5.3.3 Argon

Argon (^{36}Ar), derived from groundwater, shows a considerable range in concentrations between 1.64 x 10^{-13} to 1.81 x 10^{-8} cm^3 STP/cm^3. ^{40}Ar*/^{36}Ar ratios also vary from 336.32 to 3966.41. Three gas samples have ^{40}Ar*/^{36}Ar ratios that plot closely to the atmospheric ^{40}Ar/^{36}Ar value of 298.6 (Lee et al., 2006), DG-15 (336.32), DG-18 (390.17) and DG-10 (414.78). Besides these samples, average ^{40}Ar*/^{36}Ar across the rest of the gas samples is 2372.64, which indicates a large, resolvable contribution of radiogenic ^{40}Ar.
Employing a similar two-end-member mixing model used for ^{21}Ne with ^{40}Ar (Ballentine et al., 2002), we can also resolve the non-atmospheric, crustal-derived excess (^{40}Ar*). This purely crustal radiogenic proportion contributes between 24.26% and 92.46%.

3.5.3.4 Krypton and Xenon

Krypton (^{84}Kr) concentrations vary from 0.46 x 10^{-12} to 424.56 x 10^{-12} cm^3 STP/cm^3 in sample DG-15 from well K24 in the Koucun buried hill. Xe (^{132}Xe) concentrations are similarly the highest in this sample at 242.57 x 10^{-13} cm^3 STP/cm^3 but decrease to as low as 4.11 x 10^{-13} cm^3 STP/cm^3 in sample DG-7 from well BS16 in the Qianmiqiao buried hill Ordovician reservoir unit. ^{84}Kr/^{36}Ar ratios range from 0.019 to 0.081 and ^{132}Xe/^{36}Ar ratios range from 0.0013 to 0.065.

Table 29 - Noble gas (He, Ne, Ar, Kr and Xe) isotopic compositions of gases from the Bohai Bay Basin, China

Gas field	Sample	Well	^{4}He (x 10^{-6})	Error (1σ)	^{20}Ne (x 10^{-12})	Error (1σ)	^{36}Ar (x 10^{-11})	Error (1σ)	$^{40}Ar^{*}$ (x 10^{-8})	Error (1σ)	^{84}Kr (x 10^{-12})	Error (1σ)	^{132}Xe (x 10^{-13})	Error (1σ)
			cm^3 STP/cm^3											
Madong	DG-1	GS18-17	4.92	0.07	0.89	0.05	0.81	0.02	1.77	0.03	0.46	0.01	5.21	0.08
Gangdong	DG-2	B107X1	9.72	0.14	4.50	0.13	3.52	0.08	11.55	0.16	1.71	0.02	9.62	0.14
Madong	DG-3	B107-17	15.17	0.21	3.49	0.11	2.41	0.05	8.83	0.13	1.15	0.02	5.09	0.07
Maxi	DG-4	BS24-8	9.03	0.13	0.77	0.09	1.20	0.02	2.71	0.04	0.83	0.01	6.23	0.09
Maxi	DG-5	BS24-10	9.44	0.13	3.28	0.06	2.78	0.04	3.96	0.06	1.57	0.02	7.42	0.11
Maxi	DG-6	BS24-12	9.51	0.13	2.65	0.06	2.35	0.04	4.87	0.07	1.41	0.02	7.37	0.11
Qianmiqiao	DG-7	BS16	22.13	0.31	3.69	0.07	9.86	0.51	14.64	0.21	1.83	0.03	4.11	0.06
Banqiao	DG-8	Bai21	130.04	1.84	-	-	20.37	0.32	15.61	0.22	13.06	0.19	11.04	0.16
Banqiao	DG-9	B43-36	17.15	0.24	8.11	0.13	7.54	0.12	14.97	0.21	2.89	0.04	5.21	0.08
Gangxi	DG-10	X59	41.88	0.59	424.95	6.01	217.50	3.22	25.94	0.37	94.44	1.35	65.10	0.93
Liujianfang	DG-11	BS21X1	18.94	0.27	9.92	0.15	4.32	0.10	11.31	0.16	2.38	0.03	10.62	0.16
Liuguanzhuang	DG-12	L6	180.00	2.55	452.01	6.40	259.71	3.89	79.94	1.13	117.89	1.69	87.06	1.25
Koucun	DG-15	K24	104.09	1.47	9867.73	139.68	1811.09	26.30	73.93	1.05	424.56	6.08	242.57	3.48
Maxi	DG-16	BS22-13L	8.92	0.13	3.66	0.08	1.79	0.03	2.65	0.04	0.99	0.01	5.64	0.08
Gangbei	DG-17	Z1502	62.29	0.88	23.03	0.52	-	-	0.06	0.001	36.00	0.54	18.14	0.26
Gangzhong	DG-18	GG1503	27.02	0.38	2859.43	40.48	447.73	6.98	42.39	0.60	101.93	1.46	-	-
Wumaying	YG-2	YG2	43.49	0.62	48.85	1.06	32.67	0.68	38.55	0.55	26.47	0.38	42.91	0.66
Wumaying	Y101X1	Y101X1	57.00	0.81	45.35	0.65	44.41	0.72	46.48	0.66	24.98	0.36	15.24	0.23

Table 30 - Noble gas isotopic and elemental ratios (He, Ne, Ar, Kr and Xe) of gases from the Bohai Bay Basin, China

Gas field	Sample	Well	$^{3}He/^{4}He$ (R/Ra)	Error (1σ)	$^{20}Ne/^{22}Ne$	Error (1σ)	$^{21}Ne/^{22}Ne$	Error (1σ)	$^{40}Ar^{*}/^{36}Ar$	Error (1σ)	$^{4}He/^{20}Ne$ (x 10^{5})	Error (1σ)	$^{20}Ne/^{36}Ar$	Error (1σ)
Air			1		9.81		0.029		298.6		0.318 x 10^{-5}		0.524	
Madong	DG-1	GS18-17	0.46	0.02	-	-	0.0545	0.005	2492.57	59.07	118.79	6.81	0.05	0.003
Gangdong	DG-2	B107X1	1.68	0.05	9.15	0.31	0.0401	0.002	3573.65	94.32	21.57	0.70	0.13	0.005
Madong	DG-3	B107-17	1.35	0.04	9.52	0.29	0.0459	0.002	3966.41	97.29	43.51	1.47	0.14	0.005
Maxi	DG-4	BS24-8	0.39	0.01	-	-	0.0557	0.004	2548.35	61.69	116.99	14.28	0.06	0.008
Maxi	DG-5	BS24-10	0.35	0.01	9.54	0.24	0.0408	0.002	1719.05	36.04	28.83	0.70	0.12	0.003
Maxi	DG-6	BS24-12	0.34	0.01	9.64	0.28	0.0441	0.002	2362.65	50.84	35.88	0.94	0.11	0.003
Qianmiqiao	DG-7	BS16	0.78	0.02	8.84	0.21	0.0501	0.002	1780.88	95.38	60.00	1.37	0.04	0.002
Banqiao	DG-8	Bai21	0.59	0.02	-	-	-	-	1062.18	22.45	-	-	-	-
Banqiao	DG-9	B43-36	0.34	0.01	9.51	0.80	0.0412	0.011	2281.59	48.36	21.16	0.45	0.11	0.002
Gangxi	DG-10	X59	1.23	0.03	9.43	0.19	0.0287	0.001	414.78	8.51	0.99	0.02	0.20	0.004
Liujianfang	DG-11	BS21X1	0.84	0.02	10.59	0.22	0.0365	0.001	2915.29	78.53	19.09	0.39	0.23	0.006
Liuguanzhuang	DG-12	L6	0.34	0.01	9.49	0.19	0.0296	0.001	603.30	12.45	3.98	0.08	0.17	0.004
Koucun	DG-15	K24	0.98	0.02	9.65	0.19	0.0286	0.001	336.32	6.82	0.11	0.00	0.54	0.011
Maxi	DG-16	BS22-13L	0.29	0.01	9.11	0.25	0.0386	0.002	1775.91	39.78	24.36	0.65	0.20	0.006
Gangbei	DG-17	Z1502	2.17	0.07	9.01	0.25	0.0443	0.002	3920.61	109.54	27.04	0.72	140.25	4.631
Gangzhong	DG-18	GG1503	1.31	0.03	9.94	0.20	0.0289	0.001	390.17	8.23	0.09	0.00	0.64	0.013
Wumaying	YG-2	YG2	0.22	0.01	9.54	0.25	0.0335	0.002	1475.64	37.00	8.90	0.23	0.16	0.005
Wumaying	Y101X1	Y101X1	0.28	0.01	8.56	0.18	0.0377	0.001	1342.14	28.93	12.57	0.25	0.10	0.002

3.6 Discussion

3.6.1 Fault-driven pathways for gas charging, trapping and degassing

Utilising noble gases, it is possible to assess the extent of fault connectivity and reactivation (Scott et al., 2021). Many of the hydrocarbon discoveries made within the Bohai Bay Basin are located within complex fault-bounded traps (Song et al., 2022); however, as a result of possible fault-reactivation and breaching of the thick regional mudstone cap unit, there is a high potential for both fluid expulsion and hydrocarbon leakage, significantly impacting $^{3}He/^{4}He$ ratios and modifying noble gas signatures due to the introduction or removal of gases during migration. Transport may also be mechanically assisted due to changes in pressure or tectonic movements, while nascent fault systems may significantly influence local fluid flow, mixing and diluting gases from groundwaters, altering $^{20}Ne/^{36}Ar$ ratios due to the incorporation of atmosphere-derived noble gases. Yet, the migration pathways of subsurface gases remain challenging to predict and understand, as the movement of deep gases occurs via several complex mechanisms, including diffusion across a concentration gradient and advection across fluid flow pathways, such as faults and fracture networks.

Faulting similarly plays a crucial role in the migration and accumulation of mantle-derived CO_2, with the deep tectonic environment a key factor in the emergence of this mantle-derived CO_2 (Miao et al., 2020). Faults can act as both primary conduits, permeable pathways for the movement of subsurface fluids, and barriers (laterally and vertically) that inhibit potential fluid flow migration following the mineralisation of previously migrated fluids (Eymold et al., 2021). Consequently, faults and fault-bounded traps are significant structures for the accumulation and loss of gases in the BBB, controlling the abundance of methane, CO_2 and the suite of air, crustal and magma-derived noble gases. A high degree of fault-related degassing will result in an isotopic ratio depleted in noble gases relative to the atmosphere, as lighter isotopes are preferentially lost (Burnard et al., 1997) due to their lower solubility in water. The extent of fault-controlling processes on gas-liquid phase interactions and the fractionation of fluids arising from migration and gas loss can be determined by modelling the mixing between these noble gas components (Kipfer et al., 2002, Ballentine et al., 2002, Zhou et al., 2005). Doing so will help clarify how well (open system) or poorly interconnected (closed system) the complex reservoir systems and fault-bounded traps are within the HHD.

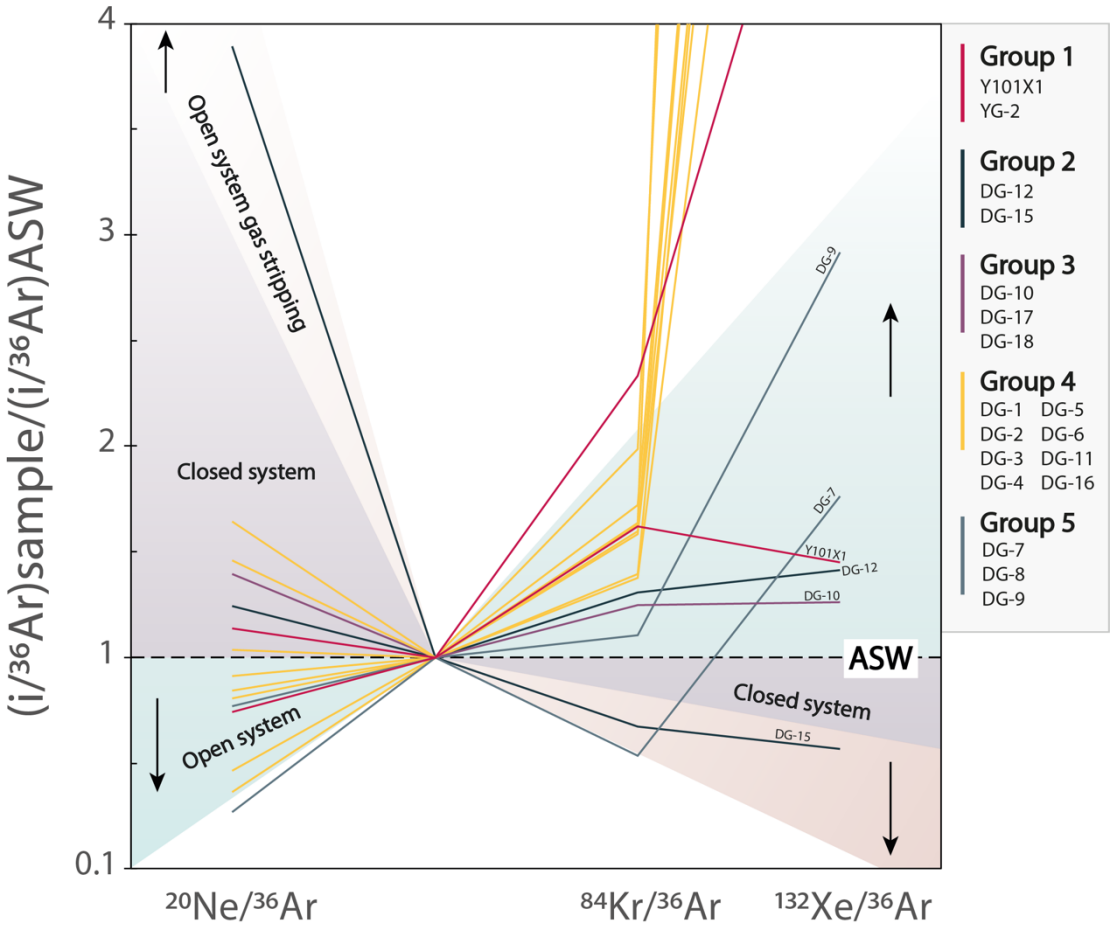

Figure 34 - Spider diagram of atmospheric-derived noble gas isotopes relative to ^{36}Ar, normalised to ASW.

Most samples display open system behaviour when assessing the air-derived gases ^{20}Ne and ^{36}Ar (Figure 34). The evolution of $^{20}Ne/^{36}Ar$ ratios below ASW may have occurred from the reactivation of normal faults in the mid-Eocene, which could have induced a significant decrease in pressure within gas-bearing formations. This event is likely to have prompted fault-associated degassing, facilitating greater mobility of gases within these structures. Under conditions of extensive degassing, characterised by a system highly open to gas exchange, gas escape could occur through permeable pathways. Air-derived $^{20}Ne/^{36}Ar$ ratios are highly fractionated across all gas samples. Samples Y101X1 and DG-1 have a $^{20}Ne/^{36}Ar$ ratio of 0.104 and 0.051, respectively, which is depleted relative to ASW (0.14). These ratios can be accounted for by migration or open system degassing, while sample DG-15 has a $^{20}Ne/^{36}Ar$ ratio of 0.54, close to that of air (0.52), which may signify an equilibrium with a liquid phase. $^{20}Ne/^{36}Ar$ ratios show little difference at shallow and deeper depths, showing that vertical equilibration has occurred, with subsurface fluids being well mixed, while buoyant $^{3}He/^{4}He$ ratios are higher at shallow depths (Figure 35).

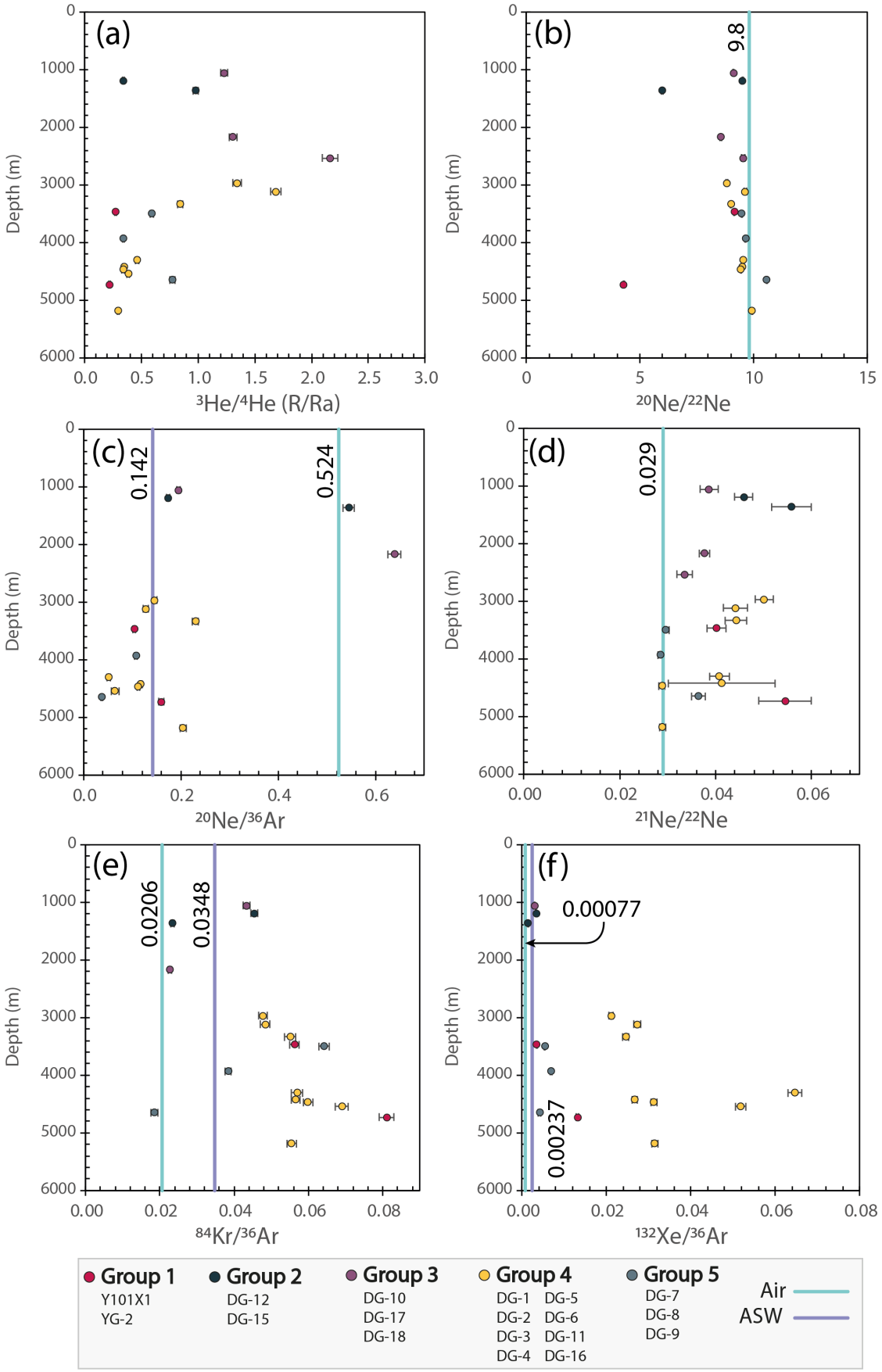

Figure 35 – Air, mantle, and crustal radiogenic noble gas ratios plotted vs well depth for Bohai Bay Basin gas samples. Air ratios are denoted by a blue line, while calculated ASW values are represented by a purple line.

3.6.2 He abundance, distribution, and mantle contributions in the HHD

Helium, the lightest and most mobile noble gas, ascends from geochemical reservoirs at variable depths within the crust and is trapped by deep circulating groundwaters on its way to the Earth's surface (Kipfer et al., 2002). Elevated ^{4}He signatures in samples are characteristic of the accumulation of a crustal component derived from the radioactive alpha decay of ^{232}Th, ^{235}U, ^{238}U (Ballentine and Burnard, 2002) along the following production pathways (Graham, 2002):

$$^{232}Th \Rightarrow {}^{208}Pb + 6\ {}^{4}He + 4\beta- \quad (80)$$

$$^{235}U \Rightarrow {}^{207}Pb + 7\ {}^{4}He + 4\beta- \quad (81)$$

$$^{238}U \Rightarrow {}^{206}Pb + 8\ {}^{4}He + 6\beta- \quad (82)$$

A prominent ^{3}He signature has long been established as a key indicator of magmatic activity and the presence of mantle-derived volatiles (Hilton et al., 2002). R/R_a ratios have been reported worldwide for various geological environments, including arc-related mid-ocean ridge basalt (MORB) mantle values of $8R_a$ (Craig and Lupton, 1976). Very high $^{3}He/^{4}He$ ratios, in excess of this MORB value, are also reported in mantle-derived xenoliths (Tolstikhin et al., 1974), Ocean Island Basalts (OIBs) (Kurz et al., 1983) and in continental rift zones (Scarsi and Craig, 1996). Magmatic He contributions are assumed when $^{3}He/^{4}He > 0.6R_a$ (Ballentine and Burnard, 2002). As many of the gas samples from the HHD are generally in excess of this value (n=8), it is reasonable to assume that these gases represent a mixture of primordial, radiogenic and atmospheric He consistent with a quantifiable input of mantle-derived gas.

Diapirisms of magma associated with the upwelling of hot, buoyant mantle material have been shown to exist at the base of large detachment faults within the Bohai Bay Basin (Wang et al., 2022a), and this is likely the source of a measurable ^{3}He influx. R/R_a values in samples from Group 3 (DG-10, DG-17 and DG-18) and Group 4 (DG-2 and DG-3) are especially consistent with the influence of a deeper magmatic component, as they have R/R_a values ranging from $1.23R_a$ – $2.37R_a$. These samples are located within the central Huanghua depression, from reservoirs located proximally to the Gangxi and Gangdong faults. Helium ratios (Figure 35) and concentrations (Figure 36a and b) correlate strongly with well depth, with high ^{3}He and ^{4}He concentrations found in shallower gas wells. Fault-controlled migration is likely the driving mechanism for the movement of He gases; however, no discernible trend exists between mantle-derived ^{3}He, crustal radiogenic ^{4}He, air-derived ^{20}Ne (Figure 36c), and $^{4}He/^{20}Ne$ ratios are far larger ($<10^{6}$) than $^{4}He/^{20}Ne_{air} = 0.319$ (Ozima and Podosek, 2002) suggesting that

atmospheric input is minimal and the accumulation of ^{3}He and ^{4}He in gas samples may not result from the same transport mechanism via groundwaters but through a degassing or dehydration of deeper material absent from the influence of water.

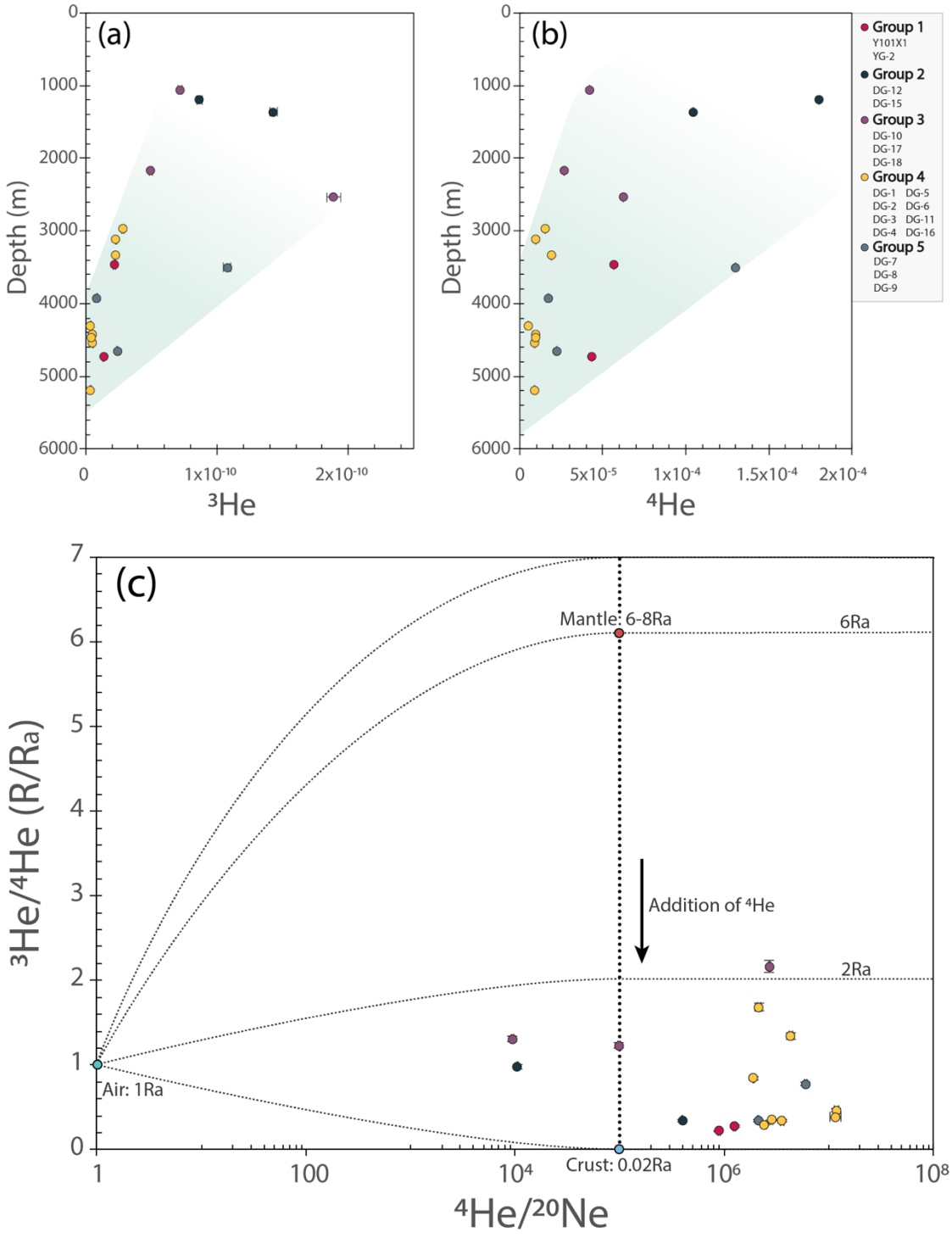

Figure 36 - (a) Mantle derived ^{3}He plotted vs well depth. (b) Crustal radiogenic ^{4}He concentrations plotted vs well depth. (c) $^{3}He/^{4}He$ vs $^{4}He/^{20}Ne$ correlation plot between crustal and mantle endmembers. Crustal-derived ^{4}He and $^{21}Ne^{*}$ record the history of fault-related fluid flow across the HHD, particularly the loss of ^{4}He due to faults acting as distributed conduits for the movement of gas to shallower regions. The interaction of ^{4}He and atmosphere-derived ^{20}Ne reveals the extent of groundwater control on the distribution of crustal radiogenic isotopes.

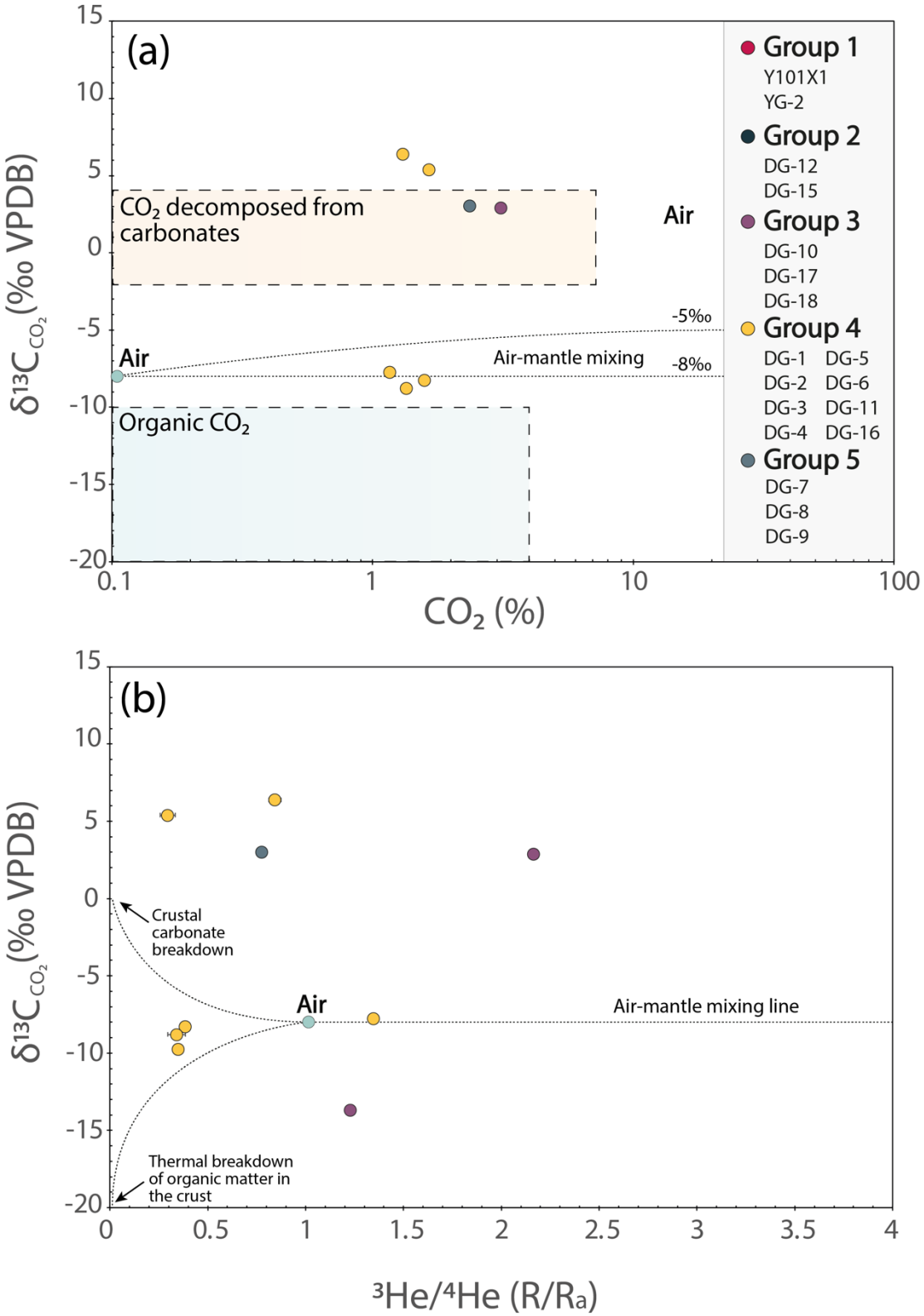

Figure 37 – Plot of $\delta^{13}C_{CO2}$ (‰ VPDB) versus (a) CO_2 content (%) and (b) R/R_a of natural gases in the Huanghua depression. These plots suggest contributions from the thermal breakdown of carbonates and the influence of a magmatic source on altering gas composition.

3.6.3 Carbon systematics; CO_2 origin, emplacement and He mixing relationships

The Bohai Bay Basin has a complex magmatic underplating where hot mantle upwelling, subsidence, and heat flow have dramatically altered the basin's evolution (Ju et al., 2022). Understanding the relationship between CO_2 production and degassing related to magmatism and other abiotic and biogenic processes is critical, thereby gaining insight into the mechanisms controlling degassing and its role in the global carbon cycle. CO_2 concentrations yielded from samples are relatively low, ranging from 0.06 to 3.1%. Although $\delta^{13}C_{CO2}$ data is not available for all samples, when plotted against CO_2 (%) and $^3He/^4He$ isotopic ratios, it reveals that two groups exist, distinguishing the origins of the CO_2 in the HHD (Figure 37a and b). Samples DG-7, DG-11, DG-16 and DG-17 have positive $\delta^{13}C_{CO2}$ values (3.02‰ to 6.39‰), highlighting that gas samples here may have been influenced by CO_2 decarbonisation from carbonate material (Marty and Tolstikhin, 1998, Deines, 1980). While DG-3, DG-4, DG-5, DG-6 and DG-10, which have $\delta^{13}C_{CO2}$ values that range from -13.695‰ to -7.756‰, are more strongly affected by organic CO_2 associated with the breakdown of organic matter due to thermal maturation (-25‰ to -35‰) and biogenic CO_2 derived from microbial metabolism (-10‰ to -24‰) (Whiticar, 1999), in addition to mantle-derived CO_2 which typically ranges from between -3‰ and -8‰ (Javoy et al., 1986).

CO_2 generation and emplacement are likely to have begun during intense Mesozoic volcanism periods associated with lithospheric thinning (Allen et al., 1997) and widespread tectonic and magmatic activity (Li and Qiu, 2017). Subsequently, the overall flux of mantle-derived CO_2 likely lessened due to reduced spreading rates toward the late Paleogene, prior to basin inversion and thermal subsidence in the early Neogene. CO_2 concentrations exhibit a linear increase in concentration with depth. These magmatic-related gases have emanated from considerable depth beneath the shale and highlight the role of magma upwelling in releasing CO_2 within the HHD, which is the main source of CO_2 (Zhang et al., 2008). CO_2 emplacement has therefore occurred before the maturation and migration of the shallower Eocene Shahejie fm. associated gases. To evaluate the complex geodynamics associated with subsurface degassing behaviours and the volatile fluxing of CO_2, we determine the extent of $CO_2/^3He$ fractionation (Figure 38). CO_2-He systematics of well gases from the HHD show mixing between crustal and magmatic gases and exhibit variable amounts of CO_2 loss relative to the initial $CO_2/^3He$. $CO_2/^3He$ ratios cluster around 10^9, consistent with MORB and hotspot gases (Marty and

Jambon, 1987). Gases from group 1 (YG-1 and Y101X1) & group 2 (DG-12 and DG-15) along the Wumaying, Koucun and Yangerzhuang faults are more distant from the large BDG detachment fault and contain $CO_2/^3He$ ratios between 10^6-10^7, with a lower contribution of CO_2 and ^3He. These eastern and southernmost gas samples also have elevated ^4He concentrations of between 43.49 to 180 x 10^{-6} cm^3 STP/cm^3, which are an order of magnitude greater than the residual gas samples and show that the processes resulting in the accumulation of CO_2 and radiogenic noble gases are varied.

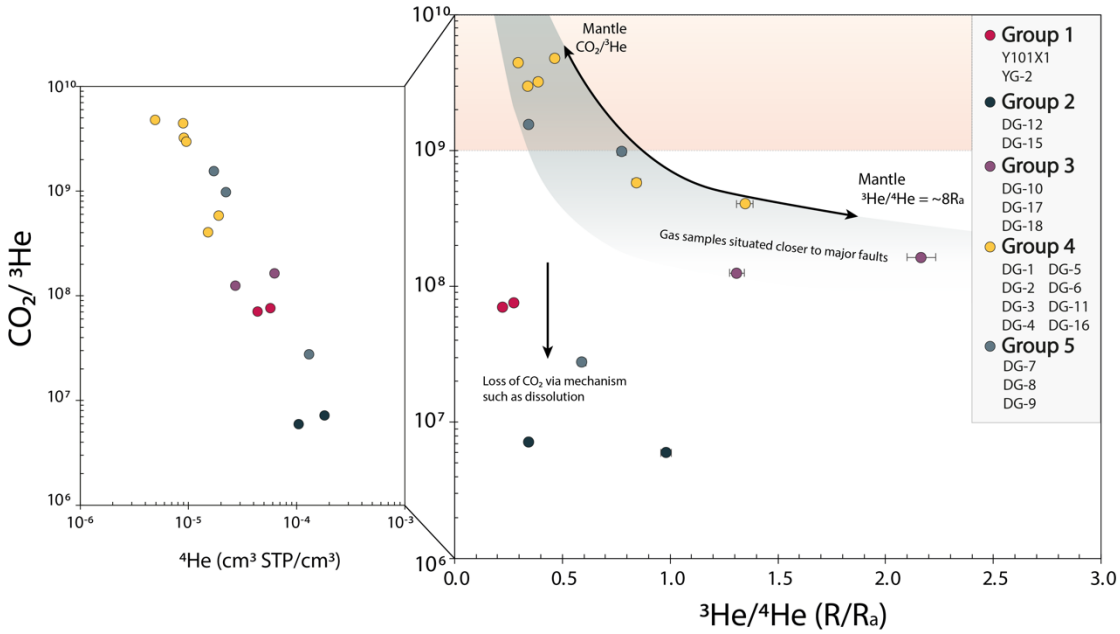

Figure 38 - $CO_2/^3He$ vs ^4He and $^3He/^4He$ (R/R_a) fractionation plot, with respective endmembers for mantle $CO_2/^3He$ and $^3He/^4He$ (Sano and Marty, 1995, Marty and Tolstikhin, 1998, Ballentine and Burnard, 2002). This plot also shows the potential loss of CO_2 by more than 2 orders of magnitude.

3.6.4 Methane and the deep carbon cycle

Methane (CH_4) is the most abundant gas in BBB samples, making up 52.69%-83.08% of the total measured sample composition. To understand the relationship between the origin of methane-rich gases and the geodynamic setting of the HHD, we closely examine the correlation between CH_4, C_2H_6 with air, crust and mantle-derived noble gases. Methane gas genesis can be characterised as abiotic, relating to the thermogenic decomposition of kerogen, or biotic, formed from the biodegradation of organic matter under anoxic conditions. Upon examination, gas samples closely resemble a thermogenic signature with low CH_4/C_2H_6 ratios. In contrast, samples from Group 2 (DG-12 and DG-15) have $CH_4/(C_2H_6+C_3H_8)$ values which are an order of magnitude higher than in other samples, which indicates these gasses have undergone greater migration (Sano et al., 2017), are sourced from a more thermally mature reservoir or result from possible mixing with microbially derived biogenic methane. Further evidence for an appreciable biogenic input within gas samples from the southern HHD is the more strongly positive $\delta^{13}C_{CH4}$ values coupled with high dryness coefficients in group 1 samples Y101X1 (0.940) and YG-2 (0.942).

$CH_4/^{36}Ar$ ratios are higher at greater depths, where predominantly thermogenic methanogenesis is responsible for methane production due to greater temperatures and pressures. Both the shallowest wells exist in Group 2 (DG-12 and DG-15), and these wells also contain higher ^{36}Ar, signifying they have likely migrated a great distance, potentially from the dehydration of the underlying Izanagi stagnant slab, while also encountering a greater abundance of air-derived noble gases dissolved in shallower groundwaters.

^3He and ^4He concentrations correlate well with CH_4 abundances, which could signify a common migration process. Progressive fault growth during periods of extension in the Paleocene-Eocene has likely allowed subsurface fluids to migrate large distances to shallower basinal margins along permeable discontinuities and large structural faults such as the Nandagang fault (NDG). In the Wumaying buried hill, the carbon isotope of ethane ($\delta^{13}C_{C2}$) is heavier than -22.0‰, consistent with coal-derived natural gases found in other basins within China, where $\delta^{13}C_{C2}$ is heavier than -28.0‰.

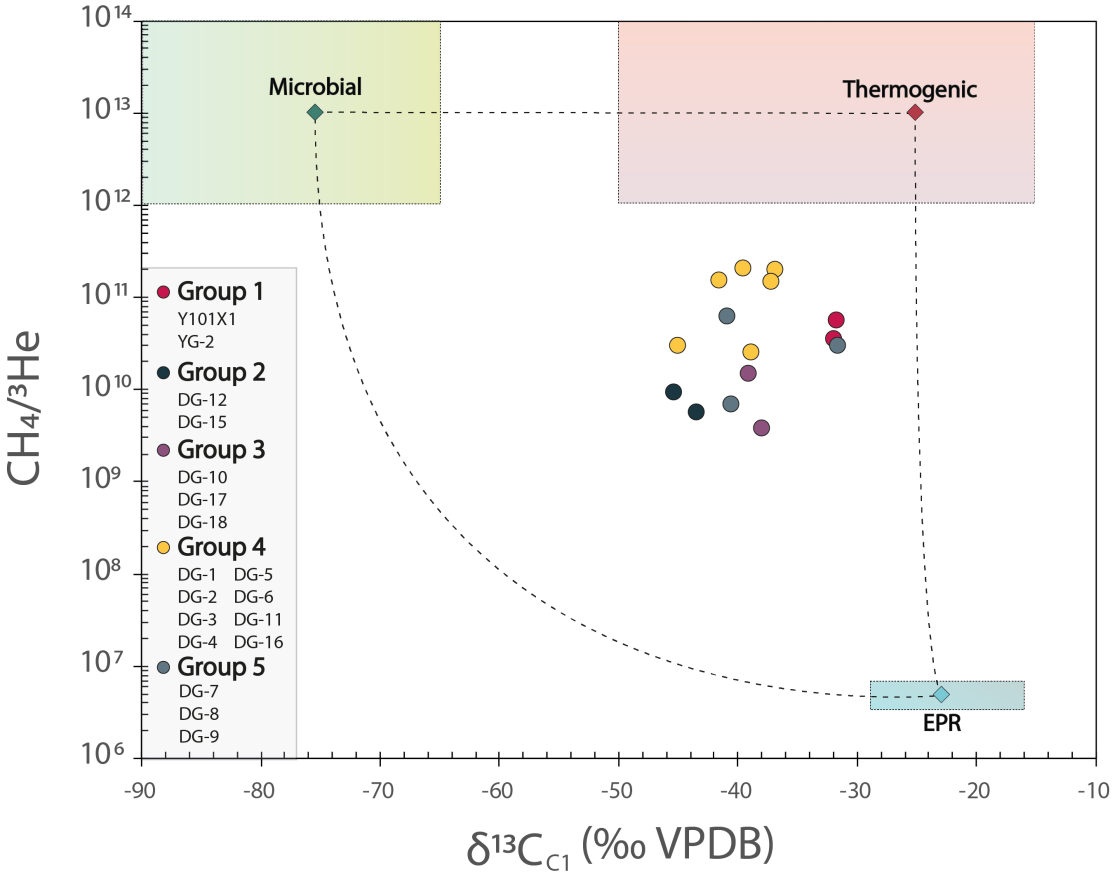

Figure 39 - $CH_4/^3He$ vs $\delta^{13}C_{CH4}$ (‰ VPDB) plot, used to understand the ratio of CH_4 to ^3He and the isotopic composition of the carbon. Dotted lines indicate the mixing lines between thermogenic, microbial and EPR (MORB, abiotic) endmembers. All gases fall within the bounds of these three end members.

Table 31 - Endmember contributions for Bohai Bay Basin gas samples following the methane deconvolution model (Sano et al., 2017).

Sample	$CH_4/^3He$ (x 10^9)	End-member contribution (%)		
		Abiotic	Thermogenic	Microbial
YG-2	57.84	8.60	77.45	13.95
Y101X1	35.66	13.98	71.44	14.58
DG-12	9.59	52.10	5.01	42.89
DG-1	199.93	2.45	73.73	23.82
DG-3	26.09	19.13	52.20	28.67
DG-4	151.14	3.26	72.01	24.73
DG-6	154.14	3.20	63.43	33.37
DG-7	30.24	16.49	69.58	13.93
DG-8	6.97	71.67	5.63	22.70
DG-9	63.92	7.78	60.08	32.15
DG-11	30.29	16.47	42.78	40.76
DG-16	209.05	2.34	68.38	29.28
DG-18	14.87	33.58	36.84	29.58

3.6.4.1 Deconvoluting methanogenic endmember contributions

All gas samples have $\delta^{13}C_1$ values that are lighter than -30‰, yet there exists a high degree of $\delta^{13}C_1$ fractionation (-31.637‰-45.050‰), which is evidence that thermogenic processes from the thermal cracking of kerogen are not purely responsible for this observed mixture and that samples comprise a mixture of methane formed via different mechanisms. We can apportion the various contributions to the mixed natural gas, as further assessment of the CH_4 in samples permits the identification of the distinct sources and processes responsible for generation related to abiotic, thermogenic and biogenic (microbial) sources (Figure 40).

As ^3He is synonymous with mantle contribution to fluids, it is possible to use $^3He/CH_4$ ratios and $\delta^{13}C_1$ values to distinguish the relative proportion in gas samples accounted for by the processes related to these three aforementioned endmembers; abiotic methanogenesis, which can result from magmatic influences such as serpentinization in ultramafic rocks, or thermogenic and microbial methanogenesis, which are both related to biogenic methane production.

Assuming that this mixing hypothesis is valid, it is possible to use the following equations (Sano et al., 2017) to determine the % contribution of E (abiotic), T (thermogenic) & M (microbial) CH_4 in samples:

$$\delta^{13}C_{Meas} = \delta^{13}C_{EPR} \times E + \delta^{13}C_{Ther} \times T + \delta^{13}C_{Micr} \times M \quad (83)$$

and,

$$\frac{1}{(CH_4/{}^3He)_{Meas}} = \frac{E}{(CH_4/{}^3He)_{EPR}} + \frac{T}{(CH_4/{}^3He)_{Ther}} + \frac{M}{(CH_4/{}^3He)_{Micr}} \quad (84)$$

where the sum of the abiotic, thermogenic and microbial CH_4 fractions is equal to 1:

$$E + T + M = 1 \quad (85)$$

For the above calculations, the following endmember values were used:

Table 32 - Endmember values used in this model. Thermogenic and microbial $CH_4/^3He$ values from Sakata et al. (1997).

	$\delta^{13}C_1$ (‰)	$CH_4/^3He$	$C_1/(C_2+C_3)$
Abiotic	-23	5×10^{-6}	625
Thermogenic	-25	1×10^{13}	10
Microbial	-75	1×10^{13}	20000

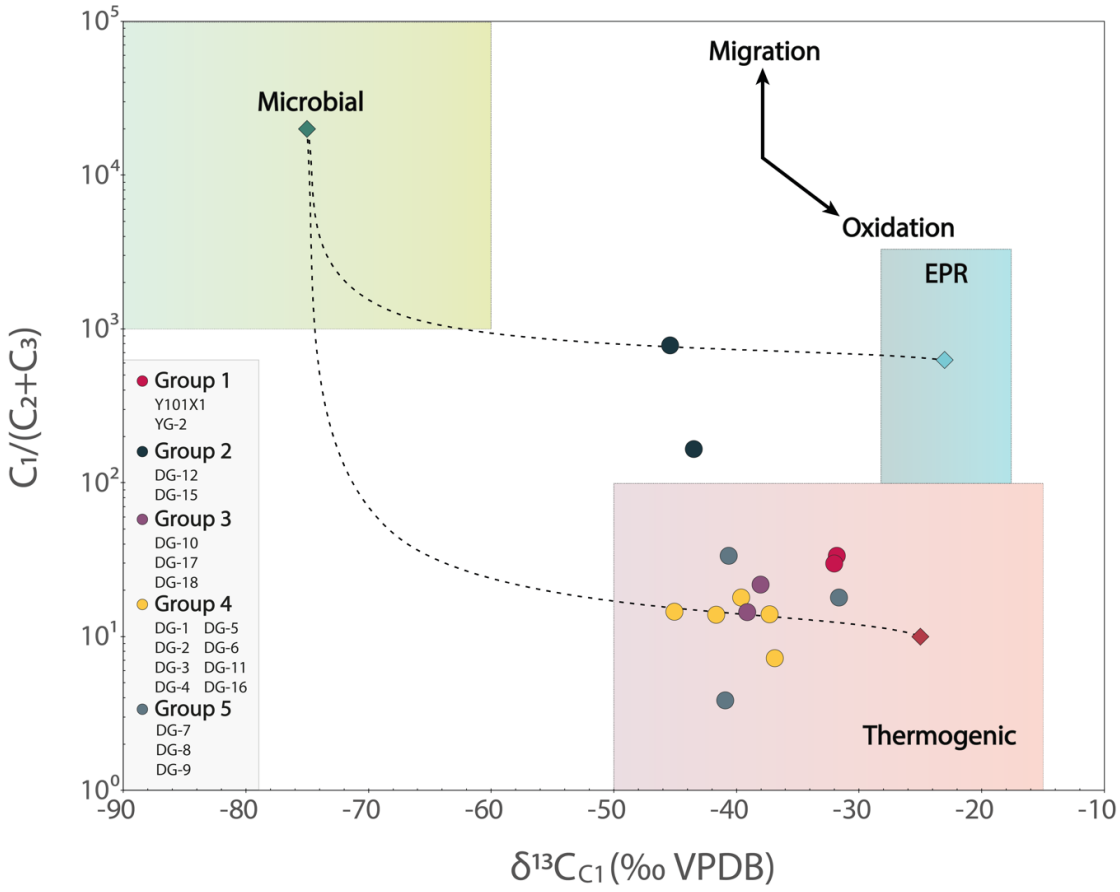

Figure 40 – Bernard diagram for gas samples within the HHD, showing $C_1/(C_2+C_3)$ vs $\delta^{13}C_{CH4}$ (‰ VPDB) and the differentiation between microbial (bacterial) methanogenesis and thermogenic methane production

Based on these deconvolution equations, the maximum abiotic methane contribution is 52.10% in sample DG-12 and 71.67% in sample DG-8. An appreciable microbial methane contribution exists in samples DG-12 and DG-15 (Figure 40), which lie east of the main central fault zone in the HHD. This sample also exhibits a gas dryness of 0.99805 and the highest CH_4 content in all gas samples (83.08%).

Group 1 samples (YG-2 and Y101X1) situated along the Wumaying Fault have $\delta^{13}C_{C2}$ values of -21.925‰ and 21.890‰, respectively, typical of coal-derived natural gases, which are generally heavier than -28.0‰ (Dai, 1992). According to the end-member contribution model, both YG-2 and Y101X1 are estimated to be highly thermogenic (77.45% and 71.44%), which is consistent with the complex multistage uplift and burial history that these Permian-age reservoirs have undergone (Zhang et al., 2019a).

This data supports the supposition that a high degree of heat flow exists in the south, near the Wumaying buried hill, and in the northeast in the Binhai slope, near the Dazhangtuo and Gangdong faults, where a similarly high thermogenic end-member contribution exists (>73.73%). DG-8, located within the Banqiao sub-sag, is distal from

these major faults, and the larger basin bounding listric faults, and the thermogenic contribution here is far lower (5.63%).

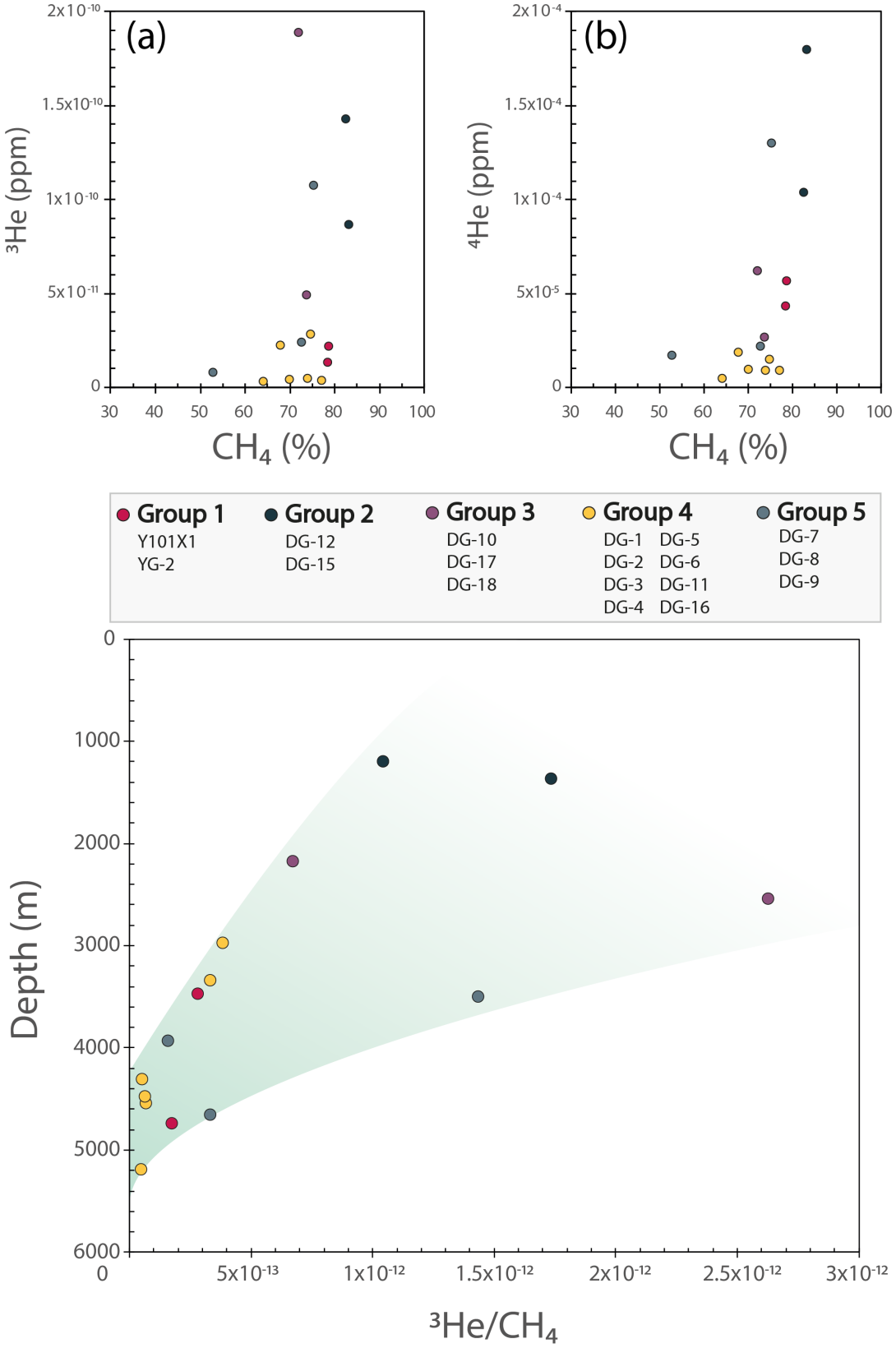

Figure 41 - (a) Magmatic-derived ^{3}He concentrations plotted against methane gas sample contribution (%). (b) Crustal radiogenic-derived ^{4}He concentrations plotted against methane gas sample contribution (%). (c) ^{3}He/CH$_4$ fractionation at differing depth intervals.

3.6.5 Methane and hydrogen generation in the HHD

3.6.5.1 CH_4 and H_2 genetic signatures

Hydrogen is widely distributed in gas samples (<22.01%), yet H_2 concentrations display little to no variance with depth between the shallowest gas wells, such as DG-12 (1196m) where H_2 = 0.14 cm^3 STP cm^{-3} and the deepest gas wells, e.g., DG-16 (5188m) where H_2 = 0.15 cm^3 STP cm^{-3}.

Uniform H_2 concentrations at different depths may be due to diffusion or a widespread, stratified mixing process in an open system. However, consumption during microbial metabolism or formation through chemical reactions (i.e., the Sabatier reaction), where coupled oxidation of H_2 and reduction of CO_2 produces CH_4, may be responsible for these phenomena, as well as the appreciable abiotic fraction and the diminished concentrations of CO_2 within gas samples. This chemical reaction is denoted by:

$$CO_2 + 4H_2 \rightarrow CH_4 + 2H_2O \quad (86)$$

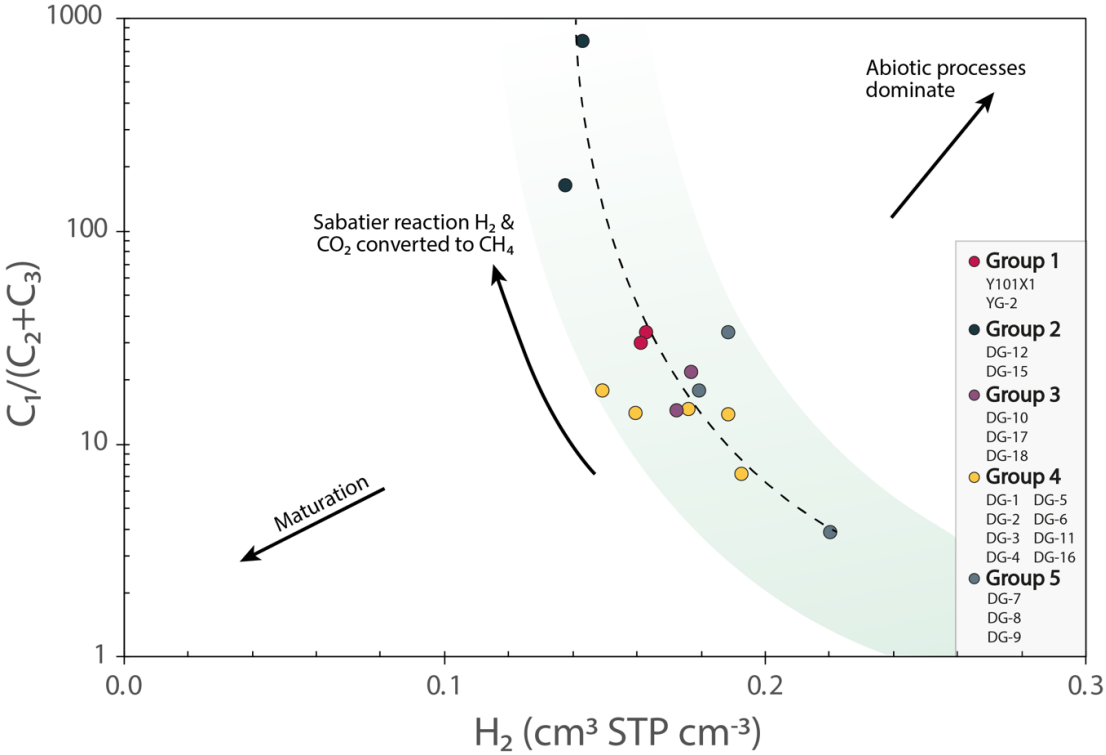

Figure 42 - Plot denoting the ratio of methane (C_1) to ethane (C_2) and propane (C_3) vs H_2 concentrations across the H.H.D. In samples DG-12 and DG-15, CH_4 predominates the gas, suggesting that it is relatively 'dry'. The dotted line represents a linear regression line between the maximum and minimum $C_1/(C_2+C_3)$ values.

3.6.5.2 Processes contributing to high CH_4 and H_2

Hydrogen can be generated abiotically through several processes, such as serpentinization, which involves the hydration of ultramafic rocks in the Earth's mantle. Fluids dominated by reduced gases such as CH_4 and high concentrations of H_2 (<30%) have been shown in various settings to be produced abiotically via water-rock interactions (Sherwood Lollar et al., 1993, Sherwood Lollar et al., 2002).

H_2 concentrations are high in gas samples that are $\delta^{13}C_{CH4}$ enriched, while H_2 concentrations are low in gas samples where $\delta^{13}C_{CH4}$ is depleted, which suggests that abiotic methanogenesis may exist in the deeper subsurface (Sherwood Lollar et al., 2006). Still, when considering δD, the deuterium to hydrogen isotope ratio involved in subsurface hydrogen production, there is a significant overlap of values, which makes delineating the source of methane and hydrogen complicated.

The Sabatier reaction and the Fischer-Tropsch process (FTP) are particularly relevant in CH_4 formation. They are prevalent abiotic mechanisms in the regions adjacent to the subduction of a hydrated oceanic lithosphere. An observable trend showing higher H_2 concentrations are associated with lower $C_1/(C_2+C_3)$ ratios suggests a mechanism where H_2 can abiotically form CH_4. (Figure 42).

Gas sample sources can be further distinguished by plotting $\delta^{13}C_{C1}$ vs δD_{C1}, which shows that diverse processes contribute to the origin of HHD gas samples (Figure 43), and gas samples are mostly early mature, thermogenic associated humic, with group 1 samples in the Wumaying buried hill have a distinctive geothermal or hydrothermal origin.

Methane-generating pathways are complicated by the interaction of H_2O from formation waters; however, H_2O can play a significant role in subsurface methanogenesis (Whiticar, 1999), namely through serpentinization. Serpentinization is common at subduction zones, whereby a mixing of serpentinite-derived water is mixed with CO_2-rich water. δD within gas samples is analysed to determine the fraction of recycled components, and those values above the reported MORB value (-60‰ to -80‰) represent a proportionally larger recycled component (Holland and Ballentine, 2006). δD in gas samples is significantly depleted in deuterium, and being much more negative than reported MORB values could suggest interaction with water with a lighter isotopic composition, such as meteoric water or hydrothermal fluids.

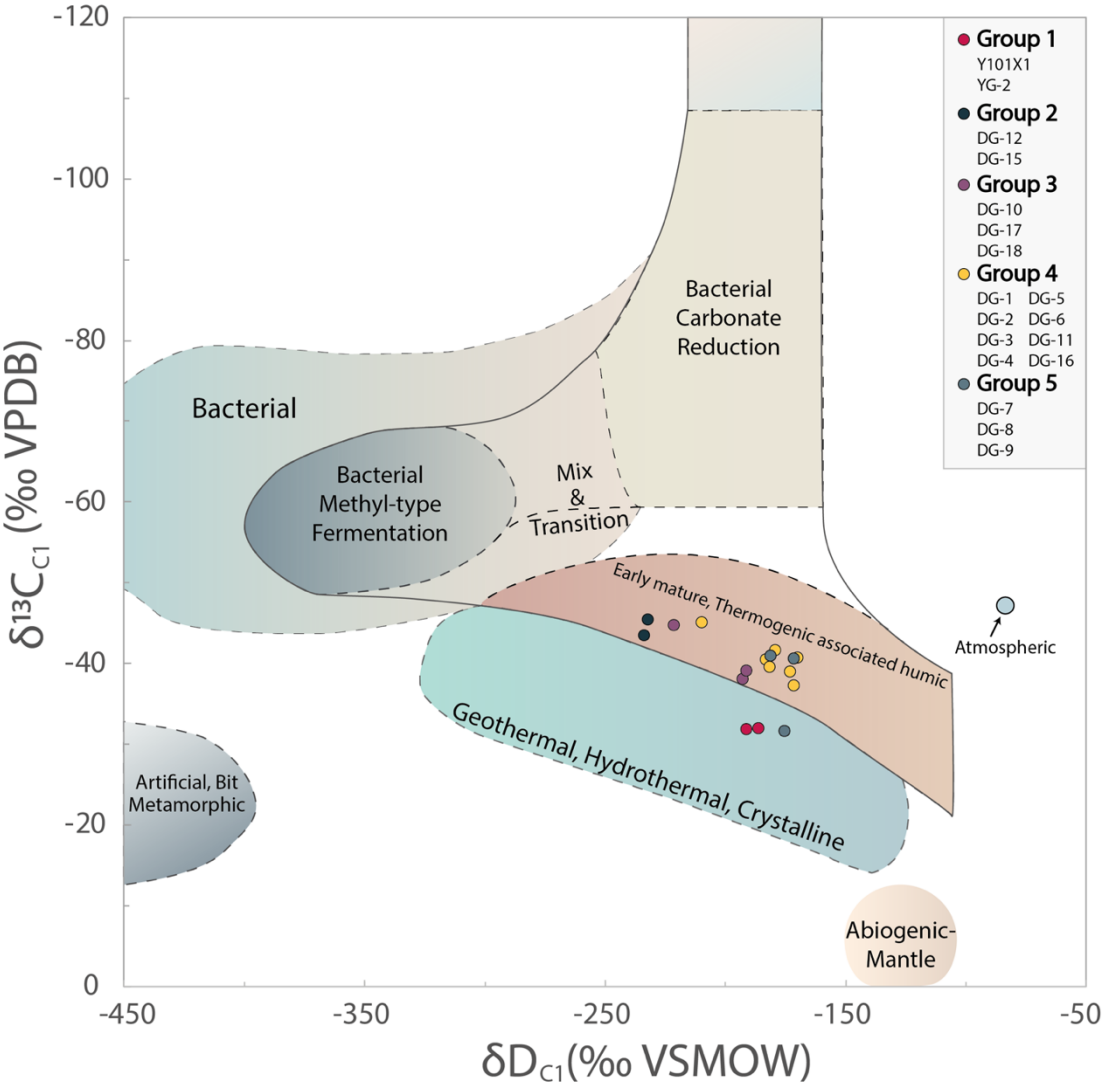

Figure 43 - CD diagram for classification of bacterial and thermogenic natural gas, comprising $\delta^{13}C_{CH4}$ vs δD_{CH4}, ranges for methanogenic types are from Whiticar (1999).

3.6.5.3 Assessing the contribution of atmosphere-derived noble gases in dissolved in water

It is possible to assess the contribution of noble gases (^{20}Ne, ^{36}Ar, ^{84}Kr, ^{132}Xe) derived from air, which are imprinted during the exchange of gas with water at recharge, then transported through the subsurface dissolved in groundwater or via water-saturated pore during sediment deposition. It is necessary to characterise the extent of atmosphere-derived noble gas interaction to determine the magnitude of the exchange of reservoir fluids with surrounding groundwaters.

The solubility (S) of the noble gases increases with atomic mass ($S_{Xe} > S_{Kr} > S_{Ar} > S_{Ne}$), and the total dissolved concentrations are principally controlled by temperature, recharge elevation and salinity. We have therefore determined the conditions for recharge as 10°C (Yuan et al., 2017) near sea-level elevation, while we also assume this air-saturated

groundwater (ASW) comprises an unfractionated excess air component, containing 15% excess Ne (Kipfer et al., 2002). Consequently, the initial ASW ratios are quantified to be $(^{20}Ne/^{36}Ar)_{ASW}$ = 0.0142, $(^{84}Kr/^{36}Ar)_{ASW}$ = 0.0348 and $(^{132}Xe/^{36}Ar)_{ASW}$ = 0.00237. The successive partitioning of this initial noble gas inventory that occurs when water is in contact with a hydrocarbon phase is governed by Henry's Law. The geothermal gradient in the Huanghua depression ranges from 24°C/km to 55°C/km, with an average value of 35°C/km (Zuo et al., 2017), while paleosalinities of the clastic terrigenous Shahejie formation have been measured at 260 g/L (4.45 M) (Zhang et al., 2019d). Incorporating the above parameters, dimensionless Henry's constants (K_i^d) have been calculated for reservoir depths ranging from 1000-5000m and corrected for fugacity and activity coefficients.

Table 33 - Henry's constants reported for Noble gases at different reservoir depths

			Dimensionless Henry's constants (K_i^d)				
	Depth (m)	Temperature °C	He	Ne	Ar	Kr	Xe
Recharge	0	10	155.7	136.2	45.4	27.9	16.6
Reservoir	1000	50	101.7	94.9	43.6	30.2	21.1
Reservoir	2000	85	77.7	77.9	45.5	35.0	23.9
Reservoir	3000	120	55.5	59.1	39.1	32.4	23.5
Reservoir	4000	155	37.8	43.0	30.3	26.8	20.7
Reservoir	5000	190	25.6	30.8	22.0	20.9	17.6

Air-derived ^{20}Ne and ^{36}Ar values show extensive fractionation from ASW and air values (0.156) and correlate negatively with magmatic-derived $CO_2/^3He$, which shows that groundwater mixing and the availability of H_2O plays a role in controlling the $CO_2/^3He$ content in different gas reservoirs (Figure 44). This correlation highlights abiotic methanation via a Sabatier reaction as a likely contributing source of determinable CH_4 and H_2 concentrations in the HHD via the removal of CO_2.

Air-derived $^{84}Kr/^{36}Ar$ values in samples are also above the calculated ASW value (Figure 46), but when adjusted for a 200% - 400% excess Kr component, these gas samples fit the modelled solubility exsolution curve. $^{132}Xe/^{36}Ar$ ratios also fit the Rayleigh fractionation line, except for group 4 samples associated with the Binhai fault, which have ~800% excess Xe (Figure 47).

During the subduction and recycling of the Pacific oceanic crust into the Earth's mantle, increases in pressure and temperature cause the expulsion of pore water and widespread dehydration of hydrous minerals, termed 'wet upwelling' (Kuritani et al., 2019). This

results in the up-dip movement of a large amount of H_2O, as well as potentially highly soluble Kr and Xe, and other volatiles into the overlying mantle wedge and crust.

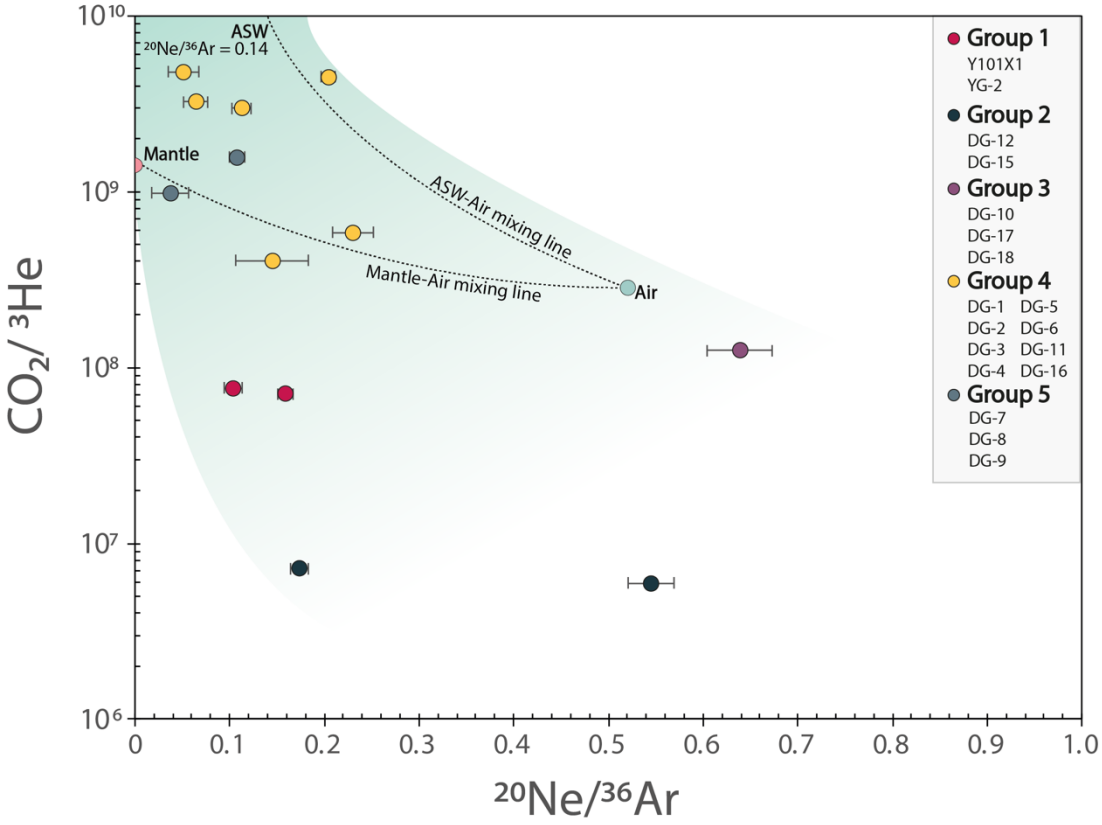

Figure 44 - $CO_2/^3He$ vs $^{20}Ne/^{36}Ar$. $CO_2/^3He$ correlates with air-derived $^{20}Ne/^{36}Ar$, which signals that groundwater plays a role in controlling $CO_2/^3He$ ratios

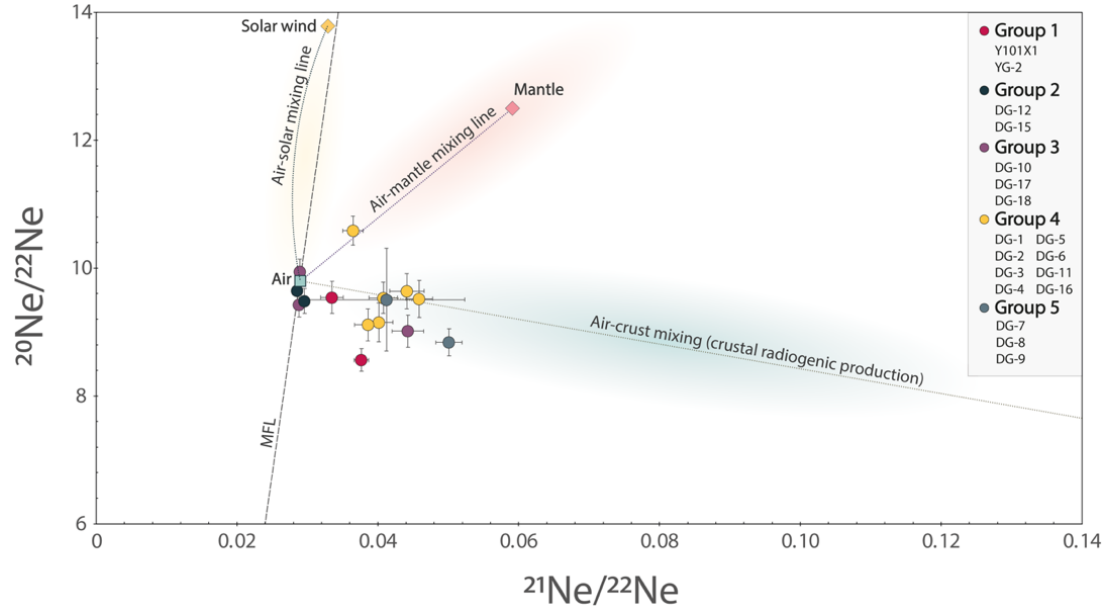

Figure 45 - Isotopic ratios of neon (Ne) in BBB gas samples plotted on a three-isotope graph. Data points represent measured $^{20}Ne/^{22}Ne$ vs $^{21}Ne/^{22}Ne$ ratios. The diagram illustrates the isotopic composition of neon from different sources, including the mantle, solar wind, and atmospheric components. Mixing lines indicate the potential mixing trends between air-derived neon and mantle-derived neon, as well as air-crust mixing, suggesting crustal radiogenic production.

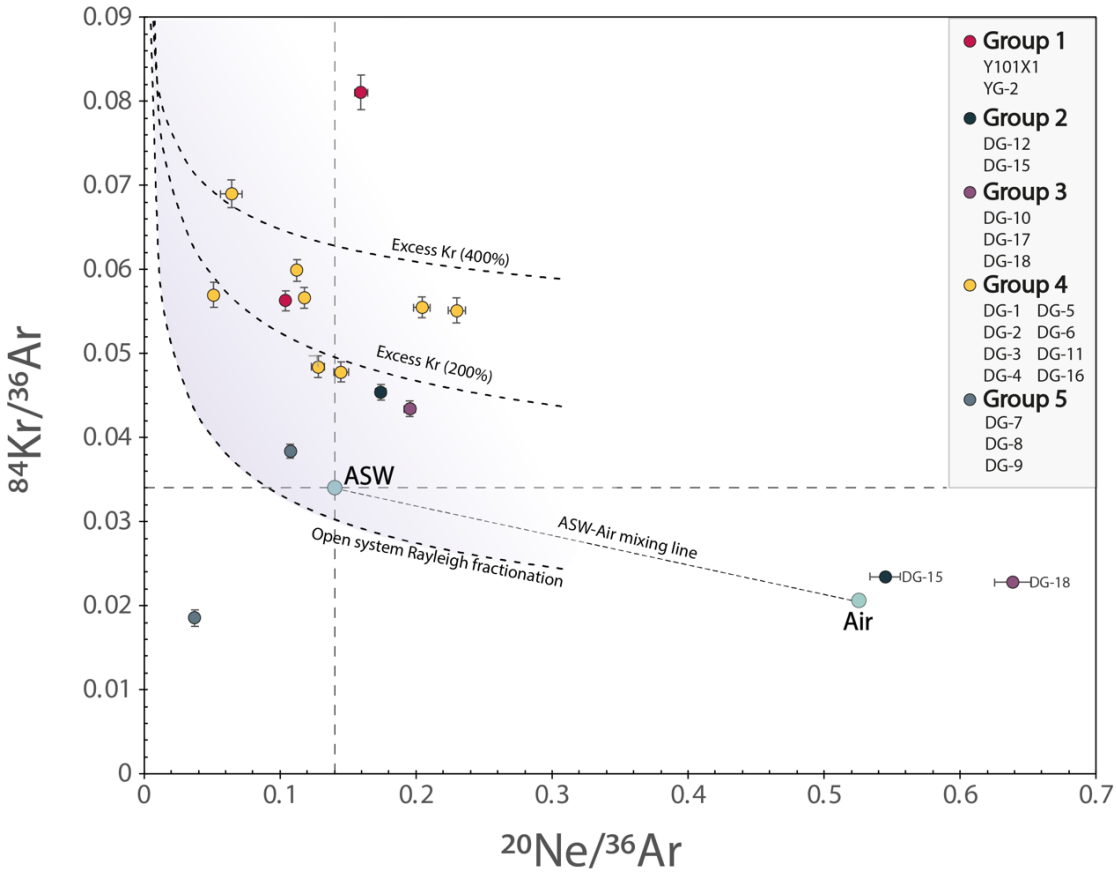

Figure 46 – Plot of elemental ratios $^{84}Kr/^{36}Ar$ vs $^{20}Ne/^{36}Ar$ for BBB gas samples, demonstrating the isotopic fractionation and mixing of heavier Kr and lighter Ne noble gases. The dashed lines represent theoretical Rayleigh fractionation curves for krypton, with the shaded area indicating excess krypton concentrations (200% and 400% above atmospheric levels). The ASW-Air mixing line denotes the mixing between air-saturated water (ASW) and atmospheric air, with the 'Air' data point showing the atmospheric endmember.

Xe/Ar elemental ratios are highly enriched in Xe compared to ASW and the atmosphere and Xe enrichment would require a gas-rich mantle reservoir which could flux large amounts of Xe into the convecting mantle (Porcelli and Wasserburg, 1995), yet there is thought to exist a large accretionary component in the mantle, where an excess of Xe isotopes could exist, possibly related to seawater recycling into the mantle (Ballentine and Holland, 2008). Kr and Xe isotope ratios are similar to air, this has been argued to arise from a recycled, unfractionated seawater component due to subduction of the oceanic lithosphere (Holland and Ballentine, 2006).

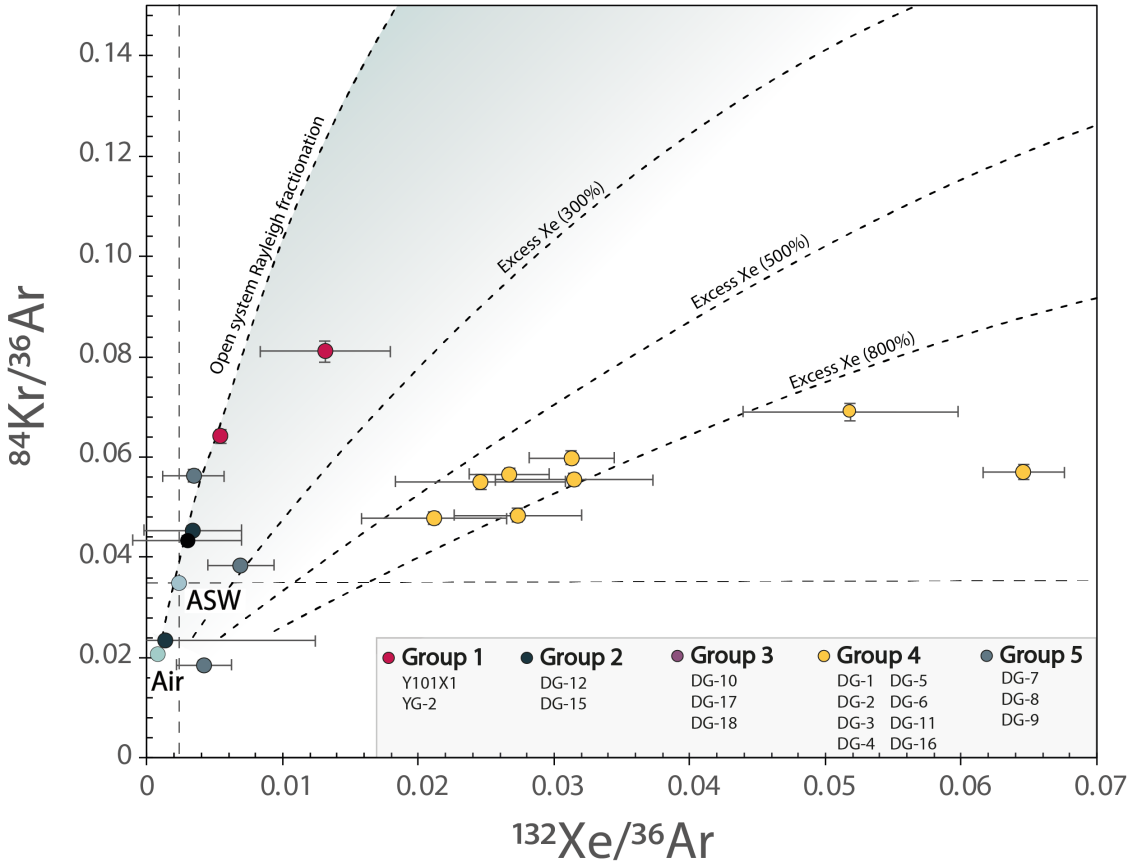

Figure 47 – Plot of elemental ratios of $^{84}Kr/^{36}Ar$ vs $^{132}Xe/^{36}Ar$. This plot delineates excess xenon isotopic ratios, denoted by the dashed lines, which indicate 300%, 500%, and 800% enrichment over ASW Xe values. The gradient-shaded area illustrates the trajectory of modelled open-system Rayleigh fractionation, which Groups 1, 2, 3 and 5 adhere to. Group 4 samples more closely match the Excess Xe (800%) modelled line.

Figure 48 – Conceptual diagram illustrating the geodynamic setting and Paleogene rifting episode associated with the development of the Huanghua depression within the Bohai Bay Basin, highlighting the source of CO_2, H_2O, H_2, CH_4, noble gases and other volatiles. CO_2 sourced from magmatic outgassing interacts with H_2 via the Sabatier reaction under high temperature and pressure, and is responsible for a proportion of the abiotic CH_4 production. Diapirisms of magma at the base of large detachment faults provide the source of the determinable magmatic ^{3}He in samples.

3.7 Conclusion

There is a distinguishable mantle component sourced from magmatic material, highlighted in $^{3}He/^{4}He$ ratios (R/R_a = 0.59 - 2.17), with a measurable influence from crustal radiogenic noble gases. Abundant H_2O fluid availability, sourced from well-mixed, recharged meteoric waters (evidenced by noble gas ratios that plot close to ASW ratios) and dehydration of minerals emanating from the subducted stagnant slab of the Izanagi plate. Basin-wide faulting facilitates fluid migration pathways, enabling this water to penetrate and circulate shallower rock and allowing mantle and crustal derived ^{3}He and ^{4}He to accumulate in shallower reservoirs. High concentrations of measured H_2 are further evidence of a redox environment that possibly expedites the production of abiotic CH_4 and microbial methanogenesis where H_2 is a by-product of biological processes. Due to the geological setting and associated magmatism of the Bohai Bay Basin, it is reasonable to assume that a portion of this H_2 derives from reactions involving high-temperature water-rock interactions (i.e., serpentinization).

The proximity of faults substantially influences the extent of fluid migration, serving as critical conduits for CO_2 mobilisation. This, in turn, can lead to the displacement of CH_4 by CO_2 in samples. In addition to facilitating fluid flow, faults can act as barriers, leading to lower atmospheric noble gas abundances in isolated samples across the BBB. The genesis of CO_2 is likely associated with intense volcanism during the Mesozoic era. However, a positive correlation exists between CO_2 concentrations and $C_1/(C_2+C_3)$ ratios, suggesting a CO_2-induced displacement of CH_4. Moreover, substantial $\delta^{13}C_{CO2}$ fractionation, ranging from -13.695‰ to -6.390‰, indicates that the injection of CO_2 postdates hydrocarbon maturation.

Unravelling the origins and routes of methane formation and migration in the basin is complicated by the basin's multi-stage tectonic history and the overlapping values of distinct methane-generating sources. Nonetheless, understanding these mechanisms is vital for future sustainable resource management and understanding the complex interplay of geochemical and geological processes shaped by the basin's dynamic tectonic history.

MANUSCRIPT 2 REFERENCES

Aeschbach-Hertig, W., Solomon, D.K., 2013. Noble gas thermometry in groundwater hydrology. The noble gases as geochemical tracers, 81-122.

Allen, M.B., Macdonald, D.I.M., Xun, Z., Vincent, S.J., Brouet-Menzies, C., 1997. Early Cenozoic two-phase extension and late Cenozoic thermal subsidence and inversion of the Bohai Basin, northern China. Marine and Petroleum Geology 14(7), 951-972. doi.org/https://doi.org/10.1016/S0264-8172(97)00027-5.

Allen, M.B., Macdonald, D.I.M., Xun, Z., Vincent, S.J., Brouet-Menzies, C., 1998. Transtensional deformation in the evolution of the Bohai Basin, northern China. Geological Society, London, Special Publications 135(1), 215-229. doi.org/doi:10.1144/GSL.SP.1998.135.01.14.

Ballentine, C.J., Burgess, R., Marty, B., 2002. Tracing Fluid Origin, Transport and Interaction in the Crust. Reviews in Mineralogy and Geochemistry 47(1), 539-614. doi.org/10.2138/rmg.2002.47.13.

Ballentine, C.J., Burnard, P.G., 2002. Production, Release and Transport of Noble Gases in the Continental Crust. Reviews in Mineralogy and Geochemistry 47(1), 481-538. doi.org/10.2138/rmg.2002.47.12.

Ballentine, C.J., Holland, G., 2008. What CO2 well gases tell us about the origin of noble gases in the mantle and their relationship to the atmosphere. Philosophical Transactions of the Royal Society A: Mathematical, Physical and Engineering Sciences 366(1883), 4183-4203.

Bottomley, D.J., Ross, J.D., Clarke, W.B., 1984. Helium and neon isotope geochemistry of some ground waters from the Canadian Precambrian Shield. Geochimica et Cosmochimica Acta 48(10), 1973-1985. doi.org/https://doi.org/10.1016/0016-7037(84)90379-X.

Burnard, P., Graham, D., Turner, G., 1997. Vesicle-Specific Noble Gas Analyses of "Popping Rock": Implications for Primordial Noble Gases in Earth. Science 276(5312), 568-571. doi.org/10.1126/science.276.5312.568.

Cao, C., Lv, Z., Li, L., Du, L., 2016. Geochemical characteristics and implications of shale gas from the Longmaxi Formation, Sichuan Basin, China. Journal of Natural Gas Geoscience 1(2), 131-138. doi.org/https://doi.org/10.1016/j.jnggs.2016.05.001.

Cao, C., Zhang, M., Li, L., Wang, Y., Li, Z., Du, L., Holland, G., Zhou, Z., 2020. Tracing the sources and evolution processes of shale gas by coupling stable (C, H) and noble gas isotopic compositions: Cases from Weiyuan and Changning in Sichuan Basin, China. Journal of Natural Gas Science and Engineering 78, 103304. doi.org/https://doi.org/10.1016/j.jngse.2020.103304.

Cao, C., Zhang, M., Tang, Q., Yang, Y., Lv, Z., Zhang, T., Chen, C., Yang, H., Li, L., 2018. Noble gas isotopic variations and geological implication of Longmaxi shale gas in Sichuan Basin, China. Marine and Petroleum Geology 89, 38-46. doi.org/10.1016/j.marpetgeo.2017.01.022.

Chang, C.-y., 1991. Geological characteristics and distribution patterns of hydrocarbon deposits in the Bohai Bay Basin, east China. Marine and Petroleum Geology 8(1), 98-106.

Chen, C., Huang, J., Chen, J., Tian, X., 1984. Depositional models of tertiary rift basins, eastern China, and their application to petroleum prediction. Sedimentary Geology 40(1), 73-88. doi.org/https://doi.org/10.1016/0037-0738(84)90040-X.

Chen, S., Wang, H., Wu, Y., Huang, C., Wang, J., Xiang, X., Ren, P., 2014. Stratigraphic architecture and vertical evolution of various types of structural slope breaks in Paleogene Qikou sag, Bohai Bay Basin, Northeastern China. Journal of Petroleum Science and Engineering 122, 567-584. doi.org/https://doi.org/10.1016/j.petrol.2014.07.003.

Craig, H., Lupton, J.E., 1976. Primordial neon, helium, and hydrogen in oceanic basalts. Earth and Planetary Science Letters 31(3), 369-385. doi.org/https://doi.org/10.1016/0012-821X(76)90118-7.

Dai, J., 1992. Identification and distinction of various alkane gases. Science in China Series B-Chemistry 35(10), 1246-1257.

Deines, P., 1980. The isotopic composition of reduced organic carbon. Handbook of environmental isotope geochemistry.

Eymold, W.K., Walsh, T.B., Moortgat, J., Grove, B.S., Darrah, T.H., 2021. Constraining fault architecture and fluid flow using crustal noble gases. Applied Geochemistry 129, 104954. doi.org/https://doi.org/10.1016/j.apgeochem.2021.104954.

Graham, D.W., 2002. Noble Gas Isotope Geochemistry of Mid-Ocean Ridge and Ocean Island Basalts: Characterization of Mantle Source Reservoirs. Reviews in Mineralogy and Geochemistry 47(1), 247-317. doi.org/10.2138/rmg.2002.47.8.

Guofa, L., Mingqiang, C., Hui, Z., 2010. Effects of Near-Surface Absorption on Reflection Characteristics of Continental Interbedded Strata: the Dagang Oilfield as an Example. Acta Geologica Sinica - English Edition 84(5), 1306-1314. doi.org/https://doi.org/10.1111/j.1755-6724.2010.00299.x.

Györe, D., Tait, A., Hamilton, D., Stuart, F.M., 2019. The formation of NeH+ in static vacuum mass spectrometers and re-determination of 21Ne/20Ne of air. Geochimica et Cosmochimica Acta 263, 1-12. doi.org/https://doi.org/10.1016/j.gca.2019.07.059.

Hellinger, S.J., Shedlock, K.M., Sclater, J.G., Ye, H., 1985. The Cenozoic evolution of the North China Basin. Tectonics 4(4), 343-358. doi.org/https://doi.org/10.1029/TC004i004p00343.

Hilton, D.R., Fischer, T.P., Marty, B., 2002. Noble gases and volatile recycling at subduction zones. Reviews in Mineralogy & Geochemistry 47, 319-370.

Holland, G., Ballentine, C.J., 2006. Seawater subduction controls the heavy noble gas composition of the mantle. Nature 441(7090), 186-191. doi.org/10.1038/nature04761.

Hunt, A., Darrah, T., J. Poreda, R., 2012. Determining the source and genetic fingerprint of natural gases using noble gas geochemistry: A northern Appalachian Basin case study. AAPG Bulletin 96, 1785-1811. doi.org/10.1306/03161211093.

Javoy, M., Pineau, F., Delorme, H., 1986. Carbon and nitrogen isotopes in the mantle. Chemical geology 57(1-2), 41-62.

Jin, F., Wang, X., Li, H., Wu, X., Fu, L., Lou, D., Zhang, J., Feng, J., 2019. Formation of the primary petroleum reservoir in Wumaying inner buried-hill of Huanghua Depression, Bohai Bay Basin, China. Petroleum Exploration and Development 46(3), 543-552. doi.org/https://doi.org/10.1016/S1876-3804(19)60034-0.

Ju, Y., Wang, G., Li, S., Sun, Y., Suo, Y., Somerville, I., Li, W., He, B., Zheng, M., Yu, K., 2022. Geodynamic mechanism and classification of basins in the Earth system. Gondwana Research 102, 200-228. doi.org/https://doi.org/10.1016/j.gr.2020.08.017.

Kipfer, R., Aeschbach-Hertig, W., Peeters, F., Stute, M., 2002. Noble Gases in Lakes and Ground Waters. Reviews in Mineralogy and Geochemistry 47(1), 615-700. doi.org/10.2138/rmg.2002.47.14.

Kuritani, T., Xia, Q.-K., Kimura, J.-I., Jia, L., Shimizu, K., Ushikubo, T., Zhao, D., Nakagawa, M., Yoshimura, S., 2019. Buoyant hydrous mantle plume from the mantle transition zone. Scientific Reports 9, 6549. doi.org/10.1038/s41598-019-43103-y.

Kurz, M.D., Jenkins, W.J., Hart, S.R., Clague, D., 1983. Helium isotopic variations in volcanic rocks from Loihi Seamount and the Island of Hawaii. Earth and Planetary Science Letters 66, 388-406. doi.org/https://doi.org/10.1016/0012-821X(83)90154-1.

Lee, J.-Y., Marti, K., Severinghaus, J.P., Kawamura, K., Yoo, H.-S., Lee, J.B., Kim, J.S., 2006. A redetermination of the isotopic abundances of atmospheric Ar. Geochimica et Cosmochimica Acta 70(17), 4507-4512. doi.org/https://doi.org/10.1016/j.gca.2006.06.1563.

Li, L., Qiu, N., 2017. The initiation and tectonic regimes of the Cenozoic extension in the Bohai Bay Basin, North China revealed by numerical modelling. Journal of Asian Earth Sciences 140, 92-107. doi.org/https://doi.org/10.1016/j.jseaes.2017.03.039.

Lu, J., Lin, R., Liu, C., Li, Y., Xiao, Z., He, Q., 2019. Genesis and origin of natural gas in the Beidagang structural belt of Dagang oilfield. Petroleum Science and Technology 37(13), 1501-1508. doi.org/10.1080/10916466.2018.1511591.

Marty, B., Jambon, A., 1987. C3He in volatile fluxes from the solid Earth: implications for carbon geodynamics. Earth and Planetary Science Letters 83(1), 16-26. doi.org/https://doi.org/10.1016/0012-821X(87)90047-1.

Marty, B., Tolstikhin, I.N., 1998. CO2 fluxes from mid-ocean ridges, arcs and plumes. Chemical Geology 145(3), 233-248. doi.org/https://doi.org/10.1016/S0009-2541(97)00145-9.

Miao, Q., Xu, C., Hao, F., Yin, J., Wang, Q., Xie, M., Cao, Y., Zou, H., 2020. Roles of fault structures on the distribution of mantle-derived CO2 in the Bohai Bay basin, NE China. Journal of Asian Earth Sciences 197, 104398. doi.org/https://doi.org/10.1016/j.jseaes.2020.104398.

Niedermann, S., Graf, T., Marti, K., 1993. Mass spectrometric identification of cosmic-ray-produced neon in terrestrial rocks with multiple neon components. Earth and Planetary Science Letters 118(1), 65-73. doi.org/https://doi.org/10.1016/0012-821X(93)90159-7.

Ozima, M., Podosek, F., 2002. Noble Gas Geochemistry. Noble Gas Geochemistry, by Minoru Ozima and Frank A. Podosek, pp. 300. ISBN 0521803667. Cambridge, UK: Cambridge University Press, December 2001. 367.

Porcelli, D., Ballentine, C., Wieler, R., 2002. An Overview of Noble Gas Geochemistry and Cosmochemistry. Reviews in Mineralogy & Geochemistry - REV MINERAL GEOCHEM 47, 1-19. doi.org/10.2138/rmg.2002.47.1.

Porcelli, D., Wasserburg, G.J., 1995. Mass transfer of xenon through a steady-state upper mantle. Geochimica et Cosmochimica Acta 59(10), 1991-2007. doi.org/https://doi.org/10.1016/0016-7037(95)00122-0.

Pu, X., Zhao, X., Li, Y., Chen, R., Zhou, L., Yan, Z., Xiao, D., 2018. Paleochannel restoration and petroleum geological significance of Neogene in Huanghua depression. Shiyou Xuebao/Acta Petrolei Sinica 39(2), 163-171. doi.org/10.7623/syxb201802004.

Pu, X., Zhou, L., Wang, W., Han, W., Xiao, D., Liu, H., Chen, C., Zhang, W., Yuan, X., Lu, Y., Liu, S., 2013. Medium-deep clastic reservoirs in the slope area of Qikou sag, Huanghua depression, Bohai Bay Basin. Petroleum Exploration and Development 40(1), 38-51. doi.org/https://doi.org/10.1016/S1876-3804(13)60004-X.

Pu, X., Zhou, L., Xiao, D., Hua, S., Chen, C., Yuan, X., Han, G., Zhang, W., 2011. Lacustrine carbonates in the southwest margin of the Qikou Sag, Huanghua Depression, Bohai Bay Basin. Petroleum Exploration and Development 38(2), 136-144. doi.org/https://doi.org/10.1016/S1876-3804(11)60022-0.

Qi, J., Yang, Q., 2010. Cenozoic structural deformation and dynamic processes of the Bohai Bay basin province, China. Marine and Petroleum Geology 27(4), 757-771. doi.org/https://doi.org/10.1016/j.marpetgeo.2009.08.012.

Qin, S., Zhang, Y., Zhao, C., Zhou, Z., 2018. Geochemical evidence for in situ accumulation of tight gas in the Xujiahe Formation coal measures in the central Sichuan Basin, China. International Journal of Coal Geology 196, 173-184. doi.org/https://doi.org/10.1016/j.coal.2018.07.009.

Ren, J., Tamaki, K., Li, S., Junxia, Z., 2002. Late Mesozoic and Cenozoic rifting and its dynamic setting in Eastern China and adjacent areas. Tectonophysics 344(3), 175-205. doi.org/https://doi.org/10.1016/S0040-1951(01)00271-2.

Sakata, S., Sano, Y., Maekawa, T., Igari, S.-I., 1997. Hydrogen and carbon isotopic composition of methane as evidence for biogenic origin of natural gases from the

Green Tuff Basin, Japan. Organic Geochemistry 26(5), 399-407. doi.org/https://doi.org/10.1016/S0146-6380(97)00005-3.

Sano, Y., Kinoshita, N., Kagoshima, T., Takahata, N., Sakata, S., Toki, T., Kawagucci, S., Waseda, A., Lan, T., Wen, H., Chen, A.-T., Lee, H., Yang, T.F., Zheng, G., Tomonaga, Y., Roulleau, E., Pinti, D.L., 2017. Origin of methane-rich natural gas at the West Pacific convergent plate boundary. Scientific Reports 7(1), 15646. doi.org/10.1038/s41598-017-15959-5.

Sano, Y., Marty, B., 1995. Origin of carbon in fumarolic gas from island arcs. Chemical Geology 119(1), 265-274. doi.org/https://doi.org/10.1016/0009-2541(94)00097-R.

Scarsi, P., Craig, H., 1996. Helium isotope ratios in Ethiopian Rift basalts. Earth and Planetary Science Letters 144(3), 505-516. doi.org/https://doi.org/10.1016/S0012-821X(96)00185-9.

Scott, J.A., Pujol, M., Györe, D., Stuart, F.M., Gilfillan, S.M.V., 2021. Determining static reservoir connectivity using noble gases. Chemical Geology 582, 120410. doi.org/https://doi.org/10.1016/j.chemgeo.2021.120410.

Sherwood Lollar, B., Frape, S.K., Fritz, P., Macko, S.A., Welhan, J.A., Blomqvist, R., Lahermo, P.W., 1993. Evidence for bacterially generated hydrocarbon gas in Canadian shield and fennoscandian shield rocks. Geochimica et Cosmochimica Acta 57(23-24), 5073-5085. doi.org/10.1016/0016-7037(93)90609-Z.

Sherwood Lollar, B., Lacrampe-Couloume, G., Slater, G.F., Ward, J., Moser, D.P., Gihring, T.M., Lin, L.H., Onstott, T.C., 2006. Unravelling abiogenic and biogenic sources of methane in the Earth's deep subsurface. Chemical Geology 226(3), 328-339. doi.org/https://doi.org/10.1016/j.chemgeo.2005.09.027.

Sherwood Lollar, B., Westgate, T.D., Ward, J.A., Slater, G.F., Lacrampe-Couloume, G., 2002. Abiogenic formation of alkanes in the earth's crust as a minor source for global hydrocarbon reservoirs. Nature 416(6880), 522-524. doi.org/10.1038/416522a.

Song, X., Wang, H., Fu, X., Meng, L., Sun, Y., Liu, Z., Du, R., 2022. Hydrocarbon retention and leakage in traps bounded by active faults: A case study from traps along the NDG fault in the Qinan area, Bohai Bay Basin, China. Journal of Petroleum Science and Engineering 208, 109344. doi.org/https://doi.org/10.1016/j.petrol.2021.109344.

Tolstikhin, I.N., Mamyrin, B.A., Khabarin, L.B., Erlikh, E.N., 1974. Isotope composition of helium in ultrabasic xenoliths from volcanic rocks of Kamchatka. Earth and Planetary Science Letters 22(1), 75-84. doi.org/https://doi.org/10.1016/0012-821X(74)90066-1.

Wang, G., Li, S., Suo, Y., Zhang, X., Zhang, Z., Wang, D., Liu, Z., Liu, Y., Zhou, J., Wang, P., Guo, L., 2022. Deep-shallow coupling response of the Cenozoic Bohai Bay Basin to plate interactions around the Eurasian Plate. Gondwana Research 102, 180-199. doi.org/https://doi.org/10.1016/j.gr.2020.09.002.

Wang, Z., Cao, Y., Swennen, R., Yuan, G., Wang, K., 2022. Meteoric freshwater leaching and its significance to reservoir quality in a buried hill of lower-middle Jurassic fluvial sandstones: A case study from the Huanghua Depression, Bohai Bay Basin, China. Journal of Petroleum Science and Engineering 210, 109834. doi.org/https://doi.org/10.1016/j.petrol.2021.109834.

Whiticar, M.J., 1999. Carbon and hydrogen isotope systematics of bacterial formation and oxidation of methane. Chemical Geology 161(1-3), 291-314.

Yang, R., Zhao, X., Li, H., Zhao, C., Pu, X., Liu, H., Fu, L., Li, C., 2020. Evolution characteristics of the upper Paleozoic source kitchen and its controlling effects on hydrocarbon accumulation in the Paleozoic petroleum system in Huanghua Depression, Bohai Bay Basin, China. Journal of Petroleum Science and Engineering 193, 107415. doi.org/https://doi.org/10.1016/j.petrol.2020.107415.

Yang, W., Peng, B., Wu, M., Li, J., Ni, P., 2016. Evaluation for CO2 Geo-storage Potential and Suitability in Dagang Oilfield. Energy Procedia 86, 41-46. doi.org/https://doi.org/10.1016/j.egypro.2016.01.005.

Yang, Y., Xu, T., 2004. Hydrocarbon habitat of the offshore Bohai Basin, China. Marine and Petroleum Geology 21, 691-708. doi.org/10.1016/j.marpetgeo.2004.03.008.

Yu, F., Koyi, H., 2016. Cenozoic tectonic model of the Bohai Bay Basin in China. Geological Magazine 153(5-6), 866-886. doi.org/10.1017/S0016756816000492.

Yuan, G., Cao, Y., Sun, P., Zhou, L., Li, W., Fu, L., Li, H., Lou, D., Zhang, F., 2021. Genetic mechanisms of Permian Upper Shihezi sandstone reservoirs with multi-stage subsidence and uplift in the Huanghua Depression, Bohai Bay Basin, East China. Marine and Petroleum Geology 124, 104784. doi.org/https://doi.org/10.1016/j.marpetgeo.2020.104784.

Yuan, G., Cao, Y., Zhang, Y., Gluyas, J., 2017. Diagenesis and reservoir quality of sandstones with ancient "deep" incursion of meteoric freshwater——An example in the Nanpu Sag, Bohai Bay Basin, East China. Marine and Petroleum Geology 82, 444-464. doi.org/https://doi.org/10.1016/j.marpetgeo.2017.02.027.

Yuan, H., Chen, S., Dai, K., Jia, G., Wang, P., Li, J., Gou, Q., 2022. Cenozoic tectonic evolution of the Bohai Bay Basin: Constraints from strike-slip activities of the Wangjiagang fault zone, NE China. Journal of Asian Earth Sciences 233, 105262. doi.org/https://doi.org/10.1016/j.jseaes.2022.105262.

Zhang, F., Wu, Z., Li, W., Zhu, J., Fu, L., Li, H., Lou, D., Zhao, Y., 2019. Structural characteristics and its tectonic evolution of Huanghua depression during the Indosinian-Yanshanian. Journal of China University of Mining & Technology 48(4), 792-807.

Zhang, T., Zhang, M., Bai, B., Wang, X., Li, L., 2008. Origin and accumulation of carbon dioxide in the Huanghua depression, Bohai Bay Basin, China. AAPG bulletin 92(3), 341-358.

Zhang, W., Hu, W., Yang, S., Kang, X., Zhu, N., 2022. Differences and constraints of varying gas dryness coefficients in the Cainan oil-gas field, Junggar Basin, NW

China. Marine and Petroleum Geology 139, 105582. doi.org/https://doi.org/10.1016/j.marpetgeo.2022.105582.

Zhang, Y., Zhang, M., Mei, H., Zeng, F., 2019. Study on salt precipitation induced by formation brine flow and its effect on a high-salinity tight gas reservoir. Journal of Petroleum Science and Engineering 183, 106384. doi.org/https://doi.org/10.1016/j.petrol.2019.106384.

Zhao, X., Pu, X., Jiang, W., Zhou, L., Jin, F., Xiao, D., Fu, L., Li, H., 2019. An exploration breakthrough in Paleozoic petroleum system of Huanghua Depression in Dagang Oilfield and its significance, North China. Petroleum Exploration and Development 46(4), 651-663. doi.org/https://doi.org/10.1016/S1876-3804(19)60224-7.

Zhou, L., Li, Y., Jin, F., Fu, L., Pu, X., Da, L., Li, H., Liu, H., Xu, W., 2021. Tight Sandstone Reservoir Formation Mechanism of Upper Paleozoic Buried Hills in the Huanghua Depression, Bohai Bay Basin, Eastern China. Minerals 11(12), 1368.

Zhou, Z., Ballentine, C.J., Kipfer, R., Schoell, M., Thibodeaux, S., 2005. Noble gas tracing of groundwater/coalbed methane interaction in the San Juan Basin, USA. Geochimica et Cosmochimica Acta 69(23), 5413-5428. doi.org/https://doi.org/10.1016/j.gca.2005.06.027.

Zuo, Y.-h., Ye, B., Wu, W.-t., Zhang, Y.-x., Ma, W.-x., Tang, S.-l., Zhou, Y.-s., 2017. Present temperature field and Cenozoic thermal history in the Dongpu depression, Bohai Bay Basin, North China. Marine and Petroleum Geology 88, 696-711. doi.org/https://doi.org/10.1016/j.marpetgeo.2017.08.037.

Chapter 4 Noble gas signatures and gas migration in deep Xujiahe formation tight sandstones in the Western Sichuan Depression, Sichuan Basin, China

(Manuscript 3)

Jamie Robert Beagle[a, b, c, *], Chunhui Cao[d], Shengfei Qin[e], Yunpeng Wang[c], Quanyou Liu[a, g], Greg Holland[f], Ben Surridge[b], Zheng Zhou[b, †]

[a]State Key Laboratory of Shale Oil and Gas Enrichment Mechanisms and Effective Development, Beijing 100083, China

[b]Lancaster Environment Centre, Lancaster University, Lancaster, LA1 4YQ, UK

[c]State Key Laboratory of Organic Geochemistry, Guangzhou Institute of Geochemistry, Chinese Academy of Sciences, Guangzhou, 510640, China

[d]Northwest Institute of Eco-Environment and Resources, Chinese Academy of Sciences, Lanzhou, 730000, China

[e]Research Institute of Petroleum Exploration & Development, PetroChina, Beijing, 100083 China

[f]Department of Earth and Environmental Sciences, The University of Manchester, M13 9PL, UK

[g]Institute of Energy, Peking University, Beijing, 100871, China

* Corresponding author. Email address: j.beagle@lancaster.ac.uk (Jamie Beagle)

† Corresponding author. Email address: z.zhou4@lancaster.ac.uk (Zheng Zhou)

4.1 Abstract

The Sichuan Basin, located in southwestern China, is recognised as the country's most important gas-producing region, with unconventional tight sandstone gas reserves recently emerging as present and future prospective reservoir targets, especially due to the decline of conventional reserves. The Triassic Xujiahe formation (T_3x) in the Xinchang gas field consists of tight sandstone reservoirs, which are hydrocarbon reservoirs characterised by low permeability and porosity. Until recently, exploration of these reservoirs was hindered by latent 20th-century drilling technologies. These tight sandstone reservoirs have undergone severe compaction and cementation of fine-grained sediments over geologic time, resulting in the closing of pore throats and porosity loss (>76%).
In this study, noble gas isotope data is utilised to understand the gas accumulation mechanisms and charging associated with the T_3x unit. 12 gas samples were collected from producing wells within the western Sichuan depression, and their elemental noble gas signatures (He, Ne, Ar, Kr and Xe) were analysed. Measured $^{20}Ne/^{36}Ar$ values have evolved beyond the calculated, original 'air-saturated water' values (<0.14), evidencing open system gas loss from the reservoir. ^{4}He and its associated production ratio (estimated from U, Th and K concentrations) have been used to define the age of fluid residence and constrain the timing of fluid charging and gas loss within the tight sandstone reservoir. Measured $^{3}He/^{4}He$ ratios range from $0.0037R_a$ to $0.025R_a$ (R_a= atmospheric $^{3}He/^{4}He$), indicating that the T_3x gases have a crustal radiogenic signature, and that gases represent a binary mixture of crustal and atmosphere derived fluids. We have resolved this atmospheric component in ^{21}Ne and ^{40}Ar, noting the crustal-derived excess, $^{21}Ne^{*}$ and $^{40}Ar^{*}$. $^{40}Ar^{*}/^{36}Ar$ ratios are marginally higher (≤858.2) than atmospheric values (295.6). $^{4}He/^{20}Ne$ ratios are far in excess of $^{4}He/^{20}Ne_{air}$ (0.318) and air sample contamination has been ruled out. Noble gas isotopes suggests that samples near fault-fracture zones show a distinct mixture of atmospheric noble gases, indicating efficient interaction with water. Fault-fracture zones can act as channels for the movement of fluids, facilitating the mixing of noble gases with water, particularly when permeability is elevated by significant fracturing. Atmospheric signatures imparted on noble gas in these areas suggests that the reservoir has been open to gas loss, driven by pressure and structural modifications that enhance fluid flow.

*Keywords: Noble gases, Unconventional reservoirs, Tight sandstone gas, Coal-derived, Sichuan Basin, Low permeability, Horizontal drilling

4.2 Introduction

As the global abundance of conventional hydrocarbon sources declines, the emergence of tight sandstone reservoirs represents a new and important source of natural gas that will aid in meeting the growing worldwide demand for energy. Tight gas reservoirs can be characterised as reservoirs with low in-situ permeability (<0.1 md) and low porosity that require the use of technology such as hydraulic fracturing and horizontal drilling for effective hydrocarbon extraction. The Xinchang gas field in the western Sichuan Basin has recently become a major region for petroleum exploration because of these recent technological breakthroughs (Zeng et al., 2023, Zhao et al., 2023b). Due to the severely low porosity and permeability of the thick terrigenous clastic rocks within the Xujiahe formation, vertical fractures are critical in the role of fluid transport (Zhou and Dai, 2008). Xinchang tight gas resources are estimated to have total proven reserves of 6 x 10^{12} m^3 (Du and Xu, 2011), highlighting the potential and economic significance of the region, yet effective development and recovery of these reserves is still ongoing (Liu et al., 2023), with 77.39 x 10^8 m^3 produced reserves in the T_3x^2 unit (Liu et al., 2020a). Similar coal-seam-sourced tight sandstone reservoirs have been studied in China for their geochemical characteristics in both the Ordos (Li et al., 2019a) and Songliao Basins (Xu et al., 2020a) in northern and northeastern China, respectively. The precise source and mode of accumulation of Xujiahe gases remain unclear, with coal-derived gases from a type-III kerogen Triassic source and the extent of vertical migration of underlying type-I Permian source rocks still undetermined (Du et al., 2023).

Noble gases, with their fully saturated outer electron shells, include the gases helium (He), neon (Ne), argon (Ar), krypton (Kr) and xenon (Xe). These inert gases and their unique isotopic compositions, which are unmodified by both biological and chemical reactions (e.g., sulphate reduction), serve as critical tracers in a variety of geological and environmental processes, from crustal fluid dynamics to cosmochemistry and are important in understanding the geochemical cycles of other volatiles such as carbon and hydrogen (Ballentine and K. O'nions, 1994, Ballentine et al., 2002, Moreira, 2013, Marty, 2020, Wieler, 2023). Noble gases have a low terrestrial abundance and possess nucleogenic and radiogenic isotopes, namely ^4He, ^{21}Ne ($^{235,238}U$ + Th) and ^{40}Ar (from the radioactive decay of ^{40}K) and non-radiogenic atmosphere-derived (^{20}Ne, ^{36}Ar, ^{84}Kr) and mantle sourced isotopes (^3He). These noble gas isotopes also span a large mass range, from between 3 amu to 136 amu, which is reflected in their solubility and results in isotopic and elemental fractionation arising from well-constrained processes such as

diffusion, solution and adsorption in response to shifting fluid conditions (Zhou et al., 2012). When integrated with hydrocarbon chemistry, noble gases emerge as a powerful tool for unravelling the origins, migration paths, and mixing behaviour of subsurface fluids (Crovetto et al., 1982, Bosch and Mazor, 1988, Ballentine and K. O'nions, 1994, Hilton et al., 2002, Ballentine et al., 2002, Zhou et al., 2005, Zhou and Ballentine, 2006, Darrah et al., 2014, Tolstikhin et al., 2017), while recent insights into the geochemistry of gases within the Sichuan basin have further affirmed the importance of noble gas studies in the region, and worldwide (Zhang et al., 2019b, Zhang et al., 2019c, Cao et al., 2016, Cao et al., 2018, Cao et al., 2020a, Li et al., 2020, Liu et al., 2021a).

Figure 49 - Map of the Sichuan Basin, showing sample locations, basin extent, major topographical features and major gas fields within the basin (modified after Ni et al. (2014) and Wang et al. (2020b). The Inset Map (top-left) shows the location of Xinchang gas field sampling wells and the distribution of proximal faults, which are key to gas accumulation and migration pathways. The depth to the top of the T_3x^5 Xujiahe reservoir unit is similarly marked for reference.

4.3 Geological and tectonic framework

The Sichuan Basin, situated in central-south-eastern China within the South China plate, represents one of Asia's most significant petroliferous basins, and covers an approximate area of 1.8 x 10^5 km^2 (Li et al., 2016b). The South China plate is demarcated by the Yangtze and Cathaysia blocks. The basin can be structurally divided into several zones based on geological features and their locations relative to major faults (Figure 49): the East Sichuan depression, positioned east of the Huayingshan fault; the South Sichuan depression, covering areas to the South and Southwest; the Western Sichuan depression, located west of the Longquanshan fault; and the Central Sichuan uplift, a low-plain tectonic belt situated between the Longquanshan and Huayingshan faults, all of which are key regions for gas and oil accumulation (Ni et al., 2014). The Western Sichuan depression is an elongated depression that trends NE-SW, covering an area of 3.1 x 10^4 km^2 (Li et al., 2023). Gas reservoirs have been discovered in the Upper Jurassic Penglaizhen Formation (J_3p), Middle Jurassic Shaximiao (J_2s) and Qianfoya Formations (J_2q) (Dai, 2016), and the Upper Triassic Xujiahe series (T_3x), which, has favourable gas-bearing properties, as the primary lithofacies are medium-to-course grain sandstones (Liu et al., 2020a), gradually thickening to its western extent where the Xinchang gas field is positioned (Liu et al., 2021b). This sequence measures 400m to 1500m in thickness (Dai et al., 2012), while source rock thickness measures ≤100m (Huang et al., 2004). Jurassic strata also consist predominantly of mixed interbedded fluvial sandstone-mudstone sequences with a combined thickness of approximately 2000m, primarily deposited during episodic flood events, which have played a crucial role in the distribution and characteristics of these strata.

The Xujiahe formation is made of 4 distinct Triassic units from its base upwards: T_3x^2, T_3x^3, T_3x^4 and T_3x^5, which correspond to the members Xu-2, Xu-3, Xu-4, and Xu-5, respectively. The Xujiahe Formation features coal-bearing deposits (Xu-3 and Xu-5), mudstones (Xu-1, Xu-3 and Xu-5), and interbedded low porosity, low permeability sandstones (Xu-2 and Xu-4), that formed during the transitional phase from marine to continental, fluvial facies in the upper Yangtze region, which occurred following Jurassic sedimentation, with a depositional setting of an underwater distributary channel in a braided river delta (Liu et al., 2020a). The Xujiahe Formation is further characterised by three layers of mudstone that are regionally interbedded with three layers of coal-gas bearing sandstones, a configuration crucial to the widespread accumulation of natural gases within the Xujiahe Formation (Dai et al., 2009). Deposition of the Triassic Xujiahe

Formation and its subsequent burial and gas accumulation has been complicated by a tectonic and depositional history controlled by multi-stage, asynchronous thrusting due to the Longmenshan, Micangshan and Dabashan fault-belts (Du et al., 2023). The Xujiahe Formation is also highly heterogeneous, having undergone extensive diagenesis within the tight sandstone reservoir units, with subsequent pore size and structure alteration due to compaction and cementation (Gong et al., 2016). The Xujiahe Formation reached its maximum burial depth of 6000m during the middle to late Cretaceous. Total organic carbon (TOC) of T_3x gases ranges between 0.5-9.7% (average: 1.96%) and is dominated by Type II and Type III kerogen (Dai et al., 2009).

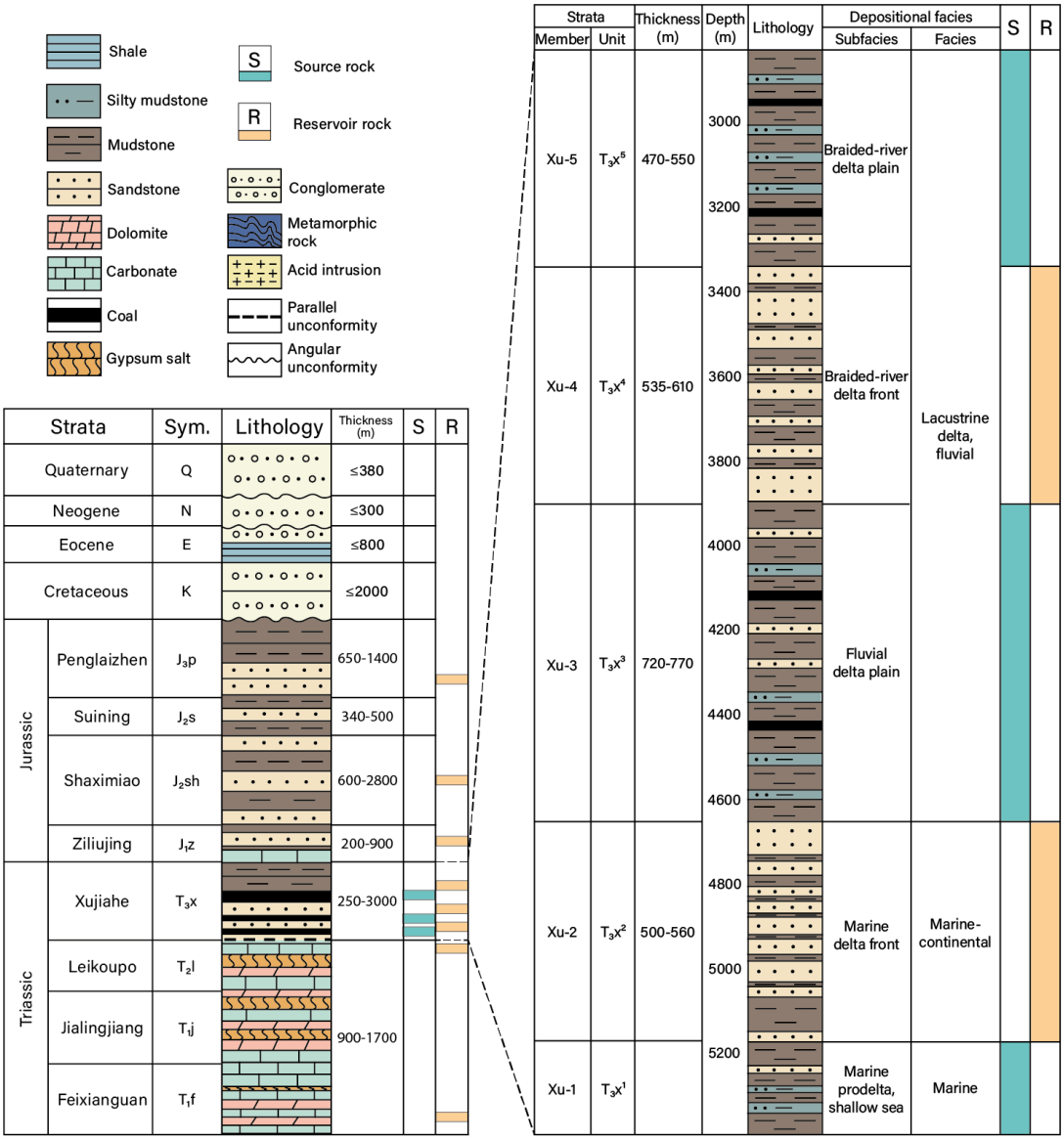

Figure 50 - Stratigraphic column for the Xinchang gas field; The thick sandstone units, Xu-2 and Xu-4 (termed T_3x^2 and T_3x^4) of the Xujiahe formation act as the main reservoir intervals and are the primary exploration and drilling targets. The tight sandstone gases of Xu-2 (T_3x^2) are sourced from the underlying black shales of the Xu-1 member (T_3x^1). Mudstones and interbedded coal seams are also found in the third and fifth members (T_3x^3 and T_3x^5 respectively)(Yang et al., 2021a).

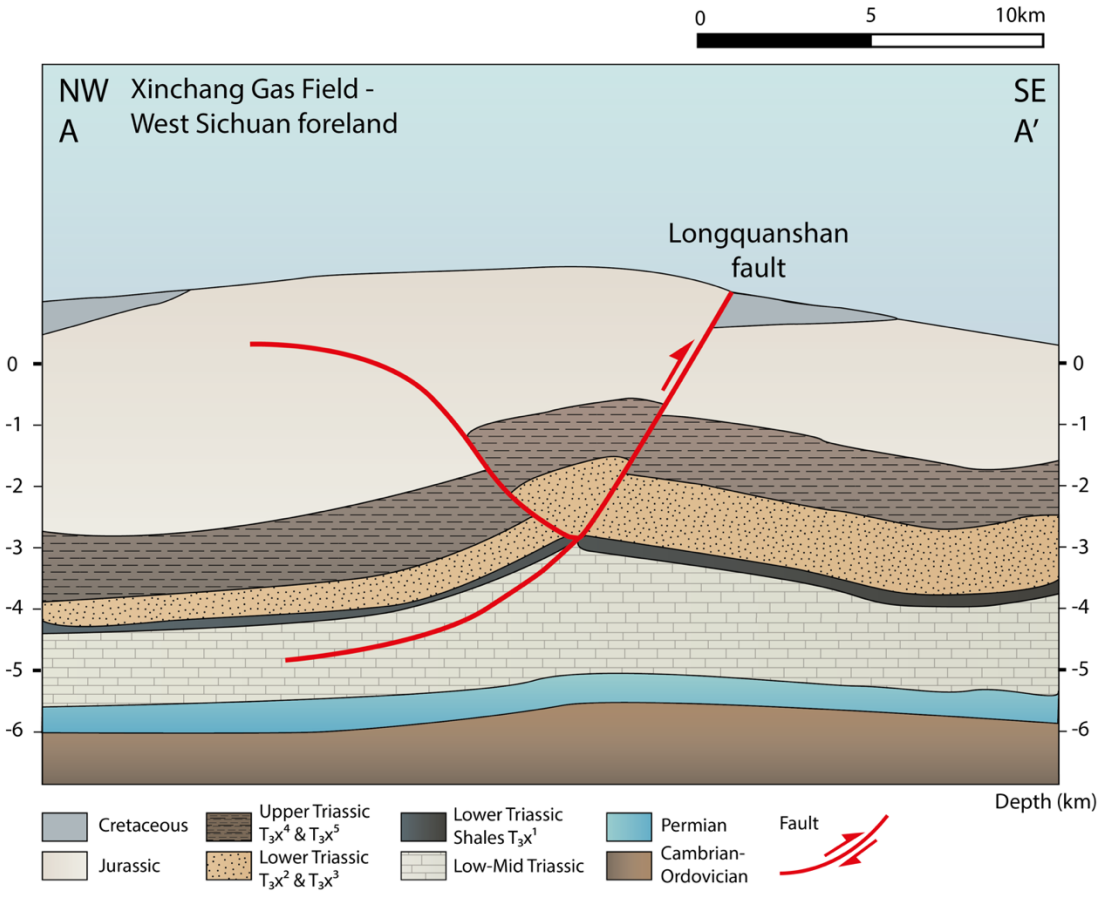

Figure 51 – Geological cross-section, which is representative of the West Sichuan foreland basin. This section illustrates the stratigraphic units from the Cretaceous to the Cambrian-Ordovician and the Longquanshan fault that dissects the Xujiahe formation within the unconventional Xinchang tight sandstone gas field, this figure is modified from Liu et al. (2021b).

4.4 Sampling and Analytical Methods

4.4.1 Gas sample collection

Gas samples (n = 12) were gathered in standard refrigeration grade, internally polished copper tubes of 10mm diameter and 50cm length. This copper tube was firstly connected to the well-head, with a stainless-steel pressure regulator and high-pressure hose. Due to the volatility of noble gases, caution was used when handling, transporting and storing these samples so as to ensure minimal loss or exchange of gases with the atmosphere (Beyerle et al., 2000). To eliminate any contamination from residual air, the gas was allowed to flow through the collection apparatus for a minimum duration of 10 minutes. Subsequently, the downstream end of the copper tubes was cold-welded closed using a steel pinch-off clamp. The upstream end was also sealed using steel pinch-off clamps while the tube was still under a pressure slightly higher than atmospheric, precisely regulated to approximately 1 bar above atmospheric pressure, to preclude any degassing and ensure sample integrity. Following these procedures; helium, the most prone among the suite of noble gases to leakage, demonstrates a maximum leakage rate into a vacuum of less than 10^{-9} cm^3 STP yr^{-1}. The methodology for sampling adhered protocols established by Zhou et al. (2005), enabling each sample to be stored and then analysed effectively.

4.4.2 Gas sample analysis

Noble gas extraction and analysis procedures were conducted using the NGX Static Multicollector Noble Gas Mass Spectrometer (Isotopx) at the Subsurface Fluid Isotope Geochemistry Laboratory within the Lancaster Environment Centre at Lancaster University. These procedures followed an analytical methodology outlined by Li et al. (2021b). Throughout the analysis, blanks and air standards were periodically measured to ensure consistency and make corrections. The precision of noble gas measurements is determined by the size of the sample and includes adjustments for blank corrections. Certain species that interfere with noble gas measurements were also accounted for. Specifically, for neon (Ne) abundance and isotopic analysis, corrections were made for interferences from doubly charged ions of argon ($^{40}Ar^{2+}$) and carbon dioxide ($^{44}CO_2^{2++}$) on the isotopes ^{20}Ne and ^{22}Ne, respectively. All potential sources of uncertainty, including statistical analytical errors, blank corrections, reproducibility of air standards, volume expansion uncertainty, and the stability of mass spectrometer sensitivity, were thoroughly evaluated.

4.5 Results

4.5.1 Bulk gas composition & stable isotope geochemistry

A total of 12 gas samples were collected from unconventional gas wells within the Sichuan Basin, belonging to the Xinchang tight sandstone gas field, with wells targeting interbedded sandstones of the Triassic Xujiahe fm. in the Western Sichuan depression. These gas samples were evaluated for their noble gas, bulk gas and stable carbon and hydrogen isotope composition. The study area comprises several gases collected from horizontal wells, signified by the sample name prefix 'H'. Sample name, bulk gas composition, stable isotope data and burial depth information are presented in Table 34, while gas concentrations and isotopic ratios for the noble gases (He, Ne, Ar, Kr and Xe) can be found in Table 35. Corresponding air-derived elemental ratios ($^{20}Ne/^{36}Ar$, $^{84}Kr/^{36}Ar$ and $^{132}Xe/^{36}Ar$) are also published in conjunction for reference (Table 36). Gas samples primarily consist of methane (95.22-97.36%), with longer chain hydrocarbons present, such as C_2H_6 (1.05-4.99%) and C_3H_8 (0.07-0.94%), as well as negligible non-hydrocarbon gases such as CO_2 (0.01-1.27%) and N_2 (0.28-3.49%). The proportion of CH_4 (C_1) to the total sum of hydrocarbons (C_1-C_4) is between 0.94 – 0.99%, while gas dryness $\left(\frac{C_1}{C_2+C_3}\right)$ ranges from 24.69 to 93.62.

Hydrogen (δD) and carbon ($\delta^{13}C$) stable isotope ratios of natural gases from the Xujiahe formation indicate that gases are primarily coal-derived, with $\delta^{13}C(C_1)$ = -34.55‰ to -30.68‰, $\delta^{13}C(C_2)$ = -22.83‰ to -22.16‰, and $\delta^{13}C(C_3)$ = -21.91‰ to -21.62‰.

Table 34 - Bulk gas composition (%) for Western Sichuan Xinchang gases. Errors are ±0.1%

Well	Strata	Major gas components (%)								$\delta^{13}C$ (‰), VPDB		
		CH_4	C_2H_6	C_3H_8	nC_4H_{10}	iC_4H_{10}	C_1/C_1-C_4	CO_2	N_2	CH_4	C_2H_6	C_3H_8
X911-5	J_2s	95.22	2.55	0.43	0.07	0.08	0.97	0.09	1.22	-32.75	-22.56	-21.70
X911-7	J_2s	93.53	2.60	0.42	0.07	0.07	0.97	-	2.58	-32.10	-22.83	-21.62
X911-6	J_2s	94.67	2.25	0.36	0.06	0.07	0.97	0.05	1.98	-32.31	-22.16	-
X911-3	J_2s	89.43	4.99	0.91	0.18	0.13	0.94	0.03	3.49	-34.55	-22.81	-
X911-4	J_2s	95.63	2.39	0.41	0.07	0.07	0.97	-	1.12	-32.13	-22.55	-21.91
X2*	T_3x^2	97.36	0.96	0.08	0.01	0.01	0.99	1.27	0.28	-	-	-
X201	T_3x^2	94.74	0.78	0.07	-	0.01	0.99	0.08	3.37	-30.68	-	-
XS23-4H	T_3x	-	-	-	-	-	-	-	-	-	-	-
XS22-6HF	T_3x	-	-	-	-	-	-	-	-	-	-	-
XS21-26H	T_3x	-	-	-	-	-	-	-	-	-	-	-
XS21-39HF	T_3x	-	-	-	-	-	-	-	-	-	-	-
CX135*	J_2q	95.29	2.92	0.94	0.19	0.21	0.96	0.01	0.34	-	-	-

Table 35 - Noble gas isotope concentrations and ratios. * represents modified radiogenic derived ^{21}Ne & ^{40}Ar values. $^{3}He/^{4}He$ (R) ratios are normalised to the air value $R_a = 1.39 \times 10^{-6}$. 1σ errors are shown in the table following a '±' sign. STP - standard temperature and pressure conditions

Sample	^{4}He x 10^{-4}	Error (1σ)	^{20}Ne x 10^{-11}	Error (1σ)	^{36}Ar x 10^{-10}	Error (1σ)	^{84}Kr x 10^{-11}	Error (1σ)	^{132}Xe x 10^{-11}	Error (1σ)	$^{3}He/^{4}He$ (R/R_a)	Error (1σ)	$^{20}Ne/^{22}Ne$	Error (1σ)	$^{21}Ne^{*}/^{22}Ne$	Error (1σ)	$^{40}Ar^{*}/^{36}Ar$	Error (1σ)	$^{86}Kr/^{84}Kr$	Error (1σ)	$^{132}Xe/^{130}Xe$	Error (1σ)
	cm^3 STP/cm^3																					
Air											1		9.81		0.029		298.6		0.31		6.61	
X911-5	1.04	1.5	14	0.4	13.55	0.45	6.66	0.11	1.05	0.18	0.015	0.0002	9.64	0.49	0.0171	0.0007	325.2	11.8	0.30	0.002	6.49	0.08
X911-7	1.11	1.6	4820	68.3	874.89	75.5	230.00	3.93	9.26	1.55	0.025	0.0004	10.03	0.01	n/a	n/a	n/a	n/a	0.30	0.003	6.44	0.06
X911-6	1.10	1.6	1110	16.3	20.35	3.74	7.90	0.13	1.09	0.2	0.015	0.0002	10.12	0.04	0.0001	0.00001	156.6	28.9	0.30	0.004	6.69	0.17
X911-3	2.61	3.7	40.9	1	32.46	2.21	15.60	0.25	8.95	0.37	0.013	0.0002	9.36	0.27	0.0201	0.0004	471.6	32.8	0.30	0.003	6.51	0.06
X911-4	9.56	1.4	11.3	1.7	11.28	1.53	6.37	0.11	4.01	0.15	0.013	0.0002	10.52	0.58	0.0171	0.0007	361.6	49.4	0.30	0.004	6.42	0.09
X2	6.86	1	6.77	7.5	5.88	1.76	2.76	0.05	0.62	0.07	0.007	0.0001	10.45	1.22	0.0141	0.0008	858.2	257	0.31	0.006	6.49	0.15
X201	7.61	1.1	4.84	1.4	9.53	2.49	3.10	0.05	0.66	0.08	0.006	0.0001	10.92	1.32	0.0211	0.001	463	121	0.30	0.005	6.43	0.15
XS23-4H	4.03	5.7	17.4	0.4	20.69	0.18	9.37	0.16	1.98	0.23	0.004	0.0001	10.75	0.38	0.0221	0.0004	303.7	5.07	0.31	0.003	6.46	0.09
XS22-6HF	1.13	1.6	10.1	0.7	17.63	0.27	11.20	0.18	2.41	0.26	0.011	0.0002	10.15	0.22	0.0181	0.0003	322.6	6.73	0.30	0.002	6.52	0.07
XS21-26H	1.60	2.3	343	4.9	66.15	1.32	61.50	1.07	9.63	1.09	0.012	0.0002	9.94	0.01	0.0011	0.00001	55.2	1.35	0.32	0.003	6.71	0.07
XS21-39HF	1.39	2.0	99.3	1.6	36.14	0.58	27.10	0.44	4.64	0.52	0.009	0.0001	9.85	0.07	0.0041	0.00001	172.1	3.68	0.31	0.002	6.59	0.06
CX135	1.65	2.3	153	2.3	61.55	0.51	42.80	0.70	8.54	0.95	0.006	0.0001	9.96	0.06	0.0051	0.00001	313.8	5.15	0.31	0.002	6.61	0.05

Table 36 – Air-derived elemental ratios for Ne, Ar, Kr and Xe. 1σ errors are shown in the table following a '±' sign.

Sample	$^{20}Ne/^{36}Ar$	error (1σ)	$^{84}Kr/^{36}Ar$	error (1σ)	$^{132}Xe/^{36}Ar$	error (1σ)	$^{132}Xe/^{84}Kr$	error (1σ)
	x 10^{-2}	x 10^{-2}	x 10^{-2}	x 10^{-2}	x 10^{-3}	x 10^{-3}		
Air	52		2.06		0.77		0.036	
X911-5	10.33	0.44	4.92	0.18	7.75	0.29	0.16	0.004
X911-7	55.09	4.82	2.63	0.23	1.06	0.09	0.04	0.001
X911-6	n/a	n/a	3.88	0.72	5.36	0.99	0.14	0.003
X911-3	12.60	0.91	4.81	0.34	6.65	0.47	0.14	0.003
X911-4	10.02	2.06	5.65	0.77	7.94	1.09	0.14	0.003
X2	11.52	13.2	4.70	1.41	6.82	2.05	0.15	0.004
X201	5.08	1.95	3.25	0.85	4.45	1.17	0.14	0.003
XS23-4H	8.41	0.21	4.53	0.09	6.19	0.12	0.14	0.003
XS22-6HF	5.73	0.39	6.35	0.14	8.90	0.2	0.14	0.003
XS21-26H	51.85	1.27	9.30	0.25	9.77	0.26	0.11	0.003
XS21-39HF	27.47	0.62	7.50	0.17	8.47	0.2	0.11	0.003
CX135	24.86	0.43	6.95	0.13	9.18	0.17	0.13	0.003

4.5.2 Noble gas isotopic signatures

4.5.2.1 Helium

Helium (^{4}He) concentrations range from 6.86 to 40.30 x 10^{-5} cm^3 $STPcm^{-3}$, one to two orders of magnitude higher than atmospheric He (2.45 x 10^{-6} cm^3 $STPcm^{-3}$). Helium isotope ratios ($^{3}He/^{4}He$) are reported relative to the atmospheric ratio R_a = 1.39 x 10^{-6} (Porcelli et al., 2002) and where air = $1R_a$. $^{3}He/^{4}He$ ratios range from $0.004R_a$ to $0.025R_a$, which indicates a strongly crustal radiogenic He signature and suggests that mantle fluids contribute a very small percentage to the He fraction. The percentage contribution of crustal radiogenic helium ($^{4}He_{rad}$) can be calculated using a simple two-component mixing model that accounts for crustal ($0.01R_a$) and mantle-like ($6.1R_a$) end members, and mantle fluid contribution of ^{4}He has been quantified to be below 1% for all gas samples. Atmosphere-derived contributions to ^{4}He are likely insignificant in all samples as measured $^{4}He/^{20}Ne$ ratios range from between 2303 to 2.32 x 10^{6}, which is far in excess of the $^{4}He/^{20}Ne$ atmospheric ratio in groundwater 0.288 (Kipfer et al., 2002); therefore He is essentially crustal-derived.

4.5.2.2 Neon

Neon (^{20}Ne) concentrations range from 1.4 to 482 x $10^{-10}$$cm^3$ STP cm^{-3}. ^{20}Ne is attributed to the recharge of meteoric groundwaters, with concentrations being affected by gas production, whereby wells at a later stage of production (and degassing) exhibit lower concentrations of ^{20}Ne (Zhou et al., 2005). ^{20}Ne in shale gas samples has also previously been shown to correlate well with maturity, with lower Ne concentrations in samples being indicative of greater thermal maturity (Byrne et al., 2018a); (Byrne et al., 2020), however, it has been noted in previous studies that unconventional hydrocarbon systems display larger variance in Ne isotope ratios relative to the Ne crustal production line. All but two gas samples (X911-5 and X911-3) have $^{20}Ne/^{22}Ne$ ratios in excess of the atmospheric ratio ($^{20}Ne/^{22}Ne_{air}$ = 9.81). Both $^{20}Ne/^{22}Ne$ and $^{21}Ne/^{22}Ne$ ratios highlight an excess of radiogenically produced ^{21}Ne and ^{22}Ne relative to air, where $^{20}Ne/^{22}Ne$ and $^{21}Ne/^{22}Ne$ ratios are 9.81 and 0.029, respectively (Porcelli et al., 2002).

4.5.2.3 Argon

^{36}Ar concentrations range between 0.59 to 87.49 x 10^{-9} cm^3 $STPcm^{-3}$. ^{36}Ar concentrations follow a similar distribution to ^{20}Ne concentrations, and this is to be expected due to their shared provenance via the introduction of air-equilibrated groundwaters. Argon

isotope ratios ($^{40}Ar^*/^{36}Ar$) vary from 55.2 to 858.2, which with the exception of sample X2, are close to the atmospheric $^{40}Ar/^{36}Ar$ value, which is 298.6 (Lee et al., 2006). $^{40}Ar/^{36}Ar$ values are lower than $^{40}Ar/^{36}Ar$ values exhibited in other unconventional reservoirs within the Sichuan Basin, e.g. the Longmaxi shale.

This variation is attributed to an excess of ^{40}Ar derived from crustal material produced by ^{40}K decay. $^{40}Ar^*/^{36}Ar$ ratios that are less than the air value might arise from a much lower contribution of ^{40}K decay which is dependent on local mineralogy, however since $^{40}Ar^*$ represents the resolved crustal excess, some values are indeed lower than this air value, which is true of samples X911-6 ($^{40}Ar^*/^{36}Ar$ = 156.6) and XS21-26H ($^{40}Ar^*/^{36}Ar$ = 55.2), however, their non-resolved $^{40}Ar/^{36}Ar$ values are all >298.6; X911-6 ($^{40}Ar/^{36}Ar$ = 452.1) and XS21-26H ($^{40}Ar/^{36}Ar$ = 350.7).

Following Ballentine and Burnard (2002), the method for quantifying the resolved non-atmospheric derived excess, denoted by $^{40}Ar^*$, is given in section 4.6.6.

4.5.2.4 Krypton and Xenon

^{84}Kr concentrations range between 0.2 to 23 x 10^{-10} cm^3 STPcm^{-3}, while ^{132}Xe concentrations range from 0.62 to 14.37 x 10^{-12} cm^3 STPcm^{-3}. Isotope ratios of Krypton and Xenon are indistinguishable from air values; $^{86}Kr/^{84}Kr$ ranges from 0.296 to 0.316, where the air value = 0.305 (Aregbe et al., 1996), and $^{132}Xe/^{130}Xe$ values vary between 6.42 to 6.71, which is close to the air value = 6.607 (Pepin, 2000). Both $^{84}Kr/^{36}Ar$ and $^{132}Xe/^{36}Ar$ are highly enriched in heavy noble gases relative to previously reported air-derived ratios (Table 36).

4.6 Discussion

4.6.1 Atmosphere-derived noble gas abundances

Atmosphere-derived noble gases (^{20}Ne, ^{36}Ar, ^{84}Kr and ^{132}Xe) are introduced into aquifers during the recharge of meteoric waters under surface conditions and lack additional significant subsurface sources (i.e., the mantle and crust). Groundwater that has equilibrated with these atmospheric isotopes is classified as air-saturated water (ASW). The noble gases that have subsequently migrated throughout the subsurface and accumulated within formations typically exhibit compositions reflecting a combination of atmospheric, radiogenic, or mantle-derived end-member sources.

Solubility defines the selective partitioning, and extent to which dissolution of noble gases occurs in a given liquid volume. Constraining the solubility of these noble gases using Henry's law is critical to resolve the contributions of the three major end-members.

4.6.2 Noble gas solubility in water

The solubility of noble gases in water is primarily influenced by temperature and salinity, increasing proportionately with atomic mass, $S_{Ne} < S_{Ar} < S_{Kr} < S_{Xe}$, where S denotes gas solubility. Under recharge conditions, which modifies solubility according to the local elevation (less gas dissolves in groundwater at greater elevations due to lower atmospheric pressure), temperature, and salinity, He exhibits the lowest solubility (Table 37, 2456.03 atm kg/mol). At reservoir conditions, He (3481.64 atm kg/mol) and Ne (3355.96 atm kg/mol) solubilities are almost indistinguishable. At the gas-liquid contact, where dissolved groundwaters encounter a CH_4-rich gaseous mixture, initially, He, then Ne and Argon (Ar) are preferentially partitioned into the gas phase, while Krypton (Kr) and Xenon (Xe) remain more dissolved in groundwater due to their greater atomic masses and higher solubility, delaying their degassing until 'later' stages.

Table 37 – Henry's constants for recharge and reservoir conditions. For this solubility model, we infer recharge conditions of 10°C, at an average elevation of 750m above sea level, where air pressure is ~0.9atm, once adjusted for relative humidity. For reservoir conditions, we consider an average geothermal gradient across the Sichuan Basin of 23°C km-1 (Liu et al., 2021a), where the reservoir temperature is 90°C at 3500m depth, and 2M NaCl.

Condition	Depth (m)	Temperature (°C)	Salinity (M NaCl)	Henry's constant's (atm kg/mol)				
				He	Ne	Ar	Kr	Xe
Recharge	0	10	0.1	2456.03	1978.70	529.14	273.75	144.59
Reservoir	3500	90	2	3481.64	3355.96	2128.86	1660.30	1301.68

Under reservoir conditions (3500m depth, 90°C), the solubilities of Argon, Krypton, and Xenon decrease approximately by factors of 4, 6, and 9, respectively, compared to their solubilities at recharge conditions (Table 37). We equate measured noble gas concentrations of the air-derived noble gases ($^{20}Ne/^{36}Ar$, $^{84}Kr/^{36}Ar$, $^{132}Xe/^{36}Ar$) to the expected ASW values, which are calculated and represent the 'initial' concentration of noble gases in equilibrium with the atmosphere at the time of recharge.

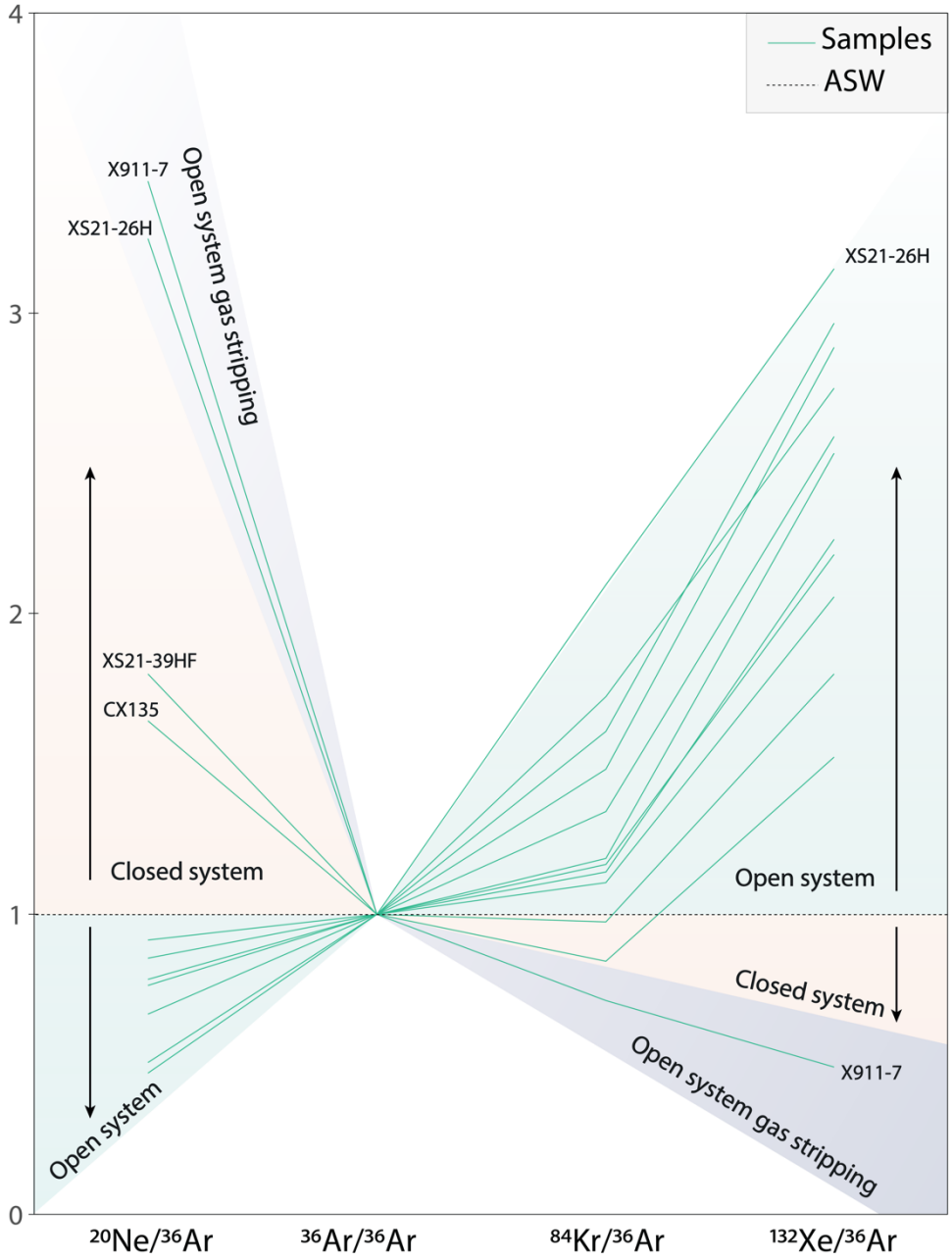

Figure 52 - Mean air-derived noble gas isotope abundances (^{20}Ne, ^{36}Ar, ^{84}Kr and ^{132}Xe) plotted relative to ^{36}Ar (normalised to ASW at 10°C, where ASW = 1). The plot illustrates different system behaviours with tight sandstone gas samples generally indicating open-system behaviour ($^{20}Ne/^{36}Ar_{meas}$ < ASW), where lighter noble gases (Ne) have been preferentially removed and potential enrichment of ^{84}Kr and ^{132}Xe ($^{132}Xe/^{36}Ar_{meas}$ > ASW). This figure also highlights regions of open-system gas stripping and closed system conditions, providing insights into the noble gas geochemistry of the samples

All gas samples have a distinct noble gas isotopic composition, as evidenced by Figure 52. $^{20}Ne/^{36}Ar$ values for many gas samples have evolved below the value of ASW for Ne (0.54), which suggests open system behaviour due to the less soluble Ne being preferentially removed over Ar during degassing, resulting in a $^{20}Ne/^{36}Ar$ ratio relatively enriched in Ar. Samples XS21-26H ($^{20}Ne/^{36}Ar_{meas}$ = 3.7), XS21-39HF ($^{20}Ne/^{36}Ar_{meas}$ = 1.96) and CX135 ($^{20}Ne/^{36}Ar_{meas}$ = 1.78), represent outlier samples that are either closed system (XS21-39HF and CX135) or have likely been totally gas stripped (XS21-26H), also inferred by this samples Kr and Xe values (<ASW). Overall, there is a determinable excess of $^{84}Kr/^{36}Ar$ (average $^{84}Kr/^{36}Ar_{meas}/^{84}Kr/^{36}Ar_{asw}$ = 1.34) and $^{132}Xe/^{36}Ar$ (average $^{132}Xe/^{36}Ar_{meas}/^{132}Xe/^{36}Ar_{asw}$ = 2.52) relative to ASW in the Xinchang tight sandstone gas samples, showing possible enrichment of Kr and Xe relative to the atmosphere. Kr and Xe show a linear relationship across samples, with those that have high $^{84}Kr/^{36}Ar$ also displaying high $^{132}Xe/^{36}Ar$. This excess can be attributed to a desorbed, gaseous phase that was previously trapped within the clay rich source rock, that since migrated along with hydrocarbon gases during accumulation into the trapping structure.

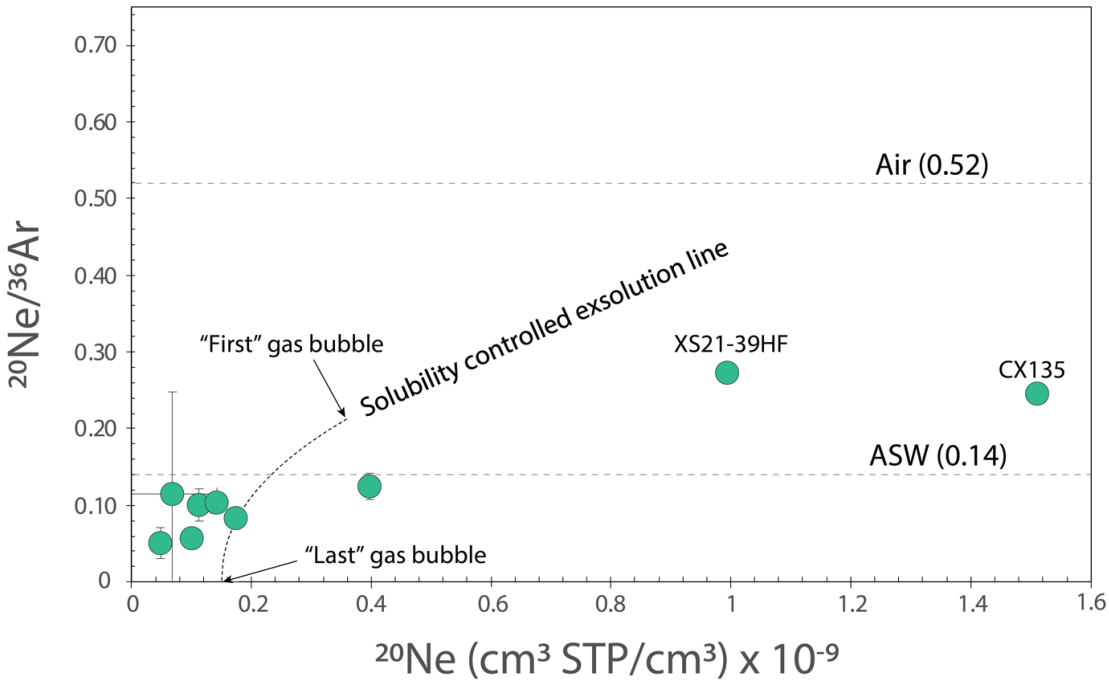

Figure 53 – Air-derived noble gases $^{20}Ne/^{36}Ar$ fractionate due to mass-dependent solubility processes. The exsolution line signifies the predicted evolution of $^{20}Ne/^{36}Ar$ ratios due to solubility-controlled processes, as Ar is incrementally exsolved from groundwater into a gaseous phase. Most gas samples plot far from air ($^{20}Ne/^{36}Ar_{air}$ = 0.52) but have values approaching and within the range of ASW ($^{20}Ne/^{36}Ar_{meas}$ < 0.14) at the 'end' of the solubility line, signalling degassing.

4.6.3 Evolution of a reservoir gas-liquid fraction

As no radiogenic or nucleogenic sources of ^{20}Ne, ^{36}Ar, ^{84}Kr and ^{132}Xe exist, the isotopic ratios ($^{20}Ne/^{36}Ar$, $^{84}Kr/^{36}Ar$, $^{132}Xe/^{36}Ar$) reflect the degree of fractionation between an ASW or migrated gas-liquid phase (Hunt et al., 2012). Due to low solubility in water, Ne begins to degas prior to Ar, resulting in initial gas bubbles that carry a higher concentration of Ne than Ar, and a signature of $^{20}Ne/^{36}Ar$ that exceeds the value of ASW (Figure 53). Samples with elevated $^{20}Ne/^{36}Ar$ values relative to ASW indicate they are at an earlier degassing stage, whereby a greater proportion of Ar remains in the liquid phase. Once the lighter noble gases (He, Ne) are entirely exsolved ($^{20}Ne/^{36}Ar \Rightarrow 0$), gas bubbles are composed of a fraction with proportionally higher concentrations of heavier noble gases. until the groundwater becomes fully degassed. According to this model, air-derived isotope ratios ($^{20}Ne/^{36}Ar$) should evolve from a value of around 0.21 (as Ne is preferentially degassed) to a value approaching zero as Ar becomes almost fully exsolved from groundwater, and the volume of total dissolved Ar approaches 0. Measured noble gas $^{20}Ne/^{36}Ar$ ratios are significantly less than the atmospheric value (0.52) and are below the ASW value (0.14). Held formation waters in the buried sandstone strata are thought to be high and T_3x gases have undergone lateral and vertical migration from source to reservoir intervals where noble gases are likely to be strongly influenced by contact with groundwater-derived fluids, and we interpret the measured $^{20}Ne/^{36}Ar$ ratios as partitioning between a gas and liquid phase due to solubility-controlled open-system Rayleigh fractionation. Ne has low solubility in water, and any increase or decrease in pressure and/or temperature results in localised groundwaters being enriched or depleted in noble gases, such as a gas component with a fractionated$^{20}Ne/^{36}Ar$ ratio.

4.6.4 Gas dynamics in diagenetic tight-sandstone reservoirs

The Xujiahe formation, a tight sandstone gas reservoir interval within the Xinchang gas field, is primarily sourced from interbedded shale gas-bearing layers. The burial and thermal history of T_3x units is well constrained, with peak burial occurring around 60 Ma, during the late Cretaceous-early-Eocene, to a maximum depth of 6000m (Leng et al., 2011, Luo et al., 2019, Pan et al., 2021). Following extensive tectonism and uplift, resulting in intense faulting, and fracturing, Xujiahe tight sandstone reservoirs have undergone heavy compaction, dissolution and cementation since burial, which has resulted in decreasing amounts of K-feldspar and an accompanying rise in silica cements, greatly reducing porosity (from 35-40% to between 1-11%), and restricting the

movement of fluids. Several studies have aimed to tie the timing of gas accumulation in the Xinchang gas field of the Xujiahe formation with that of diagenesis and in the Xu-2 reservoirs, meanwhile, diagenesis has severely impacted pore structure homogenisation temperatures (Li et al., 2016a).

During burial, the loss, expulsion and leakage of prior trapped noble gases occurs due to increasing pressure and temperature, while pore compaction and cementation reduces the porosity and permeability further, the heavier, more soluble noble gases preferentially remain within the quickly diminishing pore volume. This initiates a localised preferential enrichment of heavier noble gases resulting in low relative $^{20}Ne/^{36}Ar$ ratios, with high residual aqueous concentrations of Kr (~100% to 200% of ASW values) and Xe (~ 150% to 300% of ASW values).

4.6.5 Potential pathways for gas exchange

Measured $^{20}Ne/^{36}Ar$ values are lower than the calculated ASW value, with all but two samples (CX135 and XS21-39HF) exhibiting open system behaviour and open system gas stripping (XS21-26H and X911-7). These ratios have likely evolved in a system that is open to gas loss; as if the system were closed to gas loss, then gases could not evolve to $^{20}Ne/^{36}Ar$ values below this 'initial' point (Barry et al., 2016). Therefore, we consider a scenario in which despite extensive cementation and pore throat closing, a significant proportion of gases have been lost following exsolution from water. Secondary porosity generated by dissolution, small-scale fractures or micro-fractures developed post-compaction, or localised overpressure can also re-open pathways for gas leakage. This exsolution is likely driven by pressure changes, temperature fluctuations, and the presence of migrating hydrocarbons, which can reduce gas solubility and lead to the release of dissolved noble gases. Such conditions are consistent with the geological setting of tight sandstone formations, where upward migration of buoyant hydrocarbons can displace formation water and alter pressure conditions significantly. This open system scenario is essential for understanding the migration history and the mechanisms responsible for noble gas and natural gas enrichment in the reservoir.

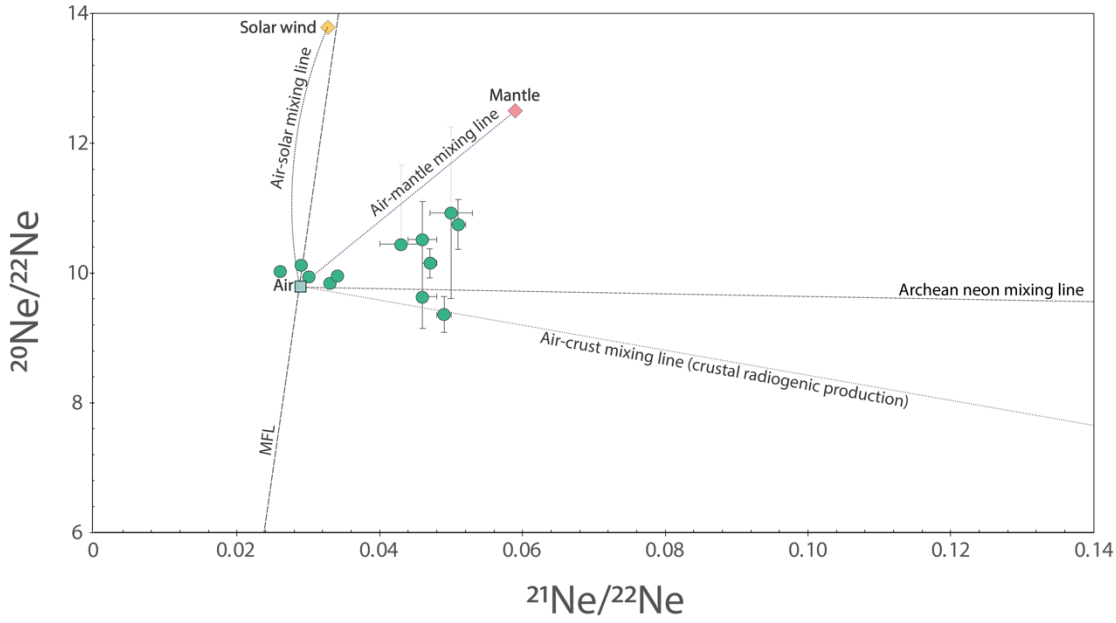

Figure 54 – Neon isotope plot showing $^{20}Ne/^{22}Ne$ vs $^{21}Ne/^{22}Ne$ ratios in samples relative to air, mantle and crustal endmembers. Values are indicative of a two-component mixture, between air and crust, with negligible mantle influence. $^{21}Ne/^{22}Ne$ ratios in late Triassic tight-sandstone gases demonstrate 'air-like' features, as they have undergone migration and potentially reside in an open system, they have a significantly low contribution of radiogenic $^{21}Ne^{*}$ (35% of total ^{21}Ne), with the remaining 65% derived from an atmospheric source.

4.6.6 Resolving atmospheric contribution to crustal noble gases

$^{20}Ne/^{22}Ne$ vs $^{21}Ne/^{22}Ne$ ratios for the Xinchang tight sandstone gas samples represent a mixture between mantle, crust and air endmembers. Ratios plot closely to the air endmember ($^{20}Ne/^{22}Ne_{air}$ = 9.8), partially along the crustal production line, which suggests natural gases are largely dominated by and have interacted significantly with the atmosphere-equilibrated fluids. Crustal and mantle contributions to 21Ne are low due to the perceived absence of deviations toward these the primordial mantle and crustal radiogenic values ($^{20}Ne/^{22}Ne_{mantle}$ = 12.5 and $^{20}Ne/^{22}Ne_{crust}$ = 0.47). Due to the relative stability since the Late Permian, it is significantly unlikely that mantle volatiles have accumulated in these tight sandstone gas reservoirs (Ni et al., 2014). Other significant contributions to the measured abundances of noble gases in gas samples include crustal radiogenic and nucleogenic isotopes of He, Ne and Ar. ^{4}He, ^{21}Ne, ^{40}Ar compositions in gas samples represent the build-up and crustal abundance of U, Th and K from the source and host rock, and the degree of interaction between hydrocarbon fluids with meteoric and sea waters (Ballentine and K. O'nions, 1994). Noble gas samples with high concentrations of these radiogenic isotopes, therefore, signify dominant crustal fluid interaction and reflect an older system where radiogenic concentrations have

accumulated over geologic time (Byrne et al., 2018b). Although predominantly crustal in origin, ^{21}Ne and ^{40}Ar are present in high concentrations within the atmosphere. We can employ a binary mixing model to resolve the measured concentrations of ^{21}Ne and ^{40}Ar which subsequently establishes the influence of this atmosphere derived component (Ballentine et al., 2002, Hunt et al., 2012). For the nucleogenic contribution to ^{21}Ne ($^{21}Ne^{*}$), we use the following:

$$^{21}Ne^{*} = {}^{21}Ne_{meas} \times \left(1 - \frac{{}^{21}Ne/{}^{22}Ne_{air}}{{}^{21}Ne/{}^{22}Ne_{meas}}\right) \quad (87)$$

To calculate the contribution of radiogenic ^{40}Ar ($^{40}Ar^{*}$), we use the following:

$$^{40}Ar^{*} = {}^{40}Ar_{meas} \times 1\left(-\frac{{}^{40}Ar/{}^{36}Ar_{air}}{{}^{40}Ar/{}^{36}Ar_{meas}}\right) \quad (88)$$

$^{21}Ne_{meas}$, $^{40}Ar_{meas}$, $^{21}Ne/^{22}Ne_{meas}$ and $^{40}Ar/^{36}Ar_{meas}$ represent the measured concentrations and isotope ratios of ^{21}Ne and ^{40}Ar, and were endmember ratios are $^{21}Ne/^{22}Ne_{air} = 0.029$ and $^{40}Ar/^{36}Ar_{air} = 298.56$ (Lee et al., 2006). The contribution of atmospheric ^{21}Ne to the total measured concentration of ^{21}Ne is high, with pure radiogenic $^{21}Ne^{*}$ only accounting for ~35% of total measured ^{21}Ne concentrations, with the remaining ^{21}Ne (~65%) determined to be sourced from air contributions. ^{40}Ar, similarly, has a discernible atmospheric derived ^{40}Ar contribution accounting for ~50% of total ^{40}Ar, which indicates variable mixing with the atmosphere. This finding aligns with the solubility partitioning behaviour of these noble gases, as Ne, which has a lower solubility in water compared to Ar, is less readily dissolved and has a higher tendency to interact with a free gaseous phase, thus more efficiently mixing with the atmospheric derived Ne component introduced via groundwaters. It is therefore reasonable to assume that higher atmospheric contributions to Ne and Ar suggests lends further evidence for open system behaviour. Consequently, we surmise that the distinctive generational history and migration of hydrocarbon gases to the tight sandstone T_3x^2 unit has given rise to a high proportion of atmospheric derived ^{21}Ne and ^{40}Ar relative to other unconventional systems in the Sichuan Basin, which have been reported to be much more strongly crustal radiogenic, and less air-dominated.

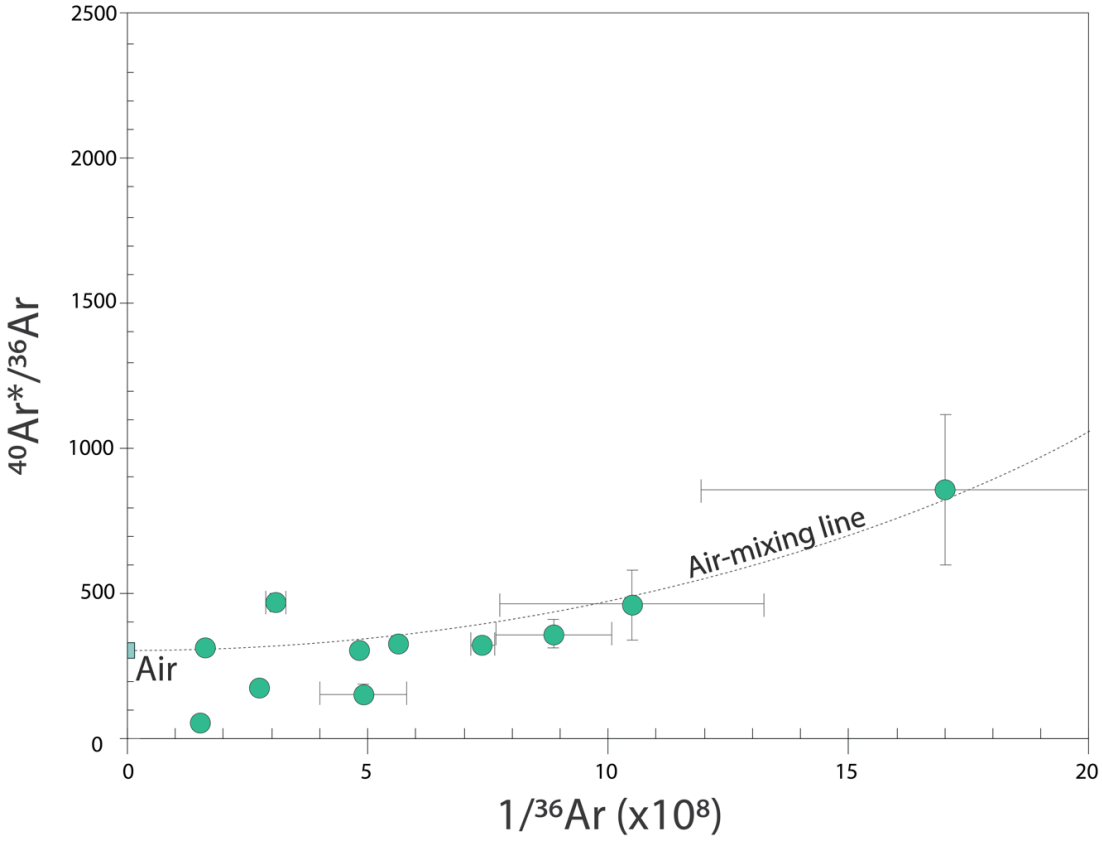

Figure 55 – Argon isotope ratios and concentrations. Atmospheric $^{40}Ar/^{36}Ar$ value: 298.6 (Lee et al., 2006); any ratios in excess of this value underline the input of the radiogenic daughter isotope ^{40}Ar, due to the decay of crustal ^{40}K. Gas signatures plot closely to this reported $^{40}Ar/^{36}Ar$ air value, $1/^{36}Ar$ ratios highlight the extent of migration, which is a major control on ^{36}Ar concentrations. The trendline signifies the evolution of $1/^{36}Ar$ from the known values of Ar in air.

Air-like Ar values are demonstrated in Figure 55, highlighting the relative fractionation of ^{36}Ar concentrations due to migration. The observed $^{40}Ar^*/^{36}Ar$ ratios measured within these gas samples are also much lower than other reported $^{40}Ar/^{36}Ar$ ratios in unconventional gas fields in the Sichuan Basin, such as the Wufeng-Longmaxi shale, as these unconventional hydrocarbon systems are geologically older (Lower Ordovician-Upper Silurian) and are less open to mixing with air-like noble gas signatures, revealing Ar ratios are governed by the mixing of deeper crustal fluids in which $^{40}Ar^*/^{36}Ar$ ratios are typically >1000.

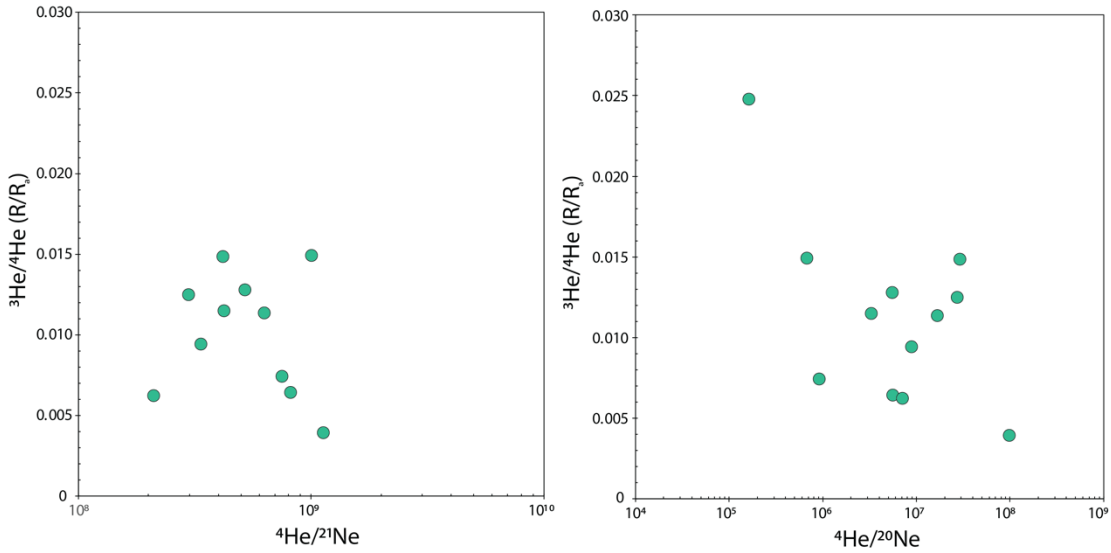

Figure 56 – He concentrations and elemental ratios ($^4He/^{21}Ne$ and $^4He/^{20}Ne$). R/R_a, denotes $^3He/^4He$ relative to atmosphere, where $R_a = 1.39 \times 10^{-6}$ (Porcelli et al., 2002). Samples have a highly radiogenic $^3He/^4He$ signature, which indicates that there exists a source for crustal decay which has imparted this component on tight sandstone gas samples. These plots illustrate the influence of mantle, crustal and atmospheric noble gas components. The lack of a strong trend indicates multiple overlapping sources with varying influence.

4.6.7 He accumulation

Although we have established the lower abundances of crustal radiogenic and mantle derived Ne; the production rate of He and the subsequent accumulation of He in groundwaters effectively describes the complex movement and mixing of deeper fluids. Typical crustal $^3He/^4He$ values are ~$0.01R_a$, whilst $^3He/^4He$ values indicative of the mantle are ~$8R_a$ (Ballentine and Burnard, 2002). ^4He concentrations are altered due to uranium abundances adjacent to the gas accumulation area and are therefore highly variable both vertically and laterally. In Figure 56, R/R_a ratios are observably low (0.004 - $0.025R_a$), and plot slightly above the typical crustal radiogenic production line, which means we can ascribe a dominantly crustal component to He. Compared with analogous unconventional systems in the Sichuan Basin, ^3He in the younger T_3x units is marginally higher, which may be in part due to Meso-Cenozoic basement faults, which has led to fracturing and minor normal faults, providing a pathway for gas migration (Wang et al., 2008) and a pathway for the minor introduction of magmatic ^3He via vertical advection. Similarly, enrichment of ^4He can arise from ^4He dissolved and transported via groundwater or via influence from an additional flux of ^4He from an adjacent granitic body (Zhang et al., 2019c). While we determine that $^3He/^4He$ (R/R_a) ratios are typical of a crustal fluids, we use the following mass balance equation to resolve the amount of helium derived from crustal and upper mantle end-members (Jenden et al., 1993).

$$\mathrm{He_{mantle}}(\%) = (\mathrm{R_{meas}} - \mathrm{R_{crust}})/(\mathrm{R_{mantle}} - \mathrm{R_{crust}}) \times 100\% \quad (89)$$

Where R represents the ratio R/R_a, and using a crustal $^3He/^4He$ value of $0.01R_a$ and a mantle $^3He/^4He$ value of $8R_a$ (Ballentine and Burnard, 2002) we determine that the fraction of mantle derived He is insignificant in all gas samples, accounting for between 0.0%3-0.19%. Sufficient deviations of $^4He/^{20}Ne$ ratios ($\leq 2.32 \times 10^6$) from air ($^4He/^{20}Ne_{air} = 0.318$) highlight a lack of atmospheric He, yet this component must still be accounted for using the following correction (Craig, 1978):

$$(^3\mathrm{He}/^4\mathrm{He})_c = \frac{(^3\mathrm{He}/^4\mathrm{He})_{meas} \times (^4\mathrm{He}/^{20}\mathrm{Ne})_{meas}/(^4\mathrm{He}/^{20}\mathrm{Ne})_{air} - (^3\mathrm{He}/^4\mathrm{He})_{air}}{(^4\mathrm{He}/^{20}\mathrm{Ne})_{meas}/(^4\mathrm{He}/^{20}\mathrm{Ne})_{air} - 1} \quad (90)$$

Highly crustal radiogenic $^4He/^{20}Ne$ values support corrected $^3He/^4He$ values, which when resolved of their air-excess component, are indistinguishable from measured $^3He/^4He$ ratios $(^3He/^4He)_c \approx (^3He/^4He)_{meas}$. Following the minor deduction of any atmosphere derived He, the resultant $^3He/^4He$ ratio represents a binary mixture of crustal, and mantle sourced He. The crustal component $^4He_{crust}$, which denotes purely radiogenic ^4He produced in the crust, can be determined using the following equation, which comprises the previously calculated corrected $(^3He/^4He)_c$ ratio, as well as mantle-derived and crustal $^3He/^4He$ ratios (Ballentine et al., 2002):

$$^4\mathrm{He}_{crust} = \frac{^4\mathrm{He}_{meas} \times ((^3\mathrm{He}/^4\mathrm{He})_{mantle} - (^3\mathrm{He}/^4\mathrm{He})_c)}{(^3\mathrm{He}/^4\mathrm{He})_{mantle} - (^3\mathrm{He}/^4\mathrm{He})_{crust}} \quad (91)$$

In a gas-liquid fraction, the original ratio of $^4He/^{36}Ar$ in the system can be calculated where all noble gases are partitioned and initially dissolved into a liquid phase ($V_g/V_l \rightarrow \infty$), with a salinity of 0.1 M at 10°C:

$$\left(\frac{^4\mathrm{He}}{^{36}\mathrm{Ar}}\right)_{initial} = \left(\frac{^4\mathrm{He}}{^{36}\mathrm{Ar}}\right)_{meas} \frac{\left(\frac{V_g}{V_l} + \frac{1}{K_{He}^d}\right)}{\left(\frac{V_g}{V_l} + \frac{1}{K_{Ar}^d}\right)} \quad (92)$$

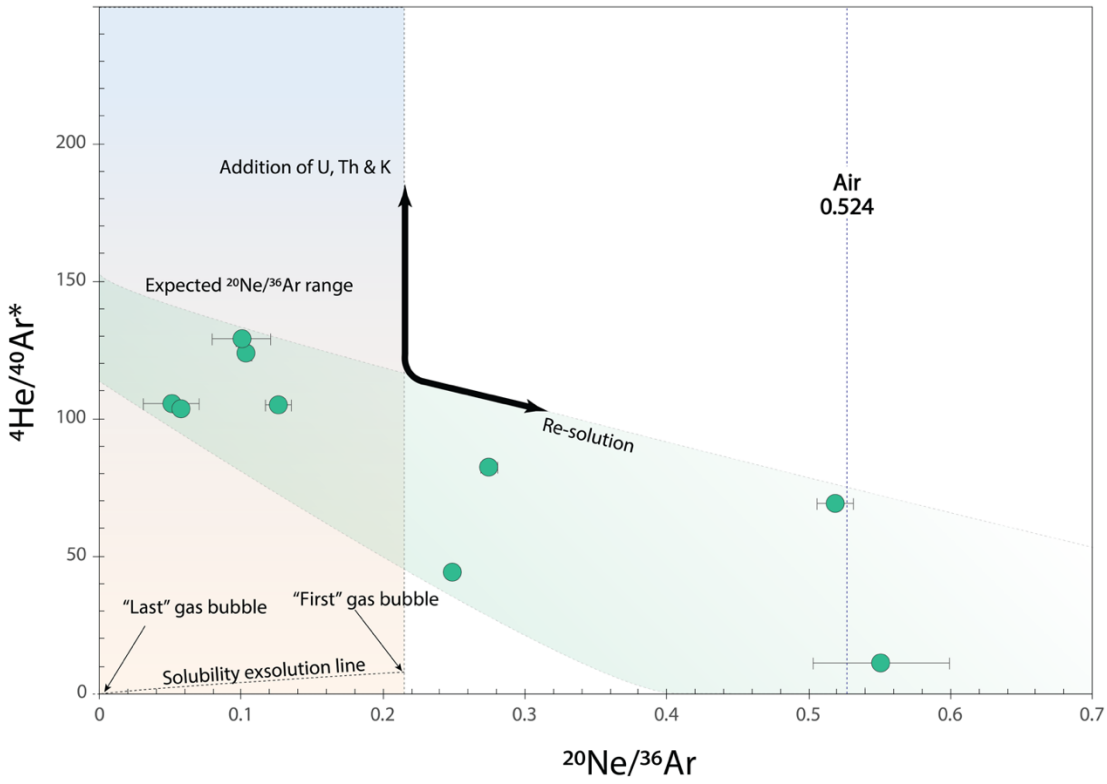

Figure 57 – Radiogenic $^{4}He/^{40}Ar^{*}$ vs air-derived $^{20}Ne/^{36}Ar$ plots ($^{40}Ar^{*}$ = air corrected radiogenic Ar). Effervescence or re-solution of gases, back into the liquid phase from the gas phase could explain $^{20}Ne/^{36}Ar$ values that exceed ASW. $^{4}He/^{40}Ar^{*}$ is dependent on the amount of localised U, Th and K, and is therefore higher in closed systems, which are less open to gas loss and have undergone less interaction with water (low $^{20}Ne/^{36}Ar$).

Figure 57 demonstrates a weakly negative correlation between $^{4}He/^{40}Ar^{*}$ and $^{20}Ne/^{36}Ar$ ratios, which denotes that radiogenic noble gases are more abundant in gas samples with lesser influence of groundwater interaction. The perceived excess radiogenic $^{4}He/^{40}Ar^{*}$, or the apparent enrichment of $^{4}He/^{40}Ar^{*}$, and abundance is primarily controlled by the amount of U, Th and K. This results in $^{4}He/^{40}Ar^{*}$ ratios outside of the expected range for the open system Rayleigh fractionation solubility controlled exsolution curve.

High $^{4}He/^{40}Ar^{*}$ ratios highlight the prospective economic potential for He resources in these areas. However, further study is needed to identify whether it meets the standards for commercial grade He.

4.6.8 He accumulation and H_2O fluid residence ages

To assess the in-situ production rates of reservoir ^{4}He in the Xujiahe tight sandstone unit, we use the following equation (Torgersen, 1980):

$$^4He_{\text{in situ production}} = \frac{\rho \Lambda J_4 (1-\varphi)}{\varphi} t \quad (93)$$

Where J_4 can be expressed as the following (Craig and Lupton, 1976):

$$J_4 = 0.2355 \times 10^{-12}(\text{U})\left(1 + 0.123\big((\text{Th}/\text{U}) - 4\big)\right) \quad (94)$$

U and Th concentrations are measured by spectral gamma ray and inferred from available wireline logging data. U is a redox-sensitive element, and as a result it is preferentially enriched in sediments deposited under anoxic conditions (Kimura and Watanabe, 2001).

Table 38 – Crustal derived radiogenic ^{4}He groundwater ages using U (ppm), Th (ppm) concentrations. (1) U concentrations in the Xujiahe formation (Ullah et al., 2022). ρrock corresponds to the reservoir rock density and ϕ corresponds to reservoir porosity for the tight sandstone unit.

	U (ppm)	Th (ppm)	ρ_{rock} (g/cm^3)	ϕ (%)	^{4}He in-situ production rate (cm^3 STP ^{4}He/cm^3 H_2O year) x 10^{-11}	Initial ^{4}He in groundwater (cm^3 STP ^{4}He/cm^3 H_2O)	^{4}He age (year) x 10^8
Xinchang gas field	5.82[1]	7.2	2.60	3.44	4.92	0.03	6.10

^{4}He concentrations in the liquid phase can be backcalculated, as they are a function of dimensionless Henry's constant, accounting for non-ideality in the gas phase, reservoir pressure and temperature. Using a simple partitioning model between a gas and liquid phase, we derive modelled groundwater ages of between 1.11 x 10^8 and 3.51 x 10^8 years.

$$^4He_w = \left(\left(\frac{^4He}{Ar_g}\right) \Big/ \left(\frac{K^d_{He}}{K^d_{Ar}}\right) \right) \times Ar_w \quad (95)$$

Xujiahe tight sandstone associated ^{4}He groundwater ages are similarly high and pre-dating a realistic time the age of deposition. In this case, ^{4}He values cannot be accounted for by in-situ production alone, and consequently, the volume of rock required to produce the measured radiogenic ^{4}He concentrations is insufficient. It is thereby inferred to be indicative of open-system behaviour, as gas has migrated through a large volume of rock containing U, K and Th, where ex-situ ^{4}He may account for a resolvable proportion.

4.6.9 Open system volumetric gas-groundwater estimates

We adopt the use of a second order open system degassing model to quantify the extent of the gas-groundwater interaction via solubility controlled processes, in accordance with Henry's law and Henry's constants, K_i^M. These models expand upon our understanding of the complex reservoir conditions and potential storage mechanisms. These tight sandstone gases have low preserved porosity (<6%), and therefore held formation waters should be insignificant. If a larger, non-trivial quantity of formation waters (in higher porosity lithologies), it is expected that a greater exchange of noble gases between water and hydrocarbons will take place.

Table 39 - Gas-groundwater volume ratios for Ne and Ar using second order degassing models

	^{20}Ne	^{36}Ar
	V_g/V_w (**PD-OS**)	V_g/V_w (**PD-OS**)
Xinchang gas field		
X911-5	0.043	0.047
X911-7	-	-
X911-6	-	0.036
X911-3	0.029	0.024
X911-4	0.046	0.051
X2	0.052	0.067
X201	0.055	0.056
XS23-4H	0.040	0.036
XS22-6HF	0.047	0.040
XS21-26H	-	0.005
XS21-39HF	0.016	0.021
CX135	0.010	0.007

The second-order model assumes partial hydrocarbon loss from the system, indicating that the reservoir is open to gas loss. Upon reaching the trap, the model presumes minimal subsequent interaction, leading to gas escape. This gas loss may result from hydrocarbon migration and accumulation occurring prior to the full development of the trapping structure or seal. Calculated volumetric ratios show the $\frac{V_g}{V_w}$ required to produce the measured gas concentrations at reservoir temperature and pressure (RTP). Gas

samples are degassed, whereby a large volume of water exists relative to gas in the system as $\frac{V_g}{V_w}$ approaches zero.

Table 40 – Formation volume estimates using average G/W volume ratio estimates, Xinchang gas field

Gas field	Proven gas reserves (m^3)	Porosity (%)	Average G/W	Total water volume (m^3)	Total rock volume (m^3)
Xinchang	1.25 x 10^{11}	4.55	0.037	3.38 x 10^{12}	7.70 x 10^{13}

With both the formation porosity and known proven gas reserves, 1.25 x 1011 m3 (Liu et al., 2020a), the average porosity of 4.55% (Yu et al., 2018), as well as the average gas-water volumetric ratio (0.037), we can estimate the total formation water volume and rock volume, producing a total water volume of 3.38 x 10^{12} m^3 and an estimated total gas bearing rock volume of 7.70 x 10^{13} m^3. These estimates are far larger than expected, but they are sensitive to the total proven gas reserve volume. Furthermore, the low porosity suggests that a very large total rock volume is required to account for the relatively small pore space. In reservoirs where faults or fractures enhance permeability, assumptions about fluid flow or gas migration may also lead to overestimates of the effective reservoir volume.

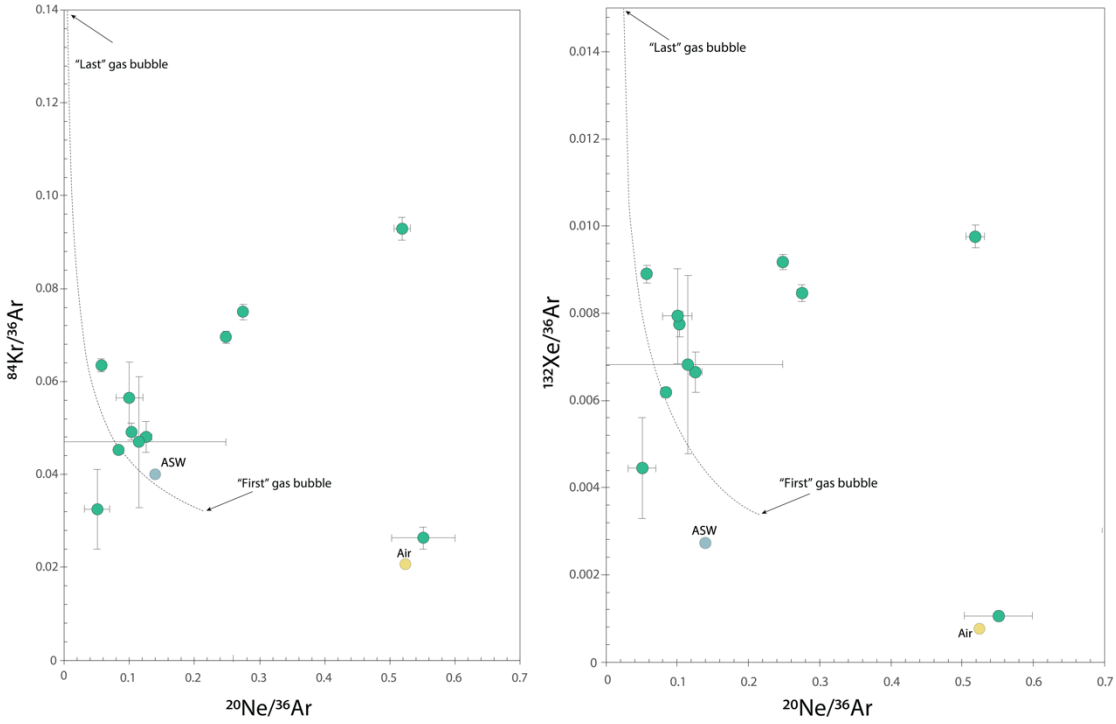

Figure 58 - Comparison of air derived noble gas elemental ratios. The observed ratios illustrate fractionation during gas dissolution and exsolution processes. These plots also highlight the progressive loss of lighter noble gases (e.g., Ne) relative to heavier ones (e.g., Kr and Xe) during degassing.

4.6.10 Excess Kr and Xe

Enriched $^{84}Kr/^{36}Ar$ and $^{132}Xe/^{36}Ar$ values relative to ASW are thought to arise following interaction with an oil phase (Barry et al., 2016); however, the Xu-2 tight sandstones, which are thought to have vertically migrated from the Xu-1 mudstone source rocks, are dominated by humic type III kerogen, which is essentially gas-prone (Lai et al., 2015). The enrichment of Kr and Xe is therefore a result of complicated processes such as adsorption in the underlying clay rich shales and mudstones.

Gas samples show an overall slight enrichment of ^{84}Kr and a depletion of ^{132}Xe concentrations with respect to initial ASW concentrations at recharge. $^{84}Kr_{meas}/^{84}Kr_{asw}$ = 1.58, whilst $^{132}Xe_{meas}/^{132}Xe_{asw}$ = 0.9. However, $(^{84}Kr/^{36}Ar)_{meas}/(^{84}Kr/^{36}Ar)_{asw}$ and $(^{132}Xe/^{36}Ar)_{meas}/(^{132}Xe/^{36}Ar)_{asw}$ are 1.4 and 2.52 times than calculated ASW ratios, respectively (Figure 58). Due to this measured enrichment of Xe, it is thereby possible to modify the Rayleigh fractionation curve to account for this 200% Xe excess. As Kr and Xe are in excess, the volumetric gas-water ratios will be unreliable for both noble gases, and the V_g/V_w of the lighter noble gases should be considered more indicative of the extent of gas-water interaction.

Kr and Xe are highly fractionated and in excess of both air and ASW (Figure 59). Following the modification of the solubility exsolution curve to account for the 200% Xe excess, gas samples appear to fit the Rayleigh fractionation model reasonably well. Elevated $^{132}Xe/^{36}Ar$ ratios and the measurable excess of Kr and Xe in tight sandstone gases versus those reported in the literature for Sichuan Basin unconventional shales are explained to be a combination of two processes, due to high efficiency for trapping in geological media and effective sorbates (i.e., shales). Kr and Xe in clay-rich environments remain trapped and forgo desorption until sufficient thermal energy is attained (Fanale and Cannon, 1971, Podosek et al., 1981). Enrichment of Kr & Xe in the tight sandstones may also be attributed to previously trapped Kr and Xe, whose signature has been imparted on hydrocarbon gases through desorption in the organic-rich source rock, at the time of expulsion and migration (when uplift altered the hydraulic gradient, inducing desorption and fluid flow). The absence of an effective 'solid phase' trapping mechanism in the tight sandstone indicates that Kr and Xe remain in a gaseous state or dissolved in water due to contact with higher volumes of water and more prevalent mixing with surrounding groundwaters.

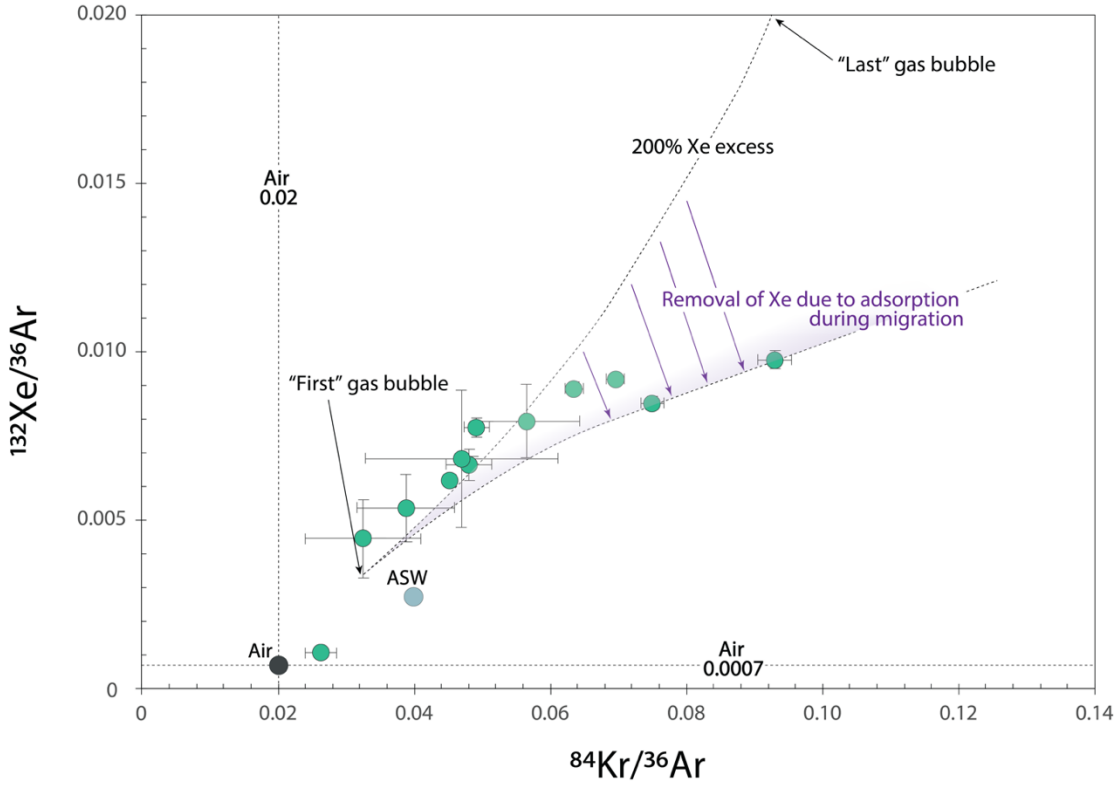

Figure 59 – Air-derived heavy noble gas ratios $^{132}Xe/^{36}Ar$ vs $^{84}Kr/^{36}Ar$. The data fits a Rayleigh fractionation curve, modified for a 200% excess Xe component. Representing remaining elemental ratios in the free gas phase. As progressive degassing of Ar ensues, elemental ratios of the heavier ^{84}Kr and ^{132}Xe increase exponentially as more is partitioned into the gas phase.

The Xujiahe tight sandstones exhibit low porosity, which generally correlates with low permeability throughout most of the formation. However, in the proximity of the fault-fracture zones, permeability is relatively higher due to processes such as pore collapse and fracturing. These processes likely result in the destruction of the original pore structure, opening secondary flow pathways that enhance permeability in these specific areas. Figure 60 illustrates how fracturing near the fault zone promotes gas migration and mixing processes in an open system. This suggests that, while much of the reservoir remains impermeable, the fault-fracture zones play a critical role in controlling gas movement and mixing with atmosphere derived components. The major consequence on hydrocarbon exploration of this natural gas accumulation model is that there is an increased risk of hydrocarbon leakage if the seal or caprock is compromised. Interactions between hydrocarbons and groundwater in these zones can significantly alter fluid compositions and affect hydrocarbon quality.

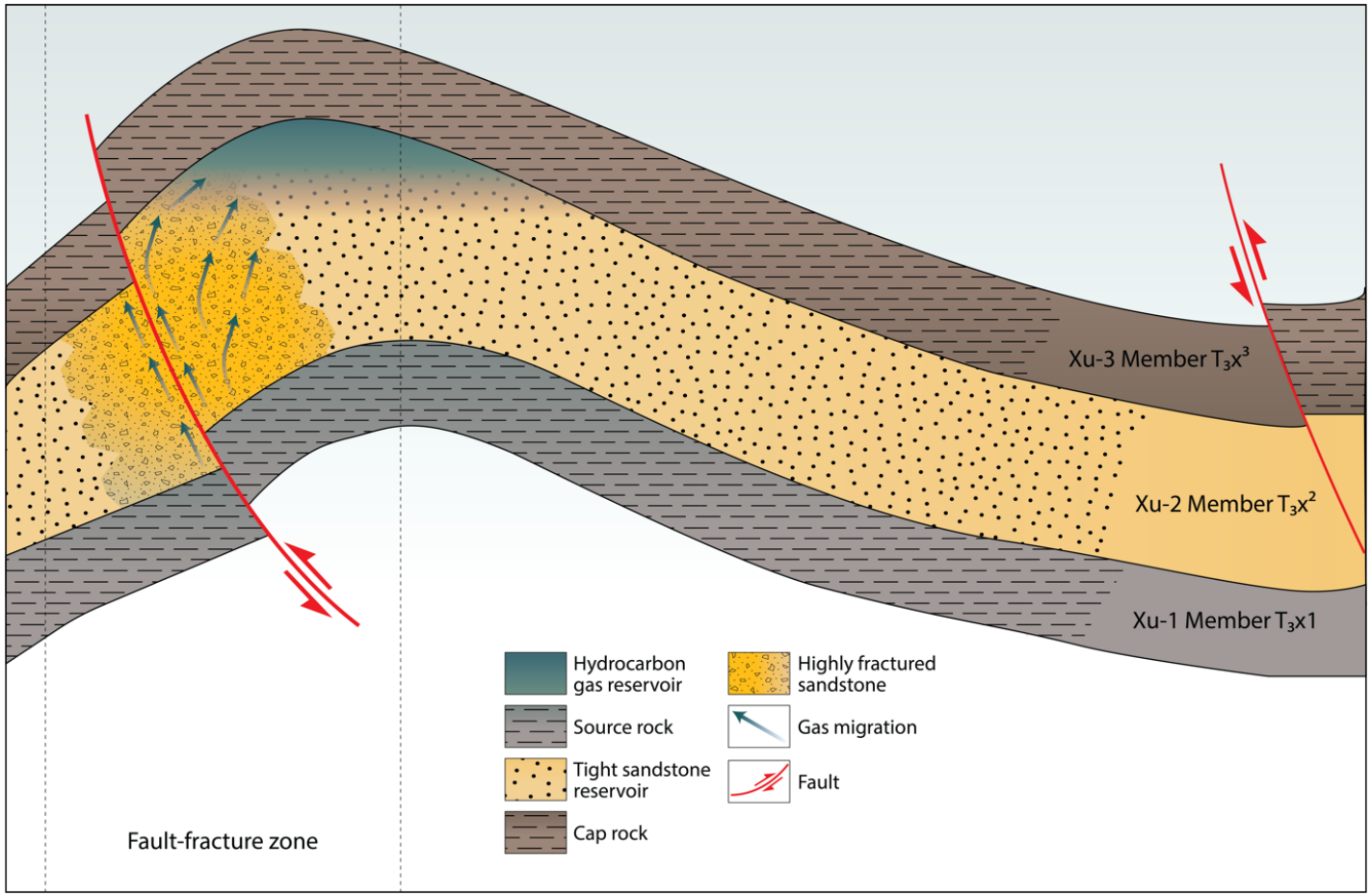

Figure 60 - This conceptual model illustrates the migration and accumulation of Xujiahe hydrocarbons within the fault-fracture zone. The Xu-2 (T_3x^2) gas reservoir is situated within a highly fractured sandstone layer and is capped by the Xu-3 (T_3x^3) member. The tight sandstone reservoir and source rock are also depicted, indicating the origin and migration pathway of the hydrocarbons. Faults facilitate the upward migration of gas from the Xu-1 (T_3x^1) source rock through the fault-fracture system into the overlying reservoir. The model demonstrates how structural and stratigraphic traps, combined with faulting and fracturing, can create an environment for hydrocarbon accumulation whereby mixing with surrounding groundwaters can occur.

4.7 Concluding remarks

Unconventional tight sandstone gases have proven to be valuable economic resources worldwide, and the pioneering application of noble gas isotope geochemistry in these areas has brought us closer than ever to understanding the complex factors that control subsurface fluid interactions, and the fluxes of gases derived from different sources. Tight sandstones represent a scenario whereby gases have migrated to a low-porosity, permeable sandstone reservoir, and during migration these gases undertake and interact with a variable fraction of ASW and crustal derived noble gas concentrations. There appears to be agreement with solubility-based models to justify the extent of fractionation in the lighter noble gases (Ne & Ar), which suggest an open system dominates. Gas samples have R/R_a values that signify a strongly crustal ($0.0037R_a$-0.038 R_a) regime with insignificant mantle input. Atmospheric ^{21}Ne contributes significantly to the total measured ^{21}Ne concentration, with only ~35% being attributable to pure radiogenic Ne ($^{21}Ne^*$), while the remaining ~65% is derived from atmospheric sources. Similarly, ^{40}Ar shows an atmospheric contribution of approximately 50% of the total ^{40}Ar, indicating varying degrees of mixing with atmospheric components. These findings are consistent with the solubility partitioning behaviour of the noble gases, as Ne, due to its lower solubility in water relative to Ar, dissolves less readily and remains prone to interaction with the gaseous phase, facilitating a higher atmospheric contribution through more efficient groundwater mixing. Gases which have undergone greater migration have a significantly lower contribution of radiogenic $^{21}Ne^*/^{22}Ne$.

We determine that fault-fracture zones act as conduits for fluid flow, allowing for the more efficient mixing of noble gases with groundwaters, particularly in regions where permeability has been increased. The presence of atmospheric noble gases in these zones suggests that the reservoir has been open to external inputs, likely driven by the increased permeability following pore collapse or reactivation of fractures. These observations underscore the importance of structural controls on noble gas migration and reservoir dynamics, particularly in systems where porosity is limited but permeability is enhanced through faulting and fracturing.

This has significant implications for hydrocarbon accumulation, as these zones could create potential migration pathways for hydrocarbons, leading to localised accumulation near faults and within the fault fracture zone. These processes also give rise to the risk of hydrocarbon leakage if caprock integrity is compromised, potentially reducing recoverable reserves. Faulting can cause compartmentalisation of the reservoir, isolating

hydrocarbon-rich sections and complicating recovery efforts. Additionally, the observable interaction between hydrocarbons and groundwaters within these zones have altered fluid compositions, affecting both gas-to-water ratios and hydrocarbon quality. While the enhanced permeability near faults can improve recovery potential, careful assessment of the structural geology is essential to mitigate leakage risks and optimise extraction strategies.

As burgeoning technologies increase the production efficiency of previously unreachable gas reserves in low porosity, low permeability tight sandstone reservoirs, uncertainties still remain regarding the migration pathways of these newly recoverable gases; however, noble gas geochemistry allows us to better constrain the complex mixing processes of these gas-liquid-solid phase interactions, in addition to the influence of crustal fluids and/or mantle-associated ^{3}He introduced into the system. While tight-sandstone reservoirs are an emerging source of hydrocarbons, Kr and Xe enrichment due to adsorption in sandstone gas-bearing units is uniquely inefficient. Therefore, the contribution of tight sandstones to any atmospheric deficit of Xe is also perceived to be minor.

MANUSCRIPT 3 REFERENCES

Aregbe, Y., Valkiers, S., Mayer, K., De Bièvre, P., 1996. Comparative isotopic measurements on xenon and krypton. International Journal of Mass Spectrometry and Ion Processes 153(1), L1-L5. doi.org/https://doi.org/10.1016/0168-1176(96)04368-6.

Ballentine, C., K. O'nions, R., 1994. The use of natural He, Ne and Ar isotopes to study hydrocarbon-related fluid provenance, migration and mass balance in sedimentary basins. Geological Society of London Special Publications 78, 347-361. doi.org/10.1144/GSL.SP.1994.078.01.23.

Ballentine, C.J., Burgess, R., Marty, B., 2002. Tracing Fluid Origin, Transport and Interaction in the Crust. Reviews in Mineralogy and Geochemistry 47(1), 539-614. doi.org/10.2138/rmg.2002.47.13.

Ballentine, C.J., Burnard, P.G., 2002. Production, Release and Transport of Noble Gases in the Continental Crust. Reviews in Mineralogy and Geochemistry 47(1), 481-538. doi.org/10.2138/rmg.2002.47.12.

Barry, P.H., Lawson, M., Meurer, W.P., Warr, O., Mabry, J.C., Byrne, D.J., Ballentine, C.J., 2016. Noble gases solubility models of hydrocarbon charge mechanism in the Sleipner Vest gas field. Geochimica et Cosmochimica Acta 194, 291-309. doi.org/https://doi.org/10.1016/j.gca.2016.08.021.

Beyerle, U., Aeschbach, W., Imboden, D., Baur, H., Graf, T., Kipfer, R., 2000. A Mass Spectrometric System for the Analysis of Noble Gases and Tritium from Water Samples. Environmental Science & Technology - ENVIRON SCI TECHNOL 34. doi.org/10.1021/es990840h.

Borjigin, T., Shen, B., Yu, L., Yunfeng, Y., Zhang, W., Cheng, T., Xi, B., Zhang, Q., Bao, F., Qin, J., 2017. Mechanisms of shale gas generation and accumulation in the Ordovician Wufeng-Longmaxi Formation, Sichuan Basin, SW China. Petroleum Exploration and Development 44, 69-78.

Bosch, A., Mazor, E., 1988. Natural gas association with water and oil as depicted by atmospheric noble gases: case studies from the southeastern Mediterranean Coastal Plain. Earth and Planetary Science Letters 87(3), 338-346. doi.org/https://doi.org/10.1016/0012-821X(88)90021-0.

Byrne, D.J., Barry, P.H., Lawson, M., Ballentine, C.J., 2018. Determining gas expulsion vs retention during hydrocarbon generation in the Eagle Ford Shale using noble gases. Geochimica et Cosmochimica Acta 241, 240-254. doi.org/https://doi.org/10.1016/j.gca.2018.08.042.

Byrne, D.J., Barry, P.H., Lawson, M., Ballentine, C.J., 2018. Noble gases in conventional and unconventional petroleum systems. Geological Society, London, Special Publications 468(1), 127-149. doi.org/10.1144/SP468.5.

Byrne, D.J., Barry, P.H., Lawson, M., Ballentine, C.J., 2020. The use of noble gas isotopes to constrain subsurface fluid flow and hydrocarbon migration in the East Texas Basin. Geochimica et Cosmochimica Acta 268, 186-208. doi.org/https://doi.org/10.1016/j.gca.2019.10.001.

Cao, C., Lv, Z., Li, L., Du, L., 2016. Geochemical characteristics and implications of shale gas from the Longmaxi Formation, Sichuan Basin, China. Journal of Natural Gas Geoscience 1(2), 131-138. doi.org/https://doi.org/10.1016/j.jnggs.2016.05.001.

Cao, C., Zhang, M., Li, L., Wang, Y., Li, Z., Du, L., Holland, G., Zhou, Z., 2020. Tracing the sources and evolution processes of shale gas by coupling stable (C, H) and noble gas isotopic compositions: Cases from Weiyuan and Changning in Sichuan Basin, China. Journal of Natural Gas Science and Engineering 78, 103304. doi.org/https://doi.org/10.1016/j.jngse.2020.103304.

Cao, C., Zhang, M., Tang, Q., Yang, Y., Lv, Z., Zhang, T., Chen, C., Yang, H., Li, L., 2018. Noble gas isotopic variations and geological implication of Longmaxi shale gas in Sichuan Basin, China. Marine and Petroleum Geology 89, 38-46. doi.org/10.1016/j.marpetgeo.2017.01.022.

Craig, H., 1978. A mantle helium component in Circum-Pacific volcanic gases : Hakone, the Marianas, and Mt. Lassen.

Craig, H., Lupton, J.E., 1976. Primordial neon, helium, and hydrogen in oceanic basalts. Earth and Planetary Science Letters 31(3), 369-385. doi.org/https://doi.org/10.1016/0012-821X(76)90118-7.

Crovetto, R., Fernández-Prini, R., Japas, M.L., 1982. Solubilities of inert gases and methane in H2O and in D2O in the temperature range of 300 to 600 K. The Journal of Chemical Physics 76(2), 1077-1086. doi.org/10.1063/1.443074.

Dai, J., 2016. Chapter 3 - Large Coal-Derived Gas Fields and Their Gas Sources in the Sichuan Basin, in: Dai, J. (Ed.) Giant Coal-Derived Gas Fields and their Gas Sources in China. Academic Press, pp. 151-268. doi.org/https://doi.org/10.1016/B978-0-12-805093-4.00003-3.

Dai, J., Ni, Y., Qin, S., Huang, S., Peng, W., Han, W., 2018. Geochemical characteristics of ultra-deep natural gas in the Sichuan Basin, SW China. Petroleum Exploration and Development 45(4), 619-628. doi.org/https://doi.org/10.1016/S1876-3804(18)30067-3.

Dai, J., Ni, Y., Zou, C., 2012. Stable carbon and hydrogen isotopes of natural gases sourced from the Xujiahe Formation in the Sichuan Basin, China. Organic Geochemistry 43, 103-111. doi.org/https://doi.org/10.1016/j.orggeochem.2011.10.006.

Dai, J., Ni, Y., Zou, C., Tao, S., Hu, G., Hu, A., Yang, C., Tao, X., 2009. Stable carbon isotopes of alkane gases from the Xujiahe coal measures and implication for gas-source correlation in the Sichuan Basin, SW China. Organic Geochemistry 40(5), 638-646. doi.org/https://doi.org/10.1016/j.orggeochem.2009.01.012.

Dai, J., Zou, C., Dong, D., Ni, Y., Wu, W., Gong, D., Wang, Y., Huang, S., Huang, J., Fang, C., Liu, D., 2016. Geochemical characteristics of marine and terrestrial shale gas in China. Marine and Petroleum Geology 76, 444-463. doi.org/https://doi.org/10.1016/j.marpetgeo.2016.04.027.

Dai, J., Zou, C., Liao, S., Dong, D., Ni, Y., Huang, J., Wu, W., Gong, D., Huang, S., Hu, G., 2014. Geochemistry of the extremely high thermal maturity Longmaxi shale gas, southern Sichuan Basin. Organic Geochemistry 74, 3-12. doi.org/https://doi.org/10.1016/j.orggeochem.2014.01.018.

Darrah, T.H., Vengosh, A., Jackson, R.B., Warner, N.R., Poreda, R.J., 2014. Noble gases identify the mechanisms of fugitive gas contamination in drinking-water wells overlying the Marcellus and Barnett Shales. Proceedings of the National Academy of Sciences 111(39), 14076-14081. doi.org/10.1073/pnas.1322107111.

Du, H., Shi, Z., Chai, H., Zeng, T., Li, B., Pan, L., Tian, Y., 2023. A New Natural Gas Accumulation Model in the Triassic Xujiahe Formation: A Case Study in the Tongjiang-Malubei Area of the Sichuan Basin. Energies 16(16), 5936.

Du, J., Xu, C., 2011. The exploration of the major gas field in Xujiahe Formation of Sichuan Basin. Beijing: Petroleum Industry Press.

Feng, Z., Dong, D., Tian, J., Wu, W., Cai, Y., Shi, Z., Peng, W., 2019. Geochemical characteristics of Lower Silurian shale gas in the Changning-Zhaotong exploration blocks, southern periphery of the Sichuan Basin. Journal of Petroleum Science and Engineering 174, 281-290. doi.org/https://doi.org/10.1016/j.petrol.2018.11.022.

Gong, L., Zeng, L., Gao, Z., Zhu, R., Zhang, B., 2016. Reservoir characterization and origin of tight gas sandstones in the Upper Triassic Xujiahe formation, Western Sichuan Basin, China. Journal of Petroleum Exploration and Production Technology 6(3), 319-329. doi.org/10.1007/s13202-015-0203-9.

Hilton, D.R., Fischer, T.P., Marty, B., 2002. Noble gases and volatile recycling at subduction zones. Reviews in Mineralogy & Geochemistry 47, 319-370.

Hu, D., Zhang, H., Ni, K., Yu, G., 2014. Main controlling factors for gas preservation conditions of marine shales in southeastern margins of the Sichuan Basin. Natural Gas Industry 34, 17-23. doi.org/10.3787/j.issn.1000-0976.2014.06.003.

Huang, S., Zhang, T., Wang, S., Xie, G., Hu, D., Jiang, Z., Dong, T., 2004. Research on source characteristics and origin of Xujiahe Formation, Upper Triassic in Chishui area, Sichuan Basin. Natural Gas Geoscience 15(6), 590-592.

Hunt, A., Darrah, T., J. Poreda, R., 2012. Determining the source and genetic fingerprint of natural gases using noble gas geochemistry: A northern Appalachian Basin case study. AAPG Bulletin 96, 1785-1811. doi.org/10.1306/03161211093.

Jenden, P.D., Hilton, D., Kaplan, I., Craig, H., Howell, D., 1993. Abiogenic hydrocarbons and mantle helium in oil and gas fields. US Geological survey professional paper 1570(1), 31-56.

Jiang, S., Tang, X., Cai, D., Xue, G., He, Z., Long, S., Peng, Y., Gao, B., Xu, Z., Dahdah, N., 2017. Comparison of marine, transitional, and lacustrine shales: A case study from the Sichuan Basin in China. Journal of Petroleum Science and Engineering 150, 334-347. doi.org/https://doi.org/10.1016/j.petrol.2016.12.014.

Jiao, F., 2019. Theoretical insights, core technologies and practices concerning "volume development" of shale gas in China. Natural Gas Industry B 6(6), 525-538. doi.org/https://doi.org/10.1016/j.ngib.2019.05.001.

Kimura, H., Watanabe, Y., 2001. Oceanic anoxia at the Precambrian-Cambrian boundary. Geology 29(11), 995-998.

Kipfer, R., Aeschbach-Hertig, W., Peeters, F., Stute, M., 2002. Noble Gases in Lakes and Ground Waters. Reviews in Mineralogy and Geochemistry 47(1), 615-700. doi.org/10.2138/rmg.2002.47.14.

Lai, J., Wang, G., Ran, Y., Zhou, Z., 2015. Predictive distribution of high-quality reservoirs of tight gas sandstones by linking diagenesis to depositional facies: Evidence from Xu-2 sandstones in the Penglai area of the central Sichuan basin, China. Journal of Natural Gas Science and Engineering 23, 97-111. doi.org/https://doi.org/10.1016/j.jngse.2015.01.026.

Lee, J.-Y., Marti, K., Severinghaus, J.P., Kawamura, K., Yoo, H.-S., Lee, J.B., Kim, J.S., 2006. A redetermination of the isotopic abundances of atmospheric Ar. Geochimica et Cosmochimica Acta 70(17), 4507-4512. doi.org/https://doi.org/10.1016/j.gca.2006.06.1563.

Li, G., Qin, Y., Shen, J., Wu, M., Li, C., Wei, K., Zhu, C., 2019. Geochemical characteristics of tight sandstone gas and hydrocarbon charging history of Linxing area in Ordos Basin, China. Journal of Petroleum Science and Engineering 177, 198-207. doi.org/https://doi.org/10.1016/j.petrol.2019.02.023.

Li, J., Hu, D., Zou, H., Shang, X., Ren, H., Wang, L., 2016. Coupling relationship between reservoir diagenesis and gas accumulation in Xujiahe Formation of Yuanba–Tongnanba area, Sichuan Basin, China. Journal of Natural Gas Geoscience 1(5), 335-352. doi.org/https://doi.org/10.1016/j.jnggs.2016.11.003.

Li, J., Liu, J., Chen, H., He, J., Wang, R., Shao, X., Fang, X., 2023. Fracture Modeling of Deep Tight Sandstone Fault-Fracture Reservoir Based on Geological Model and Seismic Attributes: A Case Study on Xu 2 Member in Western Sichuan Depression, Sichuan Basin. Geofluids 2023, 6516181. doi.org/10.1155/2023/6516181.

Li, Y., He, D., Chen, L., Mei, Q., Li, C., Zhang, L., 2016. Cretaceous sedimentary basins in Sichuan, SW China: Restoration of tectonic and depositional environments. Cretaceous Research 57, 50-65. doi.org/https://doi.org/10.1016/j.cretres.2015.07.013.

Li, Y., Qin, S., Wang, Y., Holland, G., Zhou, Z., 2020. Tracing interaction between hydrocarbon and groundwater systems with isotope signatures preserved in the Anyue gas field, central Sichuan Basin, China. Geochimica et Cosmochimica Acta 274, 261-285. doi.org/https://doi.org/10.1016/j.gca.2020.01.039.

Li, Y., Tootell, D., Holland, G., Zhou, Z., 2021. Performance of the NGX High-Resolution Multiple Collector Noble Gas Mass Spectrometer. Geochemistry, Geophysics, Geosystems 22(11), e2021GC009997. doi.org/https://doi.org/10.1029/2021GC009997.

Liang, X., Xu, Z., Zhang, Z., Wang, W., Zhang, J., Lu, H., Zhang, L., Zou, C., Wang, G., Mei, J., Rui, Y., 2020. Breakthrough of shallow shale gas exploration in Taiyang anticline area and its significance for resource development in Zhaotong, Yunnan Province, China. Petroleum Exploration and Development 47(1), 12-29. doi.org/https://doi.org/10.1016/S1876-3804(20)60002-7.

Liu, J., Liu, Z., Liu, Z., Liu, Y., Shen, B., Xiao, K., Bi, Y., Wang, X., Wang, A., Fan, L., Li, J., 2023. Geological characteristics and models of fault-fold-fracture body in deep tight sandstone of the second member of Upper Triassic Xujiahe Formation in Xinchang structural belt of Sichuan Basin, SW China. Petroleum Exploration and Development 50(3), 603-614. doi.org/https://doi.org/10.1016/S1876-3804(23)60413-6.

Liu, J., Liu, Z., Xiao, K., Huang, Y., Jin, W., 2020. Characterization of favorable lithofacies in tight sandstone reservoirs and its significance for gas exploration and exploitation: A case study of the 2nd Member of Triassic Xujiahe Formation in the Xinchang area, Sichuan Basin. Petroleum Exploration and Development 47(6), 1194-1205. doi.org/https://doi.org/10.1016/S1876-3804(20)60129-5.

Liu, R., Wen, T., Amalberti, J., Zheng, J., Hao, F., Jiang, D., 2021. The dichotomy in noble gas signatures linked to tectonic deformation in Wufeng-Longmaxi Shale, Sichuan Basin. Chemical Geology 581, 120412. doi.org/https://doi.org/10.1016/j.chemgeo.2021.120412.

Liu, S., Yang, Y., Deng, B., Zhong, Y., Wen, L., Sun, W., Li, Z., Jansa, L., Li, J., Song, J., Zhang, X., Peng, H., 2021. Tectonic evolution of the Sichuan Basin, Southwest China. Earth-Science Reviews 213, 103470. doi.org/https://doi.org/10.1016/j.earscirev.2020.103470.

Ma, X., 2017. Natural gas and energy revolution: A case study of Sichuan–Chongqing gas province. Natural Gas Industry B 4(2), 91-99. doi.org/https://doi.org/10.1016/j.ngib.2017.07.014.

Marty, B., 2020. Origins and early evolution of the atmosphere and the oceans. Geochemical Perspectives 9(2), 135-136.

Moreira, M., 2013. Noble gas constraints on the origin and evolution of Earth's volatiles. Geochemical Perspectives 2(2), 229-230.

Ni, Y., Dai, J., Tao, S., Wu, X., Liao, F., Wu, W., Zhang, D., 2014. Helium signatures of gases from the Sichuan Basin, China. Organic Geochemistry 74, 33-43. doi.org/https://doi.org/10.1016/j.orggeochem.2014.03.007.

Nie, H., Li, D., Liu, G., Lu, Z., Hu, W., Wang, R., Zhang, G., 2020. An overview of the geology and production of the Fuling shale gas field, Sichuan Basin, China. Energy Geoscience 1(3), 147-164. doi.org/https://doi.org/10.1016/j.engeos.2020.06.005.

Pepin, R.O., 2000. On the Isotopic Composition of Primordial Xenon in Terrestrial Planet Atmospheres, in: Benz, W., Kallenbach, R., Lugmair, G.W. (Eds.), From Dust to Terrestrial Planets. Springer Netherlands, Dordrecht, pp. 371-395.

Porcelli, D., Ballentine, C., Wieler, R., 2002. An Overview of Noble Gas Geochemistry and Cosmochemistry. Reviews in Mineralogy & Geochemistry - REV MINERAL GEOCHEM 47, 1-19. doi.org/10.2138/rmg.2002.47.1.

Sun, J., Bao, H., 2018. Comprehensive characterization of shale gas reservoirs: A case study from Fuling shale gas field. Petroleum Geology & Experiment 40(1), 1-12.

Tolstikhin, I.N., Ballentine, C.J., Polyak, B.G., Prasolov, E.M., Kikvadze, O.E., 2017. The noble gas isotope record of hydrocarbon field formation time scales. Chemical Geology 471(September), 141-152. doi.org/10.1016/j.chemgeo.2017.09.032.

Torgersen, T., 1980. Controls on pore-fluid concentration of 4He and 222Rn and the calculation of 4He/222Rn ages. Journal of Geochemical Exploration 13(1), 57-75. doi.org/https://doi.org/10.1016/0375-6742(80)90021-7.

Ullah, J., Luo, M., Ashraf, U., Pan, H., Anees, A., Li, D., Ali, M., Ali, J., 2022. Evaluation of the geothermal parameters to decipher the thermal structure of the upper crust of the Longmenshan fault zone derived from borehole data. Geothermics 98, 102268. doi.org/https://doi.org/10.1016/j.geothermics.2021.102268.

Wang, G., Jin, Z., Liu, G., Liu, Q., Liu, Z., Wang, H., Liang, X., Jiang, T., Wang, R., 2020. Geological implications of gamma ray (GR) anomalies in marine shales: A case study of the Ordovician-Silurian Wufeng-Longmaxi succession in the Sichuan Basin and its periphery, Southwest China. Journal of Asian Earth Sciences 199, 104359. doi.org/https://doi.org/10.1016/j.jseaes.2020.104359.

Wang, X., Liu, W., Li, X., Liu, Q., Tao, C., Xu, Y., 2020. Radiogenic helium concentration and isotope variations in crustal gas pools from Sichuan Basin, China. Applied Geochemistry 117, 104586. doi.org/https://doi.org/10.1016/j.apgeochem.2020.104586.

Wang, Z., 2018. Reservoir forming conditions and key exploration and development technologies for marine shale gas fields in Fuling area, South China. Petroleum Research 3(3), 197-209. doi.org/https://doi.org/10.1016/j.ptlrs.2018.06.008.

Wang, Z.-c., Zhao, W.-z., Li, Z.-y., Jiang, X.-f., Li, J., 2008. Role of basement faults in gas accumulation of Xujiahe Formation, Sichuan Basin. Petroleum Exploration and Development 35(5), 541-547. doi.org/https://doi.org/10.1016/S1876-3804(09)60087-2.

Wei, G., Chen, G., Du, S., Zhang, L., Yang, W., 2008. Petroleum systems of the oldest gas field in China: Neoproterozoic gas pools in the Weiyuan gas field, Sichuan Basin. Marine and Petroleum Geology 25(4), 371-386. doi.org/https://doi.org/10.1016/j.marpetgeo.2008.01.009.

Wieler, R., 2023. A Journey in Noble Gas Cosmochemistry and Geochemistry. Geochemical Perspectives 12(1), 1-2.

Xu, Z., Jiang, S., Liu, L., Wu, K., Li, R., Liu, Z., Shao, M., Jia, K., Feng, Y., 2020. Natural gas accumulation processes of tight sandstone reservoirs in deep formations of Songliao Basin, NE China. Journal of Natural Gas Science and Engineering 83, 103610. doi.org/https://doi.org/10.1016/j.jngse.2020.103610.

Xu, Z., Liang, X., Lu, H., Zhang, J., Shu, H., Xu, Y., Wu, J., Wang, G., Lu, W., Tang, X., Shi, W., 2020. Structural deformation characteristics and shale gas preservation conditions in the Zhaotong National Shale Gas Demonstration Area along the southern margin of the Sichuan Basin. Natural Gas Industry B 7(3), 224-233. doi.org/https://doi.org/10.1016/j.ngib.2019.10.004.

Yan, D., Wang, H., Fu, Q., Chen, Z., He, J., Gao, Z., 2015. Geochemical characteristics in the Longmaxi Formation (Early Silurian) of South China: Implications for organic matter accumulation. Marine and Petroleum Geology 65, 290-301. doi.org/https://doi.org/10.1016/j.marpetgeo.2015.04.016.

Yang, P., Zhang, L., Liu, K., Cao, B., Gao, J., Qiu, G., 2021. Diagenetic history and reservoir evolution of tight sandstones in the second member of the Upper Triassic Xujiahe Formation, western Sichuan Basin, China. Journal of Petroleum Science and Engineering 201, 108451. doi.org/https://doi.org/10.1016/j.petrol.2021.108451.

Yu, Y., Lin, L., Zhai, C., Wang, Y., Li, Y., Guo, Y., 2018. Diagenesis and reservoir characteristics analysis of the Late Triassic Xujiahe Formation tight gas sandstone in the northern Sichuan Basin, China. Energy Exploration & Exploitation 36(4), 743-763. doi.org/10.1177/0144598717745778.

Yue, D., Wu, S., Xu, Z., Xiong, L., Chen, D., Ji, Y., Zhou, Y., 2018. Reservoir quality, natural fractures, and gas productivity of upper Triassic Xujiahe tight gas sandstones in western Sichuan Basin, China. Marine and Petroleum Geology 89, 370-386. doi.org/https://doi.org/10.1016/j.marpetgeo.2017.10.007.

Zhang, W., Li, Y., Zhao, F., Han, W., Li, Y., Wang, Y., Holland, G., Zhou, Z., 2019a. Using noble gases to trace groundwater evolution and assess helium accumulation in Weihe Basin, central China. Geochimica et Cosmochimica Acta 251, 229-246. doi.org/https://doi.org/10.1016/j.gca.2019.02.024.

Zhang, W., Li, Y., Zhao, F., Han, W., Zhou, J., Holland, G., Zhou, Z., 2019b. Quantifying the helium and hydrocarbon accumulation processes using noble gases in the North Qaidam Basin, China. Chemical Geology 525, 368-379. doi.org/https://doi.org/10.1016/j.chemgeo.2019.07.020.

Zhang, Y., Jiang, S., He, Z., Li, Y., Xiao, D., Chen, G., Zhao, J., 2021. Coupling between Source Rock and Reservoir of Shale Gas in Wufeng-Longmaxi Formation in Sichuan Basin, South China. Energies 14(9). doi.org/10.3390/en14092679.

Zheng, H., Zhang, J., Qi, Y., 2020. Geology and geomechanics of hydraulic fracturing in the Marcellus shale gas play and their potential applications to the Fuling shale gas development. Energy Geoscience 1(1), 36-46. doi.org/https://doi.org/10.1016/j.engeos.2020.05.002.

Zhou, W., Dai, J., 2008. The characteristics and evaluation of fractures distribution in Xujiahe formation in the western depression of the Sichuan Basin. Petroleum Geology & Experiment 30(1), 20. doi.org/10.11781/sysydz200801120.

Zhou, Z., Ballentine, C.J., 2006. 4He dating of groundwater associated with hydrocarbon reservoirs. Chemical Geology 226(3), 309-327. doi.org/https://doi.org/10.1016/j.chemgeo.2005.09.030.

Zhou, Z., Ballentine, C.J., Kipfer, R., Schoell, M., Thibodeaux, S., 2005. Noble gas tracing of groundwater/coalbed methane interaction in the San Juan Basin, USA. Geochimica et Cosmochimica Acta 69(23), 5413-5428. doi.org/https://doi.org/10.1016/j.gca.2005.06.027.

Zhou, Z., Ballentine, C.J., Schoell, M., Stevens, S.H., 2012. Identifying and quantifying natural CO2 sequestration processes over geological timescales: The Jackson Dome CO2 Deposit, USA. Geochimica et Cosmochimica Acta 86, 257-275. doi.org/https://doi.org/10.1016/j.gca.2012.02.028.

Zhu, G., Wang, T., Xie, Z., Xie, B., Liu, K., 2015. Giant gas discovery in the Precambrian deeply buried reservoirs in the Sichuan Basin, China: Implications for gas exploration in old cratonic basins. Precambrian Research 262, 45-66. doi.org/https://doi.org/10.1016/j.precamres.2015.02.023.

Chapter 5 Summary of key findings

This thesis comprises three completed manuscripts and a comprehensive summary of the key scientific literature, the models and methodology that underpinned this research. The aim of this research is to critically analyse and systematically evaluate the noble gas geochemistry of deeply buried unconventional shale and tight sandstone reservoirs in the Sichuan Basin, as well as shallow interbedded sandstone reservoirs in the Bohai Bay Basin, located in southwestern and northeastern China, respectively. This research aims to advance the understanding of noble gas behaviour within hydrocarbon reservoirs, and by investigating the gas-water interactions, terrestrial endmember contributions and the fractionation of noble gases, the study seeks to refine existing models for noble gas distribution within these systems. These findings will contribute to a more accurate application of noble gases as tracers in petroleum exploration, offering a robust tool for classifying the nature and extent of hydrocarbon reserves, their mixing behaviour and understanding the overall reservoir dynamics in different tectonic settings. The broader aim of this work is to contribute to the growing body of knowledge on Earth's geochemical cycles such as the recharge of meteoric waters, the terrestrial noble gas inventory, and paleoenvironmental changes over geological timescales.

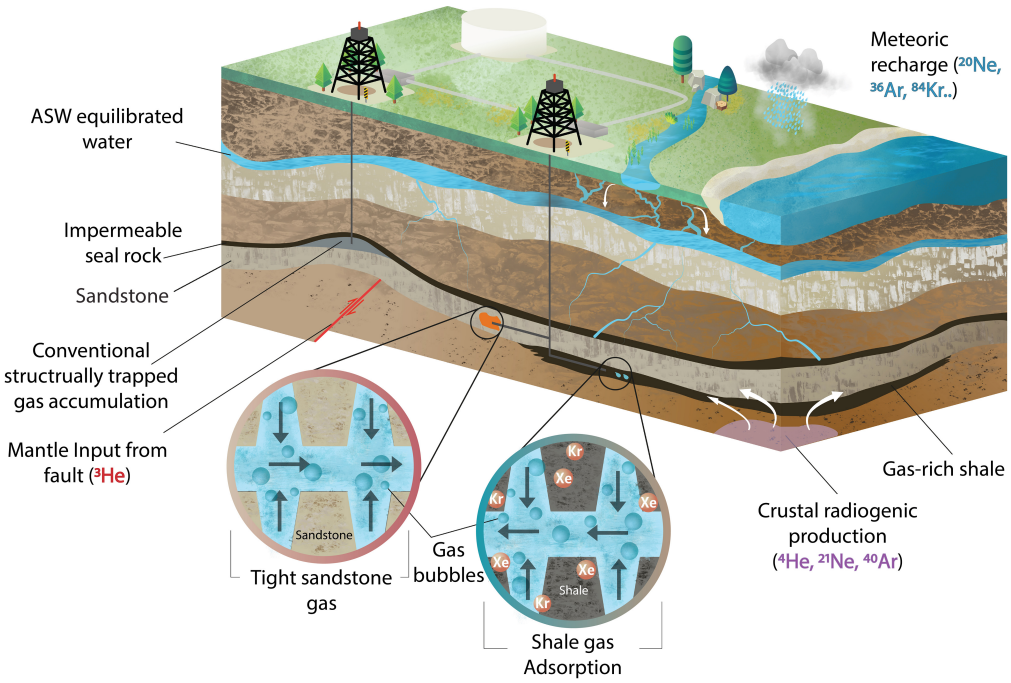

Figure 61 - 3D isometric model for the three end-member sources of noble gases found in unconventional petroleum systems, i.e. air-saturated water, crustal radiogenic and mantle fluids. Both wells represent typical modes of natural gas production. The 'L' well denotes hydrocarbons from a characteristic anticlinal structural trap. The 'R' well indicates horizontal fracturing of shale-gas and tight sandstone gas-bearing units. "Zoomed-in" sections conceptualise the flow of gas in low permeability settings, following drilling through pressure-enlarged fissures into the borehole. In shales, Kr, and to a larger extent, Xe is adsorbed.

The findings of this work were gathered utilising cutting-edge noble gas analytical techniques involving the Isotopx NGX noble gas mass spectrometer and ATONA faraday amplifier at the Lancaster Environment Centre, Lancaster University, which provided high precision and sensitivity in measuring noble gas isotopic compositions. The use of state-of-the-art multi-collector mass spectrometer enabled the acquisition of precise and reliable data, reducing uncertainty through high precision, which underpinned many of the interpretations presented throughout this thesis.

Manuscript 1 (Chapter 2); entitled "The characterisation of noble gases in organic-rich Wufeng-Longmaxi shales, Sichuan Basin and the role of adsorption and solubility-controlled fractionation" examines the origin and accumulation mechanisms of self-sourced, self-contained, in-situ shale gases and their noble gas isotope content within four major gas fields (the Fuling gas field, Changning gas field, Zhaotong gas field and Weiyuan gas field) within the basin, including the Upper Ordovician-Lower Silurian, Wufeng-Longmaxi shales.

24 gas samples were collected from producing wells within the Sichuan Basin's central, eastern, and southern margins. This study found that noble gases are valuable geo-dynamic fluid flow tracers that can provide a set of conservative tools capable of defining the physical conditions that affect crustal fluid systems. $^{3}He/^{4}He$ ratios range between $0.0037R_a$ to $0.038R_a$, indicating a strongly crustal radiogenic signature. The non-atmospheric, crustal-derived excess ($^{40}Ar^{*}$) and $^{40}Ar^{*}/^{36}Ar$ ratios are far higher ($\leq$5817) in these shale gas samples when compared to the atmospheric $^{40}Ar/^{36}Ar$ ratio (295.6). The study also found that groundwater has played a role in both the generation and migration of Wufeng-Longmaxi shale gases, with gases measuring close to or above calculated ASW ratios whereby $^{20}Ne/^{36}Ar$ ratios have evolved to exceed the value of ASW, indicating the system is partly closed to gas loss. The extent of gas-groundwater interactions has been quantified using first and second-order models, whereby the V_g/V_w volume ratio has been determined. Solubility-controlled gas-water phase interactions, governed by closed system gas evolution and equilibration, accompanied by gas-water-solid adsorption processes, are the primary mechanisms that explain the noble gas geochemistry in these unconventional gas reservoirs and may explain measurable excesses in air-derived $^{84}Kr/^{36}Ar$ and $^{132}Xe/^{36}Ar$ ratios, which are enriched relative to the atmosphere by a factor of up to 8 times. Adsorption is particularly relevant in shales due to their clay-rich mineralogy, which allows for the effective trapping of heavy noble gases, while the depletion of Xe within the atmospheric inventory is similarly well documented. The

adsorption models describe a gas-water-solid interaction and determines the evolution of Kr and Xe ratios in natural gases at various stages of degassing. The model, which utilises Henry's constants for adsorption on a shale matrix are useful in ascribing this excess to a desorbed component removed from the clay rich interface at the moment of production due to changes in pressure and temperature. A simple thermodynamic model has also been developed to describe the equilibrium of an adsorbed, dissolved and exsolved component within the pore-mineral matrix, which acts as a closed system in low porosity, low permeability reservoirs. Further research is required to better constrain these adsorption models and refine the adsorption-desorption coefficients used in these models. Henry's constants for adsorption do not exist for the Wufeng-Longmaxi shale, and instead it is necessary to utilise Henry's adsorption constants from analogous shales worldwide that have a unique composition and mineralogy, which alters the adsorption behaviour of these models.

Manuscript 3 (Chapter 4); is entitled "Noble gas signatures and gas migration in deep Xujiahe formation tight sandstones in the Western Sichuan Depression, Sichuan Basin, China". This research paper encompasses a thorough investigation of noble gas signatures of gas samples collected from across the Xinchang gas field. Natural gas samples were collected and sourced from the Xujiahe tight sandstone unit, which is a low-porosity, permeable sandstone reservoir which is highly fractured in many of the fault zones adjacent to where gas accumulation has occurred. A variable mixture of ASW and crustal-derived noble gases exists in the gas samples, whereby R/R_a values suggest a similarly strong crustal influence ($0.0037R_a$ to $0.025R_a$). Tight sandstone gases that have vertically migrated have a significantly lower contribution of radiogenic $^{21}Ne^*/^{22}Ne$ and represent a more 'air-like' mixture, having more readily been in contact with localised groundwaters. There appears to be agreement with solubility-based models, particularly Rayleigh fractionation to explain the lighter noble gas isotope fraction (Ne & Ar), and in reference to ASW, these noble gases suggest an open system dictates the evolution of noble gas ratios, as air-derived noble gases have evolved to below the ASW value, signifying extensive degassing, stripping and eventual gas loss from the system. Using crustal and air-endmembers, the contribution of crustal-derived $^{21}Ne^*$ only accounts for 35% of the total concentration of measured ^{21}Ne and ~50% for $^{40}Ar^*$, demonstrating a distinct accumulation history where groundwater and mixing with air has played an important role, as has expulsion of this gaseous admixture from the tight sandstone pore volume. This finding has important implications for hydrocarbon exploration as it

indicates pathways for natural gas escape exist, giving a critical insight into seal or trap integrity. These two papers offer the rare opportunity to directly compare the noble gas geochemistry, adsorption of heavy noble gases and fluid dynamics between two unconventional reservoir lithologies, for example much smaller $^{40}Ar/^{36}Ar$ ratios are found in the tight sandstone gases (≤858.2), while $^{20}Ne/^{22}Ne$ and $^{21}Ne/^{22}Ne$ ratios highlight a clear distinction between 'air-like' tight sandstones and strongly radiogenic shale gases. Manuscript 2 (Chapter 3) which is titled "Noble gas signatures, insights into methanogenesis and CO2 generation linked to the geodynamic setting of the Huanghua Depression, Bohai Bay Basin, China" resolves the complex fluid mixing processes in an early Cenozoic extensional basin on the eastern margin of Asia. This paper explores the mechanisms and thermal dynamics related to hydrocarbon formation during rifting in the Bohai Bay Basin, a significant oil and gas-producing region in northeastern China. 18 natural gas samples from the Huanghua Depression in the central Bohai Bay Basin were measured for their noble gas, bulk chemical composition (CO_2, N_2, H_2), and stable carbon and hydrogen isotopic compositions ($\delta^{13}C_{C1-C5}$ and δD_{C1-C2}) using Carbon VPDB (Vienna Pee Dee Belemnite) and Hydrogen VSMOW (Vienna Standard Mean Ocean Water) as reference materials for stable isotope analysis. Two endmember mixing models were applied for ^{21}Ne and ^{40}Ar to resolve their non-atmospheric, crustal-derived excess ($^{40}Ar^{*}$). $^{3}He/^{4}He$ ratios vary between a more crustal dominated $0.22R_a$ to $2.17R_a$, which highlights a variable, prevalent magmatic influence.

The results of the study reveal a distinct generational history that relates to the geodynamic setting of the BBB and a complex mixing history with groundwater that has also influenced Hydrogen (H_2) and Carbon dioxide (CO_2) concentrations. Various contributions to the mixed fraction of natural gas were identified, as further assessment of the CH_4 in samples permits the identification of the distinct sources and processes responsible for generation related to abiotic, thermogenic, and biogenic (microbial) sources. The paper also considers the role of fault proximity in governing the extent of fluid movement and providing a conduit for the mobilisation of CO_2, resulting in the loss and displacement of CH_4 by CO_2 in some samples. Faults also act as barriers to flow, where samples isolated from major bounding faults contain a lower abundance of atmospheric noble gases. The timing of CO_2 generation is linked to intense Mesozoic volcanism; however, CO_2 concentrations increase with $C_1/(C_2+C_3)$, indicating the displacement of CH_4 by CO_2. To summarise, this research has provided a valuable observations into methanogenesis and CO_2 generation related to faulting and pathways

for gas accumulation, magma kinematics, and the thermal regime of the Bohai Bay Basin, China.

A portion of the PhD project was carried out at the Guangzhou Institute of Geochemistry, Chinese Academy of Sciences under the supervision of Professor Yunpeng Wang. This experience led to much personal and professional growth and there were many opportunities within an international research setting to gain new insights into the field of geochemistry, enhance critical thinking, and hold many collaborative discussions, which benefitted the overall scientific approach of this work. Cooperation with several researchers, in academia and in industry, some of whom are named in the acknowledgements, and many of which are cited as co-authors to the three manuscripts also greatly impacted and reinforced the analytical methods and perspectives of this work. This experience underscores the importance of international collaboration in advancing scientific research, reinforcing the global relevance of the findings presented in this thesis.

In conclusion, the findings presented in this thesis represent a step forward in the study of noble gas geochemistry in conventional and unconventional hydrocarbon reservoirs, offering both immediate contributions to the field and a foundation for future research that will continue to push the boundaries of our understanding.

.

.

SYNTHESIS REFERENCES

AESCHBACH-HERTIG, W., HOFER, M., KIPFER, R., IMBODEN, D. M. & WIELER, R. 1999. Accumulation of mantle gases in a permanently stratified volcanic lake (Lac Pavin, France). *Geochimica et Cosmochimica Acta,* 63**,** 3357-3372.

AESCHBACH-HERTIG, W., PEETERS, F., BEYERLE, U. & KIPFER, R. 2000. Paleotemperature reconstruction from noble gases in ground water taking into account equilibrium with trapped air. *Nature,* 405**,** 1040-4.

AESCHBACH-HERTIG, W. & SOLOMON, D. K. 2013. Noble gas thermometry in groundwater hydrology. *The noble gases as geochemical tracers***,** 81-122.

ALLEN, M. B., MACDONALD, D. I. M., XUN, Z., VINCENT, S. J. & BROUET-MENZIES, C. 1997. Early Cenozoic two-phase extension and late Cenozoic thermal subsidence and inversion of the Bohai Basin, northern China. *Marine and Petroleum Geology,* 14**,** 951-972.

ALLEN, M. B., MACDONALD, D. I. M., XUN, Z., VINCENT, S. J. & BROUET-MENZIES, C. 1998. Transtensional deformation in the evolution of the Bohai Basin, northern China. *Geological Society, London, Special Publications,* 135**,** 215-229.

ANDERSON, D. L. 2007. Noble gas isotopes. *New Theory of the Earth***,** 198-210.

ANDERSON, S. T. 2018. Economics, helium, and the US Federal Helium Reserve: summary and outlook. *Natural Resources Research,* 27**,** 455-477.

AREGBE, Y., VALKIERS, S., MAYER, K. & DE BIèVRE, P. 1996. Comparative isotopic measurements on xenon and krypton. *International Journal of Mass Spectrometry and Ion Processes,* 153**,** L1-L5.

BABATUNDE, K. A., NEGASH, B. M., JUFAR, S. R., AHMED, T. Y. & MOJID, M. R. 2022. Adsorption of gases on heterogeneous shale surfaces: A review. *Journal of Petroleum Science and Engineering,* 208**,** 109466.

BALLENTINE, C. & K. O'NIONS, R. 1994. The use of natural He, Ne and Ar isotopes to study hydrocarbon-related fluid provenance, migration and mass balance in sedimentary basins. *Geological Society of London Special Publications,* 78**,** 347-361.

BALLENTINE, C. J., BURGESS, R. & MARTY, B. 2002. Tracing Fluid Origin, Transport and Interaction in the Crust. *Reviews in Mineralogy and Geochemistry,* 47**,** 539-614.

BALLENTINE, C. J. & BURNARD, P. G. 2002. Production, Release and Transport of Noble Gases in the Continental Crust. *Reviews in Mineralogy and Geochemistry,* 47**,** 481-538.

BALLENTINE, C. J. & HOLLAND, G. 2008. What CO2 well gases tell us about the origin of noble gases in the mantle and their relationship to the atmosphere. *Philosophical Transactions of the Royal Society A: Mathematical, Physical and Engineering Sciences,* 366**,** 4183-4203.

BALLENTINE, C. J. & O'NIONS, R. K. 1992. The nature of mantle neon contributions to Vienna Basin hydrocarbon reservoirs. *Earth and Planetary Science Letters,* 113**,** 553-567.

BARRY, P. H., LAWSON, M., MEURER, W. P., WARR, O., MABRY, J. C., BYRNE, D. J. & BALLENTINE, C. J. 2016. Noble gases solubility models of hydrocarbon charge mechanism in the Sleipner Vest gas field. *Geochimica et Cosmochimica Acta,* 194**,** 291-309.

BENSON, B. B. & KRAUSE, D., JR. 1976. Empirical laws for dilute aqueous solutions of nonpolar gases. *The Journal of Chemical Physics,* 64**,** 689-709.

BERNATOWICZ, T. J. & PODOSEK, F. A. 1986. Adsorption and isotopic fractionation of Xe. *Geochimica et Cosmochimica Acta,* 50**,** 1503-1507.

BEYERLE, U., AESCHBACH, W., IMBODEN, D., BAUR, H., GRAF, T. & KIPFER, R. 2000. A Mass Spectrometric System for the Analysis of Noble Gases and Tritium from Water Samples. *Environmental Science & Technology - ENVIRON SCI TECHNOL,* 34.

BORJIGIN, T., SHEN, B., YU, L., YUNFENG, Y., ZHANG, W., CHENG, T., XI, B., ZHANG, Q., BAO, F. & QIN, J. 2017. Mechanisms of shale gas generation and accumulation in the Ordovician Wufeng-Longmaxi Formation, Sichuan Basin, SW China. *Petroleum Exploration and Development,* 44**,** 69-78.

BOSCH, A. & MAZOR, E. 1988. Natural gas association with water and oil as depicted by atmospheric noble gases: case studies from the southeastern Mediterranean Coastal Plain. *Earth and Planetary Science Letters,* 87**,** 338-346.

BOTTOMLEY, D. J., ROSS, J. D. & CLARKE, W. B. 1984. Helium and neon isotope geochemistry of some ground waters from the Canadian Precambrian Shield. *Geochimica et Cosmochimica Acta,* 48**,** 1973-1985.

BURNARD, P., GRAHAM, D. & TURNER, G. 1997. Vesicle-Specific Noble Gas Analyses of "Popping Rock": Implications for Primordial Noble Gases in Earth. *Science,* 276**,** 568-71.

BURNARD, P., ZIMMERMANN, L. & SANO, Y. 2013. The Noble Gases as Geochemical Tracers: History and Background. *In:* BURNARD, P. (ed.) *The Noble Gases as Geochemical Tracers.* Berlin, Heidelberg: Springer Berlin Heidelberg.

BURNARD, P. G., BASSET, R., PUJOL, M. & MARTY, B. 2006. High resolution, multicollector noble gas mass spectrometry: HELIX-MC. *Geochimica et Cosmochimica Acta,* 70**,** A75.

BYRNE, D. J., BARRY, P. H., LAWSON, M. & BALLENTINE, C. J. 2018a. Determining gas expulsion vs retention during hydrocarbon generation in the Eagle Ford Shale using noble gases. *Geochimica et Cosmochimica Acta,* 241**,** 240-254.

BYRNE, D. J., BARRY, P. H., LAWSON, M. & BALLENTINE, C. J. 2018b. Noble gases in conventional and unconventional petroleum systems. *Geological Society, London, Special Publications,* 468**,** 127-149.

BYRNE, D. J., BARRY, P. H., LAWSON, M. & BALLENTINE, C. J. 2020. The use of noble gas isotopes to constrain subsurface fluid flow and hydrocarbon migration in the East Texas Basin. *Geochimica et Cosmochimica Acta,* 268**,** 186-208.

BYRNE, D. J., BROADLEY, M. W., HALLDóRSSON, S. A., RANTA, E., RICCI, A., TYNE, R. L., STEFáNSSON, A., BALLENTINE, C. J. & BARRY, P. H. 2021. The use of noble gas isotopes to trace subsurface boiling temperatures in Icelandic geothermal systems. *Earth and Planetary Science Letters,* 560**,** 116805.

CAO, C., LV, Z., LI, L. & DU, L. 2016. Geochemical characteristics and implications of shale gas from the Longmaxi Formation, Sichuan Basin, China. *Journal of Natural Gas Geoscience,* 1**,** 131-138.

CAO, C., ZHANG, M., LI, L., WANG, Y., LI, Z., DU, L., HOLLAND, G. & ZHOU, Z. 2020a. Tracing the sources and evolution processes of shale gas by coupling stable (C, H) and noble gas isotopic compositions: Cases from Weiyuan and Changning in Sichuan Basin, China. *Journal of Natural Gas Science and Engineering,* 78**,** 103304.

CAO, C., ZHANG, M., TANG, Q., YANG, Y., LV, Z., ZHANG, T., CHEN, C., YANG, H. & LI, L. 2018. Noble gas isotopic variations and geological implication of Longmaxi shale gas in Sichuan Basin, China. *Marine and Petroleum Geology,* 89**,** 38-46.

CAO, T., XU, H., LIU, G., DENG, M., CAO, Q. & YU, Y. 2020b. Factors influencing microstructure and porosity in shales of the Wufeng-Longmaxi formations in northwestern Guizhou, China. *Journal of Petroleum Science and Engineering,* 191**,** 107181.

CHANG, C.-Y. 1991. Geological characteristics and distribution patterns of hydrocarbon deposits in the Bohai Bay Basin, east China. *Marine and Petroleum Geology,* 8**,** 98-106.

CHEN, B., STUART, F. M., XU, S., GYöRE, D. & LIU, C. 2019. Evolution of coal-bed methane in Southeast Qinshui Basin, China: Insights from stable and noble gas isotopes. *Chemical Geology,* 529**,** 119298.

CHEN, B., STUART, F. M., XU, S., GYöRE, D. & LIU, C. 2022. The effect of Cenozoic basin inversion on coal-bed methane in Liupanshui Coalfield, Southern China. *International Journal of Coal Geology,* 250**,** 103910.

CHEN, C., HUANG, J., CHEN, J. & TIAN, X. 1984. Depositional models of tertiary rift basins, eastern China, and their application to petroleum prediction. *Sedimentary Geology,* 40**,** 73-88.

CHEN, F. & ZHANG, S. 1991. Tectonic Evolution and Hydrocarbon Migration in the Huanghua Basin, NE China. *Journal of Petroleum Geology,* 14**,** 197-210.

CHEN, G., LI, C., LU, S., GUO, T., WANG, M., XUE, Q., ZHANG, T., LI, Z., SUN, Y., LIU, J. & JIANG, S. 2021a. Critical factors controlling adsorption capacity of shale gas in Wufeng-Longmaxi formation, Sichuan Basin: Evidences from both

experiments and molecular simulations. *Journal of Natural Gas Science and Engineering,* 88**,** 103774.

CHEN, K., LI, J., TANG, X., SHEN, J., WANG, P., PENG, J. & MENG, J. 2021b. Key geological factors for shale gas accumulation in the Wufeng–Longmaxi Fms in the central Yangtze area. *Natural Gas Industry B,* 8**,** 1-12.

CHEN, S., WANG, H., WU, Y., HUANG, C., WANG, J., XIANG, X. & REN, P. 2014. Stratigraphic architecture and vertical evolution of various types of structural slope breaks in Paleogene Qikou sag, Bohai Bay Basin, Northeastern China. *Journal of Petroleum Science and Engineering,* 122**,** 567-584.

CHEN, S., ZHU, Y., CHEN, S., HAN, Y., FU, C. & FANG, J. 2017. Hydrocarbon generation and shale gas accumulation in the Longmaxi Formation, Southern Sichuan Basin, China. *Marine and Petroleum Geology,* 86**,** 248-258.

CHEN, Y., GUO, G., JIANG, Y.-Q. & ZHAO, J. 2007. Geochemical features of natural gas and the process of Upper Triassic hydrocarbon accumulation in middle Sichuan area. *Natural Gas Geoscience,* 18**,** 737-742.

CIESLA, F. J., KRIJT, S., YOKOCHI, R. & SANDFORD, S. 2018. The Efficiency of Noble Gas Trapping in Astrophysical Environments. *The Astrophysical Journal,* 867**,** 146.

COX, S. E., HEMMING, S. R. & TOOTELL, D. 2020. The Isotopx NGX and ATONA Faraday amplifiers. *Geochronology,* 2**,** 231-243.

CRAIG, H. A mantle helium component in Circum-Pacific volcanic gases : Hakone, the Marianas, and Mt. Lassen. 1978.

CRAIG, H. & LUPTON, J. E. 1976. Primordial neon, helium, and hydrogen in oceanic basalts. *Earth and Planetary Science Letters,* 31**,** 369-385.

CRAIG, H. & WIENS, R. C. 1996. Gravitational Enrichment of ⁸⁴Kr/³⁶Ar Ratios in Polar Ice Caps: A Measure of Firn Thickness and Accumulation Temperature. *Science,* 271**,** 1708-1710.

CROVETTO, R., FERNáNDEZ-PRINI, R. & JAPAS, M. L. 1982. Solubilities of inert gases and methane in H2O and in D2O in the temperature range of 300 to 600 K. *The Journal of Chemical Physics,* 76**,** 1077-1086.

DAI, J. 1992. Identification and distinction of various alkane gases. *Science in China Series B-Chemistry,* 35**,** 1246-1257.

DAI, J. 2016. Chapter 3 - Large Coal-Derived Gas Fields and Their Gas Sources in the Sichuan Basin. *In:* DAI, J. (ed.) *Giant Coal-Derived Gas Fields and their Gas Sources in China.* Academic Press.

DAI, J., DAI, C. & YAN, S. 1994. Geochemical characters, carbon and helium isotopic compositions of natural gas from hot springs of some areas in China. *Science in China Series B. Chemistry, Life Sciences & Earth Sciences,* 37**,** 758-767.

DAI, J., NI, Y., DONG, D., QIN, S., ZHU, G., HUANG, S., YU, C., GONG, D., HONG, F., ZHANG, Y., YAN, Z., LIU, Q., WU, X. & FENG, Z. 2021. 2021–2025 is a period of great development of China's natural gas industry: Suggestions on the exploration and development of natural gas during the 14th five-year plan in China. *Journal of Natural Gas Geoscience,* 6**,** 183-197.

DAI, J., NI, Y., QIN, S., HUANG, S., GONG, D., LIU, D., FENG, Z., PENG, W., HAN, W. & FANG, C. 2017. Geochemical characteristics of He and CO2 from the Ordos (cratonic) and Bohaibay (rift) basins in China. *Chemical Geology,* 469**,** 192-213.

DAI, J., NI, Y., QIN, S., HUANG, S., PENG, W. & HAN, W. 2018. Geochemical characteristics of ultra-deep natural gas in the Sichuan Basin, SW China. *Petroleum Exploration and Development,* 45**,** 619-628.

DAI, J., NI, Y. & ZOU, C. 2012. Stable carbon and hydrogen isotopes of natural gases sourced from the Xujiahe Formation in the Sichuan Basin, China. *Organic Geochemistry,* 43**,** 103-111.

DAI, J., NI, Y., ZOU, C., TAO, S., HU, G., HU, A., YANG, C. & TAO, X. 2009. Stable carbon isotopes of alkane gases from the Xujiahe coal measures and implication for gas-source correlation in the Sichuan Basin, SW China. *Organic Geochemistry,* 40**,** 638-646.

DAI, J., QIN, S., HU, G., NI, Y., GAN, L., SHIPENG, H. & HONG, F. 2019. Major progress in the natural gas exploration and development in the past seven decades in China. *Petroleum Exploration and Development,* 46**,** 1100-1110.

DAI, J., ZOU, C., DONG, D., NI, Y., WU, W., GONG, D., WANG, Y., HUANG, S., HUANG, J., FANG, C. & LIU, D. 2016. Geochemical characteristics of marine and terrestrial shale gas in China. *Marine and Petroleum Geology,* 76**,** 444-463.

DAI, J., ZOU, C., LIAO, S., DONG, D., NI, Y., HUANG, J., WU, W., GONG, D., HUANG, S. & HU, G. 2014. Geochemistry of the extremely high thermal maturity Longmaxi shale gas, southern Sichuan Basin. *Organic Geochemistry,* 74**,** 3-12.

DAI, J., ZOU, C., ZHANG, S., LI, J., NI, Y., HU, G., LUO, X., TAO, S., ZHU, G. & MI, J. 2008. Discrimination of abiogenic and biogenic alkane gases. *Science in China Series D: Earth Sciences,* 51**,** 1737-1749.

DARRAH, T. H., JACKSON, R. B., VENGOSH, A., WARNER, N. R., WHYTE, C. J., WALSH, T. B., KONDASH, A. J. & POREDA, R. J. 2015. The evolution of Devonian hydrocarbon gases in shallow aquifers of the northern Appalachian Basin: Insights from integrating noble gas and hydrocarbon geochemistry. *Geochimica et Cosmochimica Acta,* 170**,** 321-355.

DARRAH, T. H., VENGOSH, A., JACKSON, R. B., WARNER, N. R. & POREDA, R. J. 2014. Noble gases identify the mechanisms of fugitive gas contamination in drinking-water wells overlying the Marcellus and Barnett Shales. *Proceedings of the National Academy of Sciences,* 111**,** 14076-14081.

DAY, J. M. D., BARRY, P. H., HILTON, D. R., BURGESS, R., PEARSON, D. G. & TAYLOR, L. A. 2015. The helium flux from the continents and ubiquity of low-3He/4He recycled crust and lithosphere. *Geochimica et Cosmochimica Acta,* 153**,** 116-133.

DAY, J. M. D., JONES, T. D. & NICKLAS, R. W. 2022. Mantle sources of ocean islands basalts revealed from noble gas isotope systematics. *Chemical Geology,* 587**,** 120626.

DEINES, P. 1980. The isotopic composition of reduced organic carbon. *Handbook of environmental isotope geochemistry*.

DONG, D., GAO, S., HUANG, J., GUAN, Q., WANG, S. & WANG, Y. 2015. Discussion on the exploration & development prospect of shale gas in the Sichuan Basin. *Natural Gas Industry B,* 2**,** 9-23.

DONG, Y., ZENG, J., DONG, X., LI, C. & LIU, Y. 2022. The control effect of normal faults and caprocks on hydrocarbon accumulation: A case study from the Binhai fault nose of the Huanghua Depression, Bohai Bay Basin, China. *Journal of Petroleum Science and Engineering,* 218**,** 110918.

DU, H., SHI, Z., CHAI, H., ZENG, T., LI, B., PAN, L. & TIAN, Y. 2023. A New Natural Gas Accumulation Model in the Triassic Xujiahe Formation: A Case Study in the Tongjiang-Malubei Area of the Sichuan Basin. *Energies,* 16**,** 5936.

DU, J. & XU, C. 2011. The exploration of the major gas field in Xujiahe Formation of Sichuan Basin. *Beijing: Petroleum Industry Press*.

DYMOND, J. H. & SMITH, E. B. 1980. *Virial coefficients of pure gases and mixtures. A critical compilation,* United States, Oxford University Press,Fair Lawn, NJ.

EYMOLD, W. K., WALSH, T. B., MOORTGAT, J., GROVE, B. S. & DARRAH, T. H. 2021. Constraining fault architecture and fluid flow using crustal noble gases. *Applied Geochemistry,* 129**,** 104954.

FAN, C., LI, H., QIN, Q., HE, S. & ZHONG, C. 2020. Geological conditions and exploration potential of shale gas reservoir in Wufeng and Longmaxi Formation of southeastern Sichuan Basin, China. *Journal of Petroleum Science and Engineering,* 191**,** 107138.

FANALE, F. P. & CANNON, W. A. 1971. Physical adsorption of rare gas on terrigenous sediments. *Earth and Planetary Science Letters,* 11**,** 362-368.

FENG, Y., XIAO, X., GAO, P., WANG, E., HU, D., LIU, R., LI, G. & LU, C. 2023. Restoration of sedimentary environment and geochemical features of deep marine Longmaxi shale and its significance for shale gas: A case study of the Dingshan area in the Sichuan Basin, South China. *Marine and Petroleum Geology,* 151**,** 106186.

FENG, Z., DONG, D., TIAN, J., WU, W., CAI, Y., SHI, Z. & PENG, W. 2019. Geochemical characteristics of Lower Silurian shale gas in the Changning-Zhaotong exploration blocks, southern periphery of the Sichuan Basin. *Journal of Petroleum Science and Engineering,* 174**,** 281-290.

FENG, Z., HAO, F., DONG, D., ZHOU, S., WU, W., XIE, C., CAI, Y. & LI, Z. 2020. Geochemical anomalies in the Lower Silurian shale gas from the Sichuan Basin, China: Insights from a Rayleigh-type fractionation model. *Organic Geochemistry*, 103981.

GAO, R., CHEN, C., WANG, H., LU, Z., BROWN, L., DONG, S., FENG, S., LI, Q., LI, W. & WEN, Z. 2016. SINOPROBE deep reflection profile reveals a Neo-Proterozoic subduction zone beneath Sichuan Basin. *Earth and Planetary Science Letters,* 454**,** 86-91.

GAY, T. J. 1996. 6 - Sources of Metastable Atoms and Molecules. *In:* DUNNING, F. B. & HULET, R. G. (eds.) *Experimental Methods in the Physical Sciences.* Academic Press.

GILFILLAN, S. M., WILKINSON, M., HASZELDINE, R. S., SHIPTON, Z. K., NELSON, S. T. & POREDA, R. J. 2011. He and Ne as tracers of natural CO2 migration up a fault from a deep reservoir. *International Journal of Greenhouse Gas Control,* 5**,** 1507-1516.

GONG, L., ZENG, L., GAO, Z., ZHU, R. & ZHANG, B. 2016. Reservoir characterization and origin of tight gas sandstones in the Upper Triassic Xujiahe formation, Western Sichuan Basin, China. *Journal of Petroleum Exploration and Production Technology,* 6**,** 319-329.

GRAHAM, D. W. 2002. Noble Gas Isotope Geochemistry of Mid-Ocean Ridge and Ocean Island Basalts: Characterization of Mantle Source Reservoirs. *Reviews in Mineralogy and Geochemistry,* 47**,** 247-317.

GUO, W., HU, Z., ZHANG, X., YU, R. & WANG, L. 2017. Shale gas adsorption and desorption characteristics and its effects on shale permeability. *Energy Exploration & Exploitation,* 35**,** 463-481.

GUO, X., BORJIGIN, T., WEI, X., YU, L., LU, X., SUN, L. & WEI, F. 2022. Occurrence mechanism and exploration potential of deep marine shale gas in Sichuan Basin. *Acta Petrolei Sinica,* 43**,** 453.

GUOFA, L., MINGQIANG, C. & HUI, Z. 2010. Effects of Near-Surface Absorption on Reflection Characteristics of Continental Interbedded Strata: the Dagang Oilfield as an Example. *Acta Geologica Sinica - English Edition,* 84**,** 1306-1314.

GYöRE, D., TAIT, A., HAMILTON, D. & STUART, F. M. 2019. The formation of NeH+ in static vacuum mass spectrometers and re-determination of 21Ne/20Ne of air. *Geochimica et Cosmochimica Acta,* 263**,** 1-12.

HAMME, R. C. & EMERSON, S. R. 2004. The solubility of neon, nitrogen and argon in distilled water and seawater. *Deep Sea Research Part I: Oceanographic Research Papers,* 51**,** 1517-1528.

HANNIGAN, R. E. & BASU, A. R. Late diagenetic trace element remobilization in organic-rich black shales of the taconic foreland basin of Quebec, Ontario and New York. 1998.

HE, S., QIN, Q., LI, H. & ZHAO, S. 2022. Geological Characteristics of Deep Shale Gas in the Silurian Longmaxi Formation in the Southern Sichuan Basin, China. *Frontiers in Earth Science,* 9.

HELLINGER, S. J., SHEDLOCK, K. M., SCLATER, J. G. & YE, H. 1985. The Cenozoic evolution of the North China Basin. *Tectonics,* 4**,** 343-358.

HILTON, D. R., FISCHER, T. P. & MARTY, B. 2002. Noble gases and volatile recycling at subduction zones. *Reviews in Mineralogy & Geochemistry,* 47**,** 319-370.

HIYAGON, H. & KENNEDY, B. M. 1992. Noble gases in CH4-rich gas fields, Alberta, Canada. *Geochimica et Cosmochimica Acta,* 56**,** 1569-1589.

HOLLAND, G. & BALLENTINE, C. J. 2006. Seawater subduction controls the heavy noble gas composition of the mantle. *Nature,* 441**,** 186-91.

HOLLAND, G. & GILFILLAN, S. 2013. Application of Noble Gases to the Viability of CO2 Storage. *In:* BURNARD, P. (ed.) *The Noble Gases as Geochemical Tracers.* Berlin, Heidelberg: Springer Berlin Heidelberg.

HOLLAND, G., LOLLAR, B. S., LI, L., LACRAMPE-COULOUME, G., SLATER, G. F. & BALLENTINE, C. J. 2013. Deep fracture fluids isolated in the crust since the Precambrian era. *Nature,* 497**,** 357-360.

HOU, G. & HARI, K. R. 2014. Mesozoic-Cenozoic extension of the Bohai Sea: Contribution to the destruction of North China Craton. *Frontiers of Earth Science,* 8**,** 1-14.

HOU, G., WANG, Y. & HARI, K. R. 2010. The Late Triassic and Late Jurassic stress fields and tectonic transmission of North China craton. *Journal of Geodynamics,* 50**,** 318-324.

HU, D., ZHANG, H., NI, K. & YU, G. 2014. Main controlling factors for gas preservation conditions of marine shales in southeastern margins of the Sichuan Basin. *Natural Gas Industry,* 34**,** 17-23.

HU, S., O'SULLIVAN, P. B., RAZA, A. & KOHN, B. P. 2001. Thermal history and tectonic subsidence of the Bohai Basin, northern China: a Cenozoic rifted and local pull-apart basin. *Physics of the Earth and Planetary Interiors,* 126**,** 221-235.

HU, X., LI, R., MING, Y. & DENG, H. 2022. Insights into shale gas adsorption and an improved method for characterizing adsorption isotherm from molecular perspectives. *Chemical Engineering Journal,* 431**,** 134183.

HUANG, H., HE, D., LI, Y., LI, J. & ZHANG, L. 2018. Silurian tectonic-sedimentary setting and basin evolution in the Sichuan area, southwest China: Implications for palaeogeographic reconstructions. *Marine and Petroleum Geology,* 92**,** 403-423.

HUANG, S., ZHANG, T., WANG, S., XIE, G., HU, D., JIANG, Z. & DONG, T. 2004. Research on source characteristics and origin of Xujiahe Formation, Upper Triassic in Chishui area, Sichuan Basin. *Natural Gas Geoscience,* 15**,** 590-592.

HUNT, A., DARRAH, T. & J. POREDA, R. 2012. Determining the source and genetic fingerprint of natural gases using noble gas geochemistry: A northern Appalachian Basin case study. *AAPG Bulletin,* 96**,** 1785-1811.

IAEA, I. A. E. A. Reference and intercomparison materials for stable isotopes of light elements. Proceedings of a consultants meeting held in Vienna, 1-3 December 1993. 1995-09-01 1995 IAEA. International Atomic Energy Agency, Vienna (Austria).

IANOVSKI, D., MUNAKATA, K., KANJO, S., YOKOYAMA, Y., KOGA, A., YAMATSUKI, S., TANAKA, K., FUKUMATSU, T., NISHIKAWA, M. & IGARASHI, Y. 2002. Adsorption of Noble Gases on H-Mordenite. *Journal of Nuclear Science and Technology - J NUCL SCI TECHNOL,* 39**,** 1213-1218.

IEA 2016. Energy Supply and Consumption Revolution Strategy (2016-2030). International Energy Agency.

IEA 2019. Global Gas Security Review 2019, International Energy Agency, Paris.

INGERSOLL, R. V. 1988. Tectonics of sedimentary basins. *Geological Society of America Bulletin,* 100**,** 1704-1719.

JAVOY, M., PINEAU, F. & DELORME, H. 1986. Carbon and nitrogen isotopes in the mantle. *Chemical geology,* 57**,** 41-62.

JENDEN, P. D., HILTON, D., KAPLAN, I., CRAIG, H. & HOWELL, D. 1993. Abiogenic hydrocarbons and mantle helium in oil and gas fields. *US Geological survey professional paper,* 1570**,** 31-56.

JIA, A., HE, D., WEI, Y. & LI, Y. 2021. Predictions on natural gas development trend in China for the next fifteen years. *Journal of Natural Gas Geoscience,* 6**,** 67-78.

JIANG, S., TANG, X., CAI, D., XUE, G., HE, Z., LONG, S., PENG, Y., GAO, B., XU, Z. & DAHDAH, N. 2017. Comparison of marine, transitional, and lacustrine shales: A case study from the Sichuan Basin in China. *Journal of Petroleum Science and Engineering,* 150**,** 334-347.

JIANG, W., CAO, G., LUO, C., LIN, M., JI, L. & ZHOU, J. 2021. A composition-based model for methane adsorption of overmature shales in Wufeng and Longmaxi Formation, Sichuan Basin. *Chemical Engineering Journal***,** 130766.

JIAO, F. 2019. Theoretical insights, core technologies and practices concerning "volume development" of shale gas in China. *Natural Gas Industry B,* 6**,** 525-538.

JIN, F., WANG, X., LI, H., WU, X., FU, L., LOU, D., ZHANG, J. & FENG, J. 2019. Formation of the primary petroleum reservoir in Wumaying inner buried-hill of Huanghua Depression, Bohai Bay Basin, China. *Petroleum Exploration and Development,* 46**,** 543-552.

JIN, Z., NIE, H., LIU, Q., ZHAO, J. & JIANG, T. 2018. Source and seal coupling mechanism for shale gas enrichment in upper Ordovician Wufeng Formation - Lower Silurian Longmaxi Formation in Sichuan Basin and its periphery. *Marine and Petroleum Geology,* 97**,** 78-93.

JIN, Z., ZHANG, L., WANG, Y., CUI, Y. & MILLA, K. 2009. Using carbon, hydrogen and helium isotopes to unravel the origin of hydrocarbons in the Wujiaweizi area of the Songliao Basin, China. *Episodes Journal of International Geoscience,* 32**,** 167-176.

JU, Y., GILFILLAN, S. M. V., LEE, S.-S., KAOWN, D., HAHM, D., LEE, S., PARK, I.-W., HA, S.-W., PARK, K., DO, H.-K., YUN, S.-T. & LEE, K.-K. 2020. Application of noble gas tracers to identify the retention mechanisms of CO2 migrated from a deep reservoir into shallow groundwater. *International Journal of Greenhouse Gas Control,* 97**,** 103041.

JU, Y., WANG, G., LI, S., SUN, Y., SUO, Y., SOMERVILLE, I., LI, W., HE, B., ZHENG, M. & YU, K. 2022. Geodynamic mechanism and classification of basins in the Earth system. *Gondwana Research,* 102**,** 200-228.

KAROLYTė, R., BARRY, P. H., HUNT, A. G., KULONGOSKI, J. T., TYNE, R. L., DAVIS, T. A., WRIGHT, M. T., MCMAHON, P. B. & BALLENTINE, C. J. 2021. Noble gas signatures constrain oil-field water as the carrier phase of hydrocarbons occurring in shallow aquifers in the San Joaquin Basin, USA. *Chemical Geology,* 584**,** 120491.

KIMURA, H. & WATANABE, Y. 2001. Oceanic anoxia at the Precambrian-Cambrian boundary. *Geology,* 29**,** 995-998.

KIPFER, R., AESCHBACH-HERTIG, W., PEETERS, F. & STUTE, M. 2002. Noble Gases in Lakes and Ground Waters. *Reviews in Mineralogy and Geochemistry,* 47**,** 615-700.

KLEMME, H. & ULMISHEK, G. 1991. Effective Petroleum Source Rocks of the World: Stratigraphic Distribution and Controlling Depositional Factors. *Aapg Bulletin - AAPG BULL,* 75**,** 1809-1851.

KURITANI, T., XIA, Q.-K., KIMURA, J.-I., JIA, L., SHIMIZU, K., USHIKUBO, T., ZHAO, D., NAKAGAWA, M. & YOSHIMURA, S. 2019. Buoyant hydrous mantle plume from the mantle transition zone. *Scientific Reports,* 9**,** 6549.

KURZ, M. D., JENKINS, W. J., HART, S. R. & CLAGUE, D. 1983. Helium isotopic variations in volcanic rocks from Loihi Seamount and the Island of Hawaii. *Earth and Planetary Science Letters,* 66**,** 388-406.

KYSER, T. K. & RISON, W. 1982. Systematics of rare gas isotopes in basic lavas and ultramafic xenoliths. *Journal of Geophysical Research: Solid Earth,* 87**,** 5611-5630.

LAI, J., WANG, G., RAN, Y. & ZHOU, Z. 2015. Predictive distribution of high-quality reservoirs of tight gas sandstones by linking diagenesis to depositional facies: Evidence from Xu-2 sandstones in the Penglai area of the central Sichuan basin, China. *Journal of Natural Gas Science and Engineering,* 23**,** 97-111.

LANGMUIR, I. 1918. The Adsorption of Gases on Plane Surfaces of Glass, Mica and Platinum. *Journal of the American Chemical Society,* 40**,** 1361-1403.

LEE, A. K. K. & BASMADJIAN, D. 1970. A molecular approach to the calculation of gas adsorption isotherms on molecular sieves: Noble gases on type 4A and 5A zeolites. *The Canadian Journal of Chemical Engineering,* 48**,** 682-691.

LEE, J.-Y., MARTI, K., SEVERINGHAUS, J. P., KAWAMURA, K., YOO, H.-S., LEE, J. B. & KIM, J. S. 2006. A redetermination of the isotopic abundances of atmospheric Ar. *Geochimica et Cosmochimica Acta,* 70**,** 4507-4512.

LENG, J., LI, S. & YANG, C. 2011. Determination of the time of gas accumulation in the Xujiahe Formation of Xiaoquan-Fenggu structural belt in the Western Sichuan Depression through fluid inclusion analysis. *Natural Gas Industry,* 31**,** 38-42.

LEYA, I. & WIELER, R. 1999. Nucleogenic production of Ne isotopes in Earth's crust and upper mantle induced by alpha particles from the decay of U and Th. *Journal of Geophysical Research: Solid Earth,* 104**,** 15439-15450.

LI, G., QIN, Y., SHEN, J., WU, M., LI, C., WEI, K. & ZHU, C. 2019a. Geochemical characteristics of tight sandstone gas and hydrocarbon charging history of Linxing area in Ordos Basin, China. *Journal of Petroleum Science and Engineering,* 177**,** 198-207.

LI, H. 2023. Coordinated development of shale gas benefit exploitation and ecological environmental conservation in China: a mini review. *Frontiers in Ecology and Evolution,* 11.

LI, J., HU, D., ZOU, H., SHANG, X., REN, H. & WANG, L. 2016a. Coupling relationship between reservoir diagenesis and gas accumulation in Xujiahe Formation of Yuanba–Tongnanba area, Sichuan Basin, China. *Journal of Natural Gas Geoscience,* 1**,** 335-352.

LI, J., LI, H., YANG, C., WU, Y., GAO, Z. & JIANG, S. 2022. Geological characteristics and controlling factors of deep shale gas enrichment of the Wufeng-Longmaxi Formation in the southern Sichuan Basin, China. *Lithosphere,* 2022**,** 4737801.

LI, J., LIU, J., CHEN, H., HE, J., WANG, R., SHAO, X. & FANG, X. 2023. Fracture Modeling of Deep Tight Sandstone Fault-Fracture Reservoir Based on Geological Model and Seismic Attributes: A Case Study on Xu 2 Member in Western Sichuan Depression, Sichuan Basin. *Geofluids,* 2023**,** 6516181.

LI, J., WANG, X., HOU, L., CHEN, C., GUO, J., YANG, C., WANG, Y., LI, Z., CUI, H., HAO, A. & ZHANG, L. 2021a. Geochemical characteristics and resource potential of shale gas in Sichuan Basin. *Journal of Natural Gas Geoscience.*

LI, J., WANG, X., XU, Z., CUI, H., WANG, X., ZHANG, B., GUO, J., TAO, S., CHEN, J., XIE, Z., TIAN, J. & WANG, Y. 2024. Helium resources accumulation regulations and their development prospects in China. *Journal of Natural Gas Geoscience.*

LI, L. 2022. Development of natural gas industry in China: Review and prospect. *Natural Gas Industry B,* 9**,** 187-196.

LI, L. & QIU, N. 2017. The initiation and tectonic regimes of the Cenozoic extension in the Bohai Bay Basin, North China revealed by numerical modelling. *Journal of Asian Earth Sciences,* 140**,** 92-107.

LI, P., HAO, F., GUO, X., ZOU, H., YU, X. & WANG, G. 2015. Processes involved in the origin and accumulation of hydrocarbon gases in the Yuanba gas field, Sichuan Basin, southwest China. *Marine and Petroleum Geology,* 59**,** 150-165.

LI, Y., FENG, Y., LIU, H., ZHANG, L. & ZHAO, S. 2013. Geological characteristics and resource potential of lacustrine shale gas in the Sichuan Basin, SW China. *Petroleum Exploration and Development,* 40**,** 454-460.

LI, Y., HE, D., CHEN, L., MEI, Q., LI, C. & ZHANG, L. 2016b. Cretaceous sedimentary basins in Sichuan, SW China: Restoration of tectonic and depositional environments. *Cretaceous Research,* 57**,** 50-65.

LI, Y., QIN, S., WANG, Y., HOLLAND, G. & ZHOU, Z. 2020. Tracing interaction between hydrocarbon and groundwater systems with isotope signatures preserved in the Anyue gas field, central Sichuan Basin, China. *Geochimica et Cosmochimica Acta,* 274**,** 261-285.

LI, Y., TOOTELL, D., HOLLAND, G. & ZHOU, Z. 2021b. Performance of the NGX High-Resolution Multiple Collector Noble Gas Mass Spectrometer. *Geochemistry, Geophysics, Geosystems,* 22**,** e2021GC009997.

LI, Y., ZHANG, T., ELLIS, G. S. & SHAO, D. 2017a. Depositional environment and organic matter accumulation of Upper Ordovician–Lower Silurian marine shale in the Upper Yangtze Platform, South China. *Palaeogeography, Palaeoclimatology, Palaeoecology,* 466**,** 252-264.

LI, Z., RAN, B., XIAO, B., SONG, J., ZHENG, L., LI, J., WANG, H., XIAO, B., YE, Y., CAI, Q. & LIU, S. 2019b. Sinian to Early Cambrian uplift-depression framework along the northern margin of the Sichuan Basin, central China and its implications for hydrocarbon exploration.

LI, Z., ZUO, Y., QIU, N. & GAO, J. 2017b. Meso–Cenozoic lithospheric thermal structure in the Bohai Bay Basin, eastern North China Craton. *Geoscience Frontiers,* 8**,** 977-987.

LIANG, C., JIANG, Z., ZHANG, C., GUO, L., YANG, Y. & LI, J. 2014. The shale characteristics and shale gas exploration prospects of the Lower Silurian Longmaxi shale, Sichuan Basin, South China. *Journal of Natural Gas Science and Engineering,* 21**,** 636-648.

LIANG, X., XU, Z., ZHANG, Z., WANG, W., ZHANG, J., LU, H., ZHANG, L., ZOU, C., WANG, G., MEI, J. & RUI, Y. 2020. Breakthrough of shallow shale gas exploration in Taiyang anticline area and its significance for resource development in Zhaotong, Yunnan Province, China. *Petroleum Exploration and Development,* 47**,** 12-29.

LIU, B., XU, X. & PAN, X. 1993. Evolution and mineralization of earth crust of paleocontinent in South China. Science Press Beijing.

LIU, G. 1987. The Cenozoic rift system of the North China Plain and the deep internal process. *Tectonophysics,* 133**,** 277-285.

LIU, J., LIU, Z., LIU, Z., LIU, Y., SHEN, B., XIAO, K., BI, Y., WANG, X., WANG, A., FAN, L. & LI, J. 2023. Geological characteristics and models of fault-fold-fracture body in deep tight sandstone of the second member of Upper Triassic Xujiahe Formation in Xinchang structural belt of Sichuan Basin, SW China. *Petroleum Exploration and Development,* 50**,** 603-614.

LIU, J., LIU, Z., XIAO, K., HUANG, Y. & JIN, W. 2020a. Characterization of favorable lithofacies in tight sandstone reservoirs and its significance for gas exploration and exploitation: A case study of the 2nd Member of Triassic Xujiahe Formation in the Xinchang area, Sichuan Basin. *Petroleum Exploration and Development,* 47**,** 1194-1205.

LIU, Q., DAI, J., JIN, Z., LI, J., WU, X., MENG, Q., YANG, C., ZHOU, Q., FENG, Z. & ZHU, D. 2016. Abnormal carbon and hydrogen isotopes of alkane gases from the Qingshen gas field, Songliao Basin, China, suggesting abiogenic alkanes? *Journal of Asian Earth Sciences,* 115**,** 285-297.

LIU, Q., LI, P., ZHU, D., ZHU, D., WU, X., WANG, X., TAO, X., MENG, Q., XU, H., GAO, Y. & ZHOU, Z. 2024. Helium resource in the petroliferous basins in China and its development prospects. *Cell Reports Physical Science,* 5**,** 102031.

LIU, Q., SONG, Y., JIANG, L., CAO, T., CHEN, Z., XIAO, D., HAN, G., JI, W., GAO, F., WANG, P. & ZHANG, X. 2017. Geochemistry and correlation of oils and source rocks in Banqiao Sag, Huanghua Depression, northern China. *International Journal of Coal Geology,* 176-177**,** 49-68.

LIU, R., HAO, F., ENGELDER, T., SHU, Z., YI, J., XU, S. & TENG, C. 2020b. Influence of tectonic exhumation on porosity of Wufeng–Longmaxi shale in the Fuling gas field of the eastern Sichuan Basin, China. *AAPG Bulletin,* 104**,** 939-959.

LIU, R., WEN, T., AMALBERTI, J., ZHENG, J., HAO, F. & JIANG, D. 2021a. The dichotomy in noble gas signatures linked to tectonic deformation in Wufeng-Longmaxi Shale, Sichuan Basin. *Chemical Geology,* 581**,** 120412.

LIU, S., YANG, Y., DENG, B., ZHONG, Y., WEN, L., SUN, W., LI, Z., JANSA, L., LI, J., SONG, J., ZHANG, X. & PENG, H. 2021b. Tectonic evolution of the Sichuan Basin, Southwest China. *Earth-Science Reviews,* 213**,** 103470.

LIU, W. & XU, Y. 1993. Significance of the isotopic composition of He and Ar in natural gases. *Chinese Science Bulletin: English Edition***,** 1726-1730.

LIU, X., GUAN, M., JIN, Z., LAI, J. & CHEN, S. 2021c. Geological characteristics and shale oil potential of the lacustrine immature to low mature shale oil system: a case study of the second member of Kongdian Formation in Cangdong Sag, Huanghua Depression, Bohai Bay Basin, China. *Energy Sources, Part A: Recovery, Utilization, and Environmental Effects,* 43**,** 1577-1599.

LU, J., LIN, R., LIU, C., LI, Y., XIAO, Z. & HE, Q. 2019. Genesis and origin of natural gas in the Beidagang structural belt of Dagang oilfield. *Petroleum Science and Technology,* 37**,** 1501-1508.

LUO, L., MENG, W., GLUYAS, J., TAN, X., GAO, X., FENG, M., KONG, X. & SHAO, H. 2019. Diagenetic characteristics, evolution, controlling factors of

diagenetic system and their impacts on reservoir quality in tight deltaic sandstones: Typical example from the Xujiahe Formation in Western Sichuan Foreland Basin, SW China. *Marine and Petroleum Geology,* 103**,** 231-254.

MA, X. 2017a. A golden era for natural gas development in the Sichuan Basin. *Natural Gas Industry B,* 4**,** 163-173.

MA, X. 2017b. Natural gas and energy revolution: A case study of Sichuan–Chongqing gas province. *Natural Gas Industry B,* 4**,** 91-99.

MARK, D. F., BARFOD, D., STUART, F. M. & IMLACH, J. 2009. The ARGUS multicollector noble gas mass spectrometer: Performance for 40Ar/39Ar geochronology. *Geochemistry, Geophysics, Geosystems,* 10.

MARROCCHI, Y., BURNARD, P. G., HAMILTON, D., COLIN, A., PUJOL, M., ZIMMERMANN, L. & MARTY, B. 2009. Neon isotopic measurements using high-resolution, multicollector noble gas mass spectrometer: HELIX-MC. *Geochemistry, Geophysics, Geosystems,* 10.

MARROCCHI, Y. & MARTY, B. 2013. Experimental determination of the xenon isotopic fractionation during adsorption. *Geophysical Research Letters,* 40**,** 4165-4170.

MARTY, B. 1984. On the noble gas isotopic fractionation in naturally occuring gases; Sur le fractionnement isotopique des gaz rares dans des gaz naturels. *Geochemical journal,* 18**,** 157-162.

MARTY, B. 2020. Origins and early evolution of the atmosphere and the oceans. *Geochemical Perspectives,* 9**,** 135-136.

MARTY, B. & JAMBON, A. 1987. C3He in volatile fluxes from the solid Earth: implications for carbon geodynamics. *Earth and Planetary Science Letters,* 83**,** 16-26.

MARTY, B. & TOLSTIKHIN, I. N. 1998. CO2 fluxes from mid-ocean ridges, arcs and plumes. *Chemical Geology,* 145**,** 233-248.

MAZOR, E. 1972. Paleotemperatures and other hydrological parameters deduced from noble gases dissolved in groundwaters; Jordan Rift Valley, Israel. *Geochimica et Cosmochimica Acta,* 36**,** 1321-1336.

MAZOR, E. & FOURNIER, R. 1973. More on noble gases in Yellowstone National Park hot waters. *Geochimica et Cosmochimica Acta,* 37**,** 515-525.

MENGSHU, S., YUANSHENG, H., XIAOFENG, X. & DUNNAN, L. 2021. China's coal consumption forecasting using adaptive differential evolution algorithm and support vector machine. *Resources Policy,* 74**,** 102287.

MIAO, Q., XU, C., HAO, F., YIN, J., WANG, Q., XIE, M., CAO, Y. & ZOU, H. 2020. Roles of fault structures on the distribution of mantle-derived CO2 in the Bohai Bay basin, NE China. *Journal of Asian Earth Sciences,* 197**,** 104398.

MIXON, E. E., JICHA, B. R., TOOTELL, D. & SINGER, B. S. 2022. Optimizing 40Ar/39Ar analyses using an Isotopx NGX-600 mass spectrometer. *Chemical Geology,* 593**,** 120753.

MOORE, M. T., VINSON, D. S., WHYTE, C. J., EYMOLD, W. K., WALSH, T. B. & DARRAH, T. H. 2018. Differentiating between biogenic and thermogenic sources of natural gas in coalbed methane reservoirs from the Illinois Basin using noble gas and hydrocarbon geochemistry. *Geological Society, London, Special Publications,* 468**,** 151-188.

MOREIRA, M. 2013. Noble gas constraints on the origin and evolution of Earth's volatiles. *Geochemical Perspectives,* 2**,** 229-230.

NI, Y., DAI, J., TAO, S., WU, X., LIAO, F., WU, W. & ZHANG, D. 2014. Helium signatures of gases from the Sichuan Basin, China. *Organic Geochemistry,* 74**,** 33-43.

NIE, H., CHEN, Q., ZHANG, G., SUN, C., WANG, P. & LU, Z. 2021. An overview of the characteristic of typical Wufeng–Longmaxi shale gas fields in the Sichuan Basin, China. *Natural Gas Industry B.*

NIE, H., JIN, Z., LI, P., JAY KATZ, B., DANG, W., LIU, Q., DING, J., JIANG, S. & LI, D. 2023. Deep shale gas in the Ordovician-Silurian Wufeng–Longmaxi formations of the Sichuan Basin, SW China: Insights from reservoir characteristics, preservation conditions and development strategies. *Journal of Asian Earth Sciences,* 244**,** 105521.

NIE, H., LI, D., LIU, G., LU, Z., HU, W., WANG, R. & ZHANG, G. 2020. An overview of the geology and production of the Fuling shale gas field, Sichuan Basin, China. *Energy Geoscience,* 1**,** 147-164.

NIEDERMANN, S., GRAF, T. & MARTI, K. 1993. Mass spectrometric identification of cosmic-ray-produced neon in terrestrial rocks with multiple neon components. *Earth and Planetary Science Letters,* 118**,** 65-73.

OLIVE, K. A., STEIGMAN, G. & SKILLMAN, E. D. 1997. The Primordial Abundance of 4He: An Update. *The Astrophysical Journal,* 483**,** 788.

OSENBRüCK, K., LIPPMANN, J. & SONNTAG, C. 1998. Dating very old pore waters in impermeable rocks by noble gas isotopes. *Geochimica et Cosmochimica Acta,* 62**,** 3041-3045.

OXBURGH, E. R., O'NIONS, R. K. & HILL, R. I. 1986. Helium isotopes in sedimentary basins. *Nature,* 324**,** 632-635.

OZIMA, M. & PODOSEK, F. 2002. Noble Gas Geochemistry. *Noble Gas Geochemistry, by Minoru Ozima and Frank A. Podosek, pp. 300. ISBN 0521803667. Cambridge, UK: Cambridge University Press, December 2001.,* 367.

PAN, B., CHEN, H., LIN, L., YU, Y., WU, D. & DONG, Y. 2021. Diagenesis and reservoir quality of the second member of the Upper Triassic Xujiahe Formation tight gas sandstones in the Western Sichuan Depression, southwest China. *Geological Journal,* 56**,** 3187-3206.

PAUL, M. J., BIEGALSKI, S. R., HAAS, D. A., JIANG, H., DAIGLE, H. & LOWREY, J. D. 2018. Xenon adsorption on geological media and implications for radionuclide signatures. *Journal of Environmental Radioactivity,* 187**,** 65-72.

PEARCE, J. K., HOFMANN, H., BAUBLYS, K., CENDóN, D. I., GOLDING, S. D., HERBERT, S. J., BHEBHE, Z., NGUYEN, A. & HAYES, P. 2024. Geochemical tracers associated with methane in aquifers overlying a coal seam gas reservoir. *International Journal of Coal Geology,* 289**,** 104535.

PEETERS, F., BEYERLE, U., AESCHBACH-HERTIG, W., HOLOCHER, J., BRENNWALD, M. S. & KIPFER, R. 2003. Improving noble gas based paleoclimate reconstruction and groundwater dating using 20Ne/22Ne ratios. *Geochimica et Cosmochimica Acta,* 67**,** 587-600.

PEPIN, R. O. On the Isotopic Composition of Primordial Xenon in Terrestrial Planet Atmospheres. *In:* BENZ, W., KALLENBACH, R. & LUGMAIR, G. W., eds. From Dust to Terrestrial Planets, 2000// 2000 Dordrecht. Springer Netherlands, 371-395.

PEUCKER-EHRENBRINK, B. & HANNIGAN, R. 2000. Effects of black shale weathering on the mobility of rhenium and platinum group elements. *Geology,* 28.

PHINNEY, D. 1972. 36Ar, Kr, and Xe in terrestrial materials. *Earth and Planetary Science Letters,* 16**,** 413-420.

PINTI, D. L. & MARTY, B. 1998. Separation of noble gas mixtures from petroleum and their isotopic analysis by mass spectrometry. *Journal of Chromatography A,* 824**,** 109-117.

PODOSEK, F. A., BERNATOWICZ, T. J. & KRAMER, F. E. 1981. Adsorption of xenon and krypton on shales. *Geochimica et Cosmochimica Acta,* 45**,** 2401-2415.

PORCELLI, D., BALLENTINE, C. & WIELER, R. 2002. An Overview of Noble Gas Geochemistry and Cosmochemistry. *Reviews in Mineralogy & Geochemistry - REV MINERAL GEOCHEM,* 47**,** 1-19.

PORCELLI, D. & WASSERBURG, G. J. 1995. Mass transfer of xenon through a steady-state upper mantle. *Geochimica et Cosmochimica Acta,* 59**,** 1991-2007.

POTTER, R. W. & CLYNNE, M. A. 1978. The solubility of the noble gases He, Ne, Ar, Kr, and Xe in water up to the critical point. *Journal of Solution Chemistry,* 7**,** 837-844.

PRINZHOFER, A. 2013. Noble Gases in Oil and Gas Accumulations. *In:* BURNARD, P. (ed.) *The Noble Gases as Geochemical Tracers.* Berlin, Heidelberg: Springer Berlin Heidelberg.

PU, B., JIANG, Y., WANG, Y., BAO, S. & LIU, X. 2010. Reservoir-forming conditions and favorable exploration zones of shale gas in Lower Silurian Longmaxi Formation of Sichuan Basin. *Acta Petrolei Sinica,* 31**,** 225-230.

PU, X., ZHAO, X., LI, Y., CHEN, R., ZHOU, L., YAN, Z. & XIAO, D. 2018. Paleochannel restoration and petroleum geological significance of Neogene in Huanghua depression. *Shiyou Xuebao/Acta Petrolei Sinica,* 39**,** 163-171.

PU, X., ZHAO, X., WANG, J., WU, J., HAN, W., WANG, H., SHI, Z., JIANG, W. & ZHANG, W. 2020. Reservoirs properties of slump-type sub-lacustrine fans and their main control factors in first member of Paleogene Shahejie Formation in Binhai area, Bohai Bay Basin, China. *Petroleum Exploration and Development,* 47**,** 977-989.

PU, X., ZHOU, L., HAN, W., CHEN, C., YUAN, X., LIN, C., LIU, S., HAN, G., ZHANG, W. & JIANG, W. 2014. Gravity flow sedimentation and tight oil exploration in lower first member of Shahejie Formation in slope area of Qikou Sag, Bohai Bay Basin. *Petroleum Exploration and Development,* 41**,** 153-164.

PU, X., ZHOU, L., WANG, W., HAN, W., XIAO, D., LIU, H., CHEN, C., ZHANG, W., YUAN, X., LU, Y. & LIU, S. 2013. Medium-deep clastic reservoirs in the slope area of Qikou sag, Huanghua depression, Bohai Bay Basin. *Petroleum Exploration and Development,* 40**,** 38-51.

PU, X., ZHOU, L., XIAO, D., HUA, S., CHEN, C., YUAN, X., HAN, G. & ZHANG, W. 2011. Lacustrine carbonates in the southwest margin of the Qikou Sag, Huanghua Depression, Bohai Bay Basin. *Petroleum Exploration and Development,* 38**,** 136-144.

QI, J. & YANG, Q. 2010. Cenozoic structural deformation and dynamic processes of the Bohai Bay basin province, China. *Marine and Petroleum Geology,* 27**,** 757-771.

QIN, S., ZHANG, Y., ZHAO, C. & ZHOU, Z. 2018. Geochemical evidence for in situ accumulation of tight gas in the Xujiahe Formation coal measures in the central Sichuan Basin, China. *International Journal of Coal Geology,* 196**,** 173-184.

QIU, Z. & ZOU, C. 2019. Controlling factors on the formation and distribution of "sweet-spot areas" of marine gas shales in South China and a preliminary discussion on unconventional petroleum sedimentology. *Journal of Asian Earth Sciences***,** 103989.

REN, J., TAMAKI, K., LI, S. & JUNXIA, Z. 2002. Late Mesozoic and Cenozoic rifting and its dynamic setting in Eastern China and adjacent areas. *Tectonophysics,* 344**,** 175-205.

RUDNICK, R. L. & FOUNTAIN, D. M. 1995. Nature and composition of the continental crust: A lower crustal perspective. *Reviews of Geophysics,* 33**,** 267-309.

SAKATA, S., SANO, Y., MAEKAWA, T. & IGARI, S.-I. 1997. Hydrogen and carbon isotopic composition of methane as evidence for biogenic origin of natural gases from the Green Tuff Basin, Japan. *Organic Geochemistry,* 26**,** 399-407.

SANDER, R. 2015. Compilation of Henry's law constants (version 4.0) for water as solvent. *Atmos. Chem. Phys.,* 15**,** 4399-4981.

SANO, Y., KINOSHITA, N., KAGOSHIMA, T., TAKAHATA, N., SAKATA, S., TOKI, T., KAWAGUCCI, S., WASEDA, A., LAN, T., WEN, H., CHEN, A.-T.,

LEE, H., YANG, T. F., ZHENG, G., TOMONAGA, Y., ROULLEAU, E. & PINTI, D. L. 2017. Origin of methane-rich natural gas at the West Pacific convergent plate boundary. *Scientific Reports,* 7**,** 15646.

SANO, Y., KUSAKABE, M., HIRABAYASHI, J.-I., NOJIRI, Y., SHINOHARA, H., NJINE, T. & TANYILEKE, G. 1990. Helium and carbon fluxes in Lake Nyos, Cameroon: constraint on next gas burst. *Earth and Planetary Science Letters,* 99**,** 303-314.

SANO, Y. & MARTY, B. 1995. Origin of carbon in fumarolic gas from island arcs. *Chemical Geology,* 119**,** 265-274.

SANO, Y., MARTY, B. & BURNARD, P. 2013. Noble Gases in the Atmosphere. *In:* BURNARD, P. (ed.) *The Noble Gases as Geochemical Tracers.* Berlin, Heidelberg: Springer Berlin Heidelberg.

SCARSI, P. & CRAIG, H. 1996. Helium isotope ratios in Ethiopian Rift basalts. *Earth and Planetary Science Letters,* 144**,** 505-516.

SCHLOSSER, P. & WINCKLER, G. 2002. Noble Gases in Ocean Waters and Sediments. *Reviews in Mineralogy and Geochemistry,* 47**,** 701-730.

SCOTT, J. A., PUJOL, M., GYöRE, D., STUART, F. M. & GILFILLAN, S. M. V. 2021. Determining static reservoir connectivity using noble gases. *Chemical Geology,* 582**,** 120410.

SHERWOOD LOLLAR, B., FRAPE, S. K., FRITZ, P., MACKO, S. A., WELHAN, J. A., BLOMQVIST, R. & LAHERMO, P. W. 1993. Evidence for bacterially generated hydrocarbon gas in Canadian shield and fennoscandian shield rocks. *Geochimica et Cosmochimica Acta,* 57**,** 5073-5085.

SHERWOOD LOLLAR, B., LACRAMPE-COULOUME, G., SLATER, G. F., WARD, J., MOSER, D. P., GIHRING, T. M., LIN, L. H. & ONSTOTT, T. C. 2006. Unravelling abiogenic and biogenic sources of methane in the Earth's deep subsurface. *Chemical Geology,* 226**,** 328-339.

SHERWOOD LOLLAR, B., WESTGATE, T. D., WARD, J. A., SLATER, G. F. & LACRAMPE-COULOUME, G. 2002. Abiogenic formation of alkanes in the earth's crust as a minor source for global hydrocarbon reservoirs. *Nature,* 416**,** 522-524.

SMITH, S. P. 1985. Noble gas solubility in water at high temperature. *EOS, Trans Am. Geophys. Union,* 66.

SMITH, S. P. & KENNEDY, B. M. 1983. The solubility of noble gases in water and in NaCl brine. *Geochimica et Cosmochimica Acta,* 47**,** 503-515.

SONG, X., WANG, H., FU, X., MENG, L., SUN, Y., LIU, Z. & DU, R. 2022. Hydrocarbon retention and leakage in traps bounded by active faults: A case study from traps along the NDG fault in the Qinan area, Bohai Bay Basin, China. *Journal of Petroleum Science and Engineering,* 208**,** 109344.

STEVENS, S. H., MOODHE, K. D. & KUUSKRAA, V. A. China shale gas and shale oil resource evaluation and technical challenges. SPE Asia Pacific Oil and Gas Conference and Exhibition, 2013. SPE, SPE-165832-MS.

SUN, D. S., LIU, C. Y., YANG, M. H., DU, J., ZHANG, Y. & ZHANG, R. 2004. Evidences for the large-scale detachment structure in middle area of Jizhong Depression in Mid-Late Mesozoic period. *Geotectonica et Metallogenia,* 28**,** 126-133.

SUN, J. & BAO, H. 2018. Comprehensive characterization of shale gas reservoirs: A case study from Fuling shale gas field. *Petroleum Geology & Experiment,* 40**,** 1-12.

TANG, J., ZHANG, Y., ZHOU, J., LI, Y. & NIU, Y. 2023. Analysis of global helium industry chain and China's strategy. *Geological Bulletin of China,* 42**,** 1-13.

TAO, S., CHEN, Y. & YANG, Y. 2024. Helium resource and play classification systems, effective reservoir control elements, and enrichment patterns in China. *Journal of Natural Gas Geoscience,* 9**,** 219-241.

TIAB, D. & DONALDSON, E. C. 2016. Chapter 12 - Shale-Gas Reservoirs. *In:* TIAB, D. & DONALDSON, E. C. (eds.) *Petrophysics (Fourth Edition)*. Boston: Gulf Professional Publishing.

TIAN, H., LI, T., ZHANG, T. & XIAO, X. 2016. Characterization of methane adsorption on overmature Lower Silurian–Upper Ordovician shales in Sichuan Basin, southwest China: Experimental results and geological implications. *International Journal of Coal Geology,* 156**,** 36-49.

TOLSTIKHIN, I. N., BALLENTINE, C. J., POLYAK, B. G., PRASOLOV, E. M. & KIKVADZE, O. E. 2017. The noble gas isotope record of hydrocarbon field formation time scales. *Chemical Geology,* 471**,** 141-152.

TOLSTIKHIN, I. N., MAMYRIN, B. A., KHABARIN, L. B. & ERLIKH, E. N. 1974. Isotope composition of helium in ultrabasic xenoliths from volcanic rocks of Kamchatka. *Earth and Planetary Science Letters,* 22**,** 75-84.

TOLSTIKHIN, I. N. & O'NIONS, R. K. 1994. The Earth's missing xenon: A combination of early degassing and of rare gas loss from the atmosphere. *Chemical Geology,* 115**,** 1-6.

TORGERSEN, T. 1980. Controls on pore-fluid concentration of 4He and 222Rn and the calculation of 4He/222Rn ages. *Journal of Geochemical Exploration,* 13**,** 57-75.

TORGERSEN, T. 1989. Terrestrial helium degassing fluxes and the atmospheric helium budget: Implications with respect to the degassing processes of continental crust. *Chemical Geology: Isotope Geoscience Section,* 79**,** 1-14.

TORGERSEN, T. & KENNEDY, B. M. 1999. Air-Xe enrichments in Elk Hills oil field gases: role of water in migration and storage. *Earth and Planetary Science Letters,* 167**,** 239-253.

TUCKER, J. M., VAN KEKEN, P. E. & BALLENTINE, C. J. 2022. Earth's missing argon paradox resolved by recycling of oceanic crust. *Nature Geoscience,* 15**,** 85-90.

ULLAH, J., LUO, M., ASHRAF, U., PAN, H., ANEES, A., LI, D., ALI, M. & ALI, J. 2022. Evaluation of the geothermal parameters to decipher the thermal structure of the upper crust of the Longmenshan fault zone derived from borehole data. *Geothermics,* 98**,** 102268.

WACKER, J. F. 1989. Laboratory simulation of meteoritic noble gases. III. Sorption of neon, argon, krypton, and xenon on carbon: Elemental fractionation. *Geochimica et Cosmochimica Acta,* 53**,** 1421-1433.

WANG, G., JIN, Z., LIU, G., LIU, Q., LIU, Z., WANG, H., LIANG, X., JIANG, T. & WANG, R. 2020a. Geological implications of gamma ray (GR) anomalies in marine shales: A case study of the Ordovician-Silurian Wufeng-Longmaxi succession in the Sichuan Basin and its periphery, Southwest China. *Journal of Asian Earth Sciences,* 199**,** 104359.

WANG, G., LI, S., LI, X., ZHAO, W., ZHAO, S., SUO, Y., LIU, X., SOMERVILLE, I., LIU, Y., ZHOU, J. & WANG, Z. 2019a. Destruction effect on Meso-Neoproterozoic oil-gas traps derived from Meso-Cenozoic deformation in the North China Craton. *Precambrian Research,* 333**,** 105427.

WANG, G., LI, S., SUO, Y., ZHANG, X., ZHANG, Z., WANG, D., LIU, Z., LIU, Y., ZHOU, J., WANG, P. & GUO, L. 2022a. Deep-shallow coupling response of the Cenozoic Bohai Bay Basin to plate interactions around the Eurasian Plate. *Gondwana Research,* 102**,** 180-199.

WANG, H., FU, X., FAN, M., WANG, S., MENG, L. & DU, W. 2022b. Fault growth and linkage: Implications for trap integrity in the Qi'nan area of the Huanghua Depression in Bohai Bay Basin, China. *Marine and Petroleum Geology,* 145**,** 105875.

WANG, H., SHI, Z. & SUN, S. 2021a. Biostratigraphy and reservoir characteristics of the Ordovician Wufeng Formation—Silurian Longmaxi Formation shale in the Sichuan Basin and its surrounding areas, China. *Petroleum Exploration and Development,* 48**,** 1019-1032.

WANG, J., CHEN, M., WANG, J. & DENG, X. 1985. On the evolution of the geothermal regime of the North China Basin. *Journal of geodynamics,* 4**,** 133-148.

WANG, L., GOU, X., LIU, G., WANG, L., WANG, W. & WANG, M. 1997. The organic geochemistry and origin of natural gases in Sichuan Basin. *Acta Sedimentologica Sinica,* 15**,** 49-53.

WANG, L., LIN, S. & XIAO, W. 2023. Yangtze and Cathaysia blocks of South China: Their separate positions in Gondwana until early Paleozoic juxtaposition. *Geology,* 51**,** 723-727.

WANG, Q., HAO, F., NIU, C., ZOU, H., MIAO, Q., YIN, J., CAO, Y. & LIU, M. 2021b. Origins and deep petroleum dynamic accumulation in the southwest part of the Bozhong depression, Bohai Bay Basin: Insights from geochemical and geological evidences. *Marine and Petroleum Geology,* 134**,** 105347.

WANG, X., HE, S., JONES, S. J., YANG, R., WEI, A., LIU, C., LIU, Q., CHENG, C. & LIU, W. 2019b. Overpressure and its positive effect in deep sandstone

reservoir quality of Bozhong Depression, offshore Bohai Bay Basin, China. *Journal of Petroleum Science and Engineering,* 182**,** 106362.

WANG, X., LIU, W., LI, X., LIU, Q., TAO, C. & XU, Y. 2020b. Radiogenic helium concentration and isotope variations in crustal gas pools from Sichuan Basin, China. *Applied Geochemistry,* 117**,** 104586.

WANG, X., LIU, W., LI, X., TAO, C., BORJIGIN, T., LIU, P., LUO, H., LI, X. & ZHANG, J. 2022c. Application of noble gas geochemistry to the quantitative study of the accumulation and expulsion of lower Paleozoic shale gas in southern China. *Applied Geochemistry,* 146**,** 105446.

WANG, Z. 2018. Reservoir forming conditions and key exploration and development technologies for marine shale gas fields in Fuling area, South China. *Petroleum Research,* 3**,** 197-209.

WANG, Z., CAO, Y., SWENNEN, R., YUAN, G. & WANG, K. 2022d. Meteoric freshwater leaching and its significance to reservoir quality in a buried hill of lower-middle Jurassic fluvial sandstones: A case study from the Huanghua Depression, Bohai Bay Basin, China. *Journal of Petroleum Science and Engineering,* 210**,** 109834.

WANG, Z.-C., ZHAO, W.-Z., LI, Z.-Y., JIANG, X.-F. & LI, J. 2008. Role of basement faults in gas accumulation of Xujiahe Formation, Sichuan Basin. *Petroleum Exploration and Development,* 35**,** 541-547.

WANG, Z. S., HUA, S. J., YU, X. M. & JIANG, W. 2014. Grading evaluation and high quality source rock distribution in Qikou Sag. *Natural Gas Geoscience,* 25**,** 1896-1902.

WEI, G., CHEN, G., DU, S., ZHANG, L. & YANG, W. 2008. Petroleum systems of the oldest gas field in China: Neoproterozoic gas pools in the Weiyuan gas field, Sichuan Basin. *Marine and Petroleum Geology,* 25**,** 371-386.

WETHERILL, G. W. 1954. Variations in the Isotopic Abundances of Neon and Argon Extracted from Radioactive Minerals. *Physical Review,* 96**,** 679-683.

WHITICAR, M. J. 1999. Carbon and hydrogen isotope systematics of bacterial formation and oxidation of methane. *Chemical Geology,* 161**,** 291-314.

WIELER, R. 2014. 15.19 - Noble Gas Mass Spectrometry. *In:* HOLLAND, H. D. & TUREKIAN, K. K. (eds.) *Treatise on Geochemistry (Second Edition).* Oxford: Elsevier.

WIELER, R. 2023. A Journey in Noble Gas Cosmochemistry and Geochemistry. *Geochemical Perspectives,* 12**,** 1-2.

WOOD, D. & CAPUTI, R. 1966. Solubilities of Kr and Xe in fresh and sea water. *(No Title).*

XIAO, B., LIU, S., LI, Z., RAN, B., YE, Y., YANG, D. & LI, J. 2021. Geochemical characteristics of marine shale in the Wufeng Formation–Longmaxi Formation in

the northern Sichuan Basin, South China and its implications for depositional controls on organic matter. *Journal of Petroleum Science and Engineering,* 203**,** 108618.

XU, C., JIA-YU, R., YUE, L. & BOUCOT, A. J. 2004. Facies patterns and geography of the Yangtze region, South China, through the Ordovician and Silurian transition. *Palaeogeography, Palaeoclimatology, Palaeoecology,* 204**,** 353-372.

XU, C., SHEN, P., YANG, Y., LUO, B., HUANG, J., JIANG, X., XIE, J. & CEN, Y. 2014. Accumulation conditions and enrichment patterns of natural gas in the Lower Cambrian Longwangmiao Fm reservoirs of the Leshan-Longnǚsi Palaeohigh, Sichuan Basin. *Natural Gas Industry B,* 1**,** 51-57.

XU, Y. 1976. The application of rare gases and their isotopes in petroleum geology. *Translation Collection of Petroleum Geology,* 3.

XU, Y. & WANG, X. 1979. Rare gas isotopes in natural gas. *Geochimica.,* 4**,** 271-282.

XU, Z., JIANG, S., LIU, L., WU, K., LI, R., LIU, Z., SHAO, M., JIA, K. & FENG, Y. 2020a. Natural gas accumulation processes of tight sandstone reservoirs in deep formations of Songliao Basin, NE China. *Journal of Natural Gas Science and Engineering,* 83**,** 103610.

XU, Z., LIANG, X., LU, H., ZHANG, J., SHU, H., XU, Y., WU, J., WANG, G., LU, W., TANG, X. & SHI, W. 2020b. Structural deformation characteristics and shale gas preservation conditions in the Zhaotong National Shale Gas Demonstration Area along the southern margin of the Sichuan Basin. *Natural Gas Industry B,* 7**,** 224-233.

XUE, Y. A. & WANG, D. 2020. Formation conditions and exploration direction of large natural gas reservoirs in the oil-prone Bohai Bay Basin, East China. *Petroleum Exploration and Development,* 47**,** 280-291.

YAN, D., WANG, H., FU, Q., CHEN, Z., HE, J. & GAO, Z. 2015. Geochemical characteristics in the Longmaxi Formation (Early Silurian) of South China: Implications for organic matter accumulation. *Marine and Petroleum Geology,* 65**,** 290-301.

YANG, P., ZHANG, L., LIU, K., CAO, B., GAO, J. & QIU, G. 2021a. Diagenetic history and reservoir evolution of tight sandstones in the second member of the Upper Triassic Xujiahe Formation, western Sichuan Basin, China. *Journal of Petroleum Science and Engineering,* 201**,** 108451.

YANG, R., LIU, H., LI, H., ZHAO, C. & LI, C. 2022. Accumulation mechanism and model of coal measure derived oil and gas in the deep reservoir of Huanghua Depression, Bohai Bay Basin, China. *Journal of Natural Gas Geoscience.*

YANG, R., ZHAO, X., LI, H., ZHAO, C., PU, X., LIU, H., FU, L. & LI, C. 2020. Evolution characteristics of the upper Paleozoic source kitchen and its controlling effects on hydrocarbon accumulation in the Paleozoic petroleum system in Huanghua Depression, Bohai Bay Basin, China. *Journal of Petroleum Science and Engineering,* 193**,** 107415.

YANG, R., ZHAO, X., ZHAO, C., PU, X., LIU, H., LI, H., FU, L. & TANG, Y. 2021b. Hydrocarbon Charging and Accumulation in the Permian Reservoirs of the Wumaying Buried Hill, Huanghua Depression, Bohai Bay Basin, China. *Energies* [Online], 14.

YANG, W., PENG, B., WU, M., LI, J. & NI, P. 2016a. Evaluation for CO2 Geo-storage Potential and Suitability in Dagang Oilfield. *Energy Procedia,* 86**,** 41-46.

YANG, Y., WEN, L., LUO, B., WANG, W. & SHAN, S. 2016b. Hydrocarbon accumulation of Sinian natural gas reservoirs, Leshan-Longnüsi paleohigh, Sichuan Basin, SW China. *Petroleum Exploration and Development,* 43**,** 197-207.

YANG, Y. & XU, T. 2004. Hydrocarbon habitat of the offshore Bohai Basin, China. *Marine and Petroleum Geology,* 21**,** 691-708.

YATSEVICH, I. & HONDA, M. 1997. Production of nucleogenic neon in the Earth from natural radioactive decay. *Journal of Geophysical Research: Solid Earth,* 102**,** 10291-10298.

YE, H., ZHANG, B. & MAO, F. 1987. The Cenozoic tectonic evolution of the Great North China: two types of rifting and crustal necking in the Great North China and their tectonic implications. *Tectonophysics,* 133**,** 217-227.

YU, F. & KOYI, H. 2016. Cenozoic tectonic model of the Bohai Bay Basin in China. *Geological Magazine,* 153**,** 866-886.

YU, X., HE, Y. & JIANG, W. 2011. Hydrocarbon generation of Paleogene source rocks in Qikou Sag. *Natural Gas Geoscience,* 22**,** 1001-1008.

YU, Y., LIN, L., ZHAI, C., WANG, Y., LI, Y. & GUO, Y. 2018. Diagenesis and reservoir characteristics analysis of the Late Triassic Xujiahe Formation tight gas sandstone in the northern Sichuan Basin, China. *Energy Exploration & Exploitation,* 36**,** 743-763.

YUAN, G., CAO, Y., SUN, P., ZHOU, L., LI, W., FU, L., LI, H., LOU, D. & ZHANG, F. 2021. Genetic mechanisms of Permian Upper Shihezi sandstone reservoirs with multi-stage subsidence and uplift in the Huanghua Depression, Bohai Bay Basin, East China. *Marine and Petroleum Geology,* 124**,** 104784.

YUAN, G., CAO, Y., ZHANG, Y. & GLUYAS, J. 2017. Diagenesis and reservoir quality of sandstones with ancient "deep" incursion of meteoric freshwater——An example in the Nanpu Sag, Bohai Bay Basin, East China. *Marine and Petroleum Geology,* 82**,** 444-464.

YUAN, H., CHEN, S., DAI, K., JIA, G., WANG, P., LI, J. & GOU, Q. 2022. Cenozoic tectonic evolution of the Bohai Bay Basin: Constraints from strike-slip activities of the Wangjiagang fault zone, NE China. *Journal of Asian Earth Sciences,* 233**,** 105262.

YUAN, H., LIANG, J., GONG, D., XU, G., LIU, S. & WANG, G. 2012. Formation and evolution of Sinian oil and gas pools in typical structures, Sichuan Basin, China. *Petroleum Science,* 9**,** 129-140.

YUNYAN, N., JINXING, D., QINGHUA, Z., XIA, L., ANPING, H. & CHUN, Y. 2009. Geochemical characteristics of abiogenic gas and its percentage in Xujiaweizi Fault Depression, Songliao Basin, NE China. *Petroleum Exploration and Development,* 36**,** 35-45.

ZAIKOWSKI, A., KOSANKE, B. J. & HUBBARD, N. 1987. Noble gas composition of deep brines from the Palo Duro Basin, Texas. *Geochimica et Cosmochimica Acta,* 51**,** 73-84.

ZAIKOWSKI, A. & SPANGLER, R. R. 1990. Noble gas and methane partitioning from ground water: An aid to natural gas exploration and reservoir evaluation. *Geology,* 18**,** 72-74.

ZENG, B., DUAN, H., BAI, Y. & MENG, W. 2018. Forecasting the output of shale gas in China using an unbiased grey model and weakening buffer operator. *Energy,* 151**,** 238-249.

ZENG, L., ZHANG, H., ZHANG, X. & ZHAO, Z. 2023. Geological characteristics and gas accumulation pattern of tight gas reservoirs in the Upper Triassic Xujiahe Formation in northeastern Sichuan Basin. *China Petroleum Exploration,* 28**,** 121-131.

ZHANG, D. 2022. Development prospect of natural gas industry in the Sichuan Basin in the next decade. *Natural Gas Industry B,* 9**,** 119-131.

ZHANG, F., WU, Z., LI, W., ZHU, J., FU, L., LI, H., LOU, D. & ZHAO, Y. 2019a. Structural characteristics and its tectonic evolution of Huanghua depression during the Indosinian-Yanshanian. *Journal of China University of Mining & Technology,* 48**,** 792-807.

ZHANG, G., GUO, A., WANG, Y., LI, S., DONG, Y., LIU, S., HE, D., CHENG, S., LU, R. & YAO, A. 2013. Tectonics of South China continent and its implications. *Science China Earth Sciences,* 56**,** 1804-1828.

ZHANG, J., ZHENG, H., WANG, G., LIU, Z., QI, Y., HUANG, Z. & FAN, X. 2020. In-situ stresses, abnormal pore pressures and their impacts on the Triassic Xujiahe reservoirs in tectonically active western Sichuan basin. *Marine and Petroleum Geology,* 122**,** 104708.

ZHANG, M., CHAKRABORTY, N., KARPYN, Z. T., EMAMI-MEYBODI, H. & AYALA, L. F. 2021a. Experimental and numerical study of gas diffusion and sorption kinetics in ultratight rocks. *Fuel,* 286**,** 119300.

ZHANG, T., ZHANG, M., BAI, B., WANG, X. & LI, L. 2008. Origin and accumulation of carbon dioxide in the Huanghua depression, Bohai Bay Basin, China. *AAPG bulletin,* 92**,** 341-358.

ZHANG, W., CHEN, W., LI, Y., ZHOU, J. & YANG, G. 2024. Noble gas characteristics of microbial gas in the Qaidam Basin, China: Implications for helium enrichment processes. *Marine and Petroleum Geology,* 165**,** 106897.

ZHANG, W., HU, W., YANG, S., KANG, X. & ZHU, N. 2022a. Differences and constraints of varying gas dryness coefficients in the Cainan oil-gas field, Junggar Basin, NW China. *Marine and Petroleum Geology,* 139**,** 105582.

ZHANG, W., LI, Y., ZHAO, F., HAN, W., LI, Y., WANG, Y., HOLLAND, G. & ZHOU, Z. 2019b. Using noble gases to trace groundwater evolution and assess helium accumulation in Weihe Basin, central China. *Geochimica et Cosmochimica Acta,* 251**,** 229-246.

ZHANG, W., LI, Y., ZHAO, F., HAN, W., ZHOU, J., HOLLAND, G. & ZHOU, Z. 2019c. Quantifying the helium and hydrocarbon accumulation processes using noble gases in the North Qaidam Basin, China. *Chemical Geology,* 525**,** 368-379.

ZHANG, Y., JIANG, S., HE, Z., LI, Y., XIAO, D., CHEN, G. & ZHAO, J. 2021b. Coupling between Source Rock and Reservoir of Shale Gas in Wufeng-Longmaxi Formation in Sichuan Basin, South China. *Energies,* 14.

ZHANG, Y. & LU, B. 2015. Prediction of global energy trend and analysis on energy technology innovation characteristics. 35**,** 1-10.

ZHANG, Y., ZHANG, M., MEI, H. & ZENG, F. 2019d. Study on salt precipitation induced by formation brine flow and its effect on a high-salinity tight gas reservoir. *Journal of Petroleum Science and Engineering,* 183**,** 106384.

ZHANG, Z., WANG, C., WANG, Q. & XU, X. 2022b. Development prospects of China's helium market. *Petroleum and New Energy,* 34**,** 36-41.

ZHAO, Q., ZHOU, T., WANG, H., JIN, Y., ZHOU, S. & DUAN, X. 2023a. Determination of adsorption parameters in shale gas resource/reserve calculation: Case study of Wufeng Formation–Longmaxi Formation in the Sichuan Basin. *Natural Gas Industry B,* 10**,** 304-311.

ZHAO, W., LI, J., YANG, T., WANG, S. & HUANG, J. 2016a. Geological difference and its significance of marine shale gases in South China. *Petroleum Exploration and Development,* 43**,** 547-559.

ZHAO, X., JIN, F., LI, Y., WANG, Q., ZHOU, L., LYU, Y., PU, X. & WANG, W. 2016b. Slope belt types and hydrocarbon migration and accumulation mechanisms in rift basins. *Shiyou Kantan Yu Kaifa/Petroleum Exploration and Development,* 43**,** 841-849.

ZHAO, X., PU, X., JIANG, W., ZHOU, L., JIN, F., XIAO, D., FU, L. & LI, H. 2019. An exploration breakthrough in Paleozoic petroleum system of Huanghua Depression in Dagang Oilfield and its significance, North China. *Petroleum Exploration and Development,* 46**,** 651-663.

ZHAO, X., ZHOU, L., PU, X., JIN, F., JIANG, W., XIAO, D., HAN, W. & SHI, Z. 2018. Development and exploration practice of the concept of hydrocarbon accumulation in rifted-basin troughs: A case study of Paleogene Kongdian Formation in Cangdong sag, Bohai Bay Basin. *Petroleum Exploration and Development,* 45**,** 1166-1176.

ZHAO, X., ZHOU, L., PU, X., JIN, F., SHI, Z., HAN, W., JIANG, W., HAN, G., ZHANG, W., WANG, H. & MA, J. 2020. Formation conditions and enrichment model of retained petroleum in lacustrine shale: A case study of the Paleogene in Huanghua depression, Bohai Bay Basin, China. *Petroleum Exploration and Development,* 47**,** 916-930.

ZHAO, Z. & WINDLEY, B. 1990. Cenozoic tectonic extension and inversion of the Jizhong Basin, Hebei, northern China. *Tectonophysics,* 185**,** 83-89.

ZHAO, Z., ZHANG, H., ZHANG, X. & ZENG, L. 2023b. Geological characteristics and gas accumulation pattern of tight gas reservoirs in the Upper Triassic Xujiahe Formation in northeastern Sichuan Basin. *China Petroleum Exploration,* 28**,** 121.

ZHENG, H., ZHANG, J. & QI, Y. 2020. Geology and geomechanics of hydraulic fracturing in the Marcellus shale gas play and their potential applications to the Fuling shale gas development. *Energy Geoscience,* 1**,** 36-46.

ZHOU, J. 2022. Current status and recommendations on the theoretical and technical research on helium resource investigation. *Northwestern Geology,* 55**,** 1-10.

ZHOU, J., CHEN, Y. & WANG, X. 2022. Analysis of helium resource production and market development status. *Nat. Gas Chem.-C1 Chem. Chem,* 47**,** 42-48.

ZHOU, L., ALGEO, T. J., SHEN, J., HU, Z., GONG, H., XIE, S., HUANG, J. & GAO, S. 2015. Changes in marine productivity and redox conditions during the Late Ordovician Hirnantian glaciation. *Palaeogeography, Palaeoclimatology, Palaeoecology,* 420**,** 223-234.

ZHOU, L., HAN, G., DONG, Y., SHI, Q., MA, J., HU, J., REN, S., ZHOU, K., WANG, J. & SI, W. 2019. Fault-sand combination modes and hydrocarbon accumulation in Binhai fault nose of Qikou Sag, Bohai Bay Basin, East China. *Petroleum Exploration and Development,* 46**,** 919-934.

ZHOU, L., LI, Y., JIN, F., FU, L., PU, X., DA, L., LI, H., LIU, H. & XU, W. 2021. Tight Sandstone Reservoir Formation Mechanism of Upper Paleozoic Buried Hills in the Huanghua Depression, Bohai Bay Basin, Eastern China. *Minerals,* 11**,** 1368.

ZHOU, W. & DAI, J. 2008. The characteristics and evaluation of fractures distribution in Xujiahe formation in the western depression of the Sichuan Basin. *Petroleum Geology & Experiment,* 30**,** 20.

ZHOU, Z. & BALLENTINE, C. J. 2006. 4He dating of groundwater associated with hydrocarbon reservoirs. *Chemical Geology,* 226**,** 309-327.

ZHOU, Z., BALLENTINE, C. J., KIPFER, R., SCHOELL, M. & THIBODEAUX, S. 2005. Noble gas tracing of groundwater/coalbed methane interaction in the San Juan Basin, USA. *Geochimica et Cosmochimica Acta,* 69**,** 5413-5428.

ZHOU, Z., BALLENTINE, C. J., SCHOELL, M. & STEVENS, S. H. 2012. Identifying and quantifying natural CO2 sequestration processes over geological timescales: The Jackson Dome CO2 Deposit, USA. *Geochimica et Cosmochimica Acta,* 86**,** 257-275.

ZHU, G., WANG, T., XIE, Z., XIE, B. & LIU, K. 2015. Giant gas discovery in the Precambrian deeply buried reservoirs in the Sichuan Basin, China: Implications for gas exploration in old cratonic basins. *Precambrian Research,* 262**,** 45-66.

ZOU, C., DONG, D., WANG, Y., LI, X., HUANG, J., WANG, S., GUAN, Q., ZHANG, C., WANG, H., LIU, H., BAI, W., LIANG, F., LIN, W., ZHAO, Q.,

LIU, D., YANG, Z., LIANG, P., SUN, S. & QIU, Z. 2015. Shale gas in China: Characteristics, challenges and prospects (I). *Petroleum Exploration and Development,* 42**,** 753-767.

ZOU, C., DONG, D., WANG, Y., LI, X., HUANG, J., WANG, S., GUAN, Q., ZHANG, C., WANG, H., LIU, H., BAI, W., LIANG, F., LIN, W., ZHAO, Q., LIU, D., YANG, Z., LIANG, P., SUN, S. & QIU, Z. 2016. Shale gas in China: Characteristics, challenges and prospects (II). *Petroleum Exploration and Development,* 43**,** 182-196.

ZOU, C., ZHANG, G., TAO, S., HU, S., LI, X., LI, J., DONG, D. & ZHU, R. 2010. Geological features and exploration discoveries of unconventional resources and the petroleum geological theory. *Petroleum Exploration and Development,* 37**,** 641-653.

ZOU, C., ZHU, R., CHEN, Z.-Q., OGG, J. G., WU, S., DONG, D., QIU, Z., WANG, Y., WANG, L. & LIN, S. 2019. Organic-matter-rich shales of China. *Earth-Science Reviews,* 189**,** 51-78.

ZUO, Y.-H., YE, B., WU, W.-T., ZHANG, Y.-X., MA, W.-X., TANG, S.-L. & ZHOU, Y.-S. 2017. Present temperature field and Cenozoic thermal history in the Dongpu depression, Bohai Bay Basin, North China. *Marine and Petroleum Geology,* 88**,** 696-711.